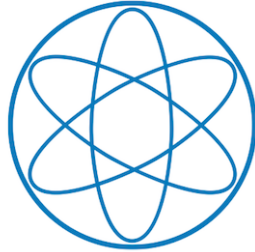Physik Department

Development of a new superfluid helium ultra-cold
neutron source and a new magnetic trap for neutron
lifetime measurements

Kent Kwan Ho Leung

Technische Universität München

TECHNISCHE UNIVERSITÄT MÜNCHEN

Lehrstuhl für Experimentalphysik E18

Development of a new superfluid helium ultra-cold neutron source and a new magnetic trap for neutron lifetime measurements

Kent Kwan Ho Leung

Vollständiger Abdruck der von der Fakultät für Physik der Technischen Universität München zur Erlangung des akademischen Grades eines

Doktors der Naturwissenschaften (Dr. rer. nat.)

genehmigten Dissertation.

<table>
<tr><td>Vorsitzender:</td><td></td><td>Univ.-Prof. Dr. A. Ibarra</td></tr>
<tr><td>Prüfer der Dissertation:</td><td>1.</td><td>Univ.-Prof. Dr. P. Fierlinger</td></tr>
<tr><td></td><td>2.</td><td>Univ.-Prof. Dr. P. Böni</td></tr>
</table>

Die Dissertation wurde am 30.10.2012 bei der Technischen Universität München eingereicht und durch die Fakultät für Physik am 12.02.2013 angenommen.

Abstract

The development of an Ultra-Cold Neutron (UCN) source at the Institut Laue-Langevin (ILL) based on super-thermal down-scattering of a Cold Neutron (CN) beam in superfluid ^{4}He is described. A continuous flow, self-liquefying ^{3}He cryostat was constructed. A beryllium coated prototype converter vessel with a vertical, window-less extraction system was tested on the PF1b CN beam at the ILL. Accumulation measurements with a mechanical valve, and continuous measurements with the vessel left open, were made.

The development of a new magnetic UCN trap for neutron lifetime (τ_β) measurements is also described. A 1.2 m long octupole made from permanent magnets, with a bore diameter of 94 mm and surface field of 1.3 T, was assembled. This will be combined with a superconducting coil assembly and used with vertical confinement of UCN by gravity. A discussion of the systematic effects, focussing on the cleaning of above-threshold UCNs, is given. The possibility of detecting the charged decay products is also discussed. UCN storage experiments with the magnetic array and a fomblin-coated piston were performed on PF2 at the ILL. These measurements studied depolarization, spectrum cleaning, and loss due to material reflections in the trap experimentally.

Contents

Acknowledgments

First off, I would like to thank Oliver Zimmer, my thesis supervisor for the past 5 years. Without his patient support, the freedom given to pursue research, and the resources made available, none of the work in this thesis would have been possible. I am also certain I still have a debt of a few bottles of wine from lost bets that is still owed!

I would like to express my gratitude to all my colleagues in the NPP group at the ILL, especially Peter Geltenbort, Michael Jentschel, Sergey Ivanov, and Torsten Soldner, for putting up with my bombardment of questions and lending me equipment at crucial times. Above all, though, I would like to acknowledge Martin Simson. He contributed greatly not only to the corrections of this thesis, but to a large part of the experimental work as well. Many hours were spent together creating "technological" solutions to problems, and engaging in an eternal conflict against cryogenics.

The experiments would also not have been achieved without the technical staff in the NPP group. I would especially like to thank Mathieu Guigou, Thomas Brenner, and Didier Berruyer for going beyond the call of duty and producing last minute parts when the need arose. The ILL *cryogénie* staff has also been most helpful, in particular Eddy Lelievre-Berna, Olivier Losserand, and Xavier Tonon.

All the fun times I've shared with my dear friends in Grenoble will be treasured. Thank you to Jessica and Mouna for your unwavering moral support. May we remain close friends well into the future. And Martin, I am glad to be able to meet someone who shares my passion and life perspective with. Thanks for all the great discussions and the innumerable, and often too many, beers we've had together.

Lastly, and also most importantly, I would like to express eternal, boundless gratitude towards my family. My parents, Angela and Stanley, have offered their indefatigable love and support throughout the whole process. Sometimes it may appear that this was taken for granted. But deep down I know the tireless effort that you have put in.

Many years ago I made a promise to my late maternal grandmother that I would do my best to simply get admitted to a university. I hope my current efforts contribute to satisfying further aspirations she may have had for me.

Chapter 1

Introduction and theory overview

Due to the wide-range of topics in the field of UCN physics covered in the two major topics in this thesis—production of Ultra-Cold Neutrons (UCNs) with a superfluid helium source and magnetic trapping of UCNs for neutron lifetime measurements, only a brief overview of the key concepts required will be given. The interested reader is referred to the books of Refs. [GRL91] and [Ign90] on the field.

1.1 Ultracold neutrons

The relationship between a neutron's kinetic energy E_n, velocity v_n, and De Broglie wavelength λ_n is given by:

$$E_n = \frac{m_n v^2}{2} = \frac{h^2}{2m_n \lambda_n^2} = \frac{\hbar^2 k^2}{2m_n} \, , \qquad (1.1)$$

where m_n is the neutron mass and $k = 2\pi/\lambda_n$ is the wavenumber. It is also conventional, due to the moderation process of neutrons, to relate the kinetic energy to a temperature T_n by $E = k_B T_n$, where k_B is Boltzmann's constant.

Neutrons are loosely categorized into (T_n, λ_n, v_n, E_n): *Thermal* [1] (300 K, 1.8 Å, 2200 m s^{-1}, 25 meV), *Cold* (0.6 − 300 K, 1.8 − 40 Å, 100 − 2200 m s^{-1}, 0.05 −

---

[1]Note that while the other categories are for a range of neutron energies, a thermal neutron refers to a specific temperature.

25 meV), *Very-Cold* ($2 - 600$ mK, $40 - 565$ Å, $7 - 100$ m s^{-1}, $0.3 - 500$ µeV), and *Ultra-Cold* (< 2 mK, > 565 Å, < 7 m s^{-1}, < 300 neV).

The former two names originate from the moderation process used to produce them (described in Sec. 1.2). The definition of UCNs are free neutrons with a sufficiently low energy such that they can undergo reflection at all incident angles from material walls due to an effective optical potential. How this can occur is described next.

The neutron is an electrically neutral hadron. It participates in all of the four-known fundamental interactions. The ability to reflect and confine UCNs offers the possibilities to perform unique experiments with them. The field of UCN physics covers all the possible experiments that can be done with this very specific subset of neutrons. This field covers a region that overlaps with particle physics (at the low-energy scale), cosmology, and nuclear physics.

1.1.1   The gravitational interaction

The neutron has a mass of $m_n \approx 940$ MeV c^{-2} or 1.6749×10^{-27} kg in SI units. Therefore, it has an interaction energy in the Earth's gravitational field of:

$$V_{\text{grav}} = m_n g h = \left(102 \, \text{neV m}^{-1}\right) h, \tag{1.2}$$

where h is the vertical displacement and $g \approx 9.8$ m s^{-2} is the acceleration of gravity. In experiments using thermal or cold neutrons, the effects of gravity can usually be negligible due to the short survival times of the neutrons. However, with UCN experiments, since they are confined for up to several hundred seconds, gravity has a significant influence.

1.1.2   The nuclear weak interaction

The mass of a neutron m_n is larger than that of a proton m_p. Therefore, the weak interaction energetically allows the free neutron to decay into a proton. However, due to the small mass difference of $(m_n - m_p)c^2 \approx 1.3$ MeV, the only possible decay channel is through the production of the electron, the lightest lepton, which has a mass $m_e \approx 0.5$ MeV, via the exchange of a virtual W boson. In the standard β-decay of a neutron, $n \rightarrow p + e^- + \bar{\nu}_e$, there is also an emission of an electron antineutrino $\bar{\nu}_e$.

Since the mass difference is similar in size to the nuclear binding energy, the half-life of the β-decay of a neutron inside a bound nucleus can vary greatly— from a few nano-seconds to stability. Since it is free from the effects of a nuclei, the β-decay of the free neutron is considered the model decay process. It proceeds with a mean lifetime of $\tau_{\beta,n} \approx 15$ mins. Due to the their low velocities, time dilation effects are negligible. The theoretical description of the weak interactions of the neutron is given in Sec. 1.3.

The value of $\tau_{\beta,n}$ sets the maximum time constant with which UCNs can be stored for. Besides in experiments that aim to measure the neutron lifetime with UCNs—which is done by storing them for time constants as close to $\tau_{\beta,n}$ as possible in specifically designed trap—other loss processes usually dominate β-decay.

1.1.3 Electromagnetic interaction

The neutron is an electrically neutral (verified to a level of $< 10^{-21}\,e$ [Ber12]), spin-1/2 particle that possesses a magnetic dipole moment due to the internal structure of the electrically charged quarks. This magnetic moment is anti-parallel to the spin of the neutron and is $\approx -2/3$ of the magnetic moment of the proton[2]. The magnitude of the neutron magnetic moment is $\mu_N = -60.3\,\mathrm{neV\,T^{-1}}$ in units most convenient for this thesis. When the neutron experiences an external magnetic field $\vec{B}$, its spin has two possible eigenstates (or "spin-states"), with their interaction energy given by:

$$V_{\mathrm{mag}} = -\vec{\mu}_N.\vec{B} = \pm\left(60.3\,\mathrm{neV\,T^{-1}}\right)|B|, \tag{1.3}$$

where the higher interaction energy (i.e. positive value) is for the neutron spin parallel to the external field (and thus magnetic moment anti-parallel) and the lower interaction energy is for the neutron spin anti-parallel (magnetic moment parallel) to the external field.

If the magnetic is inhomogeneous, that is if $|\vec{B}(\vec{r})|$ varies for different points in space, then the neutron will experience a Stern-Gerlach-type force given by:

$$\vec{F}_{\mathrm{mag}} = -\vec{\nabla}V_{\mathrm{mag}} = \pm|\vec{\mu}_n|\,\vec{\nabla}|\vec{B}(\vec{r})|. \tag{1.4}$$

---

[2]This can be argued through a simple quark model[Abe08] considering the various possible spin combinations. The experimentally measured value of $\mu_n/\mu_p = 0.68497935(17)$.

Neutrons that experience a force towards regions of higher magnetic field strength are called *high-field seekers*, if they experience a force towards regions of lower magnetic field strength they are called *low-field seekers*. It is this force that allows UCNs with sufficiently low-energy to be confined by magnetic field gradients.

If a neutron in a particular spin-state experiences a varying magnetic field—which may come from a varying magnetic field in time $\vec{B}(t)$ or from a moving UCN in a spatially-varying $\vec{B}(\vec{r}(t))$—then its spin will remain in the same spin-state with respect to the new magnetic field if the change satisfies the adiabatic condition:

$$\gamma_n B \gg \frac{d\vec{B}/dt}{B} \tag{1.5}$$

where $\gamma_n = 2\mu_n/\hbar = 1.8325 \times 10^8 \, \text{Hz} \, \text{T}^{-1}$ is the gyromagnetic ratio of the neutron and $\gamma_n B$ is the famous Larmor precession frequency. If the neutrons experience a varying magnetic field that is too rapid, then non-adiabatic transitions between the two spin-states can occur. This can turn a neutron from a high-field seeker to a low-field seeker, or vise versa. This transition can be deliberately induced, as in the case of a spin-flipper, but it can also come from unwanted interactions in the form of depolarization or Majorana spin-flips.

1.1.4   The nuclear strong interaction

Neutrons and protons are bound in the nucleus by the nuclear strong force. This short-ranged interaction in a nucleus can be represented by an effective spherical square-well potential with a depth $V_{\text{nuclear}} \approx 40 \, \text{MeV}$ and radius of $R_0 \approx (1.25 \times 10^{-15} \, \text{m}) \, A^{1/3}$, where A is the number of nucleons. For slow neutrons, where $kR_0 >> 1$, when they encounter the nuclear potential the scattered wave is spherically symmetric (s-wave only).

The Fermi potential and the optical potential

The neutron's energy is small compared to the nuclear potential, therefore its wavefunction is strongly altered in the vicinity of the nuclei. However, since the range over which this occurs is very small, the wavefunction is only slightly altered outside of this small range. It is possible to introduce an effective potential that can be used to calculate the small changes to the wavefunction

of the neutron far from the nucleus by perturbation theory [Fer36]. By applying the first Born approximation, this effective potential is given by:

$$U_{\mathrm{F}}(\vec{r}) = \frac{2\pi\hbar^2 a}{m_n}\delta^{(3)}(\vec{r}) \;,\tag{1.6}$$

which is called the Fermi pseudo-potential. In neutron physics it is customary to use this pseudo-potential from experimentally measured values of a, the neutron scattering length.

When a neutron's wavelength is large, it interacts with a "forest" of these δ-functions. An effective or optical potential $U_{\mathrm{opt}}(\vec{r})$ of a material comprising of different elements and isotopes, which is in general a complex number, is defined by:

$$U_{\mathrm{opt}}(\vec{r}) = V_{\mathrm{opt}} - iW \;,\tag{1.7}$$

with:

$$V_{\mathrm{opt}} = \frac{2\pi\hbar^2}{m_n}\sum_i n_i(\vec{r})b_i \;\; \text{and} \;\; W = \frac{\hbar}{2}\sum_i n_i(\vec{r})\sigma_{\mathrm{loss}}(v_n)v_n \;,\tag{1.8}$$

where n_i is number density of the i'th material at the location $\vec{r}$, b_i is the bound coherent scattering length, $\sigma_{\mathrm{loss}}(v_n)$ is sum of the cross-sections that causes a loss of neutrons, and v_n is the neutron velocity in the medium. V_{opt}, which is the real part of U_{opt}, can take on positive and negative values [3]. $\sigma_{\mathrm{loss}}(v_n)$ is the sum of the cross-sections of all loss processes. For UCNs this includes nuclear capture reactions σ_{cap} and also inelastic scattering transitions $\sigma_{\mathrm{i.e.}}$ that increases a neutron's energy above the UCN range. Both σ_{cap} and $\sigma_{\mathrm{i.e.}}$ are $\propto 1/k'$, where k' is the wavenumber inside a material. This makes W independent of v_n.

The wavefunction describing a neutron $\psi(\vec{r})$ obeys the Schrödinger equation with the optical potential. I.e.:

$$\left(-\frac{\hbar^2}{2m_n}\nabla + U_{\mathrm{opt}}(\vec{r})\right)\psi(\vec{r}) = E\psi(\vec{r}) \;.\tag{1.9}$$

---

[3]In general the term neutron optical potential will refer to the real part V_{opt} only. The convention used in this thesis for V_{pot} of a specific material is to have the "opt" subscript replaced with the name of the material.

1.1.5   Reflection and losses of UCNs

The surface of a smooth material can be treated as a potential step function with a height V_{opt} given by Eq. 1.7. An incoming neutron, with total kinetic energy E_n and a polar angle θ (the angle normal to the surface) has an transverse energy $E_{n,\perp} = E_n \cos^2 \theta$. The reflection coefficient R is found by solving Eq. 1.9 with boundary conditions for an incoming plane wave with $k = \sqrt{2\, m_n E_n}/\hbar$, a reflected plane wave of diminished or equal amplitude, and a transmitted wave. The transmitted wave is also a plane wave if $E_{n,\perp} > V_{\mathrm{opt}}$, but with $k' = \sqrt{2\, m_n \left(V_{\mathrm{opt}} - E_n\right)}/\hbar$ (i.e., specular reflection); or if $E_{n,\perp} < V_{\mathrm{opt}}$, it is an exponentially decaying wave with a characteristic penetration length: $\hbar/\sqrt{2 m_n (V_{\mathrm{opt}} - E_{n,\perp})}$.

The reflection probability can be defined as: $|R(E_{n,\perp})|^2 \equiv 1 - \mu(E_{n,\perp})$, where $\mu(E_{n,\perp})$ is the loss probability per bounce. For the case when $E_{n,\perp} < V_{\mathrm{opt}}$ and $W \ll V_{\mathrm{opt}}$ the reflection probability is given by:

$$|R(E_{n,\perp})|^2 = 1 - 2\frac{W}{V_{\mathrm{opt}}}\sqrt{\frac{E_{n,\perp}}{V_{\mathrm{opt}} - E_{n,\perp}}} \; . \tag{1.10}$$

When $W = 0$, it can be seen that $|R(E_{n,\perp})|^2 = 1$. And if $E_n < V_{\mathrm{opt}}$, then a neutron will be reflected at all incoming angles θ. This is the definition of a UCN. V_{opt} varies from material to material. The known material with the largest is ^{58}Ni with $V_{^{58}\mathrm{Ni}} \approx 335\,\mathrm{neV}$. This defines the highest energy of UCNs. The materials used for UCN storage in the experiments in this thesis are beryllium, stainless steel, and fomblin, with $V_{\mathrm{Be}} \approx 252\,\mathrm{neV}$, $V_{\mathrm{SS}} \approx 184\,\mathrm{neV}$, and $V_{\mathrm{fomblin}} \approx 107\,\mathrm{neV}$.

In general $W \neq 0$. It is more convenient to discuss in terms of the energy independent loss factor, defined by $f = W/V_{\mathrm{opt}}$. This value is $f \approx 10^{-4} - 10^{-5}$ for the materials that are used for UCN storage. The approximation that $f \ll 1$ is true for more materials except for very strong absorbers.

When $E_{n,\perp} > V_{\mathrm{opt}}$ and $f \ll 1$ (for both $V_{\mathrm{opt}} > 0$ and $V_{\mathrm{opt}} < 0$):

$$|R(E_{n,\perp})|^2 = \frac{V_{\mathrm{opt}}^2}{\left(2E_{n,\perp} + 2\sqrt{E_{n,\perp}}\sqrt{E_{n,\perp} - V_{\mathrm{opt}}} - V_{\mathrm{opt}}\right)^2} \; . \tag{1.11}$$

Hence, a UCN can still be reflected even if its transverse energy is greater than

the optical potential of the material [4]. And reflection occurs even when V_{opt} is negative. For example in polyethylene, which is used in the experiments of this thesis as a UCN remover, has $V_{\text{PE}} = -9\,\text{neV}$. When a UCN is not reflected, it is transmitted into the material. Unless it is a thin foil—aluminium with $V_{\text{Al}} \approx 54\,\text{neV}$ and $W_{\text{Al}} \approx 0.001\,\text{neV}$ is normally used as the material— transmission into the bulk of a material by a UCN will most likely result in the loss of the UCN unless $W = 0$ (like in the case for ^4He) due to the high density of nuclei. Polyethylene is used as a UCN remover since $W_{\text{PE}} \approx 0.5\,\text{neV}$.

Specular and non-specular reflections

The material surface above was treated as an idealized smoothed surface and only specular reflections were assumed to occur. In specular reflection, the outgoing angle θ_f, the angle between the velocity and the normal to the surface, will be equal to the incoming angle θ_i (i.e., $\theta_i = \theta_f$); and the whole process remains in the same transverse plane to the surface.

In reality, however, a surface will contain surface roughness. This can cause non-specular reflections. In the most simple model of non-specular reflections, called the Lambert model [Lam60], there is a fixed probability of "completely" diffuse reflections—otherwise it is a specular reflection. After a diffuse reflection the probability of a UCN leaving the surface with an angle θ_f into the solid angle $d\Omega$ is given by $P(\theta_f)\,d\Omega = \cos\theta_f\,d\Omega$. I.e., it is independent of the incoming angles. Using this model to describe UCN transportation in electropolished stainless steel UCN guides, the probability of diffuse reflections was found to be $\approx 5-20\%$ [5].

1.1.6 The storage of a UCN gas

The UCNs confined in a container are not in thermal equilibrium with the material side walls. Recall that their "temperature" $T_n = E_n/k_B < 2\,\text{mK}$. This is because any transfer of the thermal motion of the material to the UCNs,

---

[4]The dependence on W in this equation is to the 2nd order and is thus neglected.

[5]A rarified gas flow theory or a diffusion theory was used to describe the UCNs. This is summarized in Ref. [GRL91]. There is a more sophisticated model, called the micro-roughness model (also described in Ref. [GRL91]). Some experiments, for instance Ref. [Atc10], has found that this describes the non-specular reflections on real surfaces more accurately.

due to the low speeds of the latter, will most likely result in heating the UCN above the confinable energy range.

An ideal gas is a set of point particles that have an isotropic velocity distribution that do not interact with each other. Due to the low densities of UCNs, neutron-neutron interactions do not occur. Thus the second condition is fulfilled. Non-specular reflections with the side walls can randomize the UCN directions and create this isotropicity. Therefore, having material walls with high non-specular reflection probabilities will reduce the time it takes to reach this condition; having wavy or corrugated side walls, that is, a trap with a geometry with low symmetry, will also help.

In Ref. [GRL91], it was argued that it should not take more than a few seconds in a trap—even if the walls are highly specular—for the isotropic condition to be satisfied. This is a lot shorter than typical holding times in experiments. However, recently the problem of highly symmetric orbits in traps—in particular fluid-walled traps or magnetic traps—have been bought to attention. Understanding when, and to what degree, the isotropic assumption can be applied is investigated in this thesis.

If an isotropic UCN gas is assumed, the rate of particles incident on a surface with angle θ is $\propto \cos\theta\, d\Omega$. The reflection probabilities per bounce in Eq. 1.10 can be averaged over this. It becomes dependent only on the total kinetic energy E_n (for $E_{n,\perp} < V_{\mathrm{opt}}$ and $f \ll 1$):

$$|\bar{R}(E_n)|^2 = 1 - 2f\left[\frac{V_{\mathrm{opt}}}{E_n}\sin^{-1}\left(\frac{E_n}{V_{\mathrm{opt}}}\right)^{1/2} - \left(\frac{V_{\mathrm{opt}}}{E_n} - 1\right)^{1/2}\right]. \qquad (1.12)$$

Also for an isotropic UCN gas, the rate of collisions J off a patch of the material wall located at $\vec{r}$ with a surface area A is: $J(\vec{r}) = \frac{1}{4}\bar{\rho}_{\mathrm{UCN}}(\vec{r})\bar{v}(\vec{r})A$, where $\bar{\rho}_{\mathrm{UCN}}(\vec{r})$ and $\bar{v}(\vec{r})$ are the local density and local average velocity of the UCNs around the patch of surface.

The local density and velocities have to be used due to the variations in the potential energy $E_{\mathrm{pot}}(\vec{r})$ a UCN experiences. This can come from variations in V_{grav}, V_{mag} or V_{opt}. The total energy $E_{\mathrm{tot}} = E_n + E_{\mathrm{pot}}$, of course, remains unchanged. Thus when a UCN travels from $\vec{r}_1 \to \vec{r}_2$ and experiences a change $\Delta E_{\mathrm{pot}} = E_{\mathrm{pot}}(\vec{r}_2) - E_{\mathrm{pot}}(\vec{r}_1)$, it will have a kinetic energy $E \to E_n' = E_n - \Delta E_{\mathrm{pot}}$. Its velocity will change $v(\vec{r}_1) = \sqrt{2E_n(\vec{r}_1)/m_n} \to v(\vec{r}_2) = \sqrt{2E_n'/m_n}$. The real

space density $\rho_{\text{UCN}}(\vec{r})$ will vary since the UCNs obey Liouville's theorem, which states that the phase space density:

$$\rho_{\text{p.s.}} = \frac{d^6N}{d^3r\,d^3p_n} \tag{1.13}$$

remains a constant over the entire system ($p_n = \sqrt{2m_nE_n}$ is the momentum). The momentum space available to a neutron at $\vec{r}_2$ relative to $\vec{r}_1$ is $d^3p_n(\vec{r}_2) = [p_n(\vec{r}_2)/p_n(\vec{r}_1)]d^3p_n(\vec{r}_1)$. Thus, the real space density of UCNs is given by:

$$\rho_{\text{UCN}}(E'_n) = \frac{d^6N}{d^3r} = \sqrt{\frac{E'_n}{E_n}}\,\rho_{\text{UCN}}(E_n)\,. \tag{1.14}$$

Therefore, in regions where E_{pot} is higher, there will be a lower density of UCNs. This is because the accessible momentum space for UCNs has decreased, hence increasing the accessible real space. The conservation of phase space density is crucial for understanding the transportation of UCNs. This is what is called quasi-statistical equilibrium or "mechanical equilibrium" of a UCN gas.

From Eq. 1.14 it can be seen that at places where $E_{\text{pot}} > \Delta E_n$ the UCNs can not reach, i.e., $\rho_{\text{UCN}} = 0$. This is easily argued via energy conservation as well. This forms the basis of using V_{mag} ($\approx 60\,\text{neV T}^{-1}$) to generate ΔE_n sufficiently large to trap UCNs without wall interactions. This is called the magnetic storage of UCNs. V_{grav} ($\approx 102\,\text{neV m}^{-1}$) can also be used for confining UCNs in the upward vertical direction. When this is combined with magnetic trapping, the trap will be referred to as a magneto-gravitational trap.

The wall collision rate and the loss probability per collision can be combined and integrated over the walls of a UCN trap to give the loss rate constant $\tau_{\text{walls}}^{-1}(E_n)$, which is E_n-dependent since both these terms are also. There are other loss mechanisms for a stored UCN gas. The combined total loss rate constant is given by $\tau_{\text{tot}}^{-1} = \sum \tau_{\text{losses}}^{-1}$, where τ_{tot} is called the total storage time. Due to the E_n-dependence of $\tau_{\text{walls}}^{-1}(E_n)$ (and possibly in the other loss processes), the number of UCNs remaining in a trap $N(t)$ at a time t after the trap is closed can only be written in the differential form:

$$\frac{dN(t)}{dE_n} = \frac{dN_0}{dE_n}e^{-t/\tau_{\text{tot}}(E_n)}\,, \tag{1.15}$$

where N_0 is the initial number of UCNs stored in a trap at $t = 0$.

Of course, τ_{walls} is dependent on the volume-to-surface ratio of trap, the E_{pot} distribution in the trap, and the E_n distribution of stored UCNs. However, a relevant value measured in another experiment worth comparing is $\tau_{\mathrm{walls}} \approx 350\,\mathrm{s}$ [6] for the empty beryllium-coated cylindrical vessel shown in Fig. 1.2 cooled to $6\,\mathrm{K}$ and for $E_n < V_{\mathrm{Be}}$ [GRL91].

The other losses that can be present can come from: interactions with the medium the UCNs are, for instance, in a residual gas at a pressure of $10^{-4}\,\mathrm{mbar}$ composed only of hydrogen at room temperature $\tau_{\mathrm{gas}} > 10,000\,\mathrm{s}$; depolarization losses during magnetic storage, described in details in Chapter 5; and of course the always present $\tau_{\beta,n} \approx 900\,\mathrm{s}$.

1.1.7   Applications of UCNs

The reader to recommended to read review papers on the field in Refs. [Abe08, RMS08, DS11]. Here, I give only a brief overview.

Perhaps the most notable experiment with UCNs is the long-standing search for the neutron's electric-dipole moment (EDM), the existence of which would violate the combined charged conjugation (C) and parity (P) symmetries [PR50]. If the size of the EDM is measured to be sufficiently large, this provides new mechanisms of CP violating processes beyond that predicted by the standard model, which currently is too weak to explain the matter-antimatter asymmetry observed in the universe after baryosynthesis. The present best level of precision [Bak06] is limited by statistics and no EDM has yet been observed at this level. There are many on-going and future experiments around the world pursuing this search[DS11].

Another study that can be performed with UCNs is the β-decay of the free neutron. The neutron lifetime, along with the β-asymmetry parameter— the asymmetry of electron emission with respect to the spin of the decaying neutron—allow the study of the coupling constants in the weak interaction. These values have astrophysical implications in the calculations of reaction rates in big-bang nucleosynthesis and stellar fusion; and they are used in other processes in particle physics, such as for the calibration of anti-neutrino detectors. For the neutron lifetime, improvements in the storage of UCNs have

---

[6]This $\tau_{\mathrm{walls}}^{-1}$ actually still includes $\tau_{\mathrm{gaps}}^{-1}$, the loss rate due to gaps in the vessel.

meant that the past 5 (and more) most precise measurements were made this technique [WG11]. For the β-asymmetry, the most precise measurements have been with cold neutron beams. However, a recently experiment was made using UCNs and are continually being developed. Measurements of other β-decay parameters have also been proposed with to be made with UCNs. More details about the neutron lifetime, a major topic of this thesis, is presented later in this chapter.

Other interesting experiments with UCNs include studies of quantum states of the neutron in the Earth's gravitational potential. This can be used as a tool to search for deviations from Newton's law of gravity at micrometer length scales. There are also searches for neutron to mirror-neutron oscillations as a possible candidate for dark matter and searches for a new fundamental force mediated by axion-like bosons.

All these measurements would benefit from increased UCN numbers for obtaining improved statistical precision, which in-turn allows for more checks of systematic effects. The currently available sources do not provide more than the order of $10\,\mathrm{UCN\,cm^{-3}}$. Many research groups have invested in developing "next generation" sources which aim to improve this by more than 2 orders of magnitude. The production of UCNs will be described in the next section.

1.2 Production of ultracold neutrons

Neutrons are freed from bound nuclei through the spallation or fission process. Spallation occurs when a beam of accelerated charged particles, usually protons, are used to bombarded a heavy metal target. This causes "evaporation" and the release of neutrons from the nuclei. Nuclear fission occurs when a neutron is captured by the nucleus and is left sufficiently excited so that it undergoes fission. The most standard fuel used in scientific research reactors is $^{235}\mathrm{U}$, which releases on average 2.5 neutrons per fission (one of these is then consumed to maintain a chain reaction).

Due to the nuclear binding energy, the released neutrons have energies in the MeV-range. For instance, in the fission of $^{235}\mathrm{U}$ the mean energy per neutron is $\approx 2\,\mathrm{MeV}$. In order to slow these neutrons down for them to be useful

for experiments [7], the neutrons are exposed to a moderator. When neutrons make elastic collisions with the moderator's nuclei, they will lose energy per collision due to the conversation of momentum. After several collisions during a random diffusive walk, they will be in thermal equilibrium with the moderator. The choice of moderator requires balancing the collision and absorption cross-sections, energy loss per collision, and thermal properties. At the ILL, a heavy water D_2O moderator at 50°C is used [8] to produce thermal neutrons. To further boost neutrons at longer wavelengths, a cold source—liquid D_2 at 25 K at the ILL—is then used to produced cold neutrons.

When the neutrons reach thermal equilibrium they will have a speed distribution obeying the Maxwell-Boltzmann distribution. The density of UCNs ρ_{UCN} in the moderator with temperature T can be calculated by integrating the distribution up to the critical UCN energy V_c. This gives:

$$\rho_{\mathrm{UCN}} = \frac{2}{3} \frac{\Phi_0}{\alpha} \left(\frac{V_c}{k_B T} \right)^{3/2} , \tag{1.16}$$

where Φ_0 is the total thermal flux density and $\alpha = (2k_B T_i/m_n)^{1/2}$, with T_i being the neutron temperature before moderation. At the ILL the thermal flux $\Phi_0 \approx 1.5 \times 10^{15}\,\mathrm{cm}^{-2}\,\mathrm{s}^{-1}$, $T_i = 320\,\mathrm{K}$, and $\alpha = 2.5\,\mathrm{m\,s}^{-1}$. For the cold source $T = 25\,\mathrm{K}$, and taking $V_c = V_{\mathrm{Be}} = 252\,\mathrm{neV}$, one gets $\rho_{\mathrm{UCN}} \approx 5,000\,\mathrm{cm}^{-3}$. Due to Liouville's theorem, as mentioned earlier, this is the maximum UCN density that can be extracted from the cold source without transportation losses.

1.2.1   The PF2 source

The density of $\approx 5,000\,\mathrm{cm}^{-3}$ exists inside the cold source. However, due to the increase of the absorption cross-section at low UCN velocities, it is only possible to extract them from close to the surface of the cold source. Furthermore, materials walls are required to separate the moderator and the experiments. This can drastically reduce the extracted UCN density.

To reduce such losses, the PF2 UCN source [SM89, Ste86] at the ILL first

---

[7]In a fission source they also need to be slowed down to increase the neutron capture cross-section, which is $\propto 1/v$, for maintaining the chain reaction.

[8]To reach thermalization in D_2O the number of collisions required is ≈ 30; the "moderation length", the average distance travelled to reach thermal equilibrium, is $\approx 11\,\mathrm{cm}$; and the diffuse length, the average distance between thermalization and absorption, is $\approx 1.6\,\mathrm{m}$.

uses a vertical extraction guide [9] followed by the "Steyerl turbine", a turbine consisting of 690 curved nickel blades rotating with a linear velocity of $\approx 20\,\mathrm{m\,s^{-1}}$ away from the neutrons exiting the guide. Doppler reflections off the blades of this turbine is used to decelerate VCNs with a velocity of $\approx 40\,\mathrm{m\,s^{-1}}$ ($\approx 8\,\mathrm{\mu eV}$) to approximately the UCN energy range.
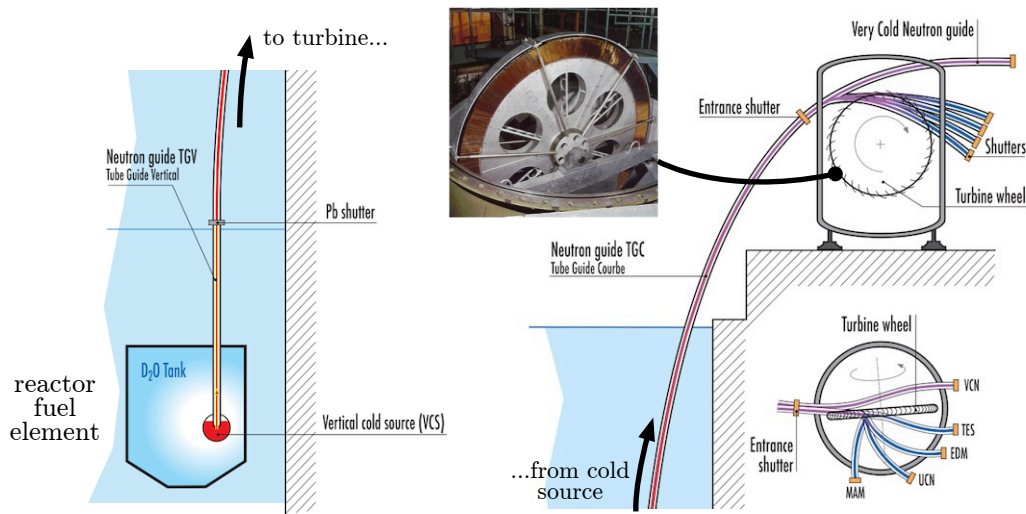
Figure 1.1: The PF2 UCN source at the ILL. The Steyerl turbine provides 4 UCN beams and 1 VCN beam.

Due to the deceleration from the turbine, the neutrons that finally end up as UCNs have much higher energies at the cold source and at the windows in between, resulting in reduced absorption losses. Coming from the PF2 turbine are 4 UCN beams: UCN, EDM, MAMBO, and TES. The first three share are switched by a beam switcher controlling a common exit from the turbine and thus can not be run simultaneously. The density of UCNs measured more than 25 years ago in a stainless steel at the exit of the source gave $\approx 50\,\mathrm{UCN\,cm^{-3}}$ [Ste86]. More recent measurements [Ser09] show that this may have reduced by a factor of ≈ 5.

---

[9]This consists of a vertical section 5 m long dipped directly into the liquid D_2 Vertical Cold Source then a curve section with a length of 13 m and a radius of curvature of 13 m.

1.2.2   Superthermal production with superfluid helium

A concept first proposed in Ref. [GP77] is to use superfluid helium for a "superthermal" UCN source. The process is based on reducing the energy of incoming neutrons with inelastic scattering via excitations of discrete energy levels in a material. The most intuitive case is to consider a moderator with two energy levels: a ground state and an excited state separated by an energy gap E^*. A neutron can excite a quasi-particle into the excited state and lose E^*; similarly, a quasi-particle can fall down to the ground state by transferring E^* to a neutron. The equation of detailed balance that links the two processes requires:

$$\sigma(E \to E + E^*) = \frac{E + E^*}{E} \exp\left(\frac{E^*}{k_B T}\right) \sigma(E + E^* \to E) \,. \qquad (1.17)$$

In general $\sigma(E + E^* \to E)$, the down-scattering cross-section (the former process), is independent of the moderator temperature so that for $E^* \gg k_b T \gg E$ $\sigma(E \to E + E^*)$, the up-scattering cross-section (the latter process), can be made arbitrarily small by reducing the temperature of the moderator T. Note, that in this process, the neutrons are not in thermal equilibrium with the moderator. As such, the material is called a converter. In superthermal down-conversion (as it is sometimes called), the density of UCNs that can be accumulated roughly increases as $\sim \exp[E^*/(k_B T)]$ (neglecting other losses for now), where as for moderation it only increases by $1/T^2$. In both these processes, one can increase the UCN real space density since entropy, and accessible momentum space, is transferred to the nuclei or quasi-particles in the moderator or converter. Therefore, Louville's theorem is not violated.

Superfluid helium can provide such a 2-level system. When normal liquid ^{4}He is cooled to below $T_\lambda = 2.17\,\mathrm{K}$ at SVP, it undergoes a second order phase transition, which causes an abrupt change of the properties of a material. This new phase is the superfluid phase and is often called He-II (compared with He-I, which is the normal fluid). The excitations in superfluid helium[10] follow the famous phonon-roton dispersion curve shown in Fig. 1.2 [Lan41, FC56], which

---

[10]In this thesis, "helium" will refer to ^{4}He due to it being the most abundant isotope of the naturally occurring element. When discussing the other naturally occurring isotope ^{3}He (natural abundance $< 10^{-4}$), it will be explicitly stated. If ^{4}He is purified to remove the ^{3}He contaminant, it will be referred to as "ultrapure ^{4}He".
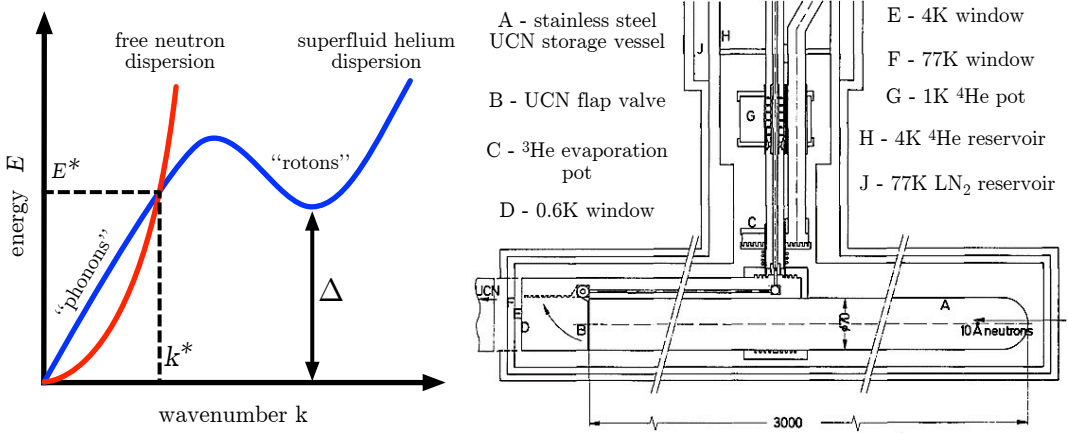
Figure 1.2: *Left*: The famous dispersion curve of the excitations in the super-fluid helium and the free neutron dispersion. This diagram is a sketch only. Δ is the roton energy gap. *Right*: A diagram of one of the first apparatus used to shown the superthermal production of UCNs in superfluid helium [Gol83]. The UCNs are accumulated then extracted through multiple thin-foils on the left-hand side using a mechanical flap valve.

describes the most prominent excitations. In the short wavenumber region the excitations are phonons, or sound waves, that come from quantization of the fluid density. The phonon energy is a linear function of k: $E_{\mathrm{phonon}} = \hbar\alpha k$, where α is the speed of sound. The excitations at larger k are called "rotons" and are the lowest elementary excitations of the vortex spectrum. They have an energy $E_{\mathrm{roton}} = \Delta + \hbar^2 K_r^2/(2\mu)$, where Δ is the energy gap above the lowest energy phonons, and $\hbar^2 K_r^2$ and μ are the momentum and effective mass of the roton, respectively.

The dispersion (momentum-energy relation) curve of a free neutron is given by: $E = \hbar^2 k^2/(2m_n)$. This curve is also shown in Fig. 1.2. Energy and momentum are needed to be conserved in inelastic scattering. Therefore, the transfer of energy and momentum between neutrons and the excitations occurs at where the two dispersion curves intersect. In superfluid helium, the intersection with the most prominent excitations occur in the phonon region at $E^* \approx 1.0\,\mathrm{meV}$ and $k^* \approx 0.71\,\text{Å}$, which corresponds to $\lambda^* \approx 8.9\,\text{Å}$. Therefore, an incoming neutron with $\lambda_i = \lambda^*$, at the lower energy range of cold neutrons, can excite a single-phonon in the superfluid helium and lose sufficient energy to become a UCN. This is called single-phonon UCN production.

UCN production rate

Obviously not all down-scattered CNs become UCNs after a single-phonon excitation. The calculation of the UCN production rate can be given by taking the integral of $S(q, \hbar\omega)$, the dynamic scattering function, evaluated along the dispersion curve of the free neutron. Making the approximation that the momenta range of UCNs $k_{\text{UCN}} \ll k^*$, approximating the single-phonon resonance by a δ-function, and making a correction to the overlap angle between the two dispersion curves, the UCN production rate can be calculated. Due to the small width of k_{UCN} the energy spectrum of the produced UCNs should come from a constant filling of the phase-space, i.e., $dN/dE_n \propto E_n^{1/2}$. For UCNs trapped in a beryllium vessel $V_{\text{Be}} = 252\,\text{neV}$ produced in superfluid helium with $V_{\text{s.f.}^4\text{He}} = 18.5\,\text{neV}$, the single-phonon UCN production rate per unit volume per unit time $P_{\text{UCN,I}}$ is given in Ref. [Kor02, SAZ09]. In a more convenient form, for a converter vessel that can trap UCNs up to energy $E_{\text{trap}} = V_{\text{walls}} - V_{^4\text{He}}$:

$$P_{\text{UCN,I}} \left[\text{cm}^{-3}\,\text{s}^{-1}\right] = \left[(1.39 \pm 0.11) \times 10^{-11}\,\text{neV}^{-3/2}\,\text{cm}^{-1}\,\text{Å}\right]\,E_{\text{trap}}^{3/2}\,\left.\frac{d\phi}{d\lambda_i}\right|_{\lambda^*}\,, \quad (1.18)$$

where E_{trap} is in units of [neV] and $\left.\frac{d\phi}{d\lambda_i}\right|_{\lambda^*}$ is the incoming intensity of CN neutrons at $\lambda^* = 8.9\,\text{Å}$ in units of $[\text{cm}^{-2}\,\text{s}^{-1}\,\text{Å}^{-1}]$. For instance, for the PF1b beam at the ILL, a value of $P_{\text{UCN,I}} \approx 10\,\text{cm}^{-3}\,\text{s}^{-1}$ for $E_{\text{trap}} = V_{\text{Be}} - V_{\text{s.f.}^4\text{He}}$ has been calculated [SAZ09].

Besides the down-scattering of CNs via single phonon excitations on the superfluid helium dispersion curve in Fig. 1.2, there can also be down-scattering from multi-phonon scattering. This occurs along the free neutron dispersion for when $S(q, \hbar\omega) > 0$. A plot of the non-zero $S(q, \hbar\omega)$ region above the single-phonon dispersion curve where multi-phonon excitations can occur is shown in Ref. [SAZ09]. The calculated UCN production from multi-phonons $P_{\text{UCN,II}}$ at $T = 1.25\,\text{K}$, also given in this reference, for the PF1b CN beam at the ILL, which is coupled to a liquid deuterium cold source at $25\,\text{K}$ (see Fig. 3.1 for the spectrum of this CN beam) gives $P_{\text{UCN,II}}/P_{\text{UCN,I}} \approx 40\%$. This value was confirmed by measurements with a velocity selector [Sch12]. Another measurement, done by Ref. [Bak03], on another CN beam coupled a cold source (the end position of the H53 beam at ILL) observed a value of $P_{\text{UCN,II}}/P_{\text{UCN,I}} \approx 30\%$.

The shape of the differential multi-phonon production rate $dP_{\mathrm{UCN,II}}/d\lambda_i$ in λ_i-space for CNs from a $25\,\mathrm{K}$ cold source has a peak centered around $\approx 6\,\text{Å}$ with a FWHM of $\approx 1.5\,\text{Å}$ (it is not fully symmetry and is much more narrow than the single-phonon peak, which is close to a δ-function). This is despite the peak in $dP_{\mathrm{UCN,II}}/d\lambda_i$ at $\lambda_i \approx 3\,\text{Å}$ with the intensity 2 times stronger here than at $6\,\text{Å}$. Therefore, $S(q,\hbar\omega) \to 0$ very quickly for $\lambda_i < 6\,\text{Å}$ along the free neutron dispersion curve.

The boost in P_{UCN} (the total production rate) of $30-40\%$ due to $P_{\mathrm{UCN,II}}$ might seem useful. However, it should be noted that a source only gets this full gain if $d\phi/d\lambda_i$ remains constant across the volume of the converter. The total cross-section of CNs in superfluid helium $\lesssim 2\,\mathrm{K}$ increases as λ_i decreases in the wavelength range of interest. At $8.9\,\text{Å}$ the mean free path of a CN in the converter is $\approx 15\,\mathrm{m}$; however, at $6\,\text{Å}$, it has shortened to $\approx 1.5\,\mathrm{m}$. Therefore, the fractional gain in the total production from multi-phonon production is only useful in sources where the CNs do not have to travel great distances in the converter. The mean free path at $\lambda^* = 8.9\,\text{Å}$ indicates that to make good use of the strong single-phonon production, one should have the CNs transverse the superfluid converter for at least several meters.

The rate of produced UCNs in the volume in an energy interval dE_n is $(dP_{\mathrm{UCN}}/dE_n)\, V_{\mathrm{CN}}\, dE_n$, where V_{CN} is the volume of converter the CN beam is incident upon. The total loss rate of UCNs in an interval dE_n is $\rho_{\mathrm{UCN}}\, V_{\mathrm{vol}}\, \tau_{\mathrm{tot}}^{-1}(E_n)\, dE_n$, where V_{vol} is the volume of the converter vessel [11]. Equilibrium is reached when the two rates equal each other, so that the differential equilibrium density $d\rho_{\mathrm{UCN},\infty}/dE_n$ is given by:

$$\frac{d\rho_{\mathrm{UCN},\infty}}{dE_n} = \tau_{\mathrm{tot}}(E_n)\, \frac{dP_{\mathrm{UCN}}}{dE_n} \;, \tag{1.19}$$

where $V_{\mathrm{CN}} = V_{\mathrm{vol}}$ is assumed. Therefore, the longer the storage time $\tau_{\mathrm{tot}}(E_n)$ the higher density of UCNs. The total storage time of UCNs in a superfluid helium source consist of: $\tau_{\mathrm{tot}}^{-1}(E_n) = \tau_{\beta}^{-1} + \tau_{\mathrm{walls}}^{-1}(E_n) + \tau_{\mathrm{abs}}^{-1} + \tau_{\mathrm{up}}^{-1}(T)$. The first two terms have been discussed already; τ_{abs}^{-1} predominately comes from absorption by trace ^{3}He. How this can be reduced to a level so that its contribution to

---

[11]As discussed just before, P_{UCN} will vary in the converter due to CN scattering (and other effects) and ρ_{UCN} will vary in the volume due to variations of E_{pot}. In this thesis, the two quantities P_{UCN} and ρ_{UCN} should be taken to mean averages, i.e., $\bar{P}_{\mathrm{UCN}}$ and $\bar{\rho}_{\mathrm{UCN}}$, to simplify the notation and discussions. If not used as such, it will be explicitly stated.

τ_{tot}^{-1} is negligible is discussed in Chapter 2. The remaining term, $\tau_{\text{up}}^{-1}(T)$ comes from up-scattering of the UCNs by the excitations in the superfluid.

UCN up-scattering

Up-scattering occurs when a UCN, which is considered to be at rest, absorbs an excitation. A good approximation is that any interaction will cause a UCN to gain enough energy to excite it above the UCN energy range. The characteristic up-scattering times for the three most prominent processes that contribute to τ_{up}^{-1} was calculated in Ref. [Gol79]. These calculations are based on the phenomenological Landau-Hamiltonian model [Gol83] and were intended to be valid for $T \lesssim 1\,\text{K}$ only. I will only give a brief summary of the final results here. The notation used follows closely that of Ref. [SW09].

Single phonon: The absorption of a single phonon by the UCN. This is the inverse process of single phonon down-conversion. From detailed balance in Eq. 1.17, it can be seen that this decreases with the converter temperature T as $\propto e^{-E^*/(k_B T)}$. The up-scattering rate constant is given by:

$$\tau_{\text{up},A}^{-1} = N_0\,\sigma\left(\frac{\hbar k^*}{m_n}\right)\left(\frac{E^*}{m_{^4\text{He}}}\right)e^{-E^*/(k_b T)} = \left(130\,\text{s}^{-1}\right)e^{-(11.8\,\text{K})/T}\,, \qquad (1.20)$$

where N_0 is the equilibrium density of the superfluid, $\sigma = 4\pi a^2$ is the coherent scattering cross-section for helium, and m_n and $m_{^4\text{He}}$ are the masses of the neutron and helium, respectively. The notation used in this thesis will follow that used in Ref. [Yos92], where this term will be written as $\tau_{\text{up},A}^{-1} = A\,e^{-(11.8\,\text{K})/T}$, with $A = 130\,\text{s}^{-1}$ [12].

Two phonons: The absorption of one phonon followed by the immediate emission of another phonon is allowed by momentum and energy conservation. This is expected to be the most significant interaction. Processes where two phonons are absorbed cannot contribute significantly to the up-scattering rate. The up-scattering rate constant for this process was derived to be:

$$\tau_{\text{up},B(T)}^{-1} = \frac{\sigma\alpha k_B^7}{(4\pi)^2}\left(\frac{T}{m_n\alpha^2}\right)^2\left(\frac{T}{m_{^4\text{He}}\alpha^2}\right)^2\left(\frac{T}{\hbar\alpha}\right)^3 I(T) = B(T)\,T^7\,, \qquad (1.21)$$

---

[12]This value was not stated in the original paper [Gol79]. However, in a comment to Ref. [Yos92] where a value of $A = 500\,\text{s}^{-1}$ was used, the authors of the original calculation recommended the value of $A = 130\,\text{s}^{-1}$ that is more appropriate [GL93].

where $I(T)$ is a dimensionless integral that contains a term dependent on the deviation between the real superfluid dispersion curve and the idealized linear phonon dispersion. This difference is T-dependent and the values used were from Ref. [Mar73]. The calculation was done for two values of T: at $0.6\,$K $\tau^{-1}_{\mathrm{up},B(0.6\,K)} = B(0.6\,\mathrm{K})\,T^7 = (4000\,\mathrm{s})^{-1}$, and at $1.0\,$K $\tau^{-1}_{\mathrm{up},B(1.0\,K)} = B(1.0\,\mathrm{K})\,T^7 = (130\,\mathrm{s})^{-1}$. That is, $B(0.6\,\mathrm{K}) = 8.8{\times}10^{-3}\,\mathrm{s}^{-1}\,\mathrm{K}^{-7}$ and $B(7.6\,\mathrm{K}) = 7.6{\times}10^{-3}\,\mathrm{s}^{-1}\,\mathrm{K}^{-7}$. Unfortunately the full T-dependence of $B(T)$ was not calculated.

Roton-photon: The last up-scattering process expected to be significant involves the absorption of a roton and then an emission of a photon. The expression for the up-scattering rate constant due to this process was derived to be:

$$\tau^{-1}_{\mathrm{up},C} = \frac{3\sigma}{8\pi^{3/2}}\frac{\mu^2}{m_n m_{^4\mathrm{He}}}\left(\frac{k_R^3}{m_n\alpha}\right)\left(\frac{k_B T}{m_{^4\mathrm{He}}\alpha^2}\right)(2\mu\alpha^2 k_B T)^{1/2}\mathrm{e}^{-\Delta/(k_B T)}$$
$$= (18\,\mathrm{s}^{-1}\,\mathrm{K}^{-3/2})\,T^{3/2}\,\mathrm{e}^{-(8.6\,\mathrm{K})/T}\,, \quad (1.22)$$

where μ is the roton reduced mass, Δ is the roton energy gap, and k_R the roton wave vector. The notation used for this term will be: $\tau^{-1}_{\mathrm{up},C} = C\,T^{3/2}\,\mathrm{e}^{-(8.6\,\mathrm{K})/T}$, with $C = 18\,\mathrm{s}^{-1}\,\mathrm{K}^{-3/2}$.

The sizes of these three terms are shown in Fig. 3.17. For the parameters used above, it can be seen that the largest contribution to τ^{-1}_{up} for $T < T_\lambda$ is $\tau^{-1}_{\mathrm{up},B(T)}$ (when $B(1.0\,\mathrm{K})$ is used), followed by $\tau^{-1}_{\mathrm{up},C}$, then $\tau^{-1}_{\mathrm{up},A}$. A discussion of measurements of these is given in Chapter 2. One can see that if $T < 0.7\,$K then $\tau_{\mathrm{up}} > 1600\,$s. Therefore, at sufficiently low converter temperatures, $\tau_{\mathrm{tot}}(E)$ in a superfluid helium source is restricted mainly by $\tau_{\mathrm{walls}}(E)$.

UCN source projects

Due to the need for stronger UCN sources for experiments, numerous groups are pursuing the development of "next generation" UCN sources based on the superthermal process. The work on the SUN-2 source described in this thesis uses superfluid helium as the converter at the end of a CN beam. Due to the long storage times $\tau_{\mathrm{tot}} \gtrsim 300\,$s that can be achieved in a superfluid helium converter vessel at sufficiently low temperatures, such a source is designed to be operated in cyclical or accumulation-and-empty mode [GRL91]. In this mode, the UCNs are accumulated then emptied into the experiment apparatus.

While the UCNs are stored and studied in the apparatus, the helium source can be filled for the next cycle. Many experiments, for example EDM and neutron lifetime measurements, use a cyclical filling of the apparatus' storage volume.

The UCN production rate from a CN beam can reach $P_{\mathrm{UCN}} \approx 10\,\mathrm{cm^{-3}\,s^{-1}}$ for a converter vessel with beryllium walls (e.g., with the PF1b beam at the ILL). The expected UCN density in the source $\rho_{\mathrm{UCN}} \gtrsim 3000\,\mathrm{cm^{-3}}$ can thus be expected. The actual density that is delivered to the experiment will depend on the transportation losses and the ratio of the apparatus volume and the converter volume. To reduce extraction losses, the SUN-2 source implements a vertical, window-less extraction system with a mechanical UCN valve on the converter volume[13]. This reduces the losses in transmission through thin-windows. For example, see the apparatus of one of the first measurements of UCN production in superfluid helium [Gol83] shown in Fig. 1.2. The heat load on the converter from a window-less extraction system has been demonstrated to be not significant enough to restrict cooling to $\leq 0.7\,\mathrm{K}$ [Zim07, ZPI11] for a technically easy to achieve cooling power.

The superfluid helium converter can also be placed in-pile (i.e., in the thermal moderator close to a reactor core or spallation target) so that the CN flux is increased by factors of $\gtrsim 10^3$ [Mas11, Mas12, Ser11]. However, in such a source, the head load on the converter, predominately from γ and β radiation heating, is significantly increased. This makes reaching the lower temperatures technically challenging. In one case [Ser11], continuous extraction of UCNs from the superfluid converter vessel is used. This is when the guides leading to the experiment are left open so that produced UCNs can find the escape from the volume before being up-scattered and lost.

Superthermal sources using solid deuterium SD_2 are also being pursued [Ang09, Kor07, Sau04, Tri00]. A SD_2 crystal can also provide the discrete excitations for superthermal production. Indeed, UCN production occurs over a wide spectrum of CN energies giving production rates of $P_{\mathrm{UCN}} \gtrsim 10^4$ [14]. However, in SD_2 the survival time of UCNs is only $\tau_{\mathrm{tot}} \approx 50\,\mathrm{ms}$ at $5\,\mathrm{K}$ [Ang09]

---

[13]The cryoEDM experiment [Bak10] keeps the produced UCNs submerged in the super-fluid helium when it is transported from the production volume, the guides, and in the measurement chamber.

[14]This depends on a lot of parameters. A part of this enhancement comes from placing it in-pile at a spallation neutron source.

due to a combination of absorption, and up-scattering by H_2, phonons, and para-D_2. Therefore, accumulation can not occur in the converter. In the design of these sources, there is usually a separate storage vessel next to the SD_2 vessel for containing the UCNs when the pulsed neutron beam is off (alternatively, the converter is made very thin at the end of a guide). The rest of the thesis will be restricted to talking about superfluid helium UCN sources.

1.3 The neutron lifetime

Some recent review papers focussed on the neutron lifetime are Refs. [Pau09, WG11]. Review papers on the field of UCN physics (listed previously), neutron β-decay [Dub91, Nic09, Kon11], or the more general field of nuclear β-decay [Sev04, SBNC06], also contain sections about the subject.

Neutron decay and the weak interaction coupling constants

In the full electroweak theory of the standard model of particle physics, the neutron is described to consist of one up quark and two down quarks (udd), and neutron β-decay, $n\,(udd) \rightarrow p\,(uud) + e^- + \bar{\nu}$, proceeds with the exchange of a virtual W boson, transforming a d quark to an u quark, as depicted in Fig. 1.3. However, due to the energy released in the decay ($\approx 780\,\mathrm{keV}$) being small compared to the mass of the W boson ($m_W c^2 \approx 80\,\mathrm{GeV}$), which determines the range of the weak interaction, the β-decay process can be approximated by a point interaction between a hadronic current and a leptonic current (also see Fig. 1.3). The model of β-decay was first proposed by Fermi [Fer34] who originally only considered vector (V) transitions [15].

In the standard model, no reason is provided *a priori* for why only vector transitions should exist. Gamow and Teller [GT36] proposed that all Lorentz-invariant interaction forms: scalar (S), pseudoscalar (P), tensor (T), axial vector (A), and vector (V) terms [16] could be included in the interaction Hamiltonian. Then, as proposed by Lee and Yang [LY56], parity violation

---

[15]A vector transition corresponds to the total spin of the electron and anti-neutrino in the $S = 0$ singlet state, so that the change of the spin of the nucleon $\Delta J = 0$. This is also called Fermi decay.

[16]These names are given by how each of the Dirac bilinear covariant fields, expressed in terms of the Dirac matrices γ^i, with $i = 0...5$, transform under spatial rotations and reflections.
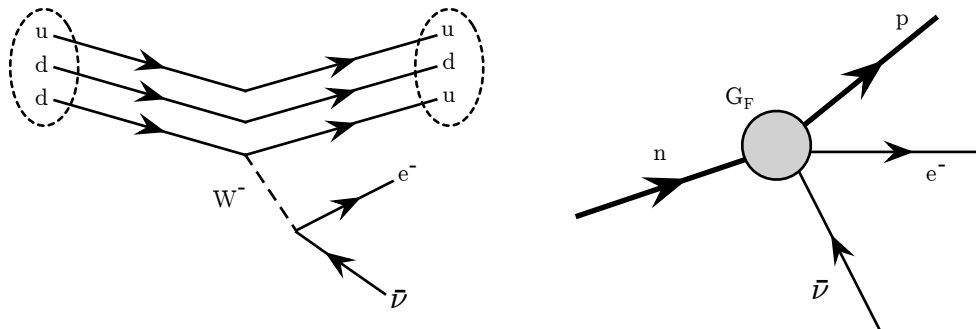
Figure 1.3: Feynman diagrams of neutron β-decay. On the *left* is the full electroweak theory describe the interaction as a conversion of down to up quark via the exchange of a virtual W boson. On the *right* is the low energy approximation point interaction between a hadronic current (thicker line) and leptonic current (thinner line) as proposed by Fermi. The time arrow points from left to right on both.

was observed in β-decay experimentally by Wu *et al.* [Wu 57]. Lee and Yang subsequently postulated that all neutrinos have left-handed helicity (and antineutrino right-handed), which was confirmed by Goldhaber *et al.* [GGS58], which led to the developed the two-component theory of the neutrino [Les09]. Feynman and Gell-man and others [FGM58, SM58] incorporated this into the interaction Hamiltonian and formed the $V - A$ theory of the weak interaction.

In the low energy limit, the matrix element of the neutron β-decay interaction Hamiltonian in this theory, following the notation of Ref. [WG11], is:

$$\mathcal{M} = \left[G_V \, \bar{p} \, \gamma_\mu \, n - G_A \, \bar{p} \, \gamma_5 \, \gamma_\mu \, n \right] \left[\bar{e} \, \gamma_\mu \left(1 - \gamma_5 \right) \nu \right] , \tag{1.23}$$

where $\bar{p}$, n, $\bar{e}$, and ν in this expression are the Dirac spinors of the fermions. The terms in the first brackets is the hadronic current and in the second brackets the leptonic current. The coupling constants G_V and G_A give the strengths of the vector and axial-vector forces in the low momentum approximation. They are given by: $G_V = G_F \, V_{ud} \, C_V$ and $G_A = G_F \, V_{ud} \, C_A$, where G_F is the Fermi coupling constant, which contains the effective W boson propagator, and is determined experimentally via muon-decay to a high precision; C_V and C_A are the constants in the Hamiltonian of Jackson et al. [JTW57], with $C_V = 1$ in the standard model following the Conserved Vector Current (CVC) hypothesis; and V_{ud} is the first element of the CKM matrix and is described

later.

The rate of a transition with a matrix element $\mathcal{M}$ can be given by Fermi's Golden rule:

$$W = \frac{2\pi}{\hbar}|\mathcal{M}|^2\rho \,, \tag{1.24}$$

where ρ is the density of the final states in the transition. The total neutron β-decay rate is then given by:

$$W = \tau_{\beta,n}^{-1} = \frac{m_e^5 c^4}{2\pi^3\hbar^7}(G_V^2 + 3G_A^2)f \,, \tag{1.25}$$

where f consists of a statistical rate function which is an integral over phase space of the final states of the electron [Glü93]:

$$f = \int_0^{E_0} F(Z,E_e')\,p_e'\,E_e'\,(E_0 - E_e')^2\,dE_e' \,, \tag{1.26}$$

where p_e', E_e', and E_0 are the electron's momentum, energy, and end-point energy, respectively. $F(Z,E_e')$ is the Fermi function and provides a correction for the Coulomb attraction between the electron and proton, Z is the charge of the daughter nucleus (in this case a proton).

From Eq. 1.25, it can be seen that a measurement of $\tau_{\beta,n}$ can not give the values for G_V and G_A independently. Instead, one needs to perform an additional measurement of an experimentally accessible parameter $\lambda \equiv C_A/C_V = G_A/G_V$, which is currently most accurate given by measurements of the asymmetry coefficient between the electron momentum and neutron spin, denoted by A [Nic09]. It can also be given by measurements of the correlation coefficient between the electron and antineutrino, denoted by a, but results from this is currently less precise.

The conserved vector current hypothesis states that G_V should be a constant for all weak interactions, including all other nuclear β-decays. However, before the G_V values can be compared, radiative corrections that result from electromagnetic interactions, for instance, from emission of bremsstrahlung photons or exchange of virtual photons between the electron and nucleus. They are split into the transition-dependent correction δ_R (also called the inner radiative correction) and the transition-independent correction Δ_R^V (also called the outer radiative correction). The former depends on the model and structure of the nucleus. For the neutron β-decay, the size of this correction

is a lot smaller than from other nuclear β-decays. The latter is present and is the same size in all β-decays. These two terms transform f and G_V by: $f \rightarrow f(1 + \delta_R)$ and $G_V \rightarrow G_V(1 + \Delta_R^V)$.

Therefore, including into Eq. 1.25 the radiative corrections, the expression for λ, and rewriting in terms of V_{ud}:

$$|V_{ud}|^2 = \frac{2\pi^3\hbar^7}{m_e^5 c^4} \frac{1}{f(1 + \delta_R)\tau_{\beta,n}} \frac{1}{G_F^2(1 + \Delta_R^V)(1 + 3\lambda^2)} . \tag{1.27}$$

So $|V_{ud}|$, the first element of the Cabbibo-Kobayashi-Maskawa (CKM) quark mixing matrix, can be determined from the experimentally observable $\tau_{\beta,n}$ and λ.

The CKM matrix

The CKM quark mixing matrix describes the transformation of quarks in the standard model. In this model there are three generations of quarks: (u, d), (c, s), and (t, b), where the first in each generation has an electric charge of $+2/3e$ and the second $-1/3e$, and the mass of the quarks increase with generation. However, the mass or strong force eigenstates of the quarks are not the weak force eigenstates, so that a quark in the eigenstate of the former can "mix" via the weak interaction into the other generations (or into the other quark in the same generation). The full CKM matrix is given by:

$$\begin{pmatrix} d' \\ s' \\ b' \end{pmatrix} = \begin{pmatrix} V_{ud} & V_{us} & V_{ub} \\ V_{cd} & V_{cs} & V_{cb} \\ V_{td} & V_{ts} & V_{tb} \end{pmatrix} \begin{pmatrix} d \\ s \\ b \end{pmatrix}, \tag{1.28}$$

where d, s, and b are the mass eigenstates, and d', s', and b' are the weak eigenstates. By convention the second quark of each generation are used in the matrix. For instance, in β-decay which is a transformation of a d quark to u quark, there is an enhancement to the semi-leptonic transitions G_V and G_A from the pure leptonic transition G_F by the enhancement factor V_{ud}. This was used earlier to related G_V and G_A with G_F.

The standard model does not prescribe the values for any of the elements so each must be determined experimentally. The matrix is expected to be unitary otherwise physics beyond the theory is involved. Neutron β-decay,

since it allows the determination of $|V_{ud}|^2$, is involved in testing of the unitarity of the first row. That is, whether $|V_{ud}|^2 + |V_{us}|^2 + |V_{ub}|^2 = 1$.

The value of $|V_{ud}|^2$ comes most precisely from nuclear β-decay studies [HT09], but a value from neutron β-decay does not contain as many nuclear structure-dependent corrections. Currently, the precision is limited by the published values of λ. But upcoming results [Mär09] should soon change this situation so that the focus is shifted to $\tau_{\beta,n}$, and then individual measurements will be competitive with the data from nuclear β-decay. However, the value of $|V_{ud}|^2$ from both are becoming close to being restricted by common precision of the outer radiative correction Δ_R^V. As for the other terms, $|V_{us}|^2$ comes from multiple kaon decay channels, and $|V_{ub}|^2$ from purely leptonic B-meson decays. Due to the constant update of the values, both on the experimental side and the theoretical side (for the calculated corrections), which alters whether unitarity is up-held or not, I will simply refer the reader to the latest review paper (known to the author) [Nic09] and the recently updated values from the Particle Data Group [Ber12].

Big Bang Nucleosynthesis

The Big Bang Nucleosynthesis (BBN) model describes the formation of the light (up to lithium), primordial elements during the short moments after the current model of the big bang; its verification is considered one of the "pillars" of experimental support. The weak coupling constants G_V and G_A, and the neutron lifetime, play several roles during the BBN process[DS11, WG11]. First, from $t \approx 0.1$–$1.0\,\mathrm{s}$, the universe consisted of a hot "plasma" of protons, neutrons, electrons, positrons, neutrinos, antineutrinos, and photons kept in thermal equilibrium by weak, strong, and electromagnetic forces. For the protons and neutrons, the weak neutrino interactions: $n + e^+ \leftrightarrow p + \bar{\nu}$ and $p + e^- \leftrightarrow n + \nu$, can proceed forwards and backwards since it was energetically allowed. At this time, the ratio of neutrons to protons can thus be given by the Boltzmann factor: $n/p = \exp[\Delta m\, c^2/(k_B T)]$, where T is the temperature of the universe and $\Delta m = m_n - m_p \approx 1.3\,\mathrm{MeV}$. The weak neutrino cross-sections are small so that during the expanding and cooling universe there reached a point in time, called the freeze-out time $t_{\mathrm{freeze}} \approx 2\,\mathrm{s}$, where these reactions stopped.

At this moment, $k_B T(t_{\text{freeze}}) \approx 0.7 \, \text{MeV}$, so that $n/p \approx 1/6$ [17].

During the next three minutes the n/p ratio decreased to n'/p' due to free neutron decay $n \to p + e^- + \bar{\nu}$; the inverse reaction does not occur due to the rarity of the 3-point collision. At $t_d \approx 150 \, \text{s}$ and $k_B T(t_d) \approx 0.1 \, \text{MeV}$, the universe was cool enough for neutrons and protons to bind; photo-disintegration that was energetically possible before was now sufficiently suppress. Then, in a complex chain of nuclear reactions, the elements such as deuterium, helium, and other light elements up to ^7Li, were formed [Coc07].

In these calculations, the neutron lifetime $\tau_{\beta,n}$ enters directly in determining $n' \approx n \exp[-t_d/\tau_{\beta,n}]$, and also in t_{freeze}, which is determined by the weak interaction coupling constants ($\tau_{\beta,n}$ enters again here), the expansion rate of the universe, the baryon-to-photon ratio η_{10}, and the number of light species of neutrino N_ν. The predicted ^4He abundance, which can be compared with astrophysical observations, is currently dominated by the experimental uncertainty in the neutron lifetime[WG11].

Other applications

As mentioned in the previous section, the interaction $p + e^- \leftrightarrow n + \nu$ depends on $\tau_{\beta,n}$ through the weak coupling constants. This process is also important in understanding the neutron star formation. There are many other weak interaction cross-sections that require $\tau_{\beta,n}$. For example[Dub91]: $p + p \to {}^2\text{H} + \nu$ and $p + p + e^- \to {}^2\text{H} + \nu$ in the solar cycle; and $\bar{v} + p \to e^+ + n$ and $\nu + n \to e^- + p$ for neutrino and antineutrino detection efficiences.

1.3.1 Experimental studies

Measurements of the neutron lifetime τ_β [18] can be divided into using the in-beam method or the storage method. The former counts the number of neutrons that have decayed $-dN$ in a time dt for a beam of neutron with density ρ_n in a volume of size V, i.e., $dN = -\rho_n V \tau_\beta^{-1} dt$. In this method the following

---

[17]This is considered "fortunate" since if the cross-sections were large, then t_{freeze} would occur much later resulting in a much smaller n/p ratio. This would result in a lack of neutrons in the BBN process.

[18]From this point forward, the previous notation $\tau_{\beta,n}$ will be replaced by τ_β since only neutron decay will be discussed.

are required to be determined separately: ρ_n, given by the velocity and intensity of the neutron beam; the size of the fiducial volume V; and the detection efficiency ϵ, since one measures $dN' = \epsilon dN$. The in-beam measurement with the lowest uncertainty is that of Ref. [Nic05], which is dominated by systematic uncertainty. There exists five other measurements based on the storage technique that are more precise—in terms of the reported uncertainties—than this measurement [Ber12].

The majority of storage measurements rely on the count-the-survivors technique. This is where a bottle or trap is filled with an initial number of UCNs N_0. Once in the trap, the differential number of UCNs $dN(t)/dE_n$ remaining in the bottle after a time t will decay according to Eq. 1.15, i.e., with characteristic decay time constant $\tau_{\text{tot}}(E_n)$. Therefore, if one stores the UCNs for some time, called the holding time, and then empty trap to count the number of UCNs remaining—and then refill the trap and repeated for a different holding times—one can determine $\tau_{\text{tot}}(E_n)$. Since the data from different fillings of the trap are combined, the initial differential number of UCNs in the trap dN_0/dE_n should remain constant. In this technique only the relative change in the number of UCNs after different holding times is needed to extract $\tau_{\text{tot}}(E_n)$.

When $\tau_{\text{tot}}^{-1}(E_n)$ is extracted, it contains other loss contributions besides τ_{β}^{-1}. For a UCN gas confined in a material trap $\tau_{\text{tot}}^{-1}(E_n) = \tau_0^{-1}(E_n) + \tau_{\text{gas}}^{-1} + \tau_{\beta}^{-1}$, where $\tau_0^{-1}(E_n) = \tau_{\text{walls}}^{-1}(E_n) + \tau_{\text{gaps}}^{-1}(E_n)$. For a well-constructed trap $\tau_{\text{gaps}}^{-1}(E_n) \to 0$. However, $\tau_{\text{walls}}^{-1}(E_n)$ will always remain. As described in Sec. 1.1.6, the calculation of this value depends on $\bar{\mu}(E_n)$, which in turn depends on the neutron optical potential V_{walls} and energy-independent loss factor f of the walls of the trap. However, since these two quantities are hard to determine directly, the volume of the trap is changed (either with a new volume or by a movable barrier in the trap), which varies the collision rate total J with the side walls, and increases the mean-free-path of the UCNs. By extrapolating $J \to 0$, equivalent to extrapolating $V \to \infty$ or the mean-free-path to infinity, the value of $\tau_{\text{tot}}^{-1}(E_n) - \tau_{\text{walls}}^{-1}(E_n)$ can be determined. Since this is UCN energy dependent, the differential spectrum of the UCNs in the trap are required to be measured in a separate procedure [19].

A history of the published τ_{β} values is shown in Fig. 1.4. The systematic

---

[19]Loss due to τ_{gas}^{-1} still remains. This can be measured by deliberately varying the gas pressure inside the trap and measuring the effect on τ_{tot}^{-1}.
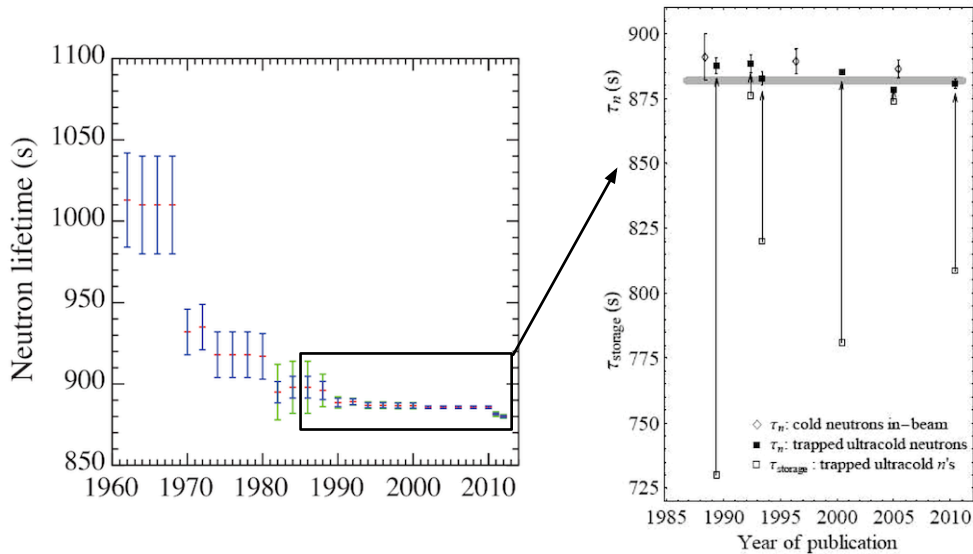
Figure 1.4: *Left*: a historic plot of the published neutron lifetime values from Ref. [Ber12]. *Right*: A plot of recently published τ_β values from Ref. [DS11]. The extrapolation required from the observed τ_{tot} (called τ_{storage} in the figure), and whether they were performed using the in-beam or the storage method, are also shown.

shift of τ_β beyond the specified error bars allude to the existence of unknown effects involved in extracting τ_β. Indeed, Ref. [GRL91] gives a nice summary of the efforts required in understanding that surface hydrogen on surfaces was the cause of the "anomalously large UCN loss rate problem" in UCN storage. To counter this, most recent τ_β measurements [20] employ Fomblin, a hydrogen-free fluorinated polyether material, for the storage wall coating. Special care is placed in the surface preparation to ensure there are no cracks present. The walls are usually cooled to suppress the up-scattering loss of UCNs. However, new mechanisms, for instance, the so-called "quasi-elastic scattering" of UCNs, which transfer energies on average $\approx 10^{-5}$ neV per collision, have been experimentally observed [Ste02, Str00, Ser03]. This is hypothesized to come from surface waves or wall vibrations. This effect will alter the UCN spectrum in the trap with holding time.

Also shown in Fig. 1.4 are the recently published values. Of special note is the measurement by Ref. [Ser05], which, when it was published in 2005, was

---

[20]Except for one that used solid oxygen.

6 standard deviations shorter than the previous world average [Yao06]. For many years, this value was not included in the new world average. Recently, however, a newly published value [Pic10], which was a repeated of a previously experiment but with more careful analysis of the trap volume, and a re-evaluation of correction in τ_{walls} from a previous measurement [Arz12] led to the world average from the Particle Data Group being updated with new and lower values [Ber12].

This situation is far from ideal. This provides the motivation to pursue a high precision τ_β with magnetic storage of UCNs, which offers the possibility of loss-free storage [Vla61]. The development and exploration of ideas and the systematics effects for a new UCN magnetic trap is discussed in this thesis. The first magnetic storage of neutrons was demonstrated in a hexapole torus storage ring [Pau89]. In this experiment only the $E_{n,\perp}$ component of cold neutrons were confined. The first demonstration of full 3D magnetic storage in a horizontal Ioffe-Pritchard-type trap was done in Ref. [Huf00]. Another demonstration of the magnetic storage in a magneto-gravitational trap was done in Ref. [Ezh09]. The discussion of these experiments, since they offer valuable lessons in UCN magnetic storage, will permeate throughout this thesis at the relevant sections.

Chapter 2

SUN2: The cryostat

In this chapter the cryostat of the SUN2 source, a next-generation UCN source that uses a superfluid ^{4}He converter coupled to the end of a cold neutron (CN) beam, will be described. The whole apparatus can be thought of as being separated into the main cooling tower, the UCN production tower, and the horizontal transfer section that connects the two (See Fig. 2.1 and Fig. 2.2). The main focus of this chapter will be on describing the various cryogenic components in the main cooling tower and horizontal transfer tube. These were constructed and tested thoroughly between 2009 and 2011. In the first UCN production experiment described in Chapter 3, the main cooling tower and horizontal transfer section was used with a prototype version of the UCN production tower.

2.1 Motivation

Having the converter at the end of a beam guide means that it is subjected to a factor of around 10^3–10^4 less flux of cold neutrons than compared to an in-pile source. This lower flux, however, can be offset by operating the source in *accumulation-and-empty* mode. In this mode, the cold beam is turned on and the UCN density in the converter is accumulated until saturation before emptying the UCNs into the experiment. Saturation occurs when the production rate P_{UCN} equals the total loss rate τ_{tot}^{-1} of UCNs in the production volume. The UCN density that can be achieved in the converter vessel ρ_∞, in

terms of rate constants, is given by:

$$\rho_\infty = P_{\mathrm{UCN}}\,\tau_{\mathrm{tot}} = P_{\mathrm{UCN}}\left(\tau_\beta^{-1} + \tau_{\mathrm{wall}}^{-1} + \tau_{\mathrm{abs}}^{-1} + \tau_{\mathrm{up}}^{-1}\right)^{-1}\,,\qquad(2.1)$$

where P_{UCN} is UCN production rate per unit volume determined by the properties of the CN beam and the maximum UCN energy that can be stored in the source and extracted by the guides. Values of $P_{\mathrm{UCN}} \approx 10\,\mathrm{cm^{-3}\,s^{-1}}$ are possible. The neutron β-decay lifetime τ_β sets a limit on the shortest storage time and is fixed at $\approx 900\,\mathrm{s}$. Other loss processes usually dominate though. They come from: storage wall-losses in the converter volume $\tau_{\mathrm{wall}}^{-1}$; UCN up-scattering in the converter τ_{up}^{-1}, caused by the inverse process of phonon down-scattering; and absorption by trace contaminants, primarily ^{3}He, in the converter τ_{abs}^{-1}. The values that are achievable are: $\tau_{\mathrm{wall}} \approx 200\,\mathrm{s}$ for materials with a neutron optical potential and low loss properties (e.g. beryllium) [AMK85], $\tau_{\mathrm{up}} \approx 1,000\,\mathrm{s}$ for superfluid ^{4}He below $0.7\,\mathrm{K}$ [Gol83], and $\tau_{\mathrm{abs}} > 4,000\,\mathrm{s}$ for a ^{3}He/^{4}He ratio of 10^{-12} [GP77], a purity reported to be achievable by superleak filtration [AM76]. Combining these losses, a total loss rate of $\tau_{\mathrm{tot}} \approx 100\text{--}150\,\mathrm{s}$ can be achieved, resulting in UCN densities of $\approx 1000\text{--}1500\,\mathrm{cm^{-3}}$ in the source.

The accumulation-and-empty mode is optimized for experiments that use a filling procedure. Since the accumulation of UCN in the source can occur during the storing period of the experiment, the continuous flux of cold neutrons is utilized even when UCN input into the experiment is not required. The accumulation in the converter vessel can only be performed with ^{4}He-based sources due to the zero absorption cross-section and the suppression of up-scattering at sufficiently low temperatures. Having the source far from the reactor core also results in a much lower heat load from gamma-heating, which allows the required low converter temperatures to be achieved without the need of extraordinary amounts of cooling power. Furthermore, extraction of UCNs vertically using a mechanical UCN valve, which removes the loss caused by transmission through thin-foil windows, allows UCN densities of ^{4}He based sources coupled to the end of a CN beam to be competitive with other proposed in-pile sources.

Another advantage of having the converter at the end of a guide is related to engineering issues. Over-coming safety standards, as well as finding the space in over-crowded neutron facilities, for in-pile sources can be cumbersome. The

high-radiation, and subsequently high activation, environment means that it becomes very difficult to make changes and repairs to a source after it has been put in place. The SUN2 superfluid helium source excels in these aspects. Focus will be giving on the versatility and short cool-down times of this source.

2.2   The main cooling tower

The schematic of the SUN2 cryostat is shown in Fig. 2.1. The whole apparatus can be logically divided into the following parts: the main cooling tower, the horizontal transfer section, and the UCN production tower (Fig. 2.2). This section will focus on describing the main cooling tower, where most of the primary cryogenic functions take place, and the horizontal transfer section.

The cryostat is a continuous flow ^{3}He refrigerator using a 2-stage Gifford-McMahon mechanical coldhead for cooling of the radiation screens. A unique feature employed is that this cold head is also used to pre-cool—directly at the 1st stage and at a special heat exchange section between the 1st and 2nd stage—and liquefy the gaseous ^{4}He and ^{3}He inputs. The 1K pot has a volume of $14\,L$, and, besides from being used to cool the ^{3}He before the ^{3}He pot, it also acts as the source of the ^{4}He for the UCN converter after filtration through a superleak. The ultrapure ^{4}He converter fills the UCN production volume in the UCN production tower and is cooled by a copper heat exchanger in thermal contact with the ^{3}He pot in the main cooling tower. The horizontal transfer tube connects the two towers and provides the thermal contact when it is filled. The geometrical arrangement of the various devices inside the main cooling tower is shown in the photos of Fig. 2.3.

The results shown in this chapter were done with just the cooling tower, unless explicitly specified. This development and testing were done in a thorough and systematic manner. See Sec. A.1 for a summary of the time-line and steps of this work.

Fundamental cryogenic principles will not be covered in detail. The primary references found useful by the author of this thesis are Refs. [Eki06, Pob07, VR08]. There are also many other texts on the subject for the interested reader.
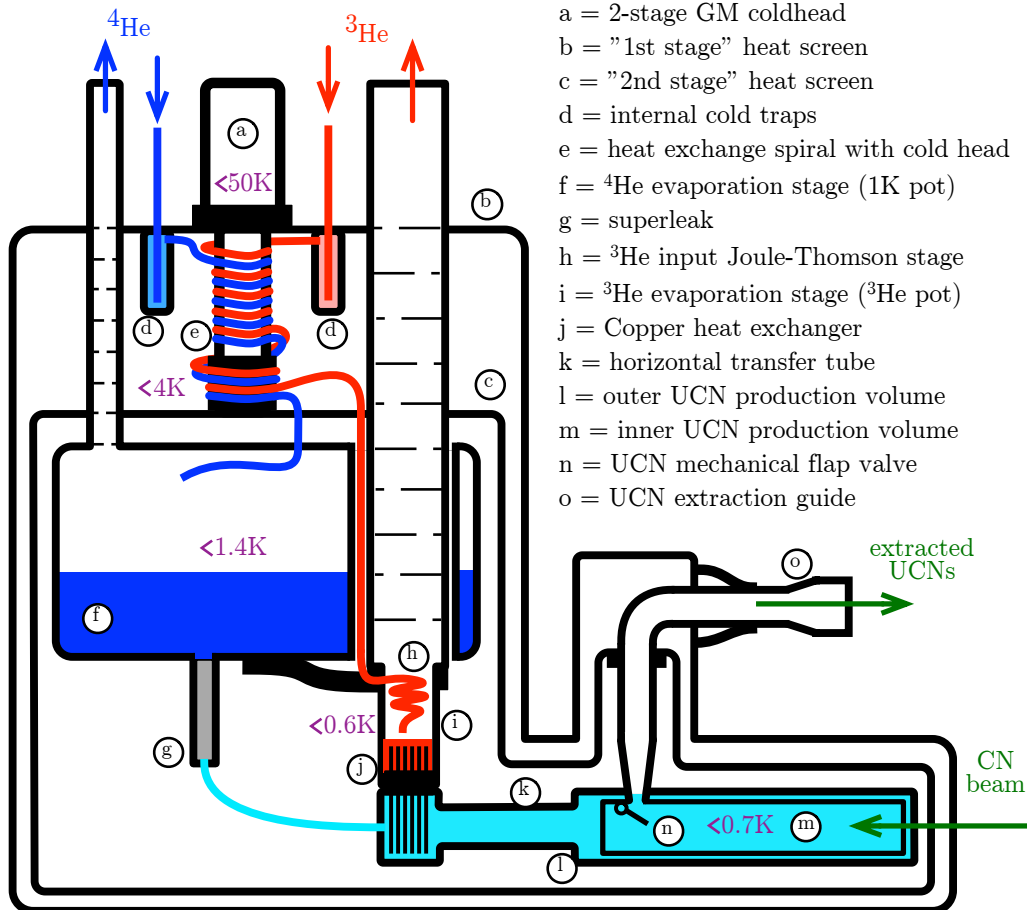
Figure 2.1: Schematic of the SUN2 source setup. In different colors are the ^{4}He circuit (■), ^{3}He circuit (■), and the ultrapure ^{4}He (■). The purple text (■) indicates the desired final operating temperatures for various sections and the green text and arrows (■) the direction of the incoming cold neutrons and the outgoing ultracold neutrons.
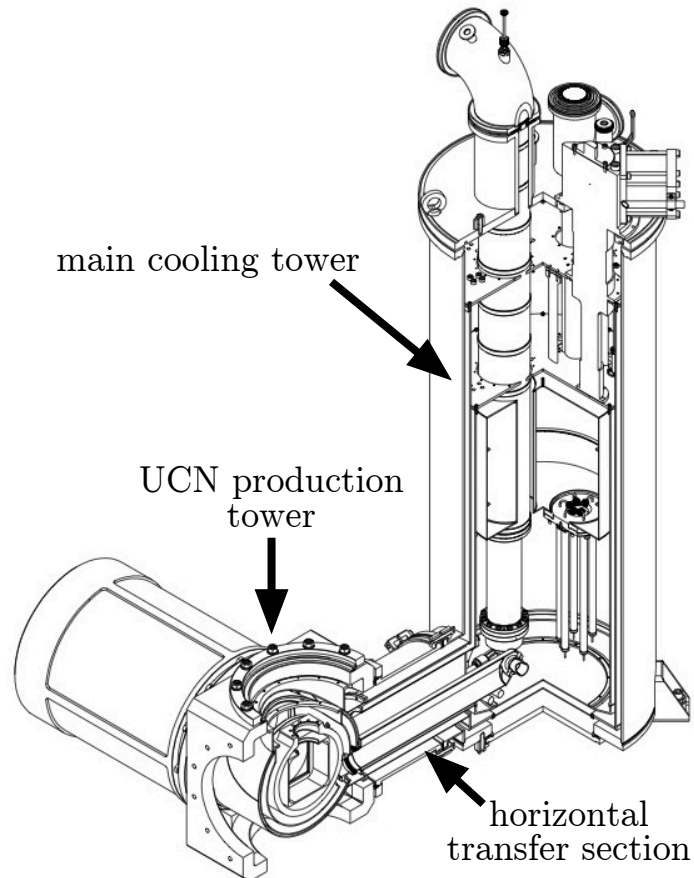
Figure 2.2: The layout of the primary sections of the SUN2 cryogenic superfluid UCN source described in this thesis. The design of many pieces has been changed since the diagram. See the individual sections for more details. The full UCN production tower is not shown. These are not shown.
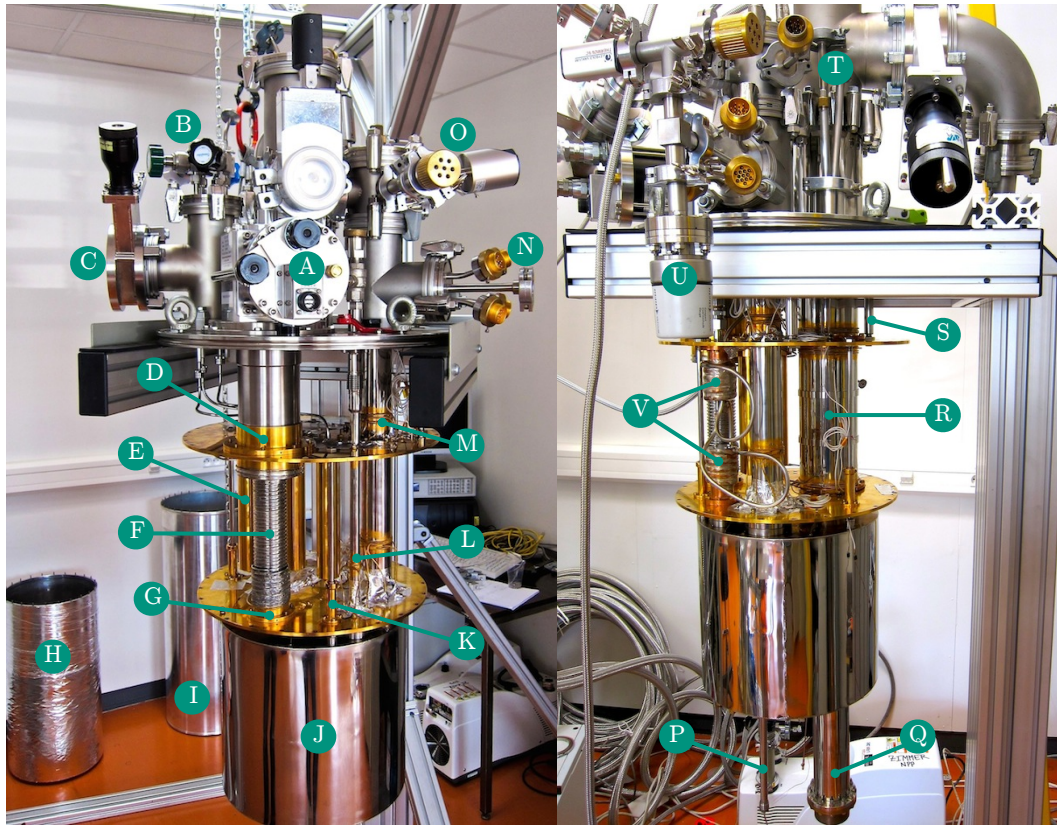
Figure 2.3: Photos of the interior of the main cooling tower. The various components are: (A) GM cold head; (B) gaseous input valves; (C) isolation vacuum pumping gate valve; (D) 1st stage of cold head; (E) internal cold trap; (F) heat exchange spiral capillary; (G) 2nd stage of cold head; (H) 2nd stage radiation screen; (I) 1st stage radiation screen; (J) 1K pot; (K) support rods of 2nd stage horizontal screen and 1K pot; (L) direct 1K pot filling feedthrough (since been removed); (M) 1K pot pumping tube; (N) vacuum electrical feedthroughs for thermometry & heaters; (O) membrane capacitance gauge and overpressure release valve of 1K pot; (P) superleak; (Q) ^{3}He pot; (R) ^{3}He pot pumping tube; (S) support rod of 1st stage horizontal screen; (T) needle valve feedthroughs; (U) isolation vacuum cold cathode gauge; and (V) liquid N$_2$ pre-cooling circuit. The photo on the *left* was taken before the ^{3}He pumping tube was installed. The photo on the *right* was taken after the removal of the direct filling line and replaced with the LN$_2$ pre-cooling line, and a standard ^{3}He pot, rather than the ^{3}He copper heat exchanger, was installed instead (see Sec. A.1). For scale, the 1K pot has a diameter of ≈ 29 cm and height of ≈ 27 cm.

2.2.1 The isolation vaccum

The isolation vacuum vessel of the main cooling tower is made from a custom ISO-K DN400 stainless steel tube 1.1 m in height with a ISO-K DN200 connector at a right-angle near the bottom for the horizontal transfer section and a ISO-K DN250 opening at the bottom to allow access for connecting the horizontal transfer tube. There are other ISO-K & ISO-KF DN 16–100 connectors on the top flange for various pumping, electrical and needle valve feedthroughs. Leak testing gives ^{4}He penetration rates on the level of $\approx 2 \times 10^{-7}\,\mathrm{mbar\,L\,s^{-1}}$ with a rise and fall time of $\approx 3\,\mathrm{hrs}$. No sharp spikes were observed. This agrees with the expected penetration of elastomer seals with a rate $\approx 1.3 \times 10^{-8}\,\mathrm{mbar\,L\,s^{-1}\,cm^{-1}}$ [VL].

Pumping of the isolation vacuum is done with a DN63 pumping port at the top of the cryostat. For most tests, a Pfeiffer TMU261P turbo molecular pump, with a ^{4}He compression ratio of 3×10^5 and a $220\,\mathrm{L\,s^{-1}}$ pumping speed, placed after 1.3 m of DN63 bellows, was used [1]. It takes typically $\approx 40\,\mathrm{hrs}$ to reach an isolation vacuum of $\approx 8 \times 10^{-6}\,\mathrm{mbar}$, close to the minimum value reachable at room temperature, as measured with a cold cathode gauge placed at the top of the cryostat and with the pumping gate valve closed. The best levels of vacuum is $\approx 4 \times 10^{-7}\,\mathrm{mbar}$ when the 1K pot is operating at $\approx 1.5\,\mathrm{K}$ and $\approx 2 \times 10^{-7}\,\mathrm{mbar}$ when the ^{3}He pot is operating at $0.4\,\mathrm{K}$.

2.2.2 The 1st and 2nd stage radiation heat screens

A 2-stage Gifford-MacMahon mechanical cold head is used for cooling the radiation screens of the cryostat. According to the specifications, the cold head provides a cooling power of 1.5 W at 4.2K at the 2nd stage and 35 W at 50 K at the 1st stage. The full cooling power curves from the manufacturer for this cryocooler are shown in Fig. 2.4.

Two horizontal circular gold-coated copper plates 5 mm thick with diameters of 37 cm and 33 cm are thermally anchored to the 1st stage and 2nd stage of the coldhead, respectively. Various apertures exist on these plates for the passage of pumping tubes, needle valves, capillaries and electrical wiring.

---

[1] During the PF1b experiment an Adixen ATP 100 turbo with a ^{4}He compression ratio of 2500 with a $60\,\mathrm{L\,s^{-1}}$ pumping speed placed after 30cm of DN63 tube connectors was used instead.
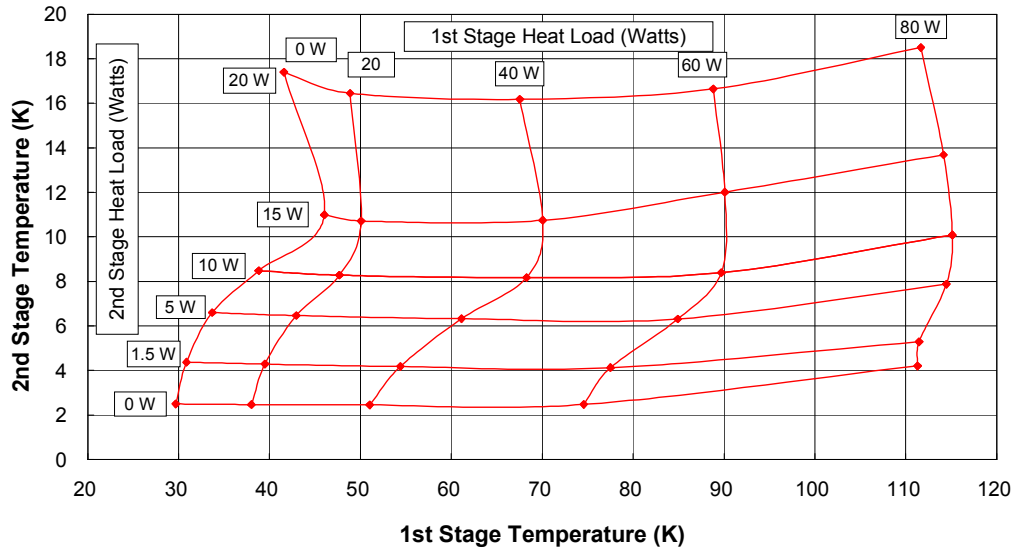
Figure 2.4: The typical cooling power capacity curves for the Sumitomo RDK415D cold head operating at 50Hz used as given by the manufacturer.

These gaps were covered as much as possible with cryogenic aluminium tape. In additional to the coldhead, mechanically supporting the 1st stage horizontal gold-coated copper plate are two thin walled stainless steel tubes attached to the top ISO-K 400 stainless flange. Similarly, the 2nd stage plate is supported by a set of 3 thin-walled stainless steel tubes attached to the 1st stage plate. These tubes also support the 1K pot. Conservative estimates of the heat load from conduction down the tubes to the 1st stage is expected to be $\approx 2\,\text{mW}$, and to the 2nd stage and 1K pot, $0.03\,\text{mW}$ and $0.02\,\text{mW}$, respectively. A photo of the horizontal screens and support rods can be seen in Fig. 2.3.

The vertical and bottom parts of the radiation screens are cylindrical and made from aluminium with thicknesses of $\approx 4\,\text{mm}$ and $\approx 3\,\text{mm}$, and heights of $94\,\text{cm}$ and $69\,\text{cm}$, for the 1st and 2nd stage screens, respectively. They are thermally attached to the horizontal screens via pressing with screws $4\,\text{cm}$ apart to provide an evenly distributed force over the contact surface areas of $80\,\text{cm}^3$ and $73\,\text{cm}^3$ for the 1st and 2nd stage. Apiezon-N cryogenic thermal contact grease [Api] was used to improve the contact. At the bottom of the screens there are two detachable plates to allow access to inside the radiation screens from the bottom.

Measurements of the temperatures at the 1st and 2nd stage are performed
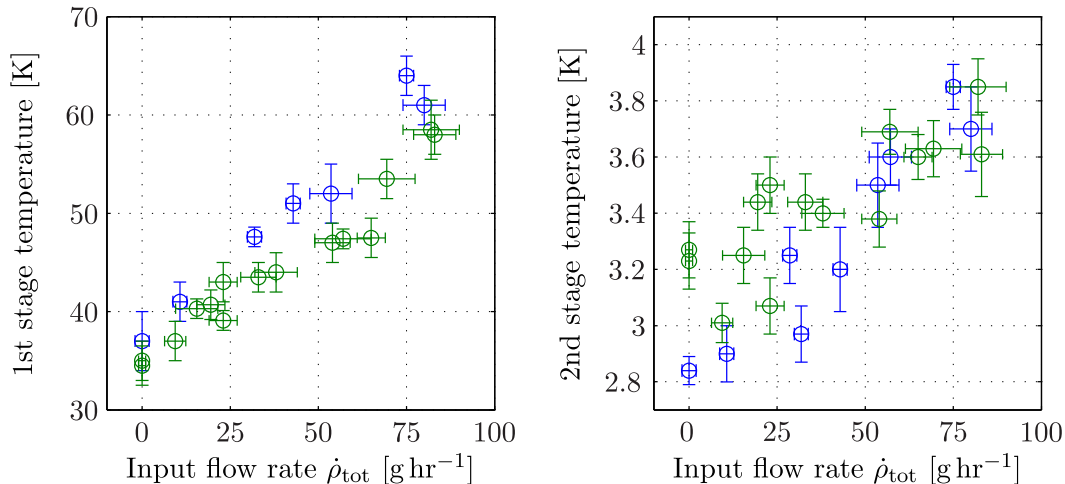
Figure 2.5: The stabilized temperatures at the 1st and 2nd stage of the cold head for various input helium mass flow rates. There are two sets of data. The blue circles ($\circ$) for the system before the ^{3}He pot was installed and the green circles ($\circ$) for after (see Sec. A.1). The mass flows are measured with the flow meters on the gas handling rack (Sec. 2.3.1), which are calibrated for ^{4}He. For the 1st case, since there is only ^{4}He input, $\dot{\rho}_{tot} = \dot{\rho}_{^4He}$. For the 2nd case, there is also input of ^{3}He, hence $\dot{\rho}_{tot} = \dot{\rho}_{^4He} + \frac{4}{3}\dot{\rho}_{^3He}$, in order to convert to a ^{4}He equivalent heat load due to the specific heat differences between the two isotopes. The error-bars are estimated from the spread and stability of the data.

with Cernox™ sensors from Lake Shore [Lak] [2] fixed onto the horizontal gold-coated copper plates < 10 cm from the cold head. Since the cold head is used to pre-cool the input ^{4}He and ^{3}He gases, the temperatures at the 1st and 2nd stage depend on the input gas flow (see Fig. 2.5). Since the pumping tubes are thermally anchored to the 1st and 2nd stage to reduce heat input from thermal conduction, there is a cooling effect depending on the output gas flow.

2.2.3 The ^{4}He circuit

Gaseous ^{4}He enters the cooling tower from a pre-pressurized bottle or from a compressor after passage through an external LN$_2$ cold trap (see Sec. 2.3.1

---

[2]Cernox™ is a thin film resistance cryogenic temperature sensor with a negative temperature co-efficent from Lake Shore Cryotronics. They can be used to measure temperatures down to 0.1 K depending on the calibration of the specific sensor. For the rest of the thesis, they will be referred to as just "Cernox" for simplicity.

about the gas handling rack). Once inside it passes through an internal cold trap thermally anchored to the 1st stage of the cold head and is cooled to $< 60\,\mathrm{K}$. There are two other of these cold traps each with their own separate input lines. One is used for the ^{3}He input and the other is spare and reserved for an auxiliary input for the time being.

After pre-cooling at the 1st stage, the gaseous ^{4}He enters through a $\approx$ $3\,\mathrm{m}$ length of capillary with an inner diameter $1.5\,\mathrm{mm}$ and wall thickness of $0.25\,\mathrm{mm}$ that is wrapped around and soft soldered on to the stainless steel jacket between the 1st stage and before the 2nd stage of the Gifford-McMahon cold head. The gas is cooled here to somewhere between the 1st and 2nd stage temperature. A small gap exists in the soldering of the capillary to avoid creating a thermal short cut between the 1st and 2nd stage. It is then soldered to the copper block of the 2nd stage of the cold head. The ^{4}He, now at a temperature close to that of the 2nd stage, passes through the 1K pot needle valve, an adjustable variable impedance, and into the 1K pot. Passage through the needle valve causes an abrupt pressure decrease that leads to cooling via the Joule-Thomson effect [Tho53]. Liquefaction of the ^{4}He is achieved at the 2nd stage or after the needle valve, just before entering the 1K pot.

The 1K pot or ^{4}He evaporation pot is a large, thin-walled (to reduce its thermal mass) vessel, an inner diameter of $28.5\,\mathrm{cm}$, a height of $27\,\mathrm{cm}$, and a volume of $14\,\mathrm{L}$. There are thicker stainless steel rings used for mechanical reinforcing it. An off-centered bore with a diameter of $11\,\mathrm{cm}$ exists for the pumping tube of the ^{3}He pot to pass through. The capillary inside the 1K pot is curled up so that it does not pass close to the bottom of the 1K pot to prevent thermal shortcuts between the bulk fluid and the 2nd stage. On the bottom of the 1K pot there is a detachable gold-plated copper flange with a diameter of $12.5\,\mathrm{cm}$ and thickness of $16\,\mathrm{mm}$. This allows access to inside of the 1K pot from the bottom. Attached to the inner side of the flange is a Cernox used to measure the temperature inside the 1K pot and on the outer side is the superleak (see Sec. 2.2.4).

The pumping tube of the 1K pot is 45 mm in diameter with a number of baffles down to just above the top of the 1K pot. Holes in the baffles alternating from left to right to minimize direct downward radiation transfer, while leaving an opening in the middle for the passage of a level meter or a direct filling line

with a maximum diameter of $\approx 5\,\text{mm}$. An Adixen ACP40 pump[3] is used for pumping on the 1K pot and a lowest continuous temperature of $1.34\,\text{K}$ in the 1K pot was reached when no heating from input ^4He and ^3He were present.

For the initial tests and PF1b experiment, the feed-through of the ^4He pumping tube through the isolation vacuum was poorly designed. A set of three O-rings that also allowed sliding due to thermal contraction of the pumping tube was used. However, if the flow rate of cold gas was too high, the O-rings could freeze, causing a leak between the isolation vacuum and 1K pot. At the time of writing this thesis, it has since been replaced with a bellows system so that this problem is not longer present.

The ^4He liquefaction rate at different temperatures in the 1K pot is shown in Fig. 2.6. The data was taken with different 1K pot needle valve openings and different input pressures (between $3-5$ bars). Continuous liquefaction at the lower temperatures was performed by continuously pumping on the 1K pot (the output rate is controlled with a KF16 angled valve). When the ^3He pot was installed and thermal contact made with the 1K pot, different input rates of ^3He were also used. This resulted in different heating loads on the 1K pot. Despite the variations in operating conditions, a general trend of the liquefaction rate with 1K pot temperature can be observed. Continuously liquefaction rates of $\approx 80\,\text{g}\,\text{hr}^{-1}$ is possible at $4.2\,\text{K}$. Liquefaction at lower temperatures were usually used since the ^4He needs to reach below $T_\lambda = 2.2\,\text{K}$ before it can be extracted through the superleak. Liquefying at 4.2K and then cooling it down via pumping, which results in a $40\,\%$ loss due to evaporation for $4.2\,\text{K}$ to $1.3\,\text{K}$, was estimated to take a longer time due to the pumping rate limitations of the poor-designed pumping tube at the end.

Initial tests of the liquefaction of gaseous helium with a GM cryocooler with a cooling stage between the 1st and 2nd stages were performed in Ref. [SWZ06]. In this study, the capillary parameters, such as its length and diameter, were varied. The thermal contact was made by first soldering the capillary onto copper plates and then clamping these plates onto the cold head. A continuous liquefaction rate into a small ^4He pot (400 mL) attached to the 2nd stage of $\approx 55\,\text{g}\,\text{hr}^{-1}$ was possible at SVP. A higher effective rate of $\approx 70\,\text{g}\,\text{hr}^{-1}$ was possible

---

[3]The ACP40 has its highest pumping speed of $35\,\text{m}^3\,\text{hr}^{-1}$ for an input pressure of $1\,\text{mbar}$ for air. At $3 \times 10^{-2}\,\text{mbar}$ this is reduced to $13\,\text{m}^3\,\text{hr}^{-1}$ for air. If pumping helium this is even lower. Hence, the ACP is not well adapted to pumping helium.
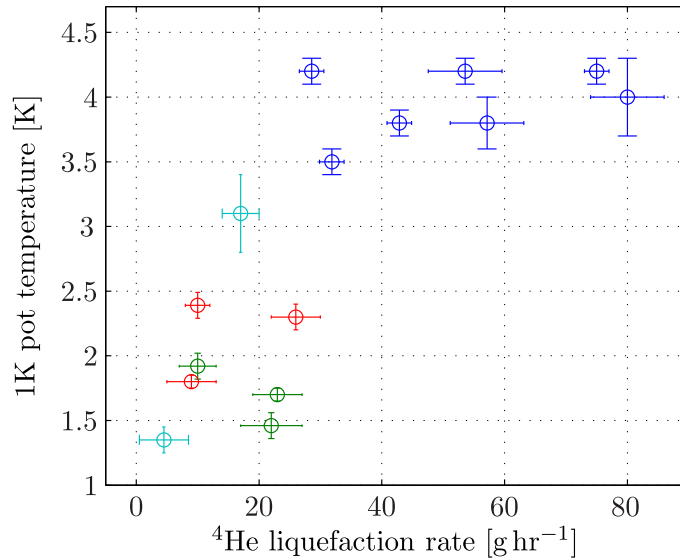
Figure 2.6: The stabilized temperature inside the 1K pot for different ^{4}He liquefaction rates. The data shown is for just the 1K pot installed (blue circles ○), with the ^{3}He pot installed (green cirlces ○), with ^{3}He pot input weakly thermally coupled to 1K pot (red circles ○), and with ^{3}He pot input strongly thermally coupled to 1K pot (cyan circles ○). The error-bars are estimated from the spread and stability of the data.

when liquefaction at a higher 1K pot pressure (and thus higher temperature) followed by cooling with the cold head down to $4.2\,$K was performed. In this cryostat, the latter technique is not possible due to the large, thin-walled 1K pot. The improved thermal contact from soft soldering of the capillary directly on the outer stainless steel jacket allowed an improved continuous liquefaction rate of $\approx 80\,$g$\,$hr^{-1} with 1 bar in the 1K pot and $3.8\,$K at the 2nd stage of the cold head. The prospect of this liquefaction rate from a GM cryocooler—which has a lower power consumption than compared with other commercially available small-scale liquefiers—has interesting practical prospects [SWZ06].

2.2.4   Superleak

The effect on the storage time from absorption of UCNs by trace ^{3}He in the production volume can be large. Commercially available ^{4}He has a ratio of ^{3}He to ^{4}He, $R_{34} \approx 10^{-6} - 10^{-7}$. The characteristic loss time is given by $\tau_{\mathrm{abs}} = \left(n R_{34} \sigma_{th} v_{th}\right)^{-1}$, where $n = 2.2 \times 10^{22}\,$cm^{-3} is the number density of He atoms at

below $2\,\mathrm{K}$ and σ_{th} = $5300\,\mathrm{barns}$ is the absorption cross-section at the neutron thermal velocity v_{th} = $2200\,\mathrm{ms^{-1}}$. Therefore, τ_{abs} = $3.9 \times 10^{-8}\,\mathrm{s}\ \mathrm{R}_{34}^{-1}$. So to reduce absorption loss from ^{3}He such that $\tau_{\mathrm{abs}} > 400\,\mathrm{s}$, a purity of $R_{34} < 10^{-10}$ is required.

A technique called superleak filtration, which exploits the difference in superfluid transition temperatures T_λ of ^{4}He ($2.2\,\mathrm{K}$) and ^{3}He ($3\,\mathrm{mK}$), can be used for purification. A superleak is essentially a material porous enough to allow the passage of superfluid while dense enough to block the transmission of normal fluids and gases. The first demonstration of this used a superleak made with jeweller's rouge (Fe_2O_3 powder around $0.5\,\mu\mathrm{m}$ in size) which produced a purity of $R_{34} < 5 \times 10^{-8}$ [MD72]. Later, a superleak made from Vycor (a porous glass with a sponge-like structure with pore sizes around $4\,\mathrm{nm}$) was used to produce a purity of R_{34} = $(4 \pm 2) \times 10^{-10}$ [Fat75]. A group later combined using the heat flush technique with superleak filtration by placing a heater just before the entrance to the superleak [4]. When heat input is applied, the superfluid component (in the 2-fluid theory of superfluidity) flows towards the point of heating while the normal fluid flows away from it. ^{3}He travels with the normal fluid component (said to be caught in the "wind" of normal fluid) and is thus carried away from the entrance of the superleak. With the combination of heat flushing and superleak filtration, a purity attained of $R_{34} < 4 \times 10^{-10}$ was measured by mass spectroscopy and $R_{34} \approx 10^{-12}$ was estimated [AM76].

In this cryostat the superleak is made with a fine Al_2O_3 powder with a $50\,\mathrm{nm}$ grain size mechanically hammered by hand into a stainless steel tube with an inner diameter of $7.6\,\mathrm{mm}$, a wall thickness of $0.5\,\mathrm{mm}$ and a length of $17\,\mathrm{cm}$. The process is described in Ref. [Zim10]. The superleak was ^{4}He leak tested and found to be tight to $< 2 \times 10^{-6}\,\mathrm{mbar\,L\,s^{-1}}$ at room temperature. Lower levels were not achievable due to trapped ^{4}He in the porous superleak.

The design of the SUN2 superleak is shown in Fig. 2.7. The heater is placed near the exit end of the superleak (similar to what is done in Ref. [YNG05]). Due to the double walled tube design (with a $\approx 1\,\mathrm{mm}$ gap), the superleak is effectively submerged in the ^{4}He bath and thus cooled along its length.

The measurements of the extraction rate through the superleak for different heat input and 1K pot bath temperatures are shown in Fig. 2.8. The superleak

---

[4]Although the superleak was claimed to be "leaky" due to visible defects and high measured leak rate and heat flushing was deemed to be the dominant effect in the purification.
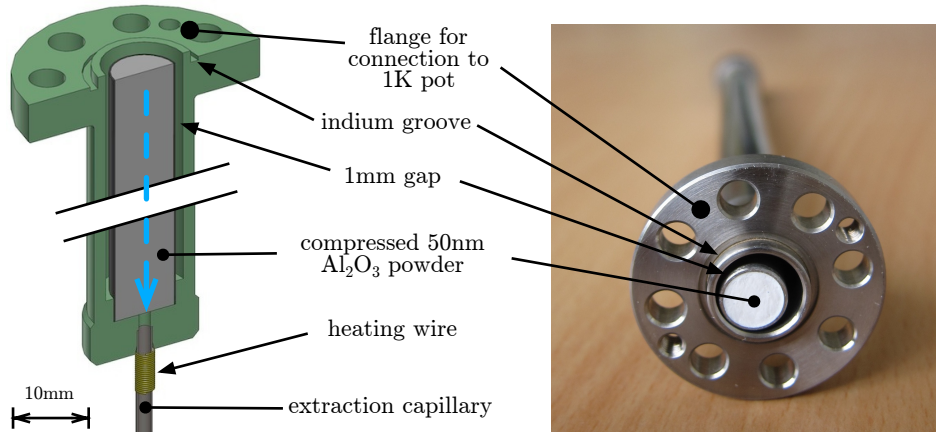
Figure 2.7: Technical drawing (*left*) and photograph (*right*) of the superleak in SUN2. The blue dotted line (– –) indicates the direction of the extracted superfluid in to the production volume. The total length of the superleak is $\approx 17\,\mathrm{cm}$, for scale.

heater was made from $30\,\mathrm{cm}$ of $0.1\,\mathrm{mm}$ diameter manganin wire (resistance of $16\,\Omega$ at room temperature) wound around the extraction capillary as close to the superleak as possible.

As expected, the extraction rate was found to increase with heating power and lower 1K pot temperatures. Values of $1.1 \pm 0.3\,\mathrm{g\,hr^{-1}\,mW^{-1}}$ at $2.0\,\mathrm{K}$, $1.6 \pm 0.5\,\mathrm{g\,hr^{-1}\,mW^{-1}}$ at 1.9K and $4 \pm 1\,\mathrm{g\,hr^{-1}\,mW^{-1}}$ at 1.6K were observed. There is an offset flow rate, for zero heat input, of $33 \pm 2\,\mathrm{g\,hr^{-1}}$ (weighted mean). A needle valve after the superleak, superfluid tight to $< 0.01\,\mathrm{g\,hr^{-1}}$, is used to stop any continuous leakage in the UCN production volume.

In the experiment of Ref. [Zim10] using ultrapure ^{4}He extracted through a superleak that was produced at the same time and in the same way as the one used in SUN2, a storage time of $\bar{\tau}_{\mathrm{tot}} = 76.5 \pm 1.4\,\mathrm{s}$ was observed. The converter vessel was cylindrical with an inner diameter of $66\,\mathrm{mm}$, a length of $70\,\mathrm{cm}$, and a volume of $2.4\,\mathrm{L}$, made from stainless steel and coated on the inner walls with fluorinated grease (Fomblin) grease [5]. The converter temperature was $0.8\,\mathrm{K}$. This storage time gives an upper limit of the purity of $R_{34} < 6 \times 10^{-10}$.

Moreover, in Ref. [Zim10], the flow rate through the superleak was generated with a separate ^{4}He input line—also cooled by the 1K pot—but put under

---

[5]The neutron optical potential of stainless steel and Fomblin grease are $V_{\mathrm{SS}} = 184 \pm 4\,\mathrm{neV}$ and $V_{\mathrm{fomblin}} = 115 \pm 10\,\mathrm{neV}$.
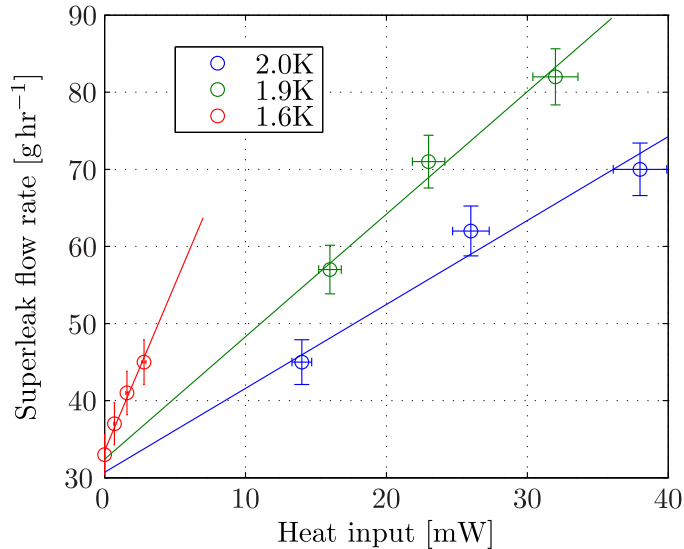
Figure 2.8: Mass flow through the SUN2 superleak at various heating power for different temperatures of the ⁴He bath in the 1K pot. These measurements were made during the PF1b experiment setup (with the copper heat exchanger, horizontal transfer tube, UCN production volume, UCN valve, and UCN extraction guide) when the production volume was > 4 K and the flow rate measured after the pump on the extraction guides.

high pressure. The pressure also pushes through ³He contaminants as well. In the SUN2 superleak, the heat flush technique is used additionally. This makes it more effective in filtering out ³He.

According to the theory and results of Ref. [YNG05, Nak96], the mass flow rate from the thermomechanical (also called "fountain") effect—superfluid flows to the downstream side to compensate for the chemical potential difference generated by the heat gradient—is expected to be:

$$\dot{\rho} = \frac{Q}{ST} \, , \tag{2.2}$$

where $\dot{\rho}$ is the mass flow rate, Q is the heat input to the downstream side, S is the specific entropy, and T is the temperature of the superfluid helium.

The linearity of $\dot{\rho}$ as a function of Q was observed in these results. However, the dependence on ST is harder to confirm since the temperature at the downstream end of the superleak is not known. It is not expected to be the same as the 1K pot temperature. Further tests are currently underway with a

small buffer volume after the superleak where a temperature sensor and heater can be placed directly in the down stream superfluid.

A hysteresis effect was observed in the opening of the superleak. There is no flow through the superleak when the 1K pot is first cooled to below T_λ. However, after applying heating to induce flow, and then turning the heating off again, the flow rate does not return to zero, but rather reaches an offset flow value. If the needle valve behind the superleak is closed for some time and then reopened, the offset flow does not reappear. This implies that it is not simply a pressure difference driving the offset flow. The cause of this is not fully understood yet.

2.2.5 ^{3}He circuit

The initial stages of the ^{3}He input pass through similar components as the ^{4}He circuit (see Sec. 2.2.3). Firstly, there is an internal cold trap, where it becomes cooled to the 1st stage temperature, and then it is followed by the spiral heat exchanger capillary, where it is cooled to the 2nd stage temperature. After this, instead of entering the 1K pot, the ^{3}He capillary passes through the 1K pot's bore next to the ^{3}He pot pumping tube (see Fig. 2.1). It is then brazed on to the ^{3}He input copper ring (see Fig. 2.9) then it enters the ^{3}He pumping tube. This copper ring is thermally anchored to the bottom of the 1K pot with copper braiding so that the ^{3}He is cooled close to the 1K pot temperature. Just before the needle valve, the ^{3}He passes through a spiral capillary (see Fig. 2.9) that provides heat exchange with the up-coming cooler vapor (after Joule-Thomson expansion). Such a setup is called a Joule-Thomson heat exchanger stage.

The ^{3}He liquid after the needle valve is collected at the bottom of the ^{3}He pot or ^{3}He evaporation stage. The bottom of the ^{3}He pot is thermally isolated from the input copper ring with a stainless steel tube with wall thickness 0.5 mm, an inner diameter of 63 mm, and a length of 20 cm. The expected heat input via conduction down this tube is 0.2 mW.

The thermal coupling of the ^{3}He input copper ring to the 1K pot is made with copper braiding wrapped around the input copper ring at one end; the braiding is wrapped and hose-clamped around the bottom flange of the 1K pot, with Apiezon-N grease used to improve the contact, at the other end. A
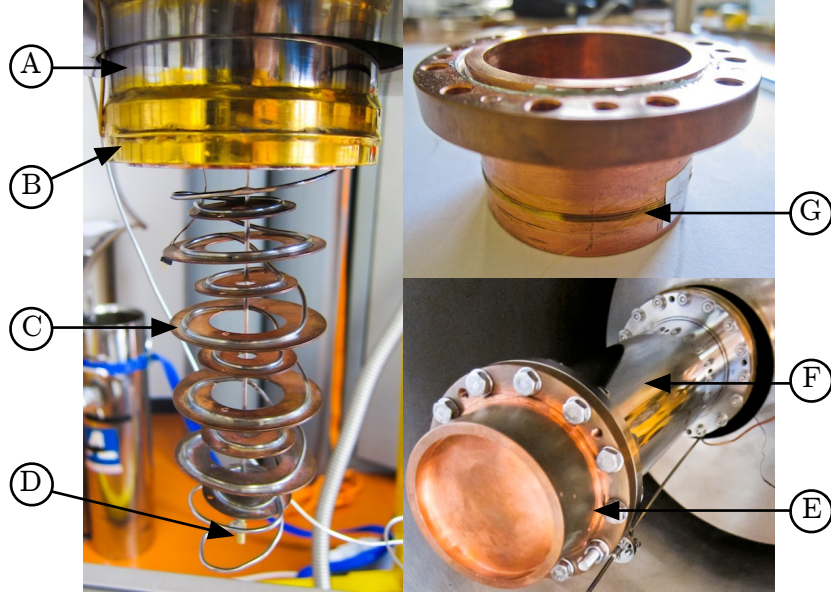
Figure 2.9: The various components making up the ^{3}He pot: (A) ^{3}He pot pumping tube; (B) ^{3}He input copper ring with the input capillary wrapped and soft soldered on; (C) Joule-Thomson heat exchanger stage; (D) the needle valve inside the ^{3}He pot; (E) standard copper ^{3}He pot used for tests; (F) thin stainless-steel tube isolating the copper input ring and ^{3}He pot; and (G) resistive heating wire wrapped around ^{3}He pot for cooling power tests. (The thermal contact between the ^{3}He input copper ring and the bottom of the 1K pot is not shown.)

test of the thermal contact between the 1K pot and ^{3}He input copper ring was made. A Cernox screwed onto a thin copper plate slid between the copper braiding and hose clamp to measure the temperature of the input copper ring was used. The results are shown in Fig. 2.10 for the initial cooldown period with low ^{3}He gas flow and for during the ^{3}He pot operation with different ^{3}He flows $\dot{\rho}_{^3\text{He in}}$. It is shown that the input ^{3}He temperature $T_{^3\text{He in}}$ is < 3.2 K (the liquefaction temperature of ^{3}He at 1 bar) for $\dot{\rho}_{^3\text{He in}} < 40$ g/hr. The temperature of the 1K pot remains $T_{1\text{Kpot}} < 1.5$ K.

The ^{3}He pumping tube inside the cryostat is a thin-walled (0.3 mm) stainless steel tube with an inner diameter of 93 mm and a vertical length of 92 cm. The tube is thermally anchored to the 1st and 2nd stage horizontal screens to reduce the conductive heat load. There are 12 baffles on the inside of the tube
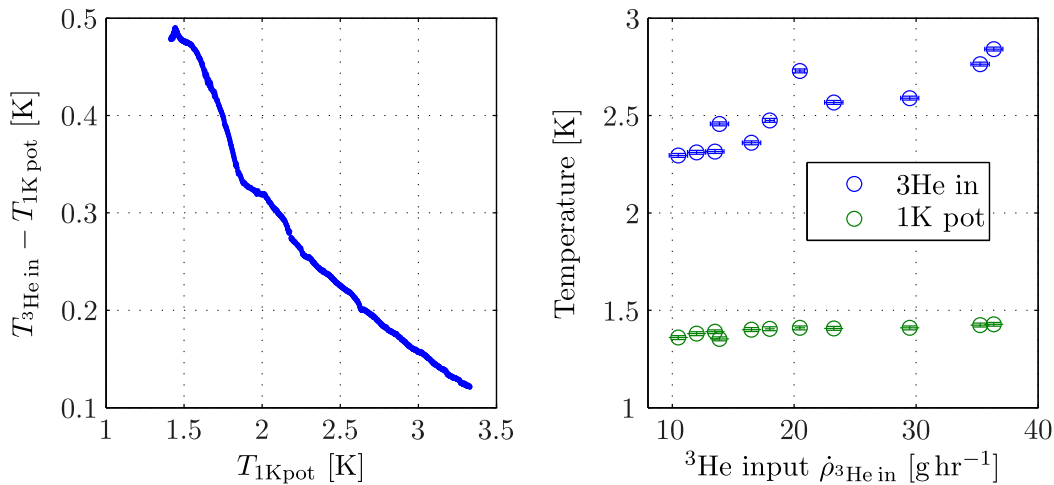
Figure 2.10: *Left*: The temperature difference between the ^{3}He input copper ring $T_{^3\mathrm{He\,in}}$ and the 1K pot $T_{1\mathrm{Kpot}}$ during the cooldown at PF1b (complete setup) with near zero ^{3}He flow. *Right*: $T_{^3\mathrm{He\,in}}$ and $T_{1\mathrm{Kpot}}$ for various ^{3}He flow rates $\dot{\rho}_{^3\mathrm{He\,in}}$ during the continuous operation of the ^{3}He pot. See Fig. 2.11 for the approximately required $\dot{\rho}_{^3\mathrm{He\,in}}$ for a given heat input.

to reduce radiative heating. The thermal contraction of this tube is compensated by the bellows on the horizontal transfer tube.

Typically $10-15\,\mathrm{m}$ of DN100 and DN150 tubing are used to connect to the ^{3}He pumping stand. The pumping stand consists 3 pumps in series: an Oerlikon RUVAC WSU 2001 Roots pump (nominal $2000\,\mathrm{m}^3\,\mathrm{hr}^{-1}$ pumping speed) backed by a smaller Pfeiffer Okta 500 AM Roots pump (nominal $500\,\mathrm{m}^3\,\mathrm{hr}^{-1}$) and then finally an Adixen ACP40 multi-Roots pump (nominal $40\,\mathrm{m}^3\,\mathrm{hr}^{-1}$).

Normally the copper heat exchanger is placed at the bottom of the ^{3}He pot. However, for testing the cooling power of the ^{3}He pot, a blank copper pot with heating wire (manganin wire, $0.1\,\mathrm{mm}$ diameter, $2.6\,\mathrm{m}$ in length with a measured resistance of $180\,\Omega$) wrapped around and glued on with GE varnish. The power deposited by the heating wire was measured using the 4-wire Kelvin method. The results of the stable, optimized ^{3}He pot temperature for different heating power (and the different $\dot{\rho}_{^3\mathrm{He\,in}}$ used) are shown in Fig. 2.11.

Since the ^{3}He circuit is closed, the flow rate in the circuit depends on the amount of ^{3}He in the circuit and the impedance of the needle valve (NV). If the amount of ^{3}He is fixed ($\approx 17\,\mathrm{bar\,L}$ of ^{3}He was used in this test) then just the NV opening determines $\dot{\rho}_{^3\mathrm{He\,in}}$. This is the parameter that needs to be optimized.
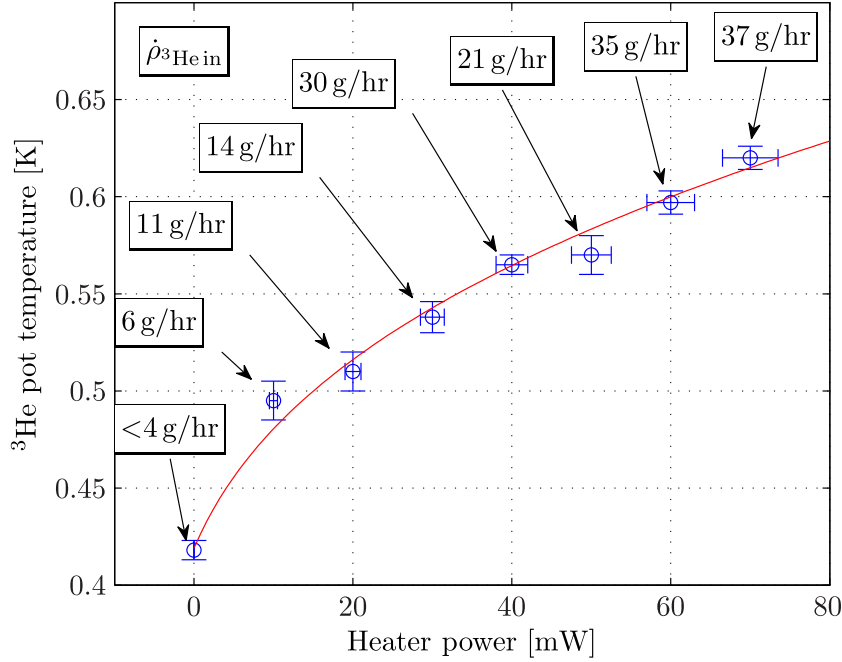
Figure 2.11: The optimized and stable temperature of the ^{3}He pot for different heat input from the resistive heater. The error-bars are estimated based on the accuracy of the heating power measurement and ability to find the optimum needle valve setting (see text). The text boxes $\square$ denote the mass flow of ^{3}He $\dot\rho_{^3\text{He in}}$ at the input flowmeter.

If the NV is closed too much (too high impedance) then $\dot\rho_{^3\text{He in}}$ is too low to replenish the evaporated liquid ^{3}He in the pot. If the NV is open too much (too low impedance) and $\dot\rho_{^3\text{He in}}$ is too high, then an unnecessary additional heat load due to the warmer input results and the lowest temperature in the ^{3}He pot is not reached. There was only one flowmeter for the ^{3}He circuit during the tests[6] and so checking if stability was reached was by looking at the input ^{3}He pressure on the gas rack. The measurements were made using an input pressure of < 1 bar (i.e. without the compressor) to avoid using ^{3}He at above atmospheric pressures.

The form of the cooling power curve in Fig. 2.11 can be approximated in the following way: the vapour pressure of helium, from the Clausius-Clapeyron equation and assuming a constant latent heat L, can be approximately given by $P_\text{vap} \propto \exp(-\frac{L}{RT})$, where T is the temperature of the helium bath and R

---

[6]A second flow meter has since been added.

is the gas constant. Pumping on a bath of helium and evaporating $\dot{n}$ number
of molecules per unit time gives a cooling power given by $\dot{Q}_{\text{evap}} = \dot{n}L$. If the
pump is assumed to have a constant volumetric pumping power then $\dot{n} \propto p_{\text{vap}}$
and the cooling power as a function of the helium bath temperature is given
by:

$$\dot{Q}_{\text{evap}} = k \cdot e^{-\frac{L}{RT}} \; , \tag{2.3}$$

where k is the constant of proportionality. At thermal equilibrium the cooling
is equal to the heating. I.e., $\dot{Q}_{\text{evap}} = \dot{Q}_{\text{heater}} + \dot{Q}_{\text{residual}}$, where $\dot{Q}_{\text{residual}}$ represents
the residual heat load[7] (e.g. by radiation) on the ^{3}He pot. Re-arranging Eq. 2.3
gives the following equation:

$$T_{\text{equil.}} = -\frac{L}{R} \ln \left(\frac{\dot{Q}_{\text{heater}} + \dot{Q}_{\text{residual}}}{k} \right)^{-1} . \tag{2.4}$$

A fit of the data in Fig. 2.11 with this equation gives the following parameters:
$k = 22,000 \pm 16,000\,\text{mW}$, $\dot{Q}_{\text{residual}} = 5 \pm 2\,\text{mW}$ and $L = 29 \pm 3\,\text{J mol}^{-1}$ with a
$\chi_\nu^2 = 1.1$. L was used as a fit-parameter since in reality it is not constant and
changes by $\approx 10\%$ over this temperature range.

The expected cooling power of the ^{3}He pot if assuming the nominal $2000\,\text{m}^3\,\text{hr}^{-1}$
pumping speed of the primary root pump is $100\,\text{mW}$ at $0.5\,\text{K}$. An analysis us-
ing the measured mass flow rates, the calculations of which are described in
Sec. A.2, gives an observed pumping speed of only $\approx 1000\,\text{m}^3\,\text{hr}^{-1}$. This is below
the rated pumping speed, implying that the pumping system is not optimized.
Unfortunately, data on the compression ratio as a function of pressure and the
pumping speed for helium could not be found for the three pumps. Hence,
a calculation of the pumping performance of the combined system could not
be made. Pressure gauges can be put in between the pumps to measure the
various intake and exit pressures to locate the problem. This can be done in
future tests. Currently, the problem is suspected to be due to the poor per-
formance of the ACP40 pump for helium or the low conductance due to the
baffles on the ^{3}He pumping tube. Root pumps have gaps between the rotors
of $\sim 0.1\,\text{mm}$. This makes them inefficient at pumping light gases, like helium,
at pressures just below the viscous flow regime due to high back flows.

---

[7]The heat load from the incoming flow of ^{3}He is neglected.

2.2.6   Heat exchanger and 90° piece

The ^{3}He evaporation pot provides the cooling power at the lowest temperature in the cryostat. Transferring heat across a material boundary becomes difficult at low temperatures due to a boundary resistance. For a liquid helium and metal interface, the boundary or Kapitza resistance R_K is defined as:

$$\Delta T = \frac{R_K \dot{Q}}{A} \,, \tag{2.5}$$

where A is the contact surface area, ΔT is the temperature difference across the boundary, and $\dot{Q}$ is the heat flow across the boundary. The source of the resistance is thought to be due to the acoustic mismatch of the phonons between the two materials, with $R_K \propto T^{-3}$. This theory predicts for ^{3}He-Cu and ^{4}He-Cu interfaces, $A R_K T^3 = 0.1 \, \mathrm{m^2 \, K^4 \, W^{-1}}$ and $0.05 \, \mathrm{m^2 \, K^4 \, W^{-1}}$, respectively. However, this theory only works well for the temperature range $20 \, \mathrm{mK} \leq T \leq 100 \, \mathrm{mK}$. It has been measured that, for $T \approx 1 \, \mathrm{K}$, R_K is typically an order of magnitude lower than the prediction. The method and quality of preparing a surface was found to have a significant difference.

To reduce the temperature step across a boundary due to the Kapitza resistance, a large contact surface area must be used. This is the idea behind the use of a heat exchanger. Instead of sintered metal that is typically used, SUN2 uses a "hair comb" shaped design. A block of copper is cut in to fine fins at its two ends (see Fig. 2.12). Such a design provides a contact surface of $\approx 1000 \, \mathrm{cm^2}$ on each side. This provides contact between the ^{3}He and the ultrapure ^{4}He in the "90° piece" that is situated directly underneath the ^{3}He pot (also see Fig. 2.12). The capillary from the needle valve directly after the superleak enters this piece. There are also electrical feedthroughs for the sensors used inside the UCN production volume here.

During the beam time on PF1b the largest temperature difference observed across the heat exchanger was $< 30 \, \mathrm{mK}$ for the lowest ^{3}He pot temperature of $1.05 \, \mathrm{K}$. This temperature was measured with a Cernox sitting on top of the fins of the heat exchanger. The temperature of the production volume was measured at the UCN production volume. This ^{3}He temperature is a lot warmer than the lowest operating temperatures expected. It is hard to extrapolate and evaluate the performance of the heat exchanger from this
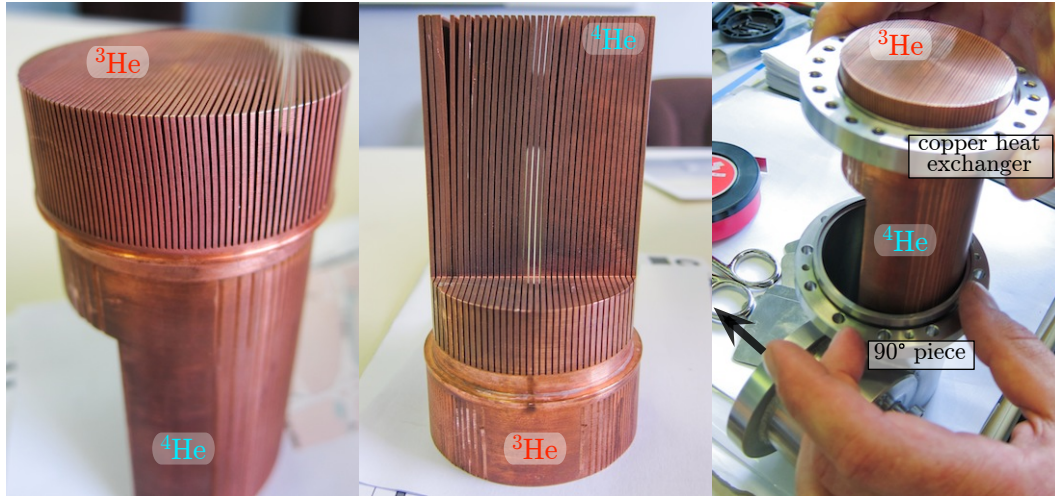
Figure 2.12: The "hair comb" copper heat exchanger used in SUN2. Labels indicate the ends used for the ^{3}He and ^{4}He. On the far right, the position of the 90° piece below the heat exchanger is shown. The arrow ← indicates the direction of the horizontal transfer tube.

result. Further measurements are currently underway.

2.3   Horizontal transfer section

The horizontal transfer section connects the main cooling tower with the UCN production tower. It contains the horizontal transfer tube, heat screens, and a ISO-K DN200 aluminium tube for the isolation vacuum. The horizontal transfer tube is connected to the 90° piece on the main cooling tower side (see Fig. 2.12) at one end, and the end aluminium piece of the outer production volume on the UCN production tower side (see Fig. 3.1) at the other. When this tube is filled with superfluid helium it provides the thermal contact of the converter in the UCN production volume to the copper heat exchanger so that it is cooled by the coldest part in the cryostat.

The conductivity of superfluid ^{4}He is very high near T_λ, but it drops off rapidly at lower temperatures. From Ref. [Pob07], at $1.2\,\mathrm{K}$ the conductivity is $160\,\mathrm{W\,cm^{-1}\,K^{-1}}$, while at $0.5\,\mathrm{K}$ this drops to $\approx 1\,\mathrm{W\,cm^{-1}\,K^{-1}}$ for a tube of $8\,\mathrm{mm}$ diameter. The conductivity of superfluid ^{4}He κ was found to depend on the diameter of the tube d as $\kappa \propto dT^3$. Since the cross-section area of a

circular tube is $\propto d^2$, the total dependance is $\propto d^3$.

The horizontal transfer tube used for the PF1b experiment was a stainless steel tube with an inner diameter of $50\,\mathrm{mm}$, a wall thickness of $1.5\,\mathrm{mm}$, and a length of $45\,\mathrm{cm}$. At $0.5\,\mathrm{K}$ with $200\,\mathrm{mW}$ of heating, the temperature difference between the two ends of $\approx 30\,\mathrm{mK}$ is theoretically expected. At the two ends of the tube there are two sets of flexible bellows so that the tube is not completely rigid. These are needed to allow its length to remain the same when cooled, to compensate for any shifts in alignment of the main cooling tower with the UCN production volume, and to allow its end flanges to pivot so that changes in position due to thermal contraction of the end pieces can be allowed. Due to the mechanical difficulties of detaching this tube at its end flanges, this has since been modified to a slightly smaller diameter.

The heat screens around the horizontal transfer tube are shown in Fig. 2.13. The horizontal copper rods with conical, tapered ends insert into a slot on the end of long vertical copper rods running down from the gold-plated horizontal copper plates inside the main cooling tower (see Fig. A.4). This system of copper rods, two for each screen, provides the thermal contact between the cold head and the heat screens in the UCN production tower. In the 2nd stage screen of the horizontal transfer tube it can be seen that two openings exists. The transfer tube is used at the bottom opening only. The top opening was initially designed for a heat switch for the initial cooling of the UCN production volume. But it has since been decided that using a heat exchange gas in the isolation vacuum is a better technique.

2.3.1   Peripheral equipment

A P&ID (Piping and Instrument diagram) of the gas handling components external to the cryostat is shown in Fig. 2.14. Further information describing the various components is given in Sec. A.3. The peripheral equipment associated with the SUN2 cryostat can be divided into: the gas handling rack, computer and electronics rack, ^{3}He pumping stand, and the LN_2 dewar. A process diagram of how these components are connected and operate together with the SUN2 cryostat and associated pumps is shown in Fig. 2.15.

The gas handling rack is an aluminium panel with the valves, flow meters and pressure indicators in the P&ID diagram of Fig. 2.14. There is a bottom
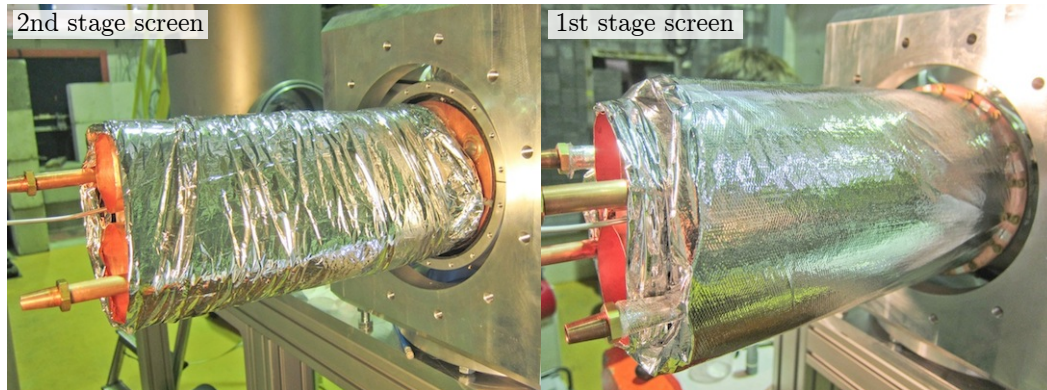
Figure 2.13: The copper heat screens of the horizontal transfer tube mounted onto the screens inside the cube of the UCN production tower side. The copper rods for its thermal contact to the main cooling tower can be seen. Just beneath the upper copper rod on the *left*, the capillary for directly cooling the heat screens around the UCN production volume can be seen.

shelf that supports the membrane compressors, scroll pumps, and ^{3}He storage bottles. This allows the user to view the state of the cryostat and perform the necessary operations in one place [Ism10]. The tasks include: initial pump down of the ^{4}He and ^{3}He circuits of the cryostat, injection and circulation of gas in the circuits[8], extraction of ultrapure ^{4}He from the production volume to an external bottle, clean an external LN_2 cold trap without stopping gas circulation, recover ^{3}He to the storage bottles, refill new ^{3}He to the storage bottles, and perform leak checks of the circuits. The ^{3}He circuit is normally operated at below atmospheric pressure to prevent loss in case of leaks. Also a double membrane compressor, with the pressure between the membranes monitored, is used to prevent ^{3}He loss in case of membrane bursts. Various overpressure valves are in place to protect pumps and compressors. The rack has been leak tested to a level of $10^{-5}\,\mathrm{mbar\,L\,s^{-1}}$ with the main leak coming from the membrane compressors.

Swagelok PGI-series analog pressure gauges are used on the rack for the higher pressures measurements, while Oerlikon CERAVAC capacitance diaphragm gauges are used for measuring the lower helium pressures on the rack and in the cryostat. The flowmeters are the Bronkhorst Massview MV-102 and

---

[8]Normally closed circulation, but for the ^{4}He circuit, pumping out to air is necessary if boiling off large amounts of liquid from the 1K pot is required.
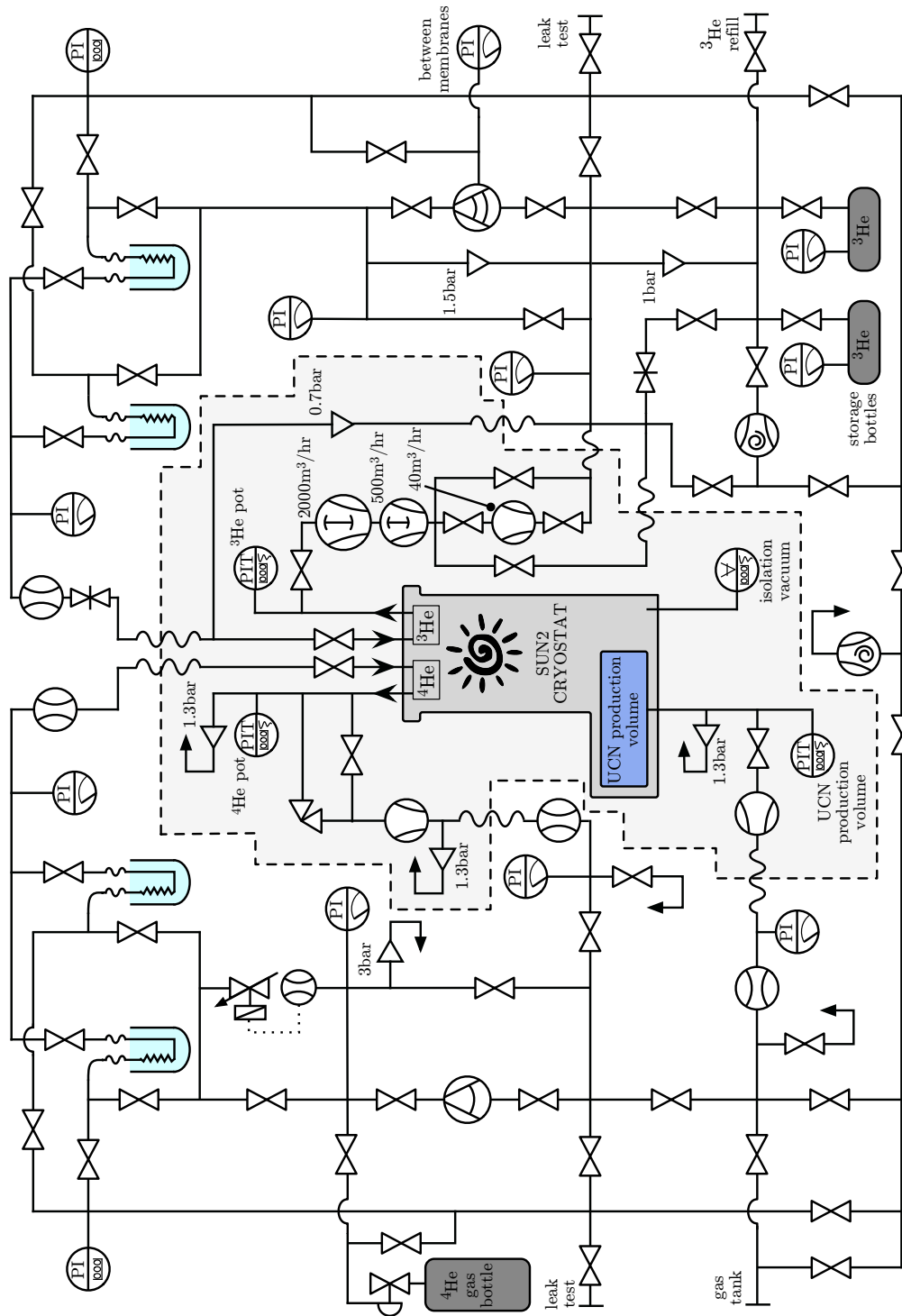
Figure 2.14: P&ID (Piping and Instrument) diagram of the gas handling components associated with the SUN2 source. For a legend of the symbols, see Fig. A.3.
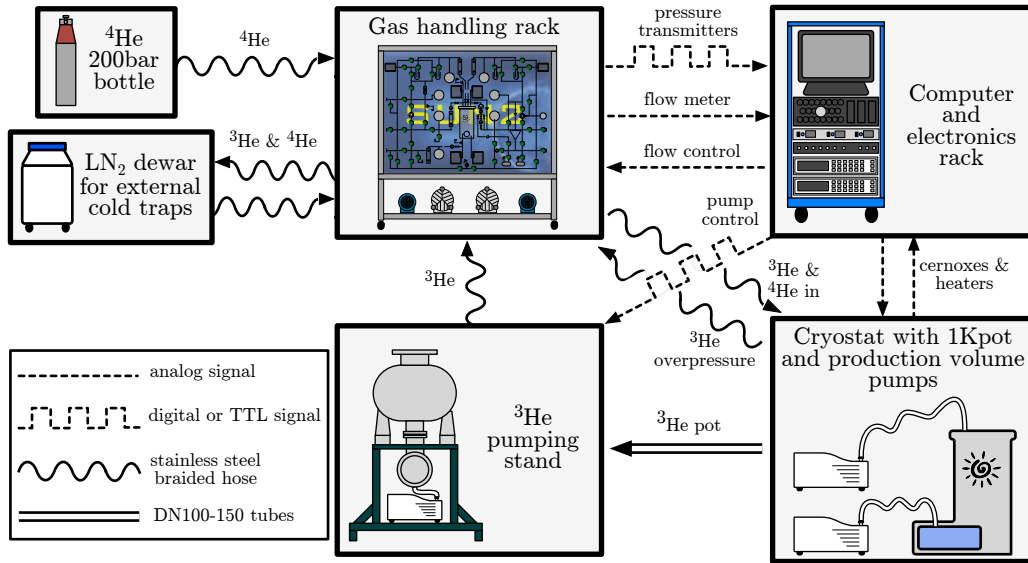
Figure 2.15: Process diagram of how the peripheral equipment of the SUN2 source are connected and operate together.

MV-104 thermal massflow meters [Bro09]. The accuracy of the flowmeters can be found in the specifications and is $\approx 2\%$. From our experience, the lowest level of flow that can be detected accurately is $\approx 5\,\mathrm{g\,hr^{-1}}$. The flowmeters display the mass flow of ^{4}He only. To convert to a ^{3}He mass flow the displayed flow is multiplied by a factor of $\frac{3}{4}$ to take into account the difference in the molar mass since the molar heat capacity of both gases are the same.

The LN_2 dewar where the external cold traps are submerged in has a capacity of $112\,\mathrm{L}$. The external cold traps are connected using stainless steel flex tubes to the gas handling rack so that they can be individually removed, heated and cleaned. The specified boil off rate of the dewar is negligible compared to the heating from the gas flow.

The ^{3}He pumping stand consists of the two blower Roots pumps and the multi-Roots backing pump described in Sec. 2.2.5 on a steel support frame. There are four valves on the stand (see Fig. 2.14): two are used to isolate the multi-Roots backing pump to reduce loss of ^{3}He here, another to open a by-pass line to speed up the initial pump down of the system, and lastly, a valve to open a line to the ^{3}He storage vessels that allows the injection of ^{3}He between the small root and the backing pump. The latter feature allows sucking out the ^{3}He in the storage bottles at a low pressure. The injection rate

can be controlled by a needle valve on the gas handling rack.

The electronics rack is a standard 19-inch rack which holds: (a) a computer for plotting and recording the temperatures, pressures and flow rates; (b) a Lakeshore 340 and a Lakeshore 370 temperature controller used to read the temperatures of the Cernoxes in the cryostat; (c) a flow meter electronic box which powers the flow meters and passes the analog voltages to and from the computer (since been replaced with a digital readout interface); (d) a home-made heater control box that provides 3 independent adjustable current supplies for the heaters inside the cryostat; and (d) a pump control box that contains relays for switching on and off the big and small root pumps. There are also controls for starting and stopping three Adixen ACP pumps. These are used for the ³He backing pump, 1K pot pump and the UCN production volume pump.

A slow control program created in Labview runs on the computer for recording and writing the measurements. The temperatures are read from the Lakeshore control boxes through a GPIB interface. The pressures are read with a USB-to-serial adaptor box connected to the computer and the RS232 interfaces on the Leybold Center 3 control boxes mounted on the gas handling rack. The program plots a history of the temperatures, pressures and flow rates on the screen and also writes this data to file. The interval between measurements can be changed by the user and is usually set to 5 s.

Chapter 3

SUN2: First UCN production results on PF1b

In this chapter the first UCN production results obtained on the PF1b cold neutron beam at the ILL in the spring of 2011 are presented. Due to the timing of the beam time, only a prototype version of the UCN production tower was used. The initial aim of the experiment was to attain the highest UCN numbers possible with the source. However, cooling problems restricted the ^{4}He converter to temperatures warmer than $\approx 1.1\,\mathrm{K}$. The key results obtained are an accumulation-and-empty measurement at close to the lowest temperature in order to deduce the UCN density in the source and the UCN production rate. Continuous measurements are done for increasing converter temperatures to determine the temperature-dependent loss in the converter. The lessons learned during this experiment lead to a redesign of many parts in the UCN production tower.

While the SUN2 source was tested on the PF1b white CN beam, it will eventually be situated on the H172b beam, a monochromatic 8.9Å beam, also at the ILL. A brief description of this new beam position is described in Chapter 8.

3.1 The prototype UCN production tower

A diagram of the prototype UCN production tower is shown in Fig. 3.1. The isolation vacuum is formed by the cube, the DN200 cross piece, a custom

DN200 tube around the production volume (not shown in the figure), and the horizontal section of the UCN extraction guide. The latter contains a vacuum feedthrough for the UCN extraction guide to be connected to the experiment to separate the converter from the isolation vacuum.

3.1.1 The eiffel tower structure and heat screens

The 1st and 2nd stage heat screens inside the cube and the DN 200 cross (called the "turret" sections) are mechanically supported by the "eiffel tower" structure. This structure starts with an aluminium ring (diameter $\approx 27\,\mathrm{cm}$) fixed onto the cube. Attached to this ring are graphite rods that form the frame of a truncated-cone. At the end of this frame, the rods are fixed to a copper ring (diameter $\approx 22\,\mathrm{cm}$) concentric to the aluminium ring. This is the 2nd stage copper ring. The graphite rods with $5\,\mathrm{mm}$ diameter have a length of $\approx 26\,\mathrm{cm}$. There is another copper ring (diameter $\approx 24\,\mathrm{cm}$) approximately halfway in between the aluminium ring and 2nd stage copper ring for the 1st stage screens. The rings and graphite rods are glued in place with Stycast® [1]. The purpose of the structure is to reduce the conductive heat load on the heat screens while reducing their diameters so that the structure is more compact.

The 1st stage heat screen inside the cube is made from several aluminum pieces screwed on to the 1st stage copper ring. The turret section then sits on top of this. The cylindrical heat screen around the UCN production volume (see Fig. 3.2) is attached to this copper ring also. The 2nd stage heat screens are in a similar configuration also, except the aluminium pieces and cylindrical screen are attached to the 2nd stage copper ring. On the far end of both screens around the production volume (where the CN beam enters) there are plastic feet for supporting their weight (see Fig. A.6). These feet are made from Synthetic Resin Bonded Paper (SRBP) PCB board. The room temperature conductivity of SRBP is $0.2\,\mathrm{W\,m^{-1}\,K^{-1}}$ [Pre], similar to other materials made from polymers. However, the values at low temperatures could not be found. If we assume it takes on similar values as the other polymers [Eki06], then the thermal load due to conduction along these feet are $\approx 0.5\,\mathrm{W}$ on the 1st stage

---

[1]Stycast® is a two-component epoxy encapsulant with high thermal conductivity at low temperatures and low coefficient of thermal expansion from Emerson and Cuming. For the remainder of the thesis, the text-registered symbol will be dropped for convenience.

Al ring fixed by threaded rods

DN100 bellows

thermal anchoring to 1st stage heat screen

ISO-K DN 200 cross piece of the isolation vacuum

UCN guide from experiment

1st stage heat screen "turret" section

UCNs

$\varnothing_{inner}$ 66mm

$\varnothing_{inner}$ 50mm

"Wilson" UCN guide connector

CN beam direction

end of vertical extraction guide of source

claw clamps fixing DN100 flange to Al ring

copper block on extraction guide

28cm

inner UCN production volume

2nd stage heat screen "turret" section

conical UCN guide piece

2nd stage heat screen inside the cube

inner copper end piece of UCN production volume

flange for horizontal transfer tube

the cube piece of the isolation vacuum

1st stage heat screen inside the cube

2nd stage heatscreen around volume w. cooling spiral

"eiffel tower" heatscreen support assembly

2nd stage heatscreen inside cube

feedthrough for UCN flapvalve

outer Al end piece of UCN production volume

outer superfluid containment vessel of UCN production volume

flange for horizontal transfer tube

Figure 3.1: The prototype UCN production tower used in the PF1b experiment. Not shown are the flanges of the DN200 cross piece and cube, and the back flanges and foils of the UCN production volume and heat screens (shown in Fig. 3.7). *Top*: Certain sections cut out to reveal the UCN extraction system and the inner UCN production volume. The end aluminium piece of the UCN production volume is shown as a black transparent frame only. *Bottom-left*: Only the 2nd stage heat screens are shown so that the "eiffel tower" can be seen. *Bottom-right*: The containment vessel of the UCN production volume.
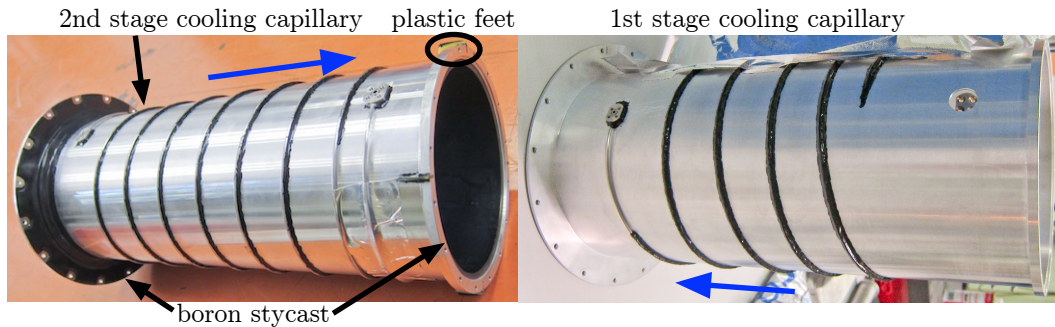
Figure 3.2: The 2nd stage and 1st stage cylindrical heat screens around the UCN production volume. Both are approximately 50 cm in length. The left-hand side is fixed onto the eiffel tower. The direct cooling spiral capillary glued on to the screens with Stycast can be seen. The flow of cold gas is from left to right on the 2nd stage screen and from right to left on the 1st stage screen (the flanges on the right of the 1st stage screen and 2nd stage screen are connected together). The black substance on the inside of the 2nd stage screen and on the end flange is boron-doped Stycast. The super-insulation wrapped around the screens is not shown.

heat screen and $\approx 0.1\,\mathrm{W}$ for 2nd stage screen, if the 1st stage screen is at 40K (however this can be as large as $\approx 0.4\,\mathrm{W}$ if the 1st stage screen at 100 K).

Cooling of both the 1st and 2nd stage heat screens at the UCN production tower comes from the thermal contact provided by the copper heat screen inside the horizontal transfer section (see Sec. 2.3). These are eventually connected to the cold head via long copper rods. However, due to the long distance, the conductivity from these is not expected to be high. Therefore, a capillary from the main cooling tower, after through the horizontal transfer tube, enters a spiral capillary system glued (with Stycast) at the cube-side of the 2nd stage heat screen. It travels to the end of the 2nd stage screen, is transferred up to the spiral capillary around the 1st stage screen at then returns towards the cube. When it reaches the end of the 1st stage screen, the helium (which should be significantly warmer now) exits at the top flange of the DN250 cross. The idea is to flush helium gas down this capillary to directly cool the screens.

A $3-4\,\mathrm{mm}$ thick coating of a special boron-doped Stycast exists on the inside of the 2nd stage screens. This can be seen on the cylindrical screens around the UCN production volume in Fig. 3.2 and on the screens inside the cube in Fig. A.6. The scattering cross-section of 8.9 Å neutrons in liquid ^{4}He below T_λ

is $\sigma_{\text{scat}} \approx 0.03$ barns, leading to a mean free path of around ≈ 15 m. For shorter wavelengths this becomes much larger—for instance at $3\,\text{Å}$, $\sigma_{\text{scat}} \approx 0.65$ barns [SDG55] and the mean free path decreases to ≈ 70 cm. Shielding is required for the scattered neutrons, particularly for a white beam like PF1b, where most of the flux lies in the shorter wavelengths. The closer to the UCN production volume the scattered neutrons can be absorbed, the less neutron absorbing material is required. A commonly used material for the absorption of neutrons is boronated-rubber sheets, which have a thickness of 3–5 mm and boron content of $\approx 40\%$. The ^{10}B content of natural boron is 20% and the neutron absorption cross-section of ^{10}B is 3835 barns for thermal neutrons, so the attenuation lengths of $8.9\,\text{Å}$ and $3\,\text{Å}$ neutrons in the boroned-rubber sheets are 0.08 mm and 0.2 mm, respectively. However, boronated rubber, due to its porous nature and out-gassing, is not designed to be used in vacuum. Therefore, Stycast mixed with boron powder, which performs well in low temperature and in vacuum, was used instead. There are still some regions, such as behind the horizontal transfer tube, that is not possible to coat with this boron glue. Hence, some boronated rubber sheets still had to be used.

3.1.2 The UCN production volume

The UCN production volume consists of an outer containment vessel, required to be tight for superfluid helium, and an inner UCN storage volume (called the "inner UCN production volume"), which is immersed in the superfluid, and whose inner surfaces are exposed to the produced UCNs for accumulation. The UCN production volume can be separated into its front parts that protrudes out from the cube and towards the incoming CN beam, and the end pieces, namely, the inner copper end piece and the outer aluminium end piece, which both sit inside the cube. The end pieces are where the parts for the UCN flap valve and vertical extraction system are located.

The front part the inner UCN production volume used for this experiment is made from four aluminium plates with a beryllium coating ($V_{\text{Be}} = 252\,\text{neV}$ [GRL91]) screwed together. This forms an inner volume with a length of 50 cm and cross-section of $8\,\text{cm} \times 8\,\text{cm}$ (see Fig. 3.3). The plates were coated via sputtering at the Petersburg Nuclear Physics Institute, Gatchina, Russia. They were coated twice in separate procedures in order to cover up any pin-
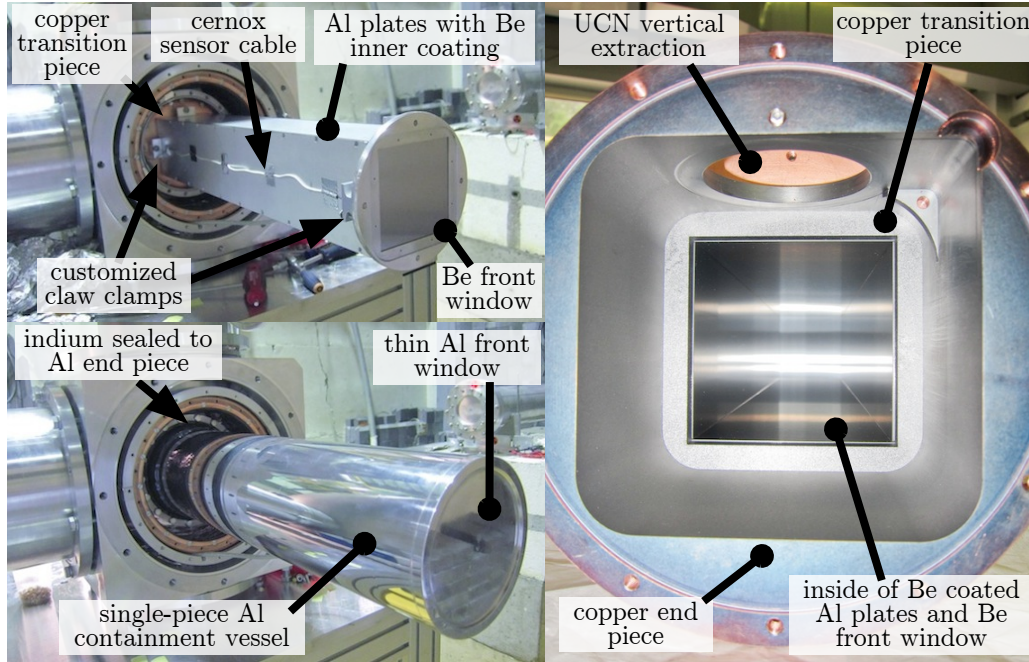
Figure 3.3: *Top-left:* The inner UCN production volume as viewed from the incoming direction of the CN beam. The front beryllium window and four aluminium plates screwed together can be seen. This construction fixed onto the copper transition piece, which in turn is fixed on to the copper end piece (see Fig. 3.4). *Bottom-left:* The outer superfluid helium containment vessel of the UCN production volume. *Right:* The inner UCN production volume viewed from the back of the copper end piece with the beryllium window removed. The quality of the beryllium coating can be seen. The UCN flap valve and the stainless steel extraction cone-piece are not installed.

holes caused by dust in the first coating. Differences in the neutron optical potential of beryllium in sputtered form compared to the standard bulk form is not important for this experiment. The $8\,\text{cm} \times 8\,\text{cm}$ cross-section was chosen to be used on the H172 beam, and is not ideal for the PF1b beam used for this experiment.

There are grooves near the ends of these plates that are used to fix a beryllium window 0.5 mm thick at the front end. At the back end, the aluminium plates are clamped onto a circular copper plate. This plate (called the "copper transition piece" in Figs. 3.3 and 3.4) is coated with beryllium on the inner surface and closes off the volume at the transition between the aluminium plates and the inner copper end piece.

The cross-section of the beryllium-coated inner surface of the copper end piece is $10\,\text{cm} \times 10\,\text{cm}$, slightly larger than the rest of the UCN production volume, and it is $7.8\,\text{cm}$ long. The UCN production volume is closed off at the back of the copper end piece with a piece of beryllium $1\,\text{mm}$ thick. This completes the inner part of the production volume where UCN production and accumulation takes place. It's volume is $\approx 3.9\,\text{L}$ for the total $50\,\text{cm} + 7.8\,\text{cm}$ length.

The inner part of the UCN production volume is not impervious to superfluid helium, therefore an outer containment volume is required. This vessel consists of a round cylindrical volume machined out of a single piece of aluminum (to avoid problems of cold leaks that can occur with aluminium welding) fixed onto the outer aluminium end piece with an indium seal. The inner diameter fits tightly around the outside of the square cross-section of the inner vessel and is used to support its weight. Its front surface is machined down to a thickness of $0.5\,\text{mm}$ to reduce scattering of the incoming CN beam. The back of the outer aluminium end piece is closed off with a thin aluminium window with an indium seal. This forms the superfluid containment vessel. The total volume of helium required to fill the UCN production volume (both inner and outer), including the $90°$ piece and the horizontal transfer tube, to the top of the inner volume is $\approx 7.3\,\text{L}$.

3.1.3 The UCN vertical extraction guides

The UCN extraction guide system exposed to the UCNs is made from polished stainless steel, which has a neutron optical potential of $V_{\text{SS}} = 184 \pm 4\,\text{neV}$. The extraction guide rises vertically out of the production volume and is sealed to the outer aluminium end piece to maintain confinement of the helium (mostly gas when in the guides, but there is some creeping of superfluid also). There is a copper block glued with Stycast to the vertical part of the UCN extraction guide. This copper block is then screwed onto the inside of the top plate of the 2nd stage heat screen's turret section in the DN200 cross. Thus, it is the 2nd stage turret (and eiffel tower structure) that supports the weight of the UCN production volume. This connection is also a thermal anchor of the UCN extraction guide to the 2nd stage heat screen for reducing conductive heat transfer to the production volume.

The vertical section of the guide is kept short to reduce the gravitational potential the UCNs have to overcome before they can be extracted. However, it should not be too short otherwise the heat transfer between the 2nd stage thermal anchor and the UCN production volume will be large. There is an elbow bend directly after the vertical guide so that the extraction guide ends up horizontal, giving room to place the next thermal anchor (to the 1st stage heat screen) further away.

The transition between the inner UCN production volume and the UCN extraction guides seen by the UCNs is the polished insides of a stainless steel cone. This cone serves two purposes. It provides a ballistic transport effect so that the UCNs trajectories are aligned more towards along the axis of the guide, helping them overcome the gravitational potential. And, the conical-shape reduces the opening exposed to the production volume. This reduces the heating via radiative transfer down the UCN extraction guides since Liouville's theorem applies for photon transportation as well. However, the opening should not be too small as to cause a long emptying time of the UCNs. In an attempt to further reduce the radiative heat transfer, the elbow on the extraction guides is thermally anchored to the 2nd stage heat screen with copper braiding as well. This was done to reduce the temperature of the parts with direct view of the production volume.

The heat transfer down this guide is difficult to calculate. It requires knowledge of the thermal profile of the guide with its various thermal anchors, as well as the probability of specular reflection of radiation from the hot regions far away. This extraction guide system, from the 90° elbow onwards, was used in the experiment of Ref. [Zim10]. The conical cone section has been changed but is not too different. In this experiment, a converter temperature of $< 0.8\,\mathrm{K}$ was achieved with a ^{3}He cryostat similar in design to this one.

The dimensions of the guide system are shown in Fig. 3.1. After the last tapered section, the extraction guide is increased to the common 66 mm inner diameter UCN guide standard (used at PF2). There is a "Wilson" UCN guide connection system built onto the source for the guide from the external apparatus to connect to. Due to the copper block being fixed onto the 2nd stage heat screen, thermal contraction in the vertical direction needs to be compensated for (there is enough sliding at the O-ring of the wilson connector to compensate for contraction in the horizontal axis). This is achieved by using

a short section of DN100 hydroformed bellows held at a defined length by connecting its claw clamps to an aluminium ring that is held in place by threaded rods. This prevents large vacuum forces crushing the bellows and prevents the O-rings on the Wilson connector to move out of place. The clearance in the holes of the aluminium ring allow for enough translational displacement of the bellows in the vertical plane to compensate for the contraction. The guide from the external apparatus (unless it is free to move vertically) should only be connected to the source after it has been cooled in this design.

3.1.4   The mechanical UCN flap valve

The mechanical UCN flap valve used in SUN2 to perform accumulation and emptying of the UCN production volume is shown in Fig. 3.4. It consists of a beryllium plate 61 mm in diameter and 3 mm thick supported by 1mm stainless steel wiring (fixed on by a M1 nut on the top side). It is connected to a rotating stainless steel axle. The rotation of this axle opens and closes the flap valve.

Fixed onto the end of the axle, after it passes behind the beryllium back window of the inner UCN production volume (see Fig. A.6), is a pulley. A stainless steel cable is fixed onto the pulley and rotates it when it is protracted and retracted by a bellow-sealed linear motion system at the top of the DN200 cross-piece. This mechanism has been verified to work with the SUN2 source cooled and UCN production volume filled with liquid helium.

In an attempt to improve the UCN reflection properties of the stainless steel parts inside the inner UCN production volume, they were coated via electro-deposition with natural nickel by hand (V_{Ni} = 252 neV). However, due to the difficult angles, not all the surfaces would have been coated and the quality and purity of the coating has not been verified. Also, the sharp angles and crevasses exposed to the stored UCNs are not ideal for storage.

When the UCN flap valve is fully closed, it is not completely tight against UCNs leaking through the small gap due to a lack of a malleable seal. However this leak rate is not significant and proves to be rather useful for monitoring the UCN density during the accumulation period.
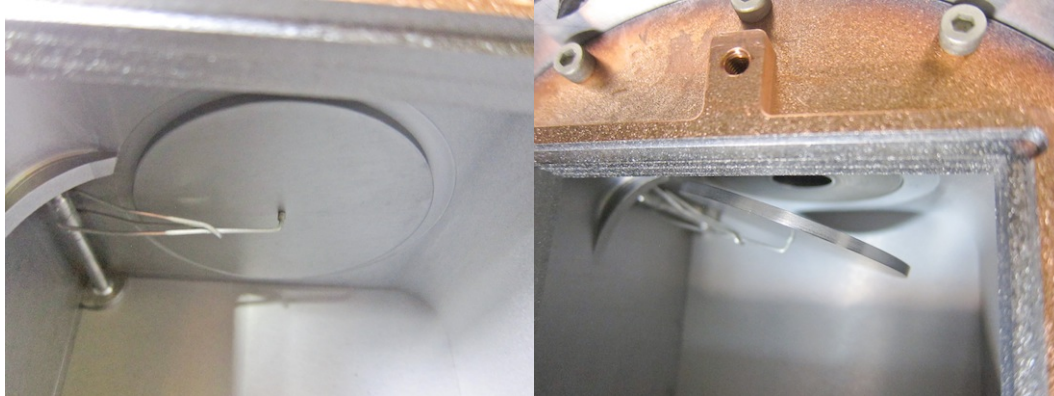
Figure 3.4: *Left:* The UCN flap valve in the closed position, as seen from the direction of the CN beam with the long aluminium inner UCN production volume removed. The beryllium plate, stainless steel wiring and stainless steel axle is visible. *Right:* The UCN flap valve opened, viewed from a similar angle as before. The bottom of the stainless steel conical piece can be seen. The copper transition plate used to fix the rectangular aluminium inner production volume to the circular copper end piece can also be seen. The opening angle of the UCN flap valve shown is just an example and does not reflect the actual angle used in the experiments. For scale, the beryllium plate is 61 mm in diameter and 3 mm thick.

3.1.5 Summary of the UCN potentials

When the CN beam is switched on, UCNs are produced isotropically [2] in the converter with an energy spectrum $dN/dE_n \propto \sqrt{E}$ (constant phase space filling). The superfluid helium has a neutron optical potential $V_{^4\mathrm{He}} = 18.5\,\mathrm{neV}$. The walls inside the production volume are coated with beryllium $V_{\mathrm{Be}} = 252\,\mathrm{neV}$, except for the mechanism for the UCN valve that is made from stainless steel ($V_{\mathrm{SS}} = 184 \pm 4\,\mathrm{neV}$) but is coated with nickel ($V_{\mathrm{Ni}} = 252\,\mathrm{neV}$)—although small spots are expected to have been missed in the hand electro-deposition process.

Due to the potential of the converter, the potential at the walls of the volume are reduced by $V_{^4\mathrm{He}}$. Also, when UCNs leave the converter they receive a gain in kinetic energy of $V_{^4\mathrm{He}}$. This helps them overcome the gravitational potential to reach the horizontal section of the extraction guide. UCNs produced at the top of the volume need a kinetic energy of 28 neV and UCNs produced

---

[2]In Ref. [LG93] calculations of the angular distribution of the produced UCNs show that they are isotropic only at zero UCN energy. At a velocity of $8\,\mathrm{m\,s^{-1}}$ the asymmetry is 6% in the forward-versus-backward direction.

at the bottom $36\,\mathrm{neV}$. Without sufficient energy to overcome the extraction threshold, they do not leave the production volume and will remain undetected. The extraction guides are made from stainless steel ($V_{\mathrm{SS}} = 184 \pm 4\,\mathrm{neV}$) only, so not all UCNs that are stored in the production volume are efficiently transported by the guides.

3.2 The experimental setup

In this section, the CN beam, shielding, the CN beam monitor, and the UCN detector, used for the experiment at PF1b will be described.

3.2.1 The PF1b beam

PF1b refers to the instrument at the ILL that provides a beam of cold neutrons, along with devices and facilities needed to polarize, characterize, shield and shape the beam [ILL08]. The guide itself is the H113 guide that ends inside the PF1b casemate after a total distance of $76\,\mathrm{m}$ from the Vertical Cold Source. The cold source is a spherical cell, 38 cm in diameter and 1.5 mm in thickness containing $\approx 20\,\mathrm{L}$ of boiling liquid deuterium ($24\,\mathrm{K}$) with a rectangular cavity to enhance the flux in the direction of the neutron guides. It is situated 70 cm from the reactor core and experiences a neutron flux of $\approx 5 \times 10^{14}\,\mathrm{n\,cm^{-2}\,s^{-1}}$ [Age89].

The guide is made of a series of $m = 2$ supermirror coated guides with a fixed height and a variable width forming a ballistic guide system [Abe06]. The dimensions of the guide inside the casement are $20\,\mathrm{cm}$ in height and $5.9\,\mathrm{cm}$ in width. Detailed measurements of the beam are described in Ref. [Abe06]. It was found that the differential particle flux $\partial\Phi/\partial\lambda$ can be approximated by:

$$\Phi(\lambda) = \Phi_0 \frac{\lambda_0}{\lambda} \frac{(\lambda/\lambda_2)^p}{1 + (\lambda/\lambda_2)^p} \mathrm{e}^{(-\lambda/\lambda_1)} \,, \tag{3.1}$$

with the parameters of best-fit found to be $\Phi_0 = 1.3 \times 10^{10}\,\mathrm{n\,cm^{-2}\,s^{-1}\,\mathring{A}^{-1}}$, $\lambda_1 = 2.6\,\mathring{A}$, $\lambda_2 = 2.4\,\mathring{A}$ and $p = 3.0$. At $8.9\,\mathring{A}$ the actual measured flux is 90% of the model equation. The spectrum of the PF1b beam is plotted in Fig. 3.5.

The beam was found to be uniform at the $20 \times 6\,\mathrm{cm}$ beam exit window to within 10% and can be described by an effective mirror constant—which
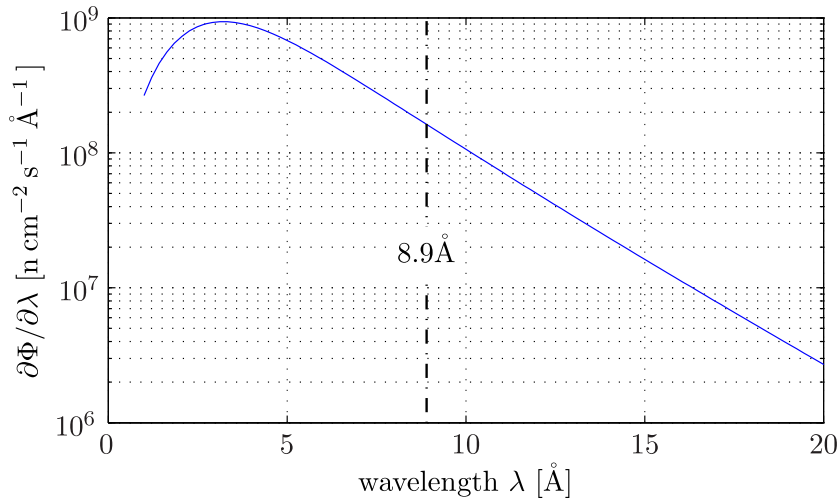
Figure 3.5: The differential particle flux $\partial\Phi/\partial\lambda$ of the PF1b beam described by a model from Ref. [Abe06]. The parameters used in Ref. [Abe06] for the capture flux converted to particle flux are shown. The model reproduces the measured value at $8.9\,\text{Å}$ to within 5%. The flux values are for the average over an area of $2\,\text{cm} \times 2\,\text{cm}$ centered on the axis only.

describes the divergence of the beam in the vertical and horizontal directions—of $0.017\,\text{rad}\,\text{nm}^{-1}$. It was proposed by the authors that these parameters are sufficient in describing the beam and can be used in the design of the equipment to be adapted to the beam.

It should be noted that since the measurements, a short-section of m=1 guide near the cold source was replaced with a new m=2 section. It is hypothesized that while this upgrade would boost the total integral flux density by 20%, the enhancements would occur only in the short wavelength region. For example, the flux at the long wavelength value of $8.9\,\text{Å}$ should remain more-or-less unaltered.

3.2.2   General layout

The primary PF1b m=2 supermirror guide, with cross-section $20\,\text{cm} \times 6\,\text{cm}$, ends in the PF1b casemate just in front of the pit of the experimental zone (see Fig. 3.6 for photographs at various stages setting up the experiment). Two additional secondary m=2 supermirror guides, both with a cross-section of $12\,\text{cm} \times 5\,\text{cm}$, forming a combined length of $2\,\text{m}$, sitting in its own separate

vacuum tube with aluminium end windows (made from 0.2 mm thick foils), were used to extend the beam into the experimental zone. The collimation of the larger primary guide to the smaller secondary guides was done with LiF rubber inside the casemate.

A table made predominately from aluminium (profiles and plates) was used to support the cryostat and the lead shielding. Adjustable feet allowed adjustment of the height for alignment with the CN beam. The main cooling tower sat on a slidable plate on the table (constructed using guide rails and bearing carriages). This sliding design allows the main cooling tower to be detached from the UCN production volume by accessing the main cooling tower at the ISO-K 250 bottom flange and freeing the horizontal transfer tube and copper rods used for heat screen thermal contact. For this installation the cube was not fixed to the table so the production volume could be displaced horizontally for alignment purposes as well. This table can be adapted for the final setup at the H172b guide position.

Due to the mismatch of the horizontal dimensions of the secondary CN guide (5 cm) with that of the UCN production volume (8 cm), misalignment in the horizontal plane (angle and displacement) is not as critical as in the vertical plane. During the initial setting up, a laser at the back of the PF1b experimental zone was used to align the production volume to the CN guide to within ≈ 1 mm. However, a few days later when pumping down the ^{3}He circuit, vacuum forces on a DN100 bellow displaced the whole cryostat, including the aluminium table. The laser could not be used again for alignment since it is known if its position has moved since, especially after moving of heavy concrete blocks near it has occurred. Best attempts were made to relocate the aligned position. While no direct measurement exists to prove this, we are confident that an alignment of $\lesssim 2$ mm was attained at the end.

3.2.3 Front and back windows and apertures

The exit of the secondary guides with a cross-section of 12 cm × 5 cm was collimated with LiF rubber to 8 cm × 5 cm to best match the 8 cm × 8 cm cross-section of the inner UCN production volume. This is, of course, not ideal but was the best that could be done given the available guides. The collimated CN beam emerging from the secondary guides also has to pass through a series of
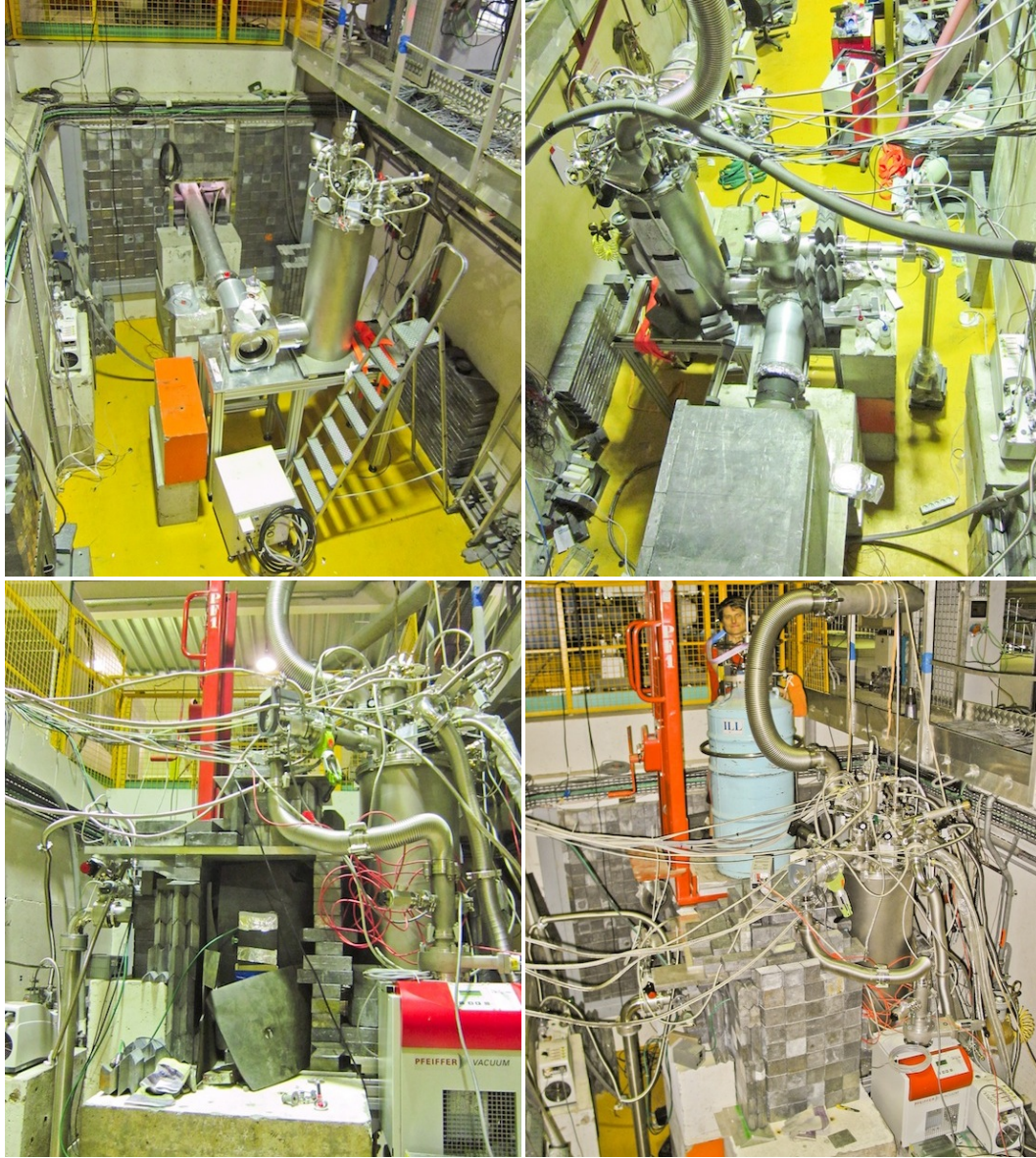
Figure 3.6: Photographs of the SUN2 source being setup in the PF1b experimental zone. *Top-left:* PF1b CN beam guide (long aluminium tube) being aligned with the UCN production volume. The main cooling tower sits on a slidable plate of the aluminium table. *Top-right:* boronated rubber sheets followed by a lead castle around the PF1b beam. The UCN detector and external guides are installed. *Bottom-left:* The lead shielding on the sides and top of the production volume. The CN monitor detector (partially hidden by the boronated rubber sheet) is installed at the back. *Bottom-right:* The complete lead shielding. The blue LHe dewar was used to directly fill the 1K pot.
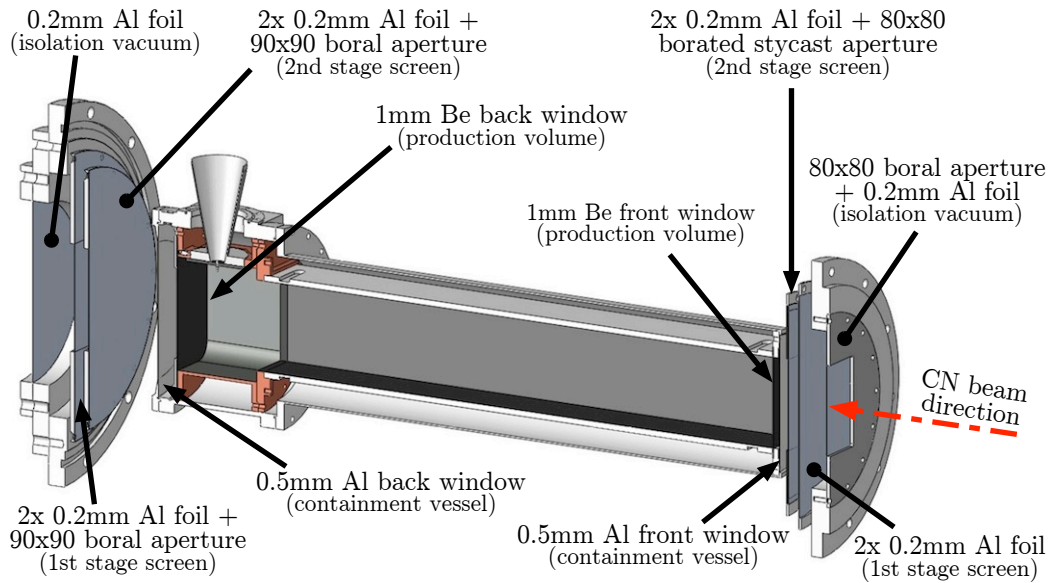
Figure 3.7: The windows and apertures the CN beam (coming from the right) has to encounter during transmission through the production volume. The Al foils are the standard 0.2 mm thick foils used at the ILL. Boral is a commercial boron aluminium alloy that comes in a range of 3-10% boron content.

aluminium windows (isolation vacuum, 1st and 2nd stage heat screens, production volume's outer containment vessel) and a beryllium window (inner UCN production volume) before reaching the superfluid helium converter. During its exit it also has to pass through a similar amount beryllium and aluminium before leaving the back window of the cube. Various apertures are used to absorb the diverged and scattered CN beam. Fig. 3.7 shows this arrangement.

The CN beam has to pass through a total of 1.5 mm of aluminium and 1 mm of beryllium before reaching the superfluid ^{4}He converter. The total cross-sections for thermal neutrons in aluminium and beryllium are 1.7 barns and 6.3 barns, respectively, with the primary interaction coming from elastic scattering (87% and 99.9%) [OEC12]. The mean free paths for 8.9 Å in aluminium and beryllium are thus ≈ 2 cm and ≈ 3 mm, and the fraction of 8.9 Å neutrons expected to have passed through without undergoing elastic scattering is around 66%. Of course, cold neutrons that undergo elastic scattering can still reach the superfluid converter, especially when it occurs close to it—like at the beryllium front window of the UCN production volume where most of the scattering occurs. However, the change of energy in the laboratory

frame of the scattered CNs could have shifted it beyond the width of the single phonon UCN production peak. Correspondingly, CNs with initially too short wavelengths could be shifted to the single phonon peak due to elastic scattering. However, for large energy changes to occur the scattering has to occur at large angles, angles at which decreases the probability of interacting with the converter due to the shorter traversed path length. For a quantitative estimate of the effects on UCN production due to the elastic scattering in the front window (and to a minor extend in the converter) a detailed calculation is required. However, this is not performed for this thesis and the 66% is thus a worst-case estimate that is correct to the first order only.

3.2.4   The monitor detector, beam dump and lead shielding

A thin ^{3}He gas-filled proportional counter, placed behind the back aluminium window of the isolation vacuum, with a sheet of boronated rubber with a small aperture placed in front of it, is used as a monitor for the CN beam. A large proportion of the cold neutrons are expected to have interacted with material (windows or the LHe itself) within the cryostat. Due to the lack of absolute calibration, this detector is used to monitor only the relative CN flux at a small opening centered around the center of the UCN production volume. The boronated rubber aperture, the monitor detector itself, and an additional sheet of boronated rubber at the back, act as the beam dump in this setup.

The completed lead shielding around the secondary CN guide and UCN production volume can be seen in Fig. 3.6. The PF1b area where the experimenters have access to while the CN beam is on is located on the upper level (just behind the yellow railing), to the left of the bottom two images on Fig. 3.6. From this direction, where the lead shielding is most critical, a thickness of no less than 15 cm of lead always present. Additional shielding (boronated rubber and lead), which cannot be seen in the photos, exists behind the axis of the horizontal transfer tube at the far side of the main cooling tower. The attenuation length of the 0.48 MeV gammas from the ^{10}B (n, α) ^{7}Li reaction in lead is approximately 6 mm.

3.2.5 The UCN detector and additional guides

After the UCN flap-valve of the production volume, the extraction guides are in an "inversed-U" orientation (see top-right of Fig. 3.6) leading to the UCN detector. The UCNs have to travel up an average height of 34 cm (measured from the center of the UCN production volume to the centre of the horizontal section of UCN extraction guides), followed by a horizontal distance of 78 cm, then undergo a 1.2 m drop to the ^{3}He UCN detector. The inner surfaces of all the guides are made from electropolished stainless steel ($V_{SS} = 184 \pm 4\,\text{neV}$).

On the horizontal UCN guide section outside of the source, a Wilson connector with a 20 mm side pumping tube in a T-shaped configuration was used. The UCN guides at connector were deliberately separated by several millimeters to allow for better pumping (less impedance) of the UCN production volume. This gap however causes a loss of UCN and thus reduces the UCN extraction efficiency. Connected to this aperture are gauges for measuring the vapor pressure inside the UCN production volume, an overpressure relief valve for emergency boil-off of the LHe inside the production volume, and a turbomolecular and ACP pump for initial evacuation of the production volume and pumping on the converter bath for cooling.

The UCN detector used is a ^{3}He gas proportional counter with a partial pressure of $\approx 10\,\text{mbar}$ of ^{3}He. The front window of the detector is made from an aluminium foil in a corrugated structure to increase its strength against vacuum forces. The 1.2 m drop increases the UCN kinetic energy in the vertical direction by $\approx 120\,\text{neV}$. The neutron optical potential of aluminium is $V_{Al} = 54\,\text{neV}$.

The charge caused by ionization from the n+^{3}He $\rightarrow$ ^{1}H+^{3}t reaction, releasing a total energy of 0.76 MeV, is collected on a single wire anode in the gas proportional counter. A pre-amplifier built into the detector is used to produce analog pulses $\approx -0.2\,\text{V}$ in amplitude and $\approx 2\,\mu\text{s}$ long in time. These pulses are then amplified by a Ortec 571 amplifier to produce pulses $\approx +1.1\,\text{V}$ in amplitude and 3 μs long. A typical pulse-height spectrum is shown in Fig. 3.8. The pulses are passed to a Ortec 455 single channel analyser (SCA) to produce the TTL pulses that are counted by the data acquisition program. It is also used to set a threshold to reject false peaks caused by electronic noise. The threshold (also shown in the figure) used for this experiment is placed at the center of
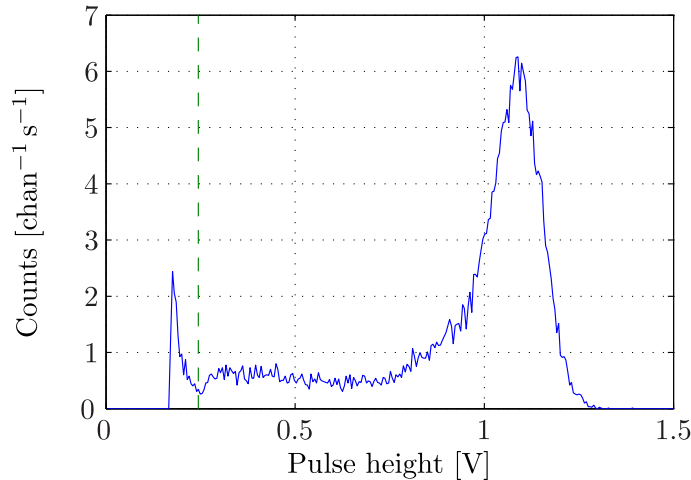
Figure 3.8: The pulse height spectrum from the ^{3}He UCN detector after the amplifier. Taken at a count rate of $\approx 300\,\mathrm{s}^{-1}$. Peak-detect mode on an Amptek MCA8000A at 1024 channels and 5 V full range was used. The threshold used to cut out electronic noise is shown as the green line (– –).

the separation of the noise and signal. For the bias voltage used, which defines the size of the separation, it can be seen than a small fraction of the noise spectrum falls above the threshold and so will also be counted. This is not problematic for this UCN production experiment since a much larger count rate of UCNs is expected.

3.2.6   The experimental control and counting program

A Labview[3] program [Pie], running on a separate computer than the cryostat control computer, is used to record the count rates in the UCN detector and CN monitor detector, as well as control the CN beam shutter and UCN flap valve. The counters used to record the counts from the UCN detector and monitor detector (as TTL pulses after the SCA) are from the National Instrument PCI-6221 or PCI-6052E DAQ cards (both can tolerate a source frequency of $> 20\,\mathrm{MHz}$). A USB relay box is used to control the pneumatic solenoid valves for opening and closing a CN beam shutter and the UCN valve.

The opening and closing times of both valves are around 1–2 seconds. The Labview program uses the built-in timing structures of the program, which of-

---

[3]A system design software from National Instruments.

fer resolutions of a few millisecond. The dead time when reading (and clearing) the counter channels, performed every 1 second, is not known but estimated to be negligible with the count rates in this experiment.

3.3 The cooldown on PF1b

In this section I describe the cooling of the main cooling tower combined with the prototype UCN production tower during the PF1b experiment. Twenty-three days were spent cooling down the system, but due to cryogenic problems only a temperature of $\approx 1.1\,\mathrm{K}$ was reached in the ^{4}He superfluid converter.

3.3.1 The cooldown summary

A plot of the temperatures at the various sections of the cryostat during the cooldown is shown in Fig. 3.9. Here I describe the various phases of the curve.

$\boxed{0}$: 2–3 days were spent pumping down the isolation vacuum. A level of $\approx 7 \times 10^{-5}\,\mathrm{mbar}$ was reached before the cold head was switched on and cooling began. Only one turbomolecular pump was used at the top of the main cooling tower. Due to the extra surfaces and super-insulation of the UCN production tower—as well as the additional distance to the pump—the vacuum level reached was not as low as with just the main cooling tower (described in Sec. 2.2.1).

$\boxed{1}$: LN$_2$ pre-cooling was used to cool the 2nd stage and 1st stage to around 100 K and 120 K over a course of ≈ 3 hours with the cold head running. ^{4}He and ^{3}He was circulated to transfer the "cold" to the 1K pot and ^{3}He pot. At the end of the pre-cooling $T_{1\mathrm{K\,pot}} \approx T_{^3\mathrm{He\,pot}} \approx 265\,\mathrm{K}$ and $T_{\mathrm{vol}} = 296\,\mathrm{K}$. To prevent a thermal short-cut between the 1st and 2nd stage after the pre-cooling, the build up of ice (e.g. water or CO_2) and the collection of LN$_2$ in the line were avoided. The tube was also pumped down and sealed off to prevent heat transfer via gas oscillations.

12 hours after the pre-cooling, flow in the direct cooling spiral capillary of the heatscreens around the production volume was initiated. It was discovered that there was a small leak in this capillary that is exposed to the isolation vacuum. Due to the limited time left in the allocated beam time, it was decided to continue the cooldown with this leak. The ^{4}He in this capillary passed

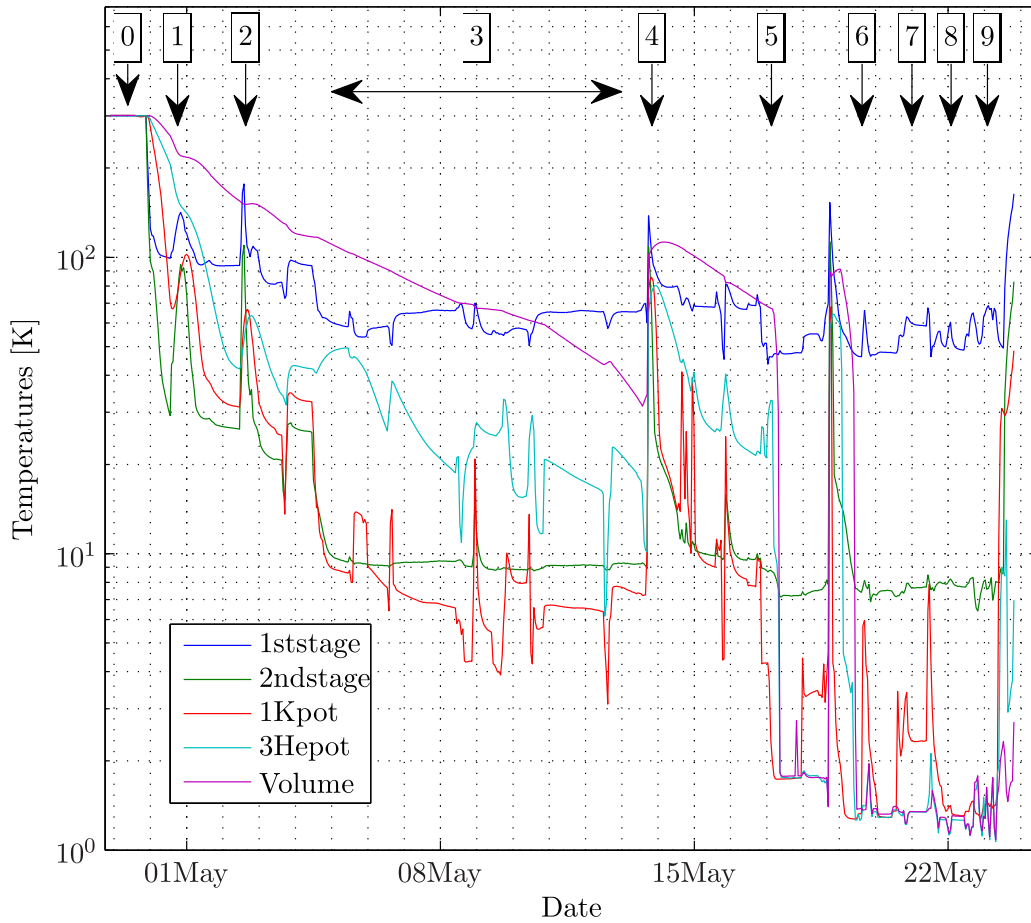Figure 3.9: The cooldown curve of the SUN2 cryostat during the experiment at PF1b. The positions of the temperature sensors are described in the text. The original data was taken at 5 s intervals by the labview program and has been smoothed (cubic spline interpolation) to a time-scale of 1 hour per point. The events described in the text are marked by the corresponding boxed numbers ☐ and arrows.

through the internal cold traps and is then only weakly thermally anchored to the 2nd stage (copper braiding brazed onto the capillary providing a contact surface of a few cm² only) [4].

^{4}He used as an exchange gas was put into the isolation vacuum to cool the large mass of the production volume since no by-pass or heat switch exists in this setup. The isolation vacuum was stabilized at various pressures between $1-5\times10^{-3}$ mbar. ^{4}He, after being passed through the external cold trap, of up to a few milli-bars was also put into the production volume. Since the exchange gas is not confined to between the 2nd stage and the production volume, if too high a gas pressure is used, heating from the room temperature walls restricts of the effectiveness of this process. Different gas pressures were tried but no significant difference in the cooling rate of the production volume was observed.

$\boxed{2}$: At around 12:00 - 02/05, it was discovered that the needle valve after the superleak was frozen stuck. The cold head was switched off and superleak heater switched on to warm up the needle valve. At 14:00, with $T_{\text{1st stage}}$ = 180 K, $T_{\text{2nd stage}}$ = 108 K, and $T_{\text{1K pot}}$ = 60 K the needle valve was unstuck again and the coldhead was switched on and cooling restarted. Approximately $0.5-1$ day of time was lost due to this partial warm up.

$\boxed{3}$: The production volume remained the hottest part and was cooling very slowly. Several attempts were made to pump down the isolation vacuum to see if the 2nd stage would be cold enough to liquefy ^{4}He—since once this happened, superfluid can be extracted through the superleak and be used to cool the production volume directly. However, on 05/05 $T_{\text{2nd stage}}$ stabilized at a temperature of ≈ 9 K. Over the next 8 days it did not cool by more than 0.1 K despite the production volume cooling from $110 \rightarrow 30$ K. This was still too warm for ^{4}He liquefaction to occur (from a previous test $T_{\text{2nd stage}} < 8$ K was required).

$\boxed{4}$: Since liquefaction with the cold head could not occur due to the cooldown problems, attempts were made to fill the 1K pot directly from a LHe dewar. Such a procedure was not initially foreseen, thus an improvised direct filling line had to be created. Using a vacuum feedthrough on ^{4}He pumping line above the 1K pot, a special double-walled capillary extension,

---

[4]It was discovered later in a separate cooldown after the experiment that even if this capillary had no leak, it would not have been enough to solve the cooldown problem.

which attaches onto the end of a standard LHe transfer tube, was made. Even with this new extension, direct filling of the 1K pot was not straight-forward. If the procedure is not performed correctly, the vacuum in the isolation vacuum would be lost and a rapid warm-up and boil-off of the liquid in the 1K pot and UCN production can occur.

$\boxed{5}$: After the 1K pot was successfully filled, it was pumped down and cooled to below T_λ so that superfluid can be extracted into the production volume. The extracted superfluid cooled it down to $T_{\text{vol}} \approx 1.8\,\text{K}$ in $3-4$ hours. When this, the previously hottest part in the cryostat, was cooled, it allowed the other parts in the cryostat to reach $T_{\text{1st stage}} \approx 50\,\text{K}$ and $T_{\text{2nd stage}} \approx 7-8\,\text{K}$.

One filling of the 1K pot is not enough to completely fill the production volume. The volume of the 1K pot is $14\,\text{L}$ and it must be filled externally at $4.2\,\text{K}$ (or $1\,\text{bar}$). Around 30% of LHe is lost from pumping down from $4.2\,\text{K}$ to T_λ, and a further amount has to be used to cool the production volume[5]. With the production volume roughly half-filled, another attempt was made to fill the 1K pot externally. However, this time the isolation vacuum was lost and the amount of LHe in the production volume boiled off rapidly. The overpressure (OP) valve on the production volume, which opens at $1.3\,\text{bar}$, was releasing cold helium at a very high rate. A snap decision was made, in order to prevent causing damage to the system, to pull off a DN40 connector to release the pressure in the production volume quickly. Best attempts were made to reconnect the connector while a small amount of overpressure remained in the volume. However, it cannot be guaranteed that some air did not become frozen in the production volume due to this incident.

$\boxed{6}$ and $\boxed{7}$: Fortunately no significant damage to the cryostat and source was caused by the incident. After a mere 3 hours, we decided to continue to refill the 1K pot. Now with more experience and with further improves to the transfer line, two successful fillings were performed.

$\boxed{8}$: The second filling of the UCN production volume, after the second filling of the 1K pot, took place. Only an estimate can be given to the amount

---

[5]There's a total mass of $\approx 5\,\text{kg}$ aluminium, $1.5\,\text{kg}$ copper, and $1\,\text{kg}$ stainless steel. If only the latent heat of vaporization of LHe is used for cooling these (i.e., worst-case scenario where the cold gaseous vapour does not provide any additional cooling), then $17\,\text{L}$ is required to cool this mass from $77 \to 4\,\text{K}$. If the latent heat and full enthalpy of the helium is combined, then this is reduced by a factor of 10. The actual amount required lies somewhere in the limits, depending on the cooling efficiency of the out-going gas.

of superfluid put in the production volume. The measurements in Fig. 2.8 of the flow rate through the superleak for different heat input and $T_{1\mathrm{K\,pot}}$ were made with $T_{\mathrm{vol}} \approx 90\,\mathrm{K}$. Since all the superfluid extracted is boiled off by the volume, the flow rate can be measured by a gaseous flow meter behind the production volume's ACP pump. The maximum extraction rate during this period is restricted by the maximum pumping speed of the pump. Once the production volume reached $< 4.2\,\mathrm{L}$ the superleak extraction rate was increased to save time. Most of the filling procedure occurred at $T_{1\mathrm{K\,pot}} \approx 1.3\,\mathrm{K} \rightarrow 1.4\,\mathrm{K}$, $T_{\mathrm{volume}} \approx 1.2\,\mathrm{K} \rightarrow 1.4\,\mathrm{K}$ and a superleak heat input of 25–$40\,\mathrm{mW}$. One cannot extrapolate the mass flow rates for these settings from the previous measurements due to turbulent flow. This effect was observed in Ref. [Nak96].

A few different methods were tried to detect the height of superfluid in the UCN production volume. These included using Cernoxes at different heights with very high excitation currents, observing the UCN count rates, and observing the CN beam monitor count rates. However, neither of these techniques gave conclusive evidence that the level of converter in the volume was full. The various techniques and the results are described in Sec. A.5. The level of converter remains an uncertainty in the measurements.

$\boxed{9}$: UCN production measurements were made at this point in time. There was one other refilling of the UCN production volume (but not a external refilling of the 1K pot) made in between the measurements. The temperatures during this period are described in the next section.

3.3.2 Final temperatures reached

Efforts were made to cool down the converter to the lowest temperatures possible. The ^{3}He pot with a high ($\approx 80\,\mathrm{g\,hr}^{-1}$) flow rate (with $T_{1\mathrm{K\,pot}} \approx 1.4\,\mathrm{K}$, $T_{2\mathrm{nd\,stage}} \approx 8\,\mathrm{K}$ and $T_{1\mathrm{st\,stage}} \approx 65\,\mathrm{K}$). And combined with pumping on the converter through the small gap in the UCN guides with an ACP28 and an ACP15 (multi-roots pumps) in parallel. By doing so, the lowest temperature of $\approx 1.1\,\mathrm{K}$ was achieved in the UCN production volume.

The temperatures are plotted in Fig. 3.10. This plot shows when two accumulation-and-empty measurements, $\boxed{1.14\mathrm{K\ accum.}}$ and $\boxed{1.08\mathrm{K\ accum.}}$, chosen to be at when the temperatures were changing slowly, were made. When the converter temperature was raising, continuous UCN production measure-
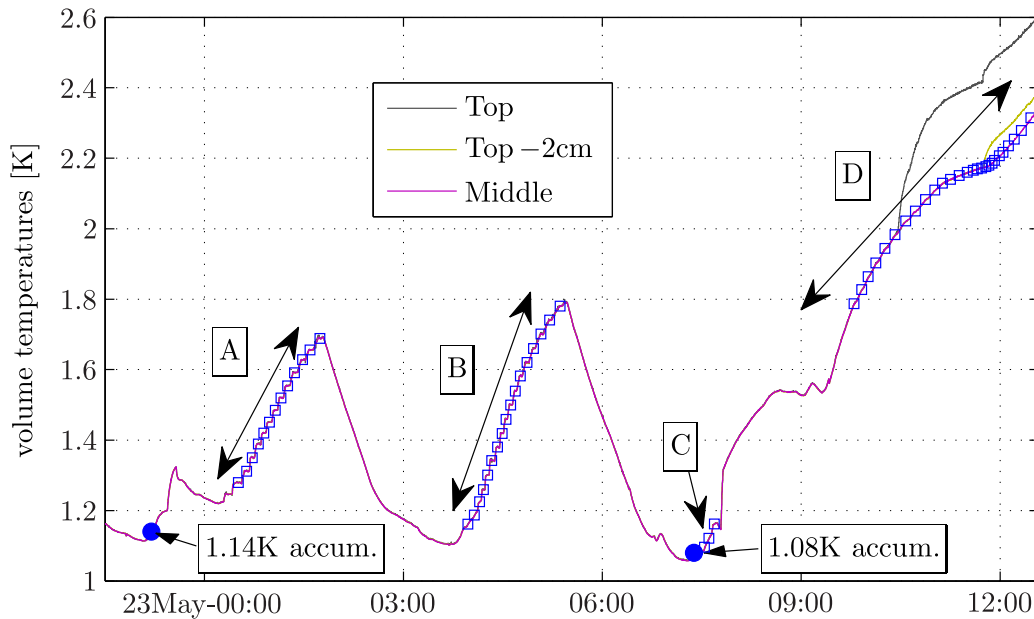
Figure 3.10: The temperature of the production volume when the UCN production results were measured. Two accumulation-and-empty measurements (filled circles ●) and four sets of continuous measurements (squares □) were made. The latter are called phase $\boxed{A}$, $\boxed{B}$, $\boxed{C}$ and $\boxed{D}$. The temperatures read from all three sensors are shown. A divergence occurs as the temperature approaches T_λ due, presumably, to diminished superfluid film-flow.

ments were made. The periods (or phases) of when this occurred are labelled in the figure. During the first three phases, $\boxed{A}$, $\boxed{B}$, and $\boxed{C}$, the temperature was increased deliberately with the use of a heater (manganin wire on the production volume at the 90° piece) and then stabilized in steps. This process causes boil-off of helium from the volume. Just after phase $\boxed{C}$, the production volume was refilled with the last of the LHe from the 1K pot. The measurements made during phase $\boxed{D}$ were done for when the cryostat was warmed up by stopping the ^{3}He circuit.

3.4   UCN production results

The results from the UCN production measurements are described in this section. In the first sub-section a description of the general principles are given.

Everything here is described in terms of differential parameters, i.e. leaving in the UCN energy-dependence. In the next sub-section, the description of accumulation-and-empty measurements and continuous production measurements are given. The experimental results are presented and observable parameters analyzed. It is here that ensemble averages over the UCN energy—when this is observed to model the data—are introduced. In the next section, a discussion of the results from these measurements is given.

The lowest temperature of the converter was warmer than desired. An accumulation-and-empty measurement, which accumulates the UCN density in the production volume, was made at close to this temperature (1.08 K). From this measurement, the storage time in the production volume can also be observed. This was found to be shorter than that expected at this converter temperature. In order to study the temperature-dependent losses, continuous UCN production measurements were used. This was done due to a problem found with the UCN valve—it was required to be manually-pulled shut before it was sufficiently closed as to not affect the total storage time significantly. This made it difficult to repeatedly perform accumulation-and-empty measurements given the limited beam time remaining. These results were used to compare with the expected loss from theory.

Another parameter worth comparing with the expected is the UCN production rate. This depends on the flux of the CN beam and the neutron optical potential in the system, both of which are known [6]. The production rate itself is temperature-independent, but the experimentally observed production rate depends on the UCN extraction efficiency, which does contain a temperature-dependence. Corrections are required so that it can be compared with the expected value. This is done to verify that we understand the number of UCNs being produced in this experiment.

3.4.1 Description

An *accumulation-and-empty* measurement is performed with the UCN valve closed and the CN beam turned on to build-up the number of UCNs in the production volume. The UCN valve is then opened and the UCNs in the production volume detected by the UCN detector via the extraction guides.

---

[6]The CN beam flux was measured in other, separate studies.

In order to deduce how many UCNs are collected in the production volume, the CN beam should be switched off just before the UCN valve is open. A variation of this kind of experiment occurs when the CN beam is left on after the UCN valve is opened. These will be called *accumulation-and-empty-with-CN-beam* measurements. Another type of measurements are the *continuous production* measurements. This involves leaving the UCN valve open and then switching on the CN beam and observing the plateau count rate of UCN detected; the CN beam is then switching off again.

The storage time in the closed production volume τ_{tot} is comprised of terms that can depend on UCN energy E_n or temperature of the converter T. It can be expressed, in terms of rate constants, as:

$$\tau_{\text{tot}}^{-1}(E_n, T) = \tau_0^{-1}(E_n) + \tau_{\text{up}}^{-1}(T) + \tau_{\text{abs}}^{-1} + \tau_\beta^{-1}, \tag{3.2}$$

where $\tau_0^{-1}(E_n)$ are the energy-dependent losses, $\tau_{\text{up}}^{-1}(T)$ is from temperature-dependent up-scattering of UCNs in the converter (Sec. 1.2.2), τ_{abs}^{-1} is from impurities (predominantly ^{3}He) distributed through the converter (this loss is UCN energy independent since the $1/v$-dependence of the cross-section is cancelled by number of impurity atoms seen by the UCN per unit time, which is $\propto v$), and τ_β^{-1} is from nuclear β-decay and is energy-independent. In the current experiment $\tau_0^{-1}(E_n)$ and $\tau_{\text{up}}^{-1}(T)$ are the most significant.

$\tau_0^{-1}(E_n)$ consists of losses on the material walls $\tau_{\text{walls}}^{-1}(E_n)$, at gaps or holes in the inner production volume $\tau_{\text{gaps}}^{-1}(E_n)$, and at the UCN valve mechanics inside the volume. The E_n-dependence of $\tau_0^{-1}(E_n)$ comes about in the followings ways. The higher the UCN energy, the faster they explore the production volume and will thus make more frequently collisions with the walls of the vessel. The average time a UCN takes to explore and collide off a given surface of area A assuming an isotropic UCN gas is given by $\tau_A = 4V_{\text{vol}}/(vA)$, where V_{vol} is the volume of the storage vessel and v is the velocity of the UCN. The area A can be an effective area modeling the gaps in the converter vessel, in which case, when the UCNs find this area they are effectively lost. The losses due to this effect are linear in v.

The area A can also refer to the surface of the reflective walls. In this case, even for UCN with energies below the neutron optical potential, loss can occur. The expression for the average loss probability per collision for an

isotropic UCN gas $\bar{\mu}(E_n)$ is given in Chapter 1. It is non-linear in E_n (and v); it is $\bar{\mu} = f$ when $E_n/V_{\text{wall}} = 0.5$ and $\bar{\mu} = \pi f$ when $E_n/V_{\text{wall}} = 1$, where f is the energy-independent loss factor defined in Ref. [GRL91] and V_{wall} is the neutron optical potential of the wall material. There is also the possibility of frozen gases on the material walls of the converter vessel that would increase $\bar{\mu}$. These types of losses vary more quickly than $\propto v$ due to the additional non-linear dependence of $\bar{\mu}$

Having sharp corners and crevasses in the production volume are also not good for τ_0. For instance if a UCN enters the gap behind the UCN flap valve's axle (see Fig. 3.4), it can make many frequent collisions (like in the bumpers section of a pinball machine) and have a large probability of being lost—even if the UCN energy is low compared to the material potential. Also, the isotropic UCN gas approximation is most likely not valid in the system. In the current production volume there is no diffuse reflecting material.

During a measurement when the UCN valve is open and CN beam switched off, a new parameter called the emptying time constant τ_e that defines the temporal decrease of the UCN population inside of the production volume, can be defined. It can be approximately given by:

$$\tau_e^{-1}(E_n, T) \approx \tau_{\text{tot}}^{-1}(E_n, T) + \tau_{\text{valve}}^{-1}(E_n), \tag{3.3}$$

where τ_{valve} defines the emptying time of the valve aperture and roughly equals $\tau_{\text{valve}} = 4V_{\text{vol}}/(vA_{\text{valve}})$, where A_{valve} is the opening area of the valve. However, this assumes that the UCN gas is isotropic and that, when the valve is opened, the value of τ_{tot}^{-1} is not perturbed. The validity of the latter assumption depends on the design of the UCN valve (e.g. a gate valve will change τ_{tot}^{-1} less when opened than say a flap valve design) and the dimension of the valve relative to V_{vol}.

The probability for a UCN in the production volume finding the valve opening, being successfully transported along the extraction guides, and finally detected in the UCN detector during emptying, can expressed as:

$$W(E_n, T) = \epsilon(E_n) \frac{\tau_{\text{valve}}^{-1}(E_n)}{\tau_e^{-1}(E_n)} = \epsilon(E_n) \frac{\tau_e(E_n)}{\tau_{\text{valve}}(E_n)}, \tag{3.4}$$

where $\epsilon(E_n)$ takes into account the efficiency of the extraction and detection

of the UCN and is dependent on UCN energy. A representation of $W(E_n, T)$ in terms of the time constants that can be directly observed in these measurements [Zim10], using Eq. 3.3, is given by:

$$W(E_n, T) = \epsilon(E_n) \frac{\tau_{\text{tot}}(E_n, T) - \tau_{\text{e}}(E_n, T)}{\tau_{\text{tot}}(E_n, T)} \, . \tag{3.5}$$

From the description above, due to the energy-dependence, there is no single storage time. When the CN beam is turned on, the differential spectrum of UCNs in the converter volume $dN(t)/dE_n$ will build-up as a function of time t as:

$$\frac{dN(t)}{dE_n} = \frac{dN_\infty}{dE_n} \left(1 - \exp[-t/\tau_{\text{tot}}(E_n, T)]\right) , \tag{3.6}$$

where

$$\frac{dN_\infty}{dE_n} = \frac{dP_{\text{UCN}}}{dE_n} V_{\text{CN}} \, \tau_{\text{tot}}(E_n, T) \tag{3.7}$$

is the equilibrium differential spectrum of UCNs when the loss rate is equal to the differential production rate at all energies. P_{UCN} is the UCN production rate (in per unit volume per unit time dimensions) and V_{CN} is the volume of converter the CN beam is incident upon (assuming no beam attenuation or divergence). Since UCNs are produced with a spectrum $dP_{\text{UCN}}/dE_n \propto \sqrt{E_n}$, the accumulated spectrum inside the production volume will be different than the produced spectrum. It will depend on the form of $\tau_{\text{tot}}(E_n, T)$, which is shorter for UCNs with higher energy. Hence, the accumulated spectrum will have its higher energies suppressed. This effect is called "spectral shaping". The spectrum in the production volume will change during accumulation from the produced spectrum $dP_{\text{UCN}}/dE_n \propto \sqrt{E_n}$ to the equilibrium spectrum dN_∞/dE_n.

Similarly, the total number of UCNs remaining in the closed converter vessel as a function of time t after the CN beam is switched off is given by:

$$N(t) = \int_{E_{\text{min}}}^{E_{\text{max}}} \frac{dN_0(E_n)}{dE_n} \exp[-t/\tau_{\text{tot}}(E_n)] \, \mathrm{d}E , \tag{3.8}$$

where N_0 is the number of UCNs in the production volume when the CN beam is switched off. If the accumulation was to equilibrium, then $N_0 = N_\infty$. Similarly, if the UCN valve is opened during the emptying and the CN beam is switched off, then the total number of UCNs remaining in the converter vessel

$N(t)$ is given by:

$$N(t) = \int_{E_{\min}}^{E_{\max}} \frac{dN_0(E_n)}{dE_n} \exp[-t/\tau_{\rm e}(E_n)] \, \mathrm{d}E \,. \tag{3.9}$$

It is $N(t)$ that determines the rate of UCNs that arrive at the detector. When the UCN valve is open this is rate is denoted by $\dot{N}_{\rm det}(t)$ and when the valve is closed, due to leakages around the valve, by $\dot{N}_{\rm det,leak}(t)$. Despite the continuum of storage times $\tau_{\rm tot}(E_n)$, if its spread is narrow, then only a single time constant $\bar{\tau}_{\rm tot}$, an ensemble average, will be observed due to the limited counting statistics. This is indeed what occurs for $\dot{N}_{\rm det,leak}(t)$ during accumulation. However, during emptying, due to the large spread of $\tau_{\rm e}(E_n)$, not one single emptying time constant can be assigned to $\dot{N}_{\rm det}(t)$.

3.4.2 Accumulation-and-empty measurements

An accumulation-and-empty measurement was made when the converter temperature was at $1.08\,\mathrm{K}$ (see Fig. 3.10). This is the measurement for which most useful data can be extracted. During accumulation, the UCN valve was hand-pulled shut since it was discovered that the closing pneumatic piston mechanism did not provide enough force. When the valve was opened, the beryllium plate is opened at an angle of $\approx 50°$. The counts recorded by the UCN detector in $1\,\mathrm{s}$ bins during the full accumulation-and empty measurement sequence are shown in Fig. 3.11.

Plots of the UCN detector count rate, along with the CN monitor counts, zoomed into when the CN beam is switched on (start of the accumulation) and when the UCN valve was opened (start of the emptying) are shown and discussed in Sec. A.6 of the Appendix. Since the CN beam was left on for $\approx 1\,\mathrm{s}$ after the UCN valve was opened, this is required to be corrected for when determining N_∞ from the emptying curve.

There was another preliminary accumulation-and-empty measurement made when the converter was at $1.14\,\mathrm{K}$ around 8 hours earlier. However, the UCN valve was not shut properly during the accumulation and the valve was also opened at a smaller angle ($\approx 30°$ only) during emptying. This measurement is also shown in the figure, as it is useful to look at its emptying curve for a discussion later. Detailed analysis of this measurement is not performed.
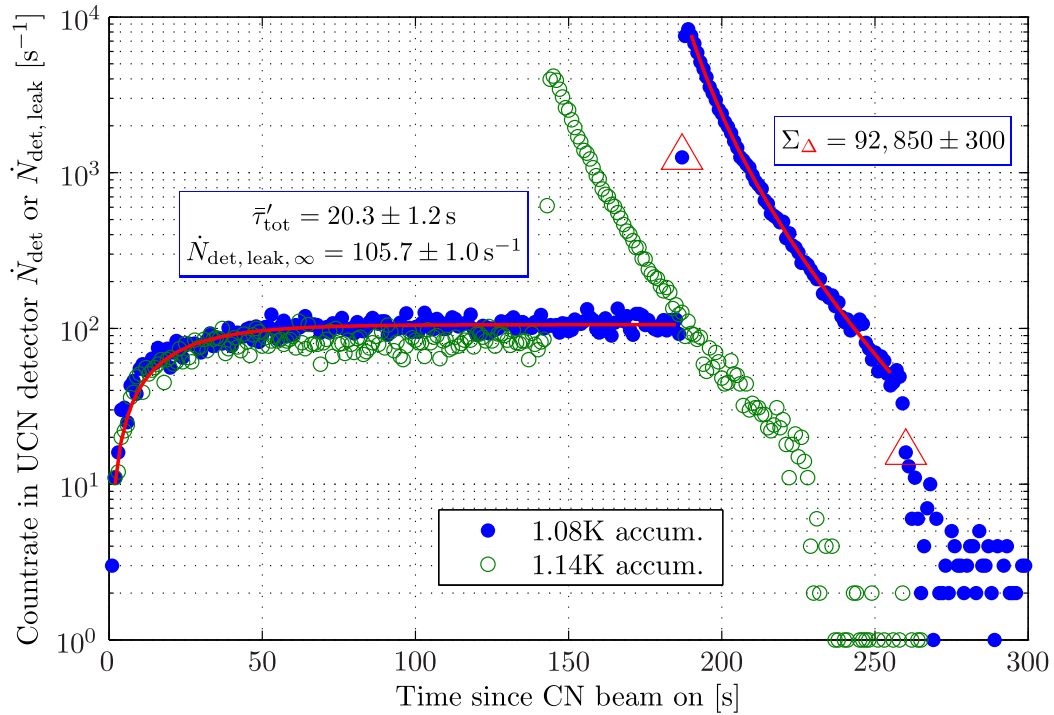
Figure 3.11: The counts in the UCN detector in 1 s bins during accumulation-and-empty measurements at two different converter temperatures. The sudden drop in the count rate at the end of the emptying curves is due to the UCN valve being closed. The red solid lines (—) are the fits to the accumulation curve and emptying curve. The red triangles ($\triangle$) show the (inclusive) limits used for summing the emptying curve giving $\Sigma_\triangle$. The sum and best-fit parameters for the accumulation curve are also in the figure. See also Fig. 3.14 for a comparison between the two emptying curves.

The accumulation curve

The leak of UCNs observed during accumulation, denoted $\dot{N}_{\text{det, leak}}(t)$, provides a probe for the number of UCNs in the production volume $N(t)$. Ignoring the time UCNs take to find leak and reach the UCN detector, it is expected that:

$$\frac{d\dot{N}_{\text{det, leak}}(t)}{dE_n} = \epsilon_{\text{leak}}(E_n)\,\tau_{\text{leak}}^{-1}(E_n)\frac{dN(t)}{dE_n}\,, \tag{3.10}$$

where $\tau_{\text{leak}} = 4V/(vA_{\text{leak}})$ for some effective area A_{leak} that models size of the gap at the valve and ϵ_{leak} is the probability of a UCN making it through the small slit between the valve's flap and the top of the converter vessel, into extraction guides, and reaching the detector. This value is expected to be smaller than $\epsilon(E_n)$.

During accumulation, due to the energy-dependence of $\tau_{\text{tot}}(E_n)$, the differential spectrum of UCNs in the production volume $dN(t)/dE_n$ evolves according to Eq. 3.6. If, however, the spread of $\tau_{\text{tot}}(E_n)$ is small, then a single ensemble average $\bar{\tau}_{\text{tot}}$ can be used. In this case, $\dot{N}_{\text{det, leak}}(t)$ during the accumulation curve can be fitted with an equation of the form:

$$\dot{N}_{\text{det, leak}}(t) = \dot{N}_{\text{det, leak}, \infty}\left(1 - \exp[-(t - \delta t)/\bar{\tau}_{\text{tot}}']\right)\,, \tag{3.11}$$

where

$$\dot{N}_{\text{det, leak}, \infty} = \bar{\epsilon}_{\text{leak}}\,P_{\text{UCN}}V_{\text{CN}}\,\bar{\tau}_{\text{tot}}\,\bar{\tau}_{\text{leak}}^{-1}\,. \tag{3.12}$$

The additional δt is used to take into account the time delay of the CN shutter and $\bar{\tau}_{\text{tot}}'$ is the observed time constant that we will identify as the storage time $\bar{\tau}_{\text{tot}}$. The fitted parameters and curve are shown on Fig. 3.11. The χ_ν^2 for the fit is 0.8, indicating that this is a sufficient description.

The emptying curve

When the CN beam is switched off, the differential number of UCNs in the closed production volume after accumulation $dN_0(t)/dE_n$ decays according to Eq. 3.8. If a single ensemble averaged storage time can be used, then the total number of UCNs remaining in the volume $N(t) = N_0 \exp(-t/\bar{\tau}_{\text{tot}})$.

However, in these measurements the UCN valve is opened around the same time as when the CN beam was shut off. When the UCN valve is open
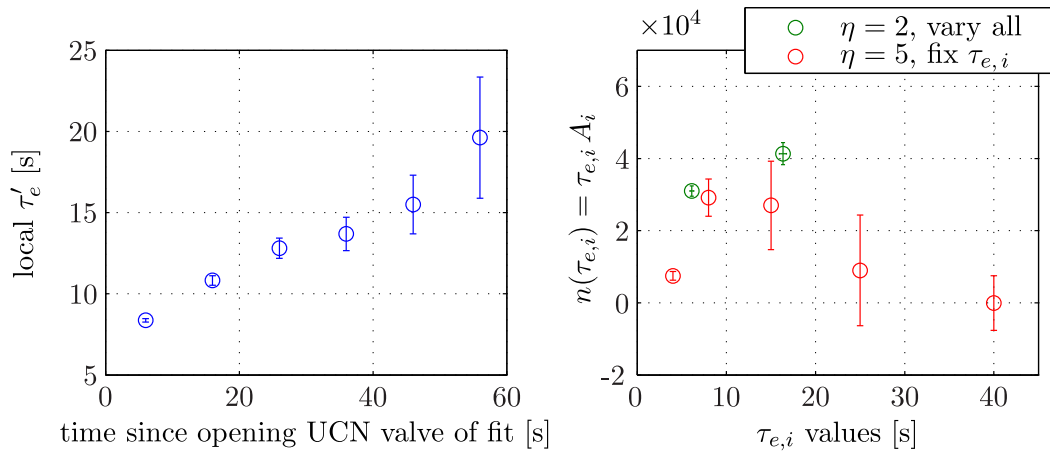
Figure 3.12: *Left*: The changing of the local emptying time constant $\tau_e'(t)$ in the emptying curve of the 1.08 K accumulation-and-empty measurement of Fig. 3.11. It is determined by locally fitting the data over a time of 10 s with a single exponential decay $A \exp(-t/\tau_e')$ at different starting times of the fit. The centers of the 10 s time width are used for the horizontal value. All the fits give a $\chi_\nu^2 < 2$, indicating an approximation of the local decay constant. *Right*: The number of UCNs with a given emptying time constant $\tau_{e,i}$ estimated by using the "$\eta = 2$, vary all" (○) and the "$\eta = 5$, fixe $\tau_{e,i}$" (○) models that are based on Eq. 3.14. The number is calculated from $n(\tau_{e,i}) = \int_{t=0}^{\infty} A_i \exp(-t/\tau_{e,i}) \mathrm{d}t = \tau_{e,i} A_i$.

$dN_0(t)/dE_n$ decreases according to Eq. 3.9. And thus, following Eq. 3.12, the count rate arriving at the UCN detector is given by:

$$\dot{N}_{\mathrm{det}}(t) = \int_{E_{\min}}^{E_{\max}} \epsilon(E_n)\, \tau_{\mathrm{valve}}^{-1}(E_n)\, \frac{dN_0}{dE_n} \exp[-t/\tau_{\mathrm{e}}(E_n)]\, dE_n \,, \qquad (3.13)$$

where $dN_0/dE_n = dN_\infty/dE_n$, given in Eq. 3.7, if accumulation was until equilibrium.

Unfortunately, in the observed emptying curves no single ensemble average of the emptying times $\bar{\tau}_e$ can be assigned due to the wide spread of $\tau_e(E_n)$ values. This is shown in Fig. 3.12. This makes the data analysis difficult. Fitting with Eq. 3.9 requires knowledge of the differential spectrum in the converter with spectral shaping effects (Eq. 3.6), which in turn is only given by knowledge of the energy-dependence of $\tau_{\mathrm{tot}}(E_n)$. But in this experiment the UCN energy information was not measured (e.g. no gravitational spectrometer was used).

Instead of an integral of exponential decays with varying $\tau_e(E_n)$, the decay

curve can be modeled with a discrete sum of exponential decays given by:

$$\dot{N}_{\text{det}}(t) = \sum_{i=1}^{\eta} A_i \exp(-t/\tau_{e,i}) , \qquad (3.14)$$

where η is the number of exponential decay terms to use in the sum. A_i and $\tau_{e,i}$ are the amplitudes and emptying time constants of the discrete decays.

The first model used based on this equation is made from a sum of two exponential decay terms, i.e. $\eta = 2$, with all four A_i and $\tau_{e,i}$ left as free parameters. This will be called the "$\eta = 2$, vary all" model and it models the decay curve quite well with $\chi_\nu^2 = 1.06$. The $\tau_{e,i}$ and A_i of best fit are shown in Table 3.1. Increasing η, while more closely resembles the continuous integral, increases the uncertainty in the fitted parameters due to the limited statistical precision of the data—coming from Poisson counting statistics. Using $\eta > 3$ and varying all parameters causes the fitting procedure not to converge.

Since the emptying curve contains a continuous spectrum of $\tau_e(E_n)$ values, it is possible to fix $\tau_{e,i}$ of the fit and leave the corresponding A_i as free parameters. However, if the $\tau_{e,i}$ values are too close together, the separate decay curves are indistinguishable due to the limited counting statistics. It was found that having $\eta = 5$ for $\tau_{e,i}$ values spread between 4–40 s provides a reasonable description of the data. This is called the "$\eta = 5$, fix $\tau_{e,i}$" model and its parameters are shown in Table 3.1).

Table 3.1: The parameters of best fit $\tau_{e,i}$ and A_i and normalized chi-squared χ_ν^2 values from modeling the emptying curves with discrete sum of exponential decays based on Eq. 3.14.

$\eta = 2$, vary all		$\eta = 5$, fix $\tau_{e,i}$	
$\tau_{e,i}$ [s]	A_i [s^{-1}]	$\tau_{e,i}$ [s]	A_i [s^{-1}]
6.1 ± 0.2	5,060 ± 160	4	1,860 ± 340
16.3 ± 0.4	2,530 ± 180	8	3,650 ± 650
$\chi_\nu^2 = 1.06$		15	1,800 ± 820
		25	360 ± 610
		40	0 ± 190
		$\chi_\nu^2 = 1.00$	

The A_i values give the initial count rate of UCNs with a given $\tau_{e,i}$. The total number of UCNs with a given $\tau_{e,i}$ is given by $\int_{t=0}^{\infty} A_i \exp(-t/\tau_{e,i}) \mathrm{d}t = \tau_{e,i} A_i$. A

plot of these values from the two different models are shown in Fig. 3.12. There is a loss in the extraction of the UCNs from the converter if τ_e is comparable to τ_{tot} (see Eq. 3.5). The "$\eta = 2$, vary all" model is useful for giving an estimate of this loss. An idea of the distribution of $\tau_{\text{tot}}(E_n)$ is given by the "$\eta = 5$, fix $\tau_{e,i}$" model. Since UCNs with higher E_n will have a shorter $\tau(E_n)$, the suppression of UCNs with higher energy in the production volume due to spectral shaping can be seen with this model.

The number of accumulated UCNs

The integral of the UCNs over the emptying curve, from integrating Eq. 3.13 w.r.t. t and using the definition in Eq. 3.4, is given by:

$$\int_{t=0}^{\infty} \dot{N}_{\text{det}}(t)\, dt = \int_{E_{\min}}^{E_{\max}} \epsilon(E_n)\, \tau_{\text{valve}}^{-1}(E_n)\, \tau_e(E_n)\, \frac{dN_0(E_n)}{dE_n} dE_n$$

$$= \int_{E_{\min}}^{E_{\max}} W(E_n)\, \frac{dN_0(E_n)}{dE_n}\, dE_n \equiv N_0' , \quad (3.15)$$

where N_0', with the primed superscript, denotes the number of UCNs that are counted after the probability of reaching the UCN detector and being detected caused by $W(E_n)$. Since the accumulation in these experiments is to equilibrium $N_0' = N_\infty'$. The sum of the UCN counts observed during the emptying between the two red triangles ($\triangle$) in Fig. 3.11 is denoted by $\Sigma_\triangle$. Before it can be identified as N_∞', a few corrections are required (i.e. $N_\infty' = \Sigma_\triangle$ + corrections).

The first correction is due to the early shutting of the UCN valve causing some UCNs remaining in the vessel to not reach the detector. A correction for the lost counts is estimated using an extrapolation of the emptying curve. This is done by fitting the last $20\,\text{s}$ of the emptying curve just before the UCN valve was shut with a single exponential decay. This single exponential decay curve was found to be $(143 \pm 6\,\text{s}^{-1})\, \exp[-t/(17 \pm 1\,\text{s})]$ giving a $\chi_\nu^2 = 1.1$. Using this, the loss of UCN counts due to the valve shutting early can be estimated to be 660 ± 110.

The second correction that is required comes from the timing of switching off the CN beam. It was deduced in Sec. A.6 that for the $1.08\,\text{K}$ accumulation measurement the CN beam was left on for $1.1 \pm 0.5\,\text{s}$ (full CN intensity equivalent) after the opening of the UCN valve. From the continuous measurements

in the next section, the continuously produced and detected rate at this temperature is $\dot{N}_c(1.08\,\mathrm{K}) \approx 6{,}100\,\mathrm{s}^{-1}$. Therefore, the estimate of the number of UCNs produced that were not accumulated due the CN beam being left on is $6{,}700 \pm 3{,}100$.

Combining these corrections (see Table 3.2), one gets $N_0' = 86{,}750 \pm 3{,}500$ for the $1.08\,\mathrm{K}$ accumulation-and-empty measurement. With this the density of UCNs in the converter vessel and the production rate number of UCNs that can be extracted and detected can be deduced. This is discussed in Sec. 3.5.

Table 3.2: Summary of the observables and the corrections in the $1.08\,\mathrm{K}$ accumulation-and-empty measurement.

$\Sigma_\Delta =$	$92{,}850 \pm 300$
UCN valve closing earlier correction $=$	$+(600 \pm 110)$
CN beam & UCN valve timing correction $=$	$-(6{,}700 \pm 3{,}100)$
$N_\infty' =$	$86{,}750 \pm 3{,}500$
from accumulation curve $\bar{\tau}_{\mathrm{tot}} =$	$20.3 \pm 1.2\,\mathrm{s}$

3.4.3   Continuous measurements

A continuous measurement is when the UCN valve is left open and the CN beam turned on until a stable count rate in the UCN detector is reached; and then the CN beam is turned off again. This was done for a wide range of temperatures so that $\tau_{\mathrm{up}}^{-1}(T)$ can be studied. An example of a sequence of continuous measurements is shown in Fig. 3.13. For each measurement there is: a build-up curve, that is described by Eq. 3.11, but with τ_{tot} replaced with τ_e and τ_{leak} replaced with τ_{valve}; a stable continuous count rate $\dot{N}_c$; and an emptying curve described by Eq. 3.13.

Four sets of continuous UCN production measurements exist. Referring to Fig. 3.10, they are called the phase A, B, C, and D measurements. Phase A, which covers $T = 1.3 \rightarrow 1.7\,\mathrm{K}$, was done first and occurred while still adjusting and understanding the system. For instance, during these the UCN valve opening angle was increased from $\approx 30° \rightarrow 50°$. Phase B covers $T = 1.2 \rightarrow 1.8\,\mathrm{K}$, a wider temperature range than phase A, and thus more useful. It was done when the system was finalized. Phase C covers a narrow temperature range of $T = 1.1 \rightarrow 1.2\,\mathrm{K}$ with one overlapping point at the same temperature as
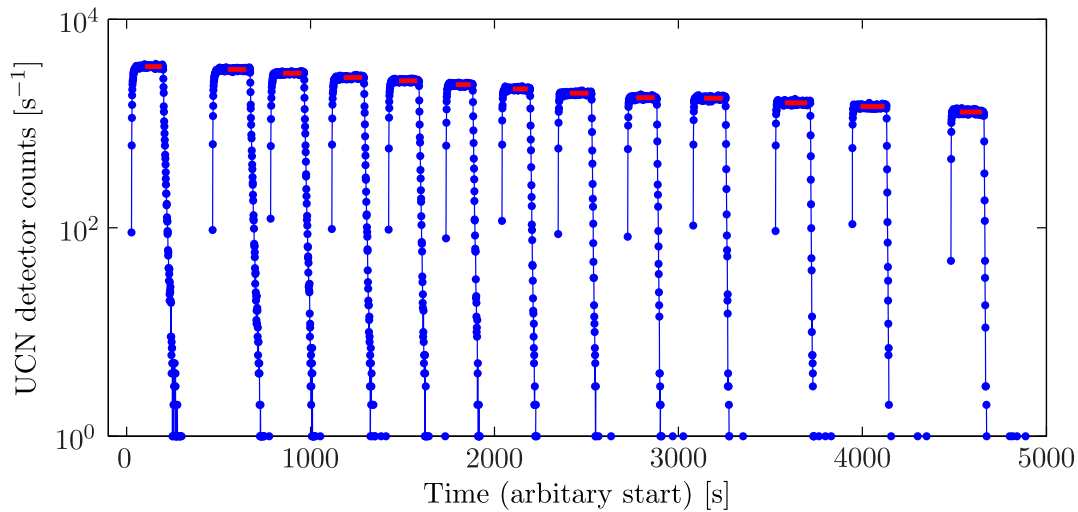
Figure 3.13: The counts in 1 s bins in the UCN detector during the phase A continuous UCN production measurement shown as an example. The CN beam is pulsed on and off for 180 s and produces a corresponding pulse in UCN counts. The solid blue lines (—) connect the points directly. The horizontal red lines (—) indicate the time range, when the count rate is stabilized, used for finding $\dot{N}_c$.

phase B (at 1.16 K to be specific). The production volume was then refilled with LHe, and the phase D measurements, covering a temperature range of $T = 1.8 \rightarrow 2.4$ K, were made.

The emptying curves

A comparison of various emptying curves from the continuous measurements are compared with those from the two accumulation-and-empty measurements is shown in Fig. 3.14. It can be seen that for the same temperature, the emptying curve decays faster in the continuous measurements than in the accumulation-and-empty experiments. This is because there is stronger spectral shaping in the latter measurements. This comes from $\tau_{\text{tot}}^{-1}(E_n, T)$ increasing more quickly with E_n than $\tau_e^{-1}(E_n, T)$ does. The suppression of the higher energy UCNs in the accumulated spectrum for accumulation-and-empty measurements was shown in Fig. 3.12. When a similar analysis is done for the continuous measurements, it can be seen that this suppression effect is not as strong. Since there is weaker spectral shaping for the continuous measure-
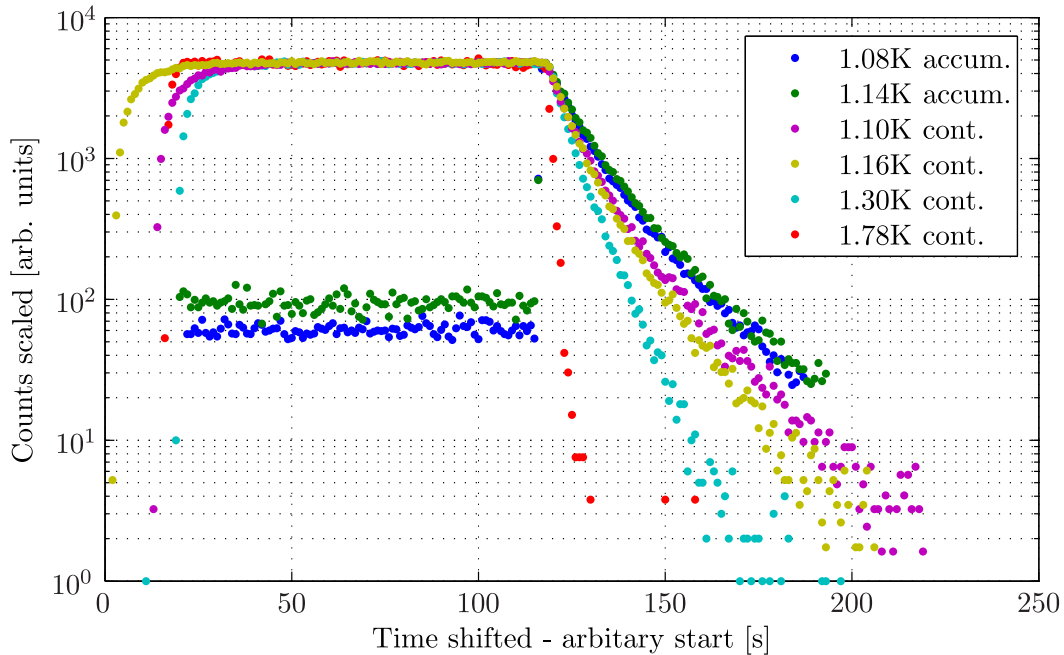
Figure 3.14: The emptying curves from the two accumulation and empty experiments plotted together with various emptying curves from the continuous measurements (taken from phase B & C). In order to clearly see the differences, the time axes are shifted (but not scaled) and the counts axes scaled so that the point at the start of the emptying (CN beam off for the continuous measurements and UCN valve open for the accumulation measurements) are aligned. The time for which the CN beam is on is not the same for the three continuous measurements. The start of the accumulation-and-empty measurements is not shown.

ments, it implies that the energy-dependence in τ_{valve} is less strong than in τ_{walls}, as expected.

From the plot, it can also be seen that the continuous measurement's emptying curve decays faster for increasing temperatures. This is expected since $\tau_e^{-1}(E_n, T)$ contains the $\tau_{\text{up}}^{-1}(T)$ term, which increases with T. Also, for $T > 1.5\,\text{K}$ a sum of at least two exponential decay terms (i.e. $\eta > 1$) is required in Eq. 3.14 for modeling the emptying curve. However, for $T < 1.5\,\text{K}$ a single exponential decay can be used so that an ensemble average $\bar{\tau}_e$ is well-defined. This occurs because the losses start to be dominated by the energy-independent $\tau_{\text{up}}^{-1}(T)$ term. This implies that when $T < 1.5\,\text{K}$ energy-dependent losses, which come primarily from τ_{walls}^{-1}, already start to become dominant. Since for most

of the measurements it is not possible to use a single $\bar{\tau}_e$, it is difficult to perform detailed quantitative with the emptying curves.

The continuous count rate $\dot{N}_c$

The $\dot{N}_c$ values from the 4 sets of data are shown in Fig. 3.15. These are calculated by taking the average of the plateau count rate for times range sufficiently far from the exponential build-up (for example, see Fig. 3.13).

The effects of increasing the UCN valve opening angle from 30° → 50° during the phase A measurements can be seen. It caused an increase in $\dot{N}_c$ of $\approx 11\%$ (when extrapolated to the same converter temperature). It can be seen that the $\dot{N}_c$ values for phase A are much lower than compared to phase B; the $\dot{N}_c$ values of phase B are 33% higher than those in phase A when the UCN valve opening angle is the same. This is thought to be due to an increased gap at the UCN guides for pumping on the converter. Similarly, $\dot{N}_c$ from phase C is lower than when compared to phase B. At the 1.16 K common point[7], the value from phase C is $(4.94 \pm 0.01)\%$ lower than B. This could be explained by a combination of the change in the gap at the UCN guides and boil-off of the converter.

The data from phase D covers the higher temperatures. A noticeable "kink" is observed in the $\dot{N}_c$ data at $T \approx T_\lambda = 2.17$ K. This is most likely caused by a transition of UCN production from super-thermal production scheme to moderation. The count rates at the colder temperatures match closely with that expected from the phase B measurements. The production volume was refilled between the phase C and D measurements.

The continuous count rate $\dot{N}_c$ occurs when the rate of produced UCNs equals the loss rate from the production volume when the UCN valve is opened

---

[7]The 1.16 K value is the nominal value; The actual temperatures calculated by averaging over the time range of the $\dot{N}_c$ measurement are 1.1612 ± 0.0005 K for the phase B point and 1.1621 ± 0.0002 K for the phase C point.
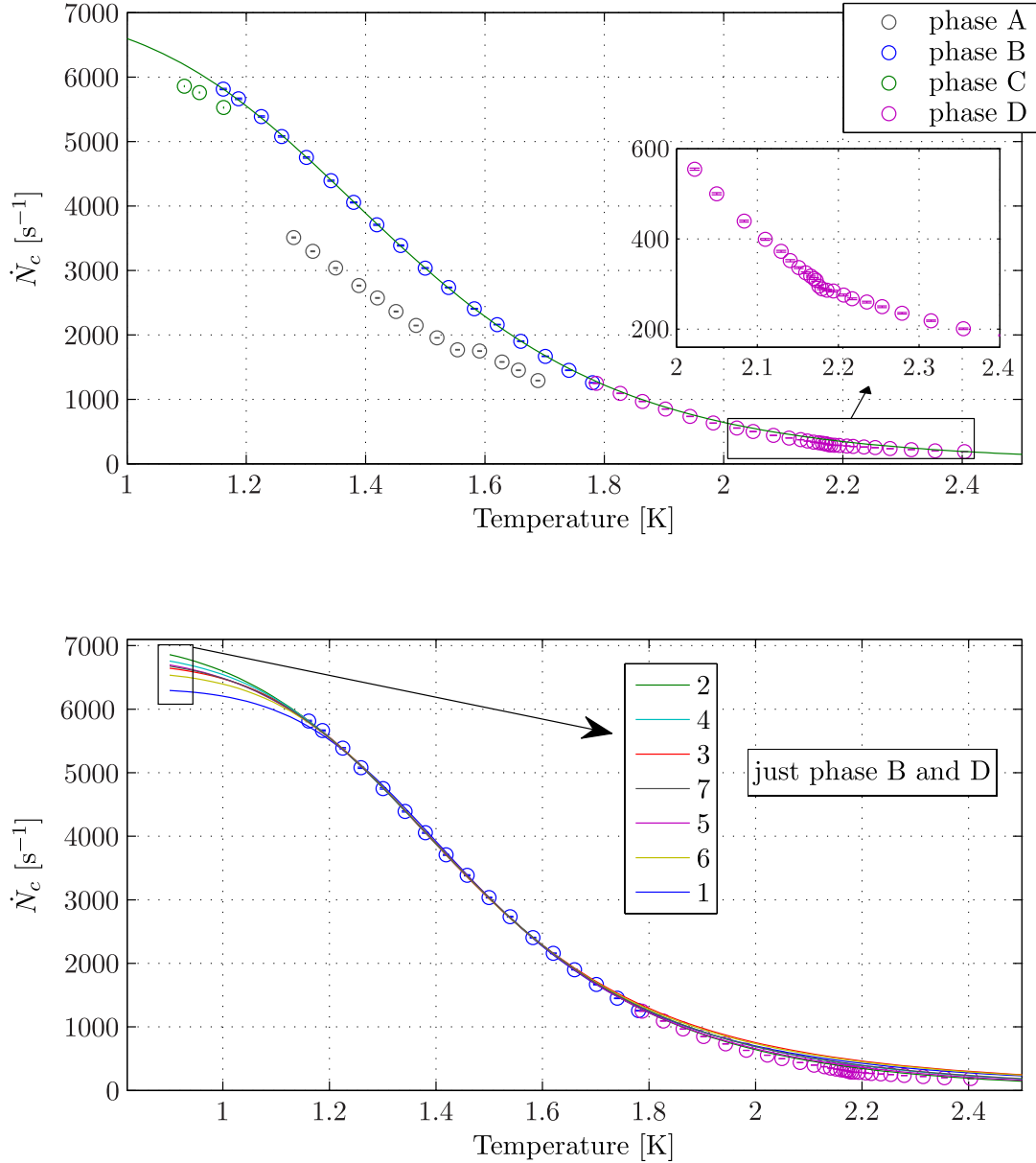
Figure 3.15: *Top*: A plot of the $\dot{N}_c$ values from the four sets of continuous measurement data. The solid green line (—) is the fit with the "B-fixed = $7.6 \times 10^{-3}\,\mathrm{s}^{-1}$" term only in $\tau_{\mathrm{up}}^{-1}(T)$, and for a temperature range $1.5\,\mathrm{K}-1.7\,\mathrm{K}$ (i.e., just the phase B data). *Bottom*: Showing just the phase B and D data and the lines of best-fit from all the different combinations of terms in $\tau_{\mathrm{up}}^{-1}(T)$. The corresponding number of the curve is shown in Table 3.3. The temperature range for all the fits is $1.5\,\mathrm{K}-1.7\,\mathrm{K}$ also.

for all UCN energies. It is given by:

$$\dot{N}_c(T) = \int_{E_{\min}}^{E_{\max}} \frac{dP_{\mathrm{UCN}}}{dE_n} V_{\mathrm{CN}} W(E_n) dE_n = \int_{E_{\min}}^{E_{\max}} \frac{dP_{\mathrm{UCN}}}{dE_n} V_{\mathrm{CN}} \frac{\tau_{\mathrm{valve}}^{-1}(E_n)}{\tau_e(E_n, T)} dE_n$$

$$= \int_{E_{\min}}^{E_{\max}} \frac{dP_{\mathrm{UCN}}}{dE_n} V_{\mathrm{CN}} \epsilon(E_n) \frac{\tau_{\mathrm{valve}}^{-1}(E_n)}{\tau_{\mathrm{wall}}^{-1}(E_n) + \tau_{\mathrm{up}}^{-1}(T) + \tau_{\mathrm{abs}}^{-1} + \tau_{\beta}^{-1} + \tau_{\mathrm{valve}}^{-1}(E_n)} dE_n .$$

$$(3.16)$$

This continuous integral will be replaced with single ensemble average values to see if this provides a reasonable description of the data; $\dot{N}_c$. Recall, from the previous section, the spectral shaping in continuous measurements—since it is $\tau_e(E_n)$ that determines the amount of shaping—is not as strong as in accumulation-and-empty measurements. Hence, Eq. 3.16 is expressed as:

$$\dot{N}_c(T) \approx P_{\mathrm{UCN}} V_{\mathrm{CN}} \bar{\epsilon} \frac{\bar{\tau}_{\mathrm{valve}}^{-1}}{\bar{\tau}_{\mathrm{wall}}^{-1} + \tau_{\mathrm{up}}^{-1}(T) + \tau_{\mathrm{abs}}^{-1} + \tau_{\beta}^{-1} + \bar{\tau}_{\mathrm{valve}}^{-1}} . \qquad (3.17)$$

In order to deduce the temperature-dependent effects, the emptying time constant $\bar{\tau}_e^{-1}(E_n, T)$ is separated into its T-independent and T-dependent parts:

$$\bar{\tau}_e^{-1}(T) = \bar{\tau}_{\mathrm{valve}}^{-1} + \bar{\tau}_{\mathrm{wall}}^{-1} + \tau_{\mathrm{abs}}^{-1} + \tau_{\beta}^{-1} + \tau_{\mathrm{up}}^{-1}(T) = \bar{\tau}_{\mathrm{e-up}}^{-1} + \tau_{\mathrm{up}}^{-1}(T) , \qquad (3.18)$$

where it is assumed that spectral shaping due to changing T does not change $\bar{\tau}_{\mathrm{e-up}}^{-1}$. Thus, $\dot{N}_c$ can be expressed as:

$$\dot{N}_c(T) \approx P_{\mathrm{UCN}} V_{\mathrm{CN}} \bar{\epsilon} \frac{\bar{\tau}_{\mathrm{valve}}^{-1}}{\bar{\tau}_{\mathrm{e-up}}^{-1} + \tau_{\mathrm{up}}^{-1}(T)} . \qquad (3.19)$$

Fitting of the temperature-dependence of $\dot{N}_c(T)$ is based on the strategy employed in Ref. [Yos92], where $\tau_{\mathrm{up}}^{-1}(T)$ from Ref. [Gol79] was used. The expression derived here is:

$$\tau_{\mathrm{up}}^{-1}(T) = \tau_{\mathrm{up,A}}^{-1}(T) + \tau_{\mathrm{up,B}}^{-1}(T) + \tau_{\mathrm{up,C}}^{-1}(T)$$

$$= A\,e^{-(12\,\mathrm{K})/T} + B\,T^7 + C\,T^{3/2}\,e^{-(8.6\,\mathrm{K})/T} , \quad (3.20)$$

where the first term comes from one-phonon absorption with $A = 130\,\mathrm{s}^{-1}$ [8];

---

[8]In Ref. [Yos92] a value of $A = 500\,\mathrm{s}^{-1}$ was used; but in a comment to the paper [GL93], the authors of the original paper, pointed out a new value that is more appropriate.

the second from two-phonon scattering with $B = (8.8 \text{ and } 7.6) \times 10^{-3}\,\mathrm{s}^{-1}\,\mathrm{K}^{-7}$ at $0.6\,\mathrm{K}$ and $1.0\,\mathrm{K}$, respectively; and the third is from two-roton scattering with $C = 18\,\mathrm{s}^{-1}\,\mathrm{K}^{-3/2}$.

Fits were made using different combinations (or "admixtures") of the fixed values for $\tau_{\mathrm{up,A}}^{-1}$, $\tau_{\mathrm{up,B}}^{-1}$ and $\tau_{\mathrm{up,C}}^{-1}$ to see its effect on the χ_ν^2 value to determine the best description for $\tau_{\mathrm{up}}^{-1}(T)$. The free parameters of the fit are $P_{\mathrm{UCN}} V_{\mathrm{CN}} \bar\epsilon \bar\tau_{\mathrm{valve}}^{-1}$ and $\bar\tau_{\mathrm{e-up}}^{-1}$. Our data exists only for $T > 1\,\mathrm{K}$ so $B = 7.6 \times 10^{-3}\,\mathrm{s}^{-1}\,\mathrm{K}^{-7}$ was used. Since this description of $\tau_{\mathrm{up}}^{-1}(T)$ is only expected to be valid for low temperatures (indeed, the authors intended it only for $T \leq 1\,\mathrm{K}$), the temperature range of the fitting was changed to include higher temperatures to see the effect of this. The χ_ν^2 values and parameters from fitting of the phase B measurements are shown in Table 3.3.

Table 3.3: The parameters and χ_ν^2 of fitting the $\dot N_c$ data from the phase B continuous measurements with Eq. 3.19 by letting $P_{\mathrm{UCN}} V_{\mathrm{CN}} \bar\epsilon \bar\tau_{\mathrm{valve}}^{-1}$ and $\bar\tau_{\mathrm{e-up}}^{-1}$ to vary and trying different combinations of the terms in $\tau_{\mathrm{up}}^{-1}(T)$ from Eq. 3.20. The temperature range of the fit was also changed. The "#" column are the curve numbers shown in Fig. 3.15.

fitting range	$P_{\mathrm{UCN}}V_{\mathrm{CN}}\bar\epsilon\bar\tau_{\mathrm{valve}}^{-1}$ [s^{-2}] (vary)	$\bar\tau_{\mathrm{e-up}}$ [s] (vary)	$\tau_{\mathrm{up,A}}^{-1}$ (fixed)	$\tau_{\mathrm{up,B}}^{-1}$ (fixed)	$\tau_{\mathrm{up,C}}^{-1}$ (fixed)	χ_ν^2	#
1.1–1.5 K	246 ± 1	26.0 ± 0.1	✓	–	–	21	1
	683 ± 2	**10.44 ± 0.05**	–	✓	–	**2.2**	2
	590 ± 2	11.36 ± 0.06	–	–	✓	3.2	3
	1274 ± 4	5.44 ± 0.03	–	✓	✓	2.5	4
	929 ± 3	7.45 ± 0.04	✓	✓	–	4.5	5
	836 ± 3	7.90 ± 0.04	✓	–	✓	6.3	6
	1519 ± 5	4.50 ± 0.02	✓	✓	✓	3.9	7
1.1–1.7 K	254 ± 1	24.91 ± 0.07	✓	–	–	25	
	686 ± 1	**10.37 ± 0.03**	–	✓	–	**2.1**	
	585 ± 1	11.49 ± 0.04	–	–	✓	5.8	
	1272 ± 3	5.45 ± 0.02	–	✓	✓	2.8	
	940 ± 2	7.32 ± 0.02	✓	✓	–	5.0	
	839 ± 2	7.87 ± 0.02	✓	–	✓	6.0	
	1526 ± 3	4.47 ± 0.01	✓	✓	✓	3.7	

From this analysis, it can be seen from the χ_ν^2 values that $\tau_{\mathrm{up}}^{-1} = \tau_{\mathrm{up,B}}^{-1} = B\,T^7$, the term from one-phonon absorption with one-phonon emission, provides the best description of the temperature-dependent losses. The $\bar\tau_{\mathrm{e-up}}$ value, which

is the emptying time without temperature-dependent losses, from the fit is also close to what is expected in the system (see Fig. 3.14) [9].

One of the problems with fixing the B in the fitting procedure is that it is weakly temperature-dependent (compared to the T^7 dependence). As mentioned earlier, it is $8.8 \times 10^{-3}\,\mathrm{s^{-1}\,K^{-7}}$ for $T = 0.6\,\mathrm{K}$ and $7.6 \times 10^{-3}\,\mathrm{s^{-1}\,K^{-7}}$ for $T = 1\,\mathrm{K}$ [Gol79]. We have fixed it to the latter value despite our temperatures being warmer than $1\,\mathrm{K}$. Unfortunately, using B as a free-parameter of the fit does not allow the minimize-χ^2 fitting procedure to converge. This is because the fit does not depend too strongly on the value of B. For instance, fixing B from $(5 \to 10) \times 10^{-3}\,\mathrm{s^{-1}\,K^{-7}}$ in the fit gives the same $\chi_\nu^2 \approx 2$ for both the 1.1–1.5 K and 1.1–1.7 K temperature ranges.

In fact, it can be argued further that the temperature range of the $\dot{N}_c$ measurements made is not too sensitive to the temperature-dependence of $\tau_{\mathrm{up}}^{-1}(T)$. Shown in Fig. 3.15 are the curves for all the difference fits of Table 3.3. It can be seen that more points at lower temperatures are required to start differentiating between them.

An improvement in the fit of $\dot{N}_c$ due to a constant background rate was also attempted. The background rate was found to be consistent with zero. Direct measurements of the background are described in the next section. It can be concluded from these measurements that background is negligible in the $\dot{N}_c$ measurements.

3.4.4 Background measurements

In between the continuous measurements it can be seen when the UCN valve open and the CN beam switched off (see Fig. 3.13), the ambient background rate is $< 0.05\,\mathrm{s^{-1}}$. Most of the non-UCN background comes from the PF1b CN beam are prompt events such as scattering of CNs or (n, γ) reactions. Two separate background measurements were made to observe this. The first was with a full production volume and the LHe at $2.4\,\mathrm{K}$. The second was with the production volume empty at $\approx 20\,\mathrm{K}$. In the former, the UCN valve was shut and then the CN beam switched on and then off again. In the latter, there is data for the UCN valve open and shut with the CN beam on. The plots of

---

[9] While using $\tau_{\mathrm{up}}^{-1} = B\,T^7 + C\,T^{3/2}\,\mathrm{e}^{-(8.6\,\mathrm{K})/T}$ (i.e. adding the two-roton scattering contribution) also gives a small χ_ν^2, but the $\bar{\tau}_{\mathrm{e-up}}$ from the fit is too short and not realistic.

the count rates seen in the UCN detector and CN monitor during these two measurements are shown in Fig. 3.16.

From the empty volume measurement, the background due to scattering of CNs from the front and back windows that reach the detector is $\approx 1.3\,\mathrm{s}^{-1}$. This rate does not come from CN moderated down to the UCN energy range by the cooled beryllium windows at the inner production volume since it remains the same regardless of whether the UCN valve is open or closed.

From the measurement with LHe at $2.4\,\mathrm{K}$ and UCN valve closed, a rate in the detector of $\approx 12\,\mathrm{s}^{-1}$ was observed. For the same temperature and UCN valve open, the rate is $\approx 200\,\mathrm{s}^{-1}$. The UCN valve is not fully tight when closed, and, furthermore, for this particularly measurement the UCN valve was only closed with the pneumatic piston so it is even more leaky than when it was hand-pulled shut. Hence, it is not possible to conclude that the observed $\approx 12\,\mathrm{s}^{-1}$ comes solely from extra CN scattering by the LHe.

There exists another measurement with the UCN valve only shut by the pneumatic piston. In this measurement, with the converter at $1.2\,\mathrm{K}$, the equilibrium leak rate at the valve was $\approx 700\,\mathrm{s}^{-1}$. During the accumulation curve, the storage time with the extra leaky UCN valve was found to be $\approx 11\,\mathrm{s}$. The continuous count rate at this temperature with the UCN valve open is $\dot{N}_c \approx 5,500\,\mathrm{s}^{-1}$. The ratio of the two count rates (leaky closed valve and completely open valve) should be approximately equal to the ratio of the density of UCNs in the production volume. The density of UCNs in the production volume (since P_{UCN} is constant and assuming V_{CN} remains constant) is proportional to the storage times. The storage time at $2.4\,\mathrm{K}$, even with the UCN valve open is dominated by τ_{up}^{-1}. Using $\tau_{\mathrm{up}}^{-1} = B\,T^7$ from Eq. 3.20 it is $\approx 0.3\,\mathrm{s}$. From this, it can be concluded that most of the $\approx 12\,\mathrm{s}^{-1}$ observed at $2.4\,\mathrm{K}$ with the loosely shut UCN valve (besides $\approx 1\,\mathrm{s}^{-1}$ of estimated CN related background) comes from UCNs leaking through the UCN valve.

Therefore, the boronated-stycast on the 2nd stage heat screen, the boronated-rubber sheets, and the lead shielding was effective in suppressing CN-related backgrounds in the UCN ³He gas proportional counter detector. This is despite the total proportion of $3\,\text{Å}$ CNs from the initial beam expected to pass through the cryostat without undergoing an interaction with the material is only $\approx 32\%$; $\approx 3\%$ scatter at the front and back aluminium windows, $\approx 15\%$ at the front and back beryllium windows, and $\approx 50\%$ in the LHe at $2.4\,\mathrm{K}$.
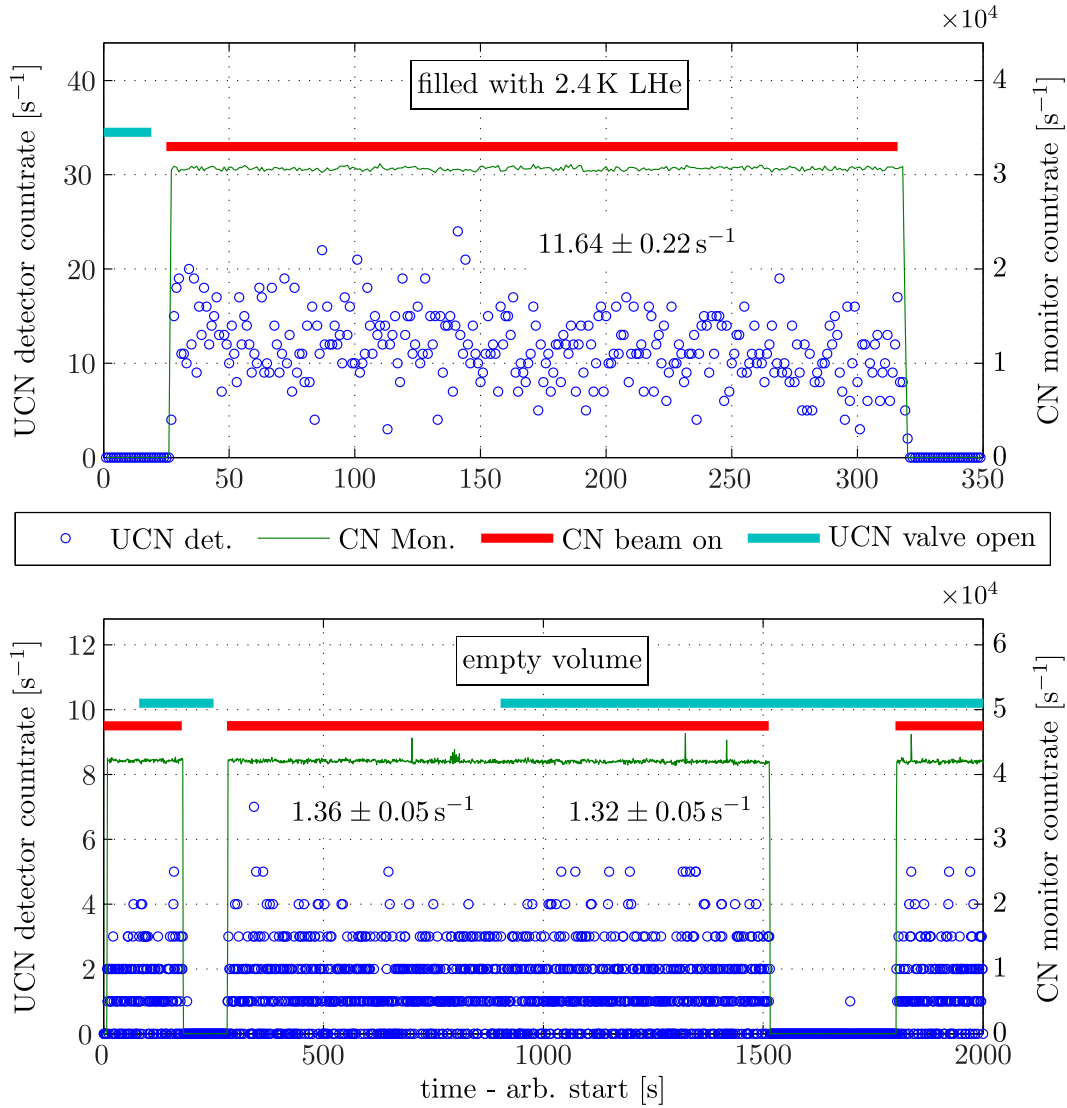
Figure 3.16: The UCN detector background measurements taken when the volume was filled with LHe at $2.4\,\mathrm{K}$ at 09:50, 23/05 and with an empty production volume at 23:30, 23/05. The vertical scale is for the UCN detector counts only. The CN monitor detector counts are shown in arbitrary units. The CN shutter and UCN valve lines show the binary status of the shutter and valve, with zero being closed. The UCN valve was loosely shut with the pneumatic piston only and not "hand-pulled shut".
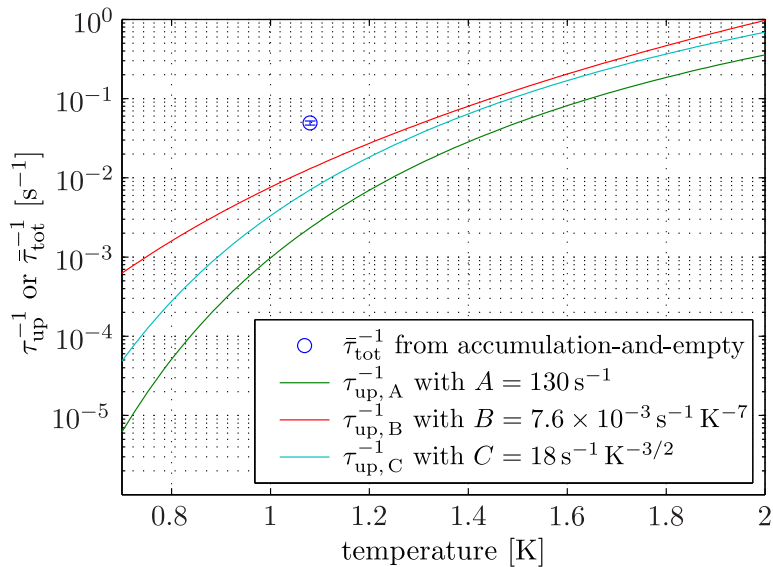
Figure 3.17: The up-scattering rate constants plotted against temperature T for the three different processes of $\tau_{\mathrm{up}}^{-1}(T)$ described in Eq. 3.20. The storage time constant $\bar{\tau}_{\mathrm{tot}}^{-1}$ from the 1.08 K accumulation-and-empty measurement is also shown.

3.5 Discussion

3.5.1 Temperature-dependence of up-scattering τ_{up}^{-1}

From the continuous UCN production measurements at $T \approx 1.1 - 1.7$ K it was found that the best fit of the $\dot{N}_c$ values comes from using the B-term only in the description of τ_{up}^{-1} from Eq. 3.20 [Gol79]. In a separate study, Ref. [Yos92] also observed that the best description of τ_{up}^{-1} comes from using the B-term only for $T \approx 0.5 - 1.6$ K. However, there is some dispute over the $B + C$ term being also valid; and how the expression is only applicable for $T \leq 1$ K [GL93, Yos93]. As can be seen in Fig 3.17, the size of the B and C terms only start to separate from each other at $T < 1.2$ K. Therefore, more measurements are required at lower temperatures to differentiate between the different forms contributing to τ_{up}^{-1} in this experiment. The small size of the A-term relative to the other two also explains why adding it in a fit does not cause a significant difference to the fit.

Also shown in Fig. 3.17 is the $\bar{\tau}_{\mathrm{tot}}^{-1}$ determined by the accumulation-and-empty measurement at 1.08 K. It can be seen that regardless of the combination

of B, $B + C$ or $A + B + C$ terms for τ_{up}^{-1}, a much bigger part of $\bar{\tau}_{\mathrm{tot}}^{-1}$ comes from the other losses.

The remaining losses are $\bar{\tau}_{\mathrm{tot-up}}^{-1} = \tau_0^{-1}(E_n) + \tau_{\mathrm{abs}}^{-1} + \tau_{\beta}^{-1}$. The largest contribution is not $\tau_{\beta}^{-1} \approx 1 \times 10^{-3}\,\mathrm{s}^{-1}$ and is most likely not τ_{abs}^{-1} (see the discussion of the superleak in Sec. 2.2.4). The processes that make up $\tau_0^{-1}(E_n)$ are the losses due to: (a) the beryllium walls, (b) the UCN flap valve mechanism, (c) possible "ice" collected on the walls, and (d) the leak at the UCN valve $\bar{\tau}_{\mathrm{leak}}^{-1}$.

There was a problem with the UCN valve shutting mechanism. However, when the valve was hand-pulled shut, as it was done for the $1.08\,\mathrm{K}$ accumulation-and-empty measurement, the leak rate observed was only $\dot{N}_{\mathrm{det,leak},\infty} \approx 106\,\mathrm{s}^{-1}$. Given that the number of UCNs at equilibrium that was extracted from the volume was $N_{\infty}' = 87{,}000$, the loss rate constant of the valve can be estimated [10] to be $\bar{\tau}_{\mathrm{leak}}^{-1} \approx 1 \times 10^{-3}\,\mathrm{s}^{-1}$. This is small compared to $\bar{\tau}_{\mathrm{tot}}^{-1}$.

Therefore, it is concluded that the major loss in the closed production volume comes from processes (a), (b) and/or (c). This is also supported by the stronger spectral shaping observed in the accumulation-and-empty emptying curves compared to the continuous production curves (seen in Fig. 3.14 and discussed in the text). It was argued that the energy-dependence of $\tau_{\mathrm{tot}}^{-1}(E_n)$ was stronger than for $\tau_{\mathrm{valve}}^{-1}(E_n)$, which is proportional to v only (for isotropic UCNs). Indeed, processes (a), (b) and (c) have the $\propto v$ dependence multiplied by the further non-linear dependence (in E_n and v) due to the average loss per collision $\bar{\mu}(E_n)$.

3.5.2   The UCN density accumulated in the source

The UCN density in the production volume at equilibrium is given by:

$$\rho_{\mathrm{UCN},\infty} = \frac{N_{\infty}}{V_{\mathrm{vol}}} = \frac{P_{\mathrm{UCN}}\, V_{\mathrm{CN}}\, \bar{\tau}_{\mathrm{tot}}}{V_{\mathrm{vol}}} \ . \tag{3.21}$$

What we observe in the accumulation-and-empty experiments is N_{∞}', which is related to N_{∞} by Eq. 3.15, and so the equilibrium density of UCNs that is

---

[10]The loss in the UCN guides and detection efficiency are already inside the observed N_{∞}'. An additional loss factor the UCNs experience when squeezing through the small gap between the beryllium flap and the top of the inner UCN production volume (stainless steel and beryllium here) is not, however.

extracted and detected from the source is, instead, given by:

$$\rho'_{\text{UCN},\infty} = \frac{N'_\infty}{V_{\text{vol}}} = \frac{P'_{\text{UCN}}\, V_{\text{CN}}\, \bar{\tau}_{\text{tot}}}{V_{\text{vol}}} \ . \tag{3.22}$$

The experimental setup of the current experiment is not optimized for the highest density since the CN beam is not incident on the entire production volume, i.e. $V_{\text{vol}} > V_{\text{CN}}$. Also, the storage time in the closed production volume was shorter than expected due to material losses. Using $V_{\text{vol}} = 4{,}000 \pm 100\,\text{cm}^3$ [11], the density of UCNs in the production volume that was extracted and detected at $1.08\,\text{K}$ was $\rho'_{\text{UCN},\infty} = 22 \pm 1\,\text{cm}^{-3}$.

3.5.3 The UCN production rate

The UCN production rate (per unit volume per unit time) P_{UCN} is not dependent on the converter temperature—although the observed $P'_{\text{UCN}}(T)$ is—or the ratio $V_{\text{CN}}/V_{\text{vol}}$. It can be compared with the expected production rate given by the intensity of the CN beam.

The observed production rate can be extracted from the accumulation-and-empty, from Eq. 3.22, via:

$$P'_{\text{UCN, accum.}}(T) = \frac{N'_\infty}{V_{\text{CN}}\, \bar{\tau}_{\text{tot}}} \ . \tag{3.23}$$

The cross-section of the CN beam used was collimated down to $8\,\text{cm} \times 5\,\text{cm}$. If we take the cross-section of the CN beam with conservatively estimated systematic uncertainties in the beam dimensions taking into account differences in the converter height $(80 \pm 6\,\text{mm}) \times (50 \pm 2\,\text{mm})$, then $V_{\text{CN}} = 2{,}300 \pm 200\,\text{cm}^3$, then we arrive at $P'_{\text{UCN, accum.}}(1.08\,\text{K}) = 1.9 \pm 0.2\,\text{cm}^{-3}\,\text{s}^{-1}$ for the extracted and detected production rate for the accumulation-and-empty measurement.

The observed production rate can also be extracted from the continuous measurements via:

$$P'_{\text{UCN, cont.}}(T) = \frac{\dot{N}_c}{V_{\text{CN}}} \ . \tag{3.24}$$

The largest directly observed value in these measurements occurs at the lowest

---

[11] $8\,\text{cm} \times 8\,\text{cm} \times 50\,\text{cm}$ for the aluminium section of the production volume and $10\,\text{cm} \times 10\,\text{cm} \times 8\,\text{cm}$ (with $15\,\text{mm}$ rounded corners) at the copper end piece with a conservatively estimated uncertainty of $1\,\text{mm}$ in each of the dimension.

temperature point of the phase C data. Using $V_{\mathrm{CN}} = 2,300 \pm 200\,\mathrm{cm}^3$ again, this gives $P'_{\mathrm{UCN,cont.}}(1.16\,\mathrm{K}) = 2.5 \pm 0.2\,\mathrm{cm}^{-3}\,\mathrm{s}^{-1}$. In order to compare with $P'_{\mathrm{UCN,accum.}}(1.08\,\mathrm{K})$, the data from Fig. 3.15 is extrapolated to the same temperature to give $\dot{N}_c(1.08\,\mathrm{K}) = 6,100 \pm 200\,\mathrm{s}^{-1}$ [12]. With this extrapolated value, $P'_{\mathrm{UCN,cont.}}(1.08\,\mathrm{K}) = 2.7 \pm 0.3\,\mathrm{cm}^{-3}\,\mathrm{s}^{-1}$ is obtained.

The larger observed production rate in continuous measurements is comes from more UCNs with higher energy reaching the detector. Some of these can have $E_n > V_{\mathrm{Be}}$ since they don't fully explore the volume. The difference between the production rate in continuous and accumulation-and-empty measurements is similar in Ref. [Zim10], where a ratio of $P_{\mathrm{UCN,cont.}}/P_{\mathrm{UCN,accum.}} = 1.20 \pm 0.03$ was observed. From Monte-Carlo studies, the ratio expected was $P_{\mathrm{UCN,cont.}}/P_{\mathrm{UCN,accum.}} \approx 1.3$.

3.5.4 Comparing with the expected value

The final part of the discussion is given to reconciling the observed production rate with that expected from the PF1b CN beam. The observed differential UCN production rate is given by $dP'_{\mathrm{UCN}}(E_n,T)/dE_n = W(E_n,T)\,dP_{\mathrm{UCN}}(E_n)/dE_n$. It is the temperature-dependence in $W(E_n,T)$ that gives $P'_{\mathrm{UCN}}(E_n,T)$ its dependence on temperature. From this relation, to calculate the true production rate from an accumulation-and-empty measurement, the following needs to be calculated:

$$
\begin{aligned}
P_{\mathrm{UCN}} &= \int_{E_{\min}}^{E_{\max}} \frac{1}{W(E_n,T)} \frac{dP'_{\mathrm{UCN}}}{dE_n}\,dE_n \\
&= \frac{1}{V_{\mathrm{CN}}\bar{\tau}_{\mathrm{tot}}} \int_{E_{\min}}^{E_{\max}} \frac{1}{\epsilon(E_n)} \frac{\bar{\tau}_{\mathrm{tot}}}{\bar{\tau}_{\mathrm{tot}} - \tau_e(E_n,T)} \frac{dN'_\infty}{dE_n}\,dE_n ,
\end{aligned}
\quad (3.25)
$$

since it was possible to extract a single ensemble average for $\tau_{\mathrm{tot}}(E_n)$. However, we do not know the accumulated UCN spectrum dN'_∞/dE_n or the energy-dependence of the emptying time $\tau_e(E_n,T)$. A model of the emptying curve with Eq. 3.14, a discrete summation of two exponential decay curves, gives an estimate of the population of UCNs dN'_∞/dE_n with a given $\tau_e(E_n)$. With the $\tau_{e,i}$ and A_i values from this model, the production rate without the losses in

---

[12]The error bar is estimated by the systematic error between all the different expressions for τ_{up}^{-1}.

the production volume can be estimated by:

$$P_{\text{UCN}} \approx \frac{P'_{\text{UCN}}}{\bar{\epsilon}} \left(\sum_{i=1}^{\eta} \frac{\bar{\tau}_{\text{tot}}}{\bar{\tau}_{\text{tot}} - \tau_{\text{e,i}}} \, \tau_{e,i} \, A_i \right) \left(\sum_{i=1}^{\eta} \tau_{e,i} \, A_i \right)^{-1} . \qquad (3.26)$$

This assumes that the efficiency of transportation and detection in the UCN guides and detector can be described by an ensemble average $\bar{\epsilon}$. This value can not be extracted from the current experiment. The $\tau_{e,i} A_i$ term gives the population of UCNs with a specific $\tau_{e,i}$ from the model. The last term in the brackets is used to normalize the $\tau_{e,i} A_i$ values from the model since it does not contain the corrections required for extracting N'_{∞} (see Table 3.2). The normalization factor $\sum_{i=1}^{\eta} \tau_{e,i} A_i = 72,00 \pm 3,000$ is also smaller than $\Sigma_{\triangle}$ since the fit with the model was only started 3 s after the opening of the UCN valve (see Fig. 3.11).

Putting the terms into Eq. 3.26, one obtains $\bar{\epsilon} P_{\text{UCN}} \approx 7\,\text{cm}^{-3}\,\text{s}^{-1}$. Propagating the statistical errors from each term through the equation, one gets $\sigma_{\text{stat}} = 2\,\text{cm}^{-3}\,\text{s}^{-1}$ (or $\approx 30\%$). Within this statistical error, the approximations used in the equation is most likely to be valid.

An estimate for $\bar{\epsilon} = 38\%$ was given in Ref. [Zim10] for a vertical UCN extraction guide system very similar to the one used here [13]. This was deduced by comparing the observed UCN production rate with the expected rate from time-of-flight and gold foil activation measurements of the CN beam. No uncertainty in $\bar{\epsilon}$ was quoted.

Unfortunately, in the current experiment no characterization of the PF1b beam was made. To estimate the expected production rate, we take the values calculated in Ref. [SAZ09] for the PF1b beam based on the beam flux measurements in Ref. [Abe06]. It was quoted that $P_{\text{UCN}} = P_{\text{I}} + P_{\text{II}} = 13.9 \pm 0.9\,\text{cm}^{-3}\,\text{s}^{-1}$, where $P_{\text{I}} = 9.5 \pm 0.7\,\text{cm}^{-3}\,\text{s}^{-1}$ is from single-phonon production and P_{II} from multi-phonon. This was calculated for UCN energies $E_n < 252\,\text{neV}$. We have to correct for the optical potential of the ^{4}He converter $V_{^4\text{He}} = 18.5\,\text{neV}$ and the vertical extraction threshold. For the latter, we take the height difference between the bottom of the horizontal section of the extraction guides to the center of the $8\,\text{cm} \times 8\,\text{cm}$ volume (with a spread of $\pm 4\,\text{cm}$), i.e. $33 \pm 4\,\text{neV}$. The correction factor is thus: $([252 - 18.5]^{3/2} - [(33 \pm 4) - 18.5]^{3/2})/(252 -$

---

[13]The elbow and horizontal sections were the same pieces. The vertical and conical parts were different, but the design was still very similar.

$18.5)^{3/2} = 0.985 \pm 0.007$. However, since the extraction guides are only stainless steel—and there exists small sections of stainless steel inside the production volume (UCN flap valve mechanism)—a pessimistic correction factor where only UCNs with $E_n < V_{SS} - V_{^4\text{He}}$ in the volume are detected is given by $([(184 \pm 4) - 18.5]^{3/2} - [(33 \pm 4) - 18.5]^{3/2}]/(252 - 18.5)^{3/2} = 0.58 \pm 0.02$. In reality, the production rate is expected to lie somewhere the two. That is, P_{UCN} is between $(13.7 \pm 0.9)\,\text{cm}^{-3}\,\text{s}^{-1}$ and $(8.1 \pm 0.6)\,\text{cm}^{-3}\,\text{s}^{-1}$.

Within the level of precision of this experiment we can say this value is confirmed. There are other adjustments to the expected production value that were not discussed. They include: changes in the CN flux since the measurements of Ref. [Abe06] made 10 years ago, losses in CN from the extra $2\,\text{m}$ extension of m=2 super-mirror guides used to extend the CN beam into the PF1b experimental zone, elastic scattering of CNs at the front windows and converter of the UCN production volume tower, and divergence of the CN beam.

Chapter 4

HOPE: The magnetic trap design

This chapter and subsequent chapters on "HOPE" describe the progress towards an improved measurement of the neutron lifetime using the storage of ultracold neutrons (UCN) in a magnetic trap. The design of the trap consists of a 1.2 m long array of Halbach-type Octupole PErmanent (HOPE) magnets with an inner diameter of ≈ 9 cm and a magnetic field strength at the walls of ≈ 1.3 T. Two end superconducting coils, and a bias field solenoid along the length, surrounds the octupole array on the outside. This trap can be used horizontally, forming an Ioffe-Pritchard trap [Pri83, Huf00], or it can be used vertically as a magneto-gravitational UCN trap[Zim00, Ezh01]. The details of the permanent magnets and superconducting coil assembly are described in this chapter.

The main motivation for using magnetically stored UCNs is to avoid the need for systematic corrections for UCNs losses from material interactions. Whenever one technique is replaced with another, there are usually new systematic effects introduced. In this case, it is UCN loss due to depolarization (described Sec. 5.7). Of course, there are also the same or analogous systematic effects, such as long survival times of above-threshold UCNs, which can be enhanced in a magnetic trap (Sec. 5.4), and losses due to UCN interactions with residual gas that are still present (Sec. 5.8). Due to the importance of understanding the former, emphasis is placed on discussing different techniques that can be used for cleaning the UCN spectrum in the trap. Other concepts

related to the experiment such as filling of the trap and its effective volume are also discussed. The latter is important since the main trade-off from using a magnetic trap is the smaller number of stored UCN due to the lower trapping potential and smaller volumes due to cost constraints.

An incremental strategy is employed for developing the setup, with an strong emphasis on experimental tests. Experiments with UCNs using incremental versions of the magnetic trap were performed and are presented in Chapter 6.

The use of a trap with magnetic walls opens up the possibility of *in-situ* extraction and detection of the charged decay products from neutron β-decay. A discussion of the trajectories of the protons and electrons from simulations, possible detection systems, and additional magnetic and electric fields that may be required is given in Chapter 7.

4.1   The permanent magnet array

The center-piece of the magnetic UCN trap is the array of **H**albach-type **O**ctupole **PE**rmanent magnets (source for the name HOPE) made from $Nd_2Fe_{14}B$ material. One of the advantages of using a high-order multi-pole field for radial confinement is the increase in phase-space or effective volume for trapping UCNs (see Sec. 5.2). For example, a horizontal trap using a radial octupole field ($|B| \propto \rho^2$, where ρ is the distance from the central axis) has the same effective volume as one with a radial quadruple ($|B| \propto \rho$) with 1.8 times the $|B|$ at the trap wall, assuming other dimensions remain the same.

The concept of a segmented multipole magnet was given in Ref. [Hal80]. The Halbach-type octupole ($N = 4$) modules used in this experiment consist of 32 trapezoidal NdFeB pieces ($M = 32$) forming an internal bore with a radius $\rho_{\mathrm{trap}} = 46.8\,\mathrm{mm}$ where the octupole field exists (see Fig. 4.1). Each module is 10 cm long. The pieces are held together with a circular stainless steel outer jacket with an inner radius of 95 mm. A Halbach-type multipole is formed by having the magnetization vector of each piece advance by an angle of $2\pi N/M$ (45° in this case) relative to the adjacent piece [1]. Therefore, there are three kinds of pieces: 8 *pole pieces*, 8 *off-pole pieces*, and 16 *between pieces* (see

---

[1]The magnetization is parallel to the top and bottom planes of the module and is the uniformly the same throughout a piece.
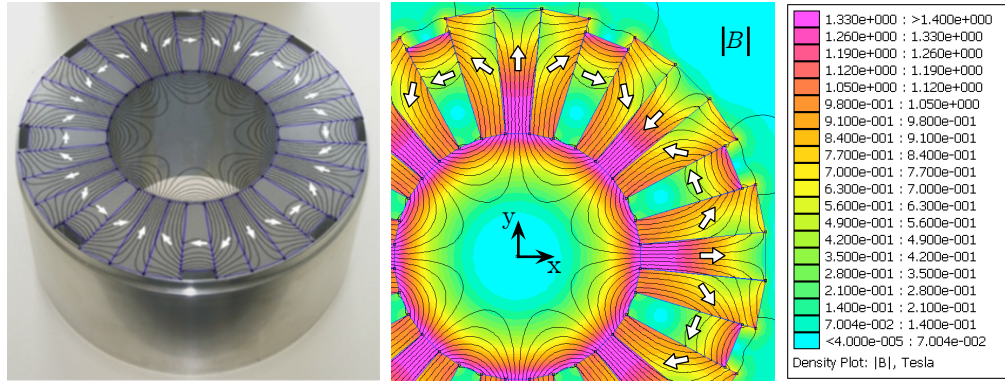
Figure 4.1: *Left:* A photo of a Halbach-type Octupole permanent magnet module; digitally super-imposed on top are the magnetic field lines from the FEMM simulations. *Right:* The output from the FEMM simulations zoomed in (slice in the xy-plane). The shading is of the magnitude of the flux density $|B|$. The magnetic field lines are shown as the black lines ($-$). In both diagrams, the magnetization of the 32 NdFeB pieces are shown by the white arrows ($\Rightarrow$). Discussions in this thesis using the cartesian coordinates is based on the x and y axes (with the z-axis coming out of the page) shown here.

Fig. 4.3). The off-pole pieces are shortened for technical reasons (Fig. 4.2).

The permanent magnetic material used is Vacodym 745HR on all the pieces except the off-pole pieces, which use Vacodym 633HR[2]. The properties of the materials are shown in Table 4.1. H_{cB} is called the coercivity of flux density and is the field strength H at which the flux density B is reduced to zero. H_{cJ} is called the coercivity of polarization or magnetization (sometimes also called the intrinsic coercivity) and is the field strength H at which the magnetization J of the material is reduced to zero. For the former, when the external field is removed the remanence is recovered; However, for the latter this is not the case. At H_{cJ} the material starts becoming permanently demagnetized[3]. This property requires careful consideration when designing the system in which permanent magnetic materials are to be used.

The mechanics of the combined 12 modules that make up the 1.2 m long Halbach octupole are described in Fig. 4.2. The glue used on the inner walls of the magnet modules can be clearly seen in this figure. Glue is also used in-

---

[2]These are the trade-names of the high remanence isostatically pressed neodynium-iron-boron magnets from Vacuumschmelze GmbH [Vac].

[3]The term "depolarized", sometimes used in literature, is avoided in this thesis to avoid confusion with the spin-flip transitions of UCNs.

Table 4.1: The properties from Vacuumschmelze, the manufacturer, of the NdFeB materials used. More details are given in Ref. [Vac]. See text for definition of the terms.

Material	Remanence typical B_r	relative permeability	Coercivities (at 20°C)		Density
			minimum H_{cB}	minimum H_{cJ}	
745HR	1.47 T	$\mu_x = \mu_y = 1.045$	1065 kA m^{-1}	1115 kA m^{-1}	7.6 g cm^{-3}
633HR	1.35 T	$\mu_x = \mu_y = 1.049$	980 kA m^{-1}	1275 kA m^{-1}	7.7 g cm^{-3}

between the pieces as well. An out-gassing rate measurement was made. After two days of pumping an outgasing rate of 6×10^{-5} mbar L s^{-1} was measured from one module. Most of the out-gassing is likely to be hydrocarbons from the glue, i.e. containing a high content of hydrogen nuclei. This could be problematic for the stored UCNs in the trap due to the large inelastic scattering cross-section of ^{1}H. In the experimental design, a thin-walled stainless steel tube inside the trapping volume will be used to separate the two vacuum spaces.

4.1.1   2D finite element calculations of the octupole field

Two-dimensional simulations of the magnetic field configuration from the Halbach octupole magnets were performed with FEMM [Mee06]. In Ref. [Suo06], the FEMM program was tested against other 2D and 3D programs for a Nd-FeB Halbach sextupole with similar dimensions to our magnets. The results were found to be nearly identical.

FEMM uses the finite element method where the geometry of the problem is divided into a mesh of triangles, and the magnetic vector potential is solved iteratively for each element by minimizing the energy and applying continuous boundary conditions. The program only deals with 2D systems and so the octupole magnets are assumed to be plane-symmetric (i.e. infinitely long). The magnetic field at the end of the array requires 3D simulations that are done with Radia (see Sec. 4.4). The computing time of the full 360° 2D simulation was below one minute. The output from the FEMM calculation of the B-field lines and the magnetic flux density magnitude $|B|$ is shown in Fig. 4.1. A cartesian coordinate is shown in the figure. Cylindrical and spherical systems according to the standard definitions (ρ, ϕ, z) and (ρ, θ, ϕ), respectively, are
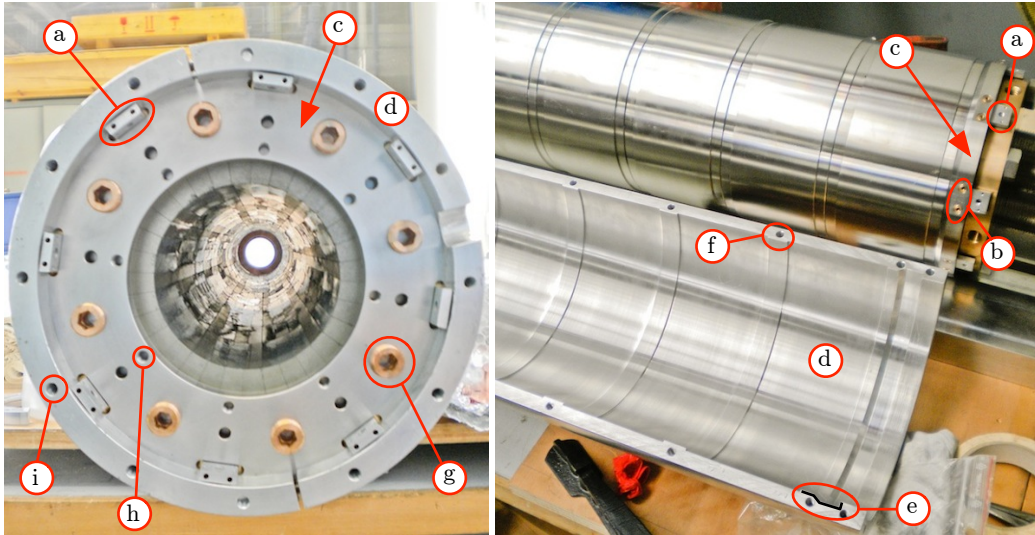
Figure 4.2: The mechanics of the 1.2 m long Halbach-type octupole permanent magnet array. Eight aluminium rods (a) that fit snuggly through the trapezoidal-shaped slots between the far edge of the off-pole pieces and the outer stainless steel jacket, are used to fix the rotational orientation between the modules. These rods are fixed by brass pins (b) to the stainless steel (type 316L) end plates (c). The repulsive force between the magnets are supported by an outer aluminium jacket (d). It is also used for thermal contact along the length of the array. Silicon vacuum grease is applied between the aluminium outer jacket and the stainless steel outer jacket of the modules to improve the thermal contact. The jacket defines the distance between the outer surface of the stainless steel end plates with the grooves (e) (its cross-section is outlined so it can be seen more clearly). The outer aluminium jacket is split into two-half cylindrical shells that are fixed together by a series of screws (f). The clearance holes on the other aluminium shell (not shown) are counter-sunk to avoid the screws protruding out from the outer aluminium jacket. The final adjustment ensuring the modules are pressed together without gaps is done by 16 brass grub screws (g) fixed onto threaded holes on the end stainless steel plates. Another series of threaded holes in the stainless steel end plates (h) allow attachment of various pieces to be used for experiments. Threaded holes on the end of the outer aluminium jacket (i) can be used for thermal contact with the permanent magnet.
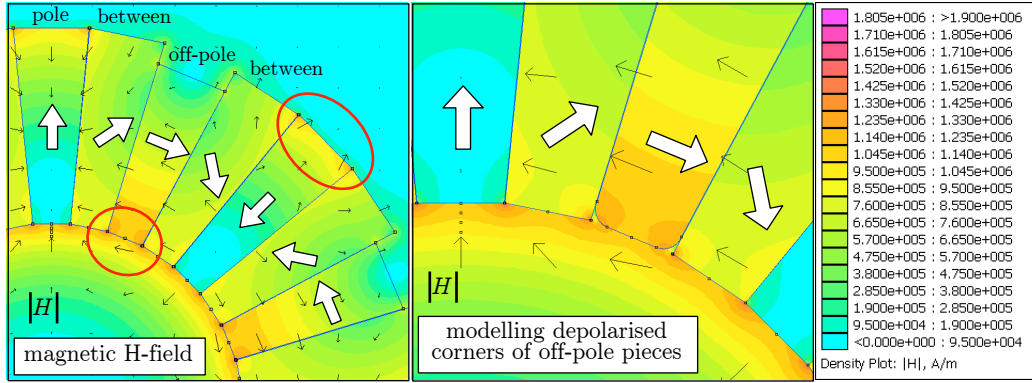
Figure 4.3: The calculations from FEMM. The shading is $|\vec{H}|$, the thin black arrows ($\rightarrow$) are the H-field vectors, the large white arrows ($\Rightarrow$) are the magnetization direction of the pieces, and the text labels are the naming conventions used for the octupole pieces. Two problematic areas where demagnetization might occur are marked with a red circle ($-$). To model the effects of this, the permanent magnetic material at the corners are removed (substitute with a rounded air gap), as shown on the *right*. The effect of this on $|B|$ is shown in Fig. 4.4.

also used.

The inputs used by FEMM for the calculations are the relative magnetic permeability and the coercivity of flux density of the NdFeB materials from Table. 4.1. The material was assumed to have a linear $B - H$ relationship. The FEMM calculations show that the H-field at the inner corner of the off-pole pieces is directly opposed to the magnetization of the piece with values $|\vec{H}| > H_{cJ,633\mathrm{HR}} = 1275\,\mathrm{kA\,m^{-1}}$ over quarter-circular segments with radius $\approx$ $1\,\mathrm{mm}$. To model the effects of the possible demagnetization of the magnetic material at the corners, the calculations were repeated with small segments cut off (replaced with an air gap) at the corners (see Fig. 4.3). There are also small quarter-circular regions (radius $\approx 1.5\,\mathrm{mm}$) at the outer corners of the pole-pieces that have an opposing $|\vec{H}| > H_{cJ,745\mathrm{HR}} = 1115\,\mathrm{kA\,m^{-1}}$. These regions have little effect on the magnetic field inside the inner walls if they remain this size. Demagnetization of the magnets may only become a problem when used with the superconducting coils (Sec. 4.2).

The magnitude of the flux density $|B|$ from FEMM calculations at fixed radial distances close to the walls of the magnets are shown in Fig. 4.4. The values from the standard calculations are compared to those with the modeled
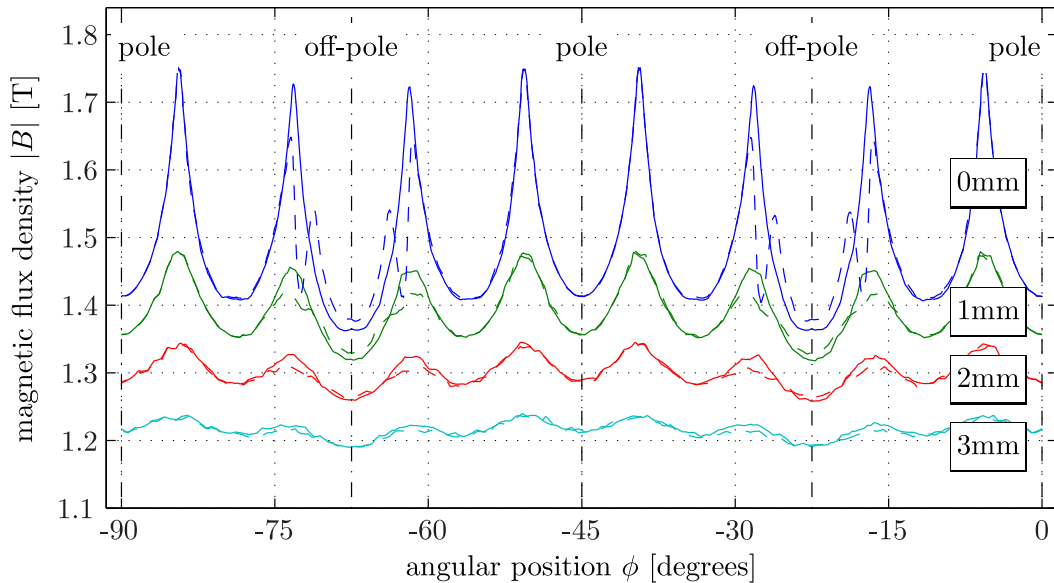
Figure 4.4: The magnitude of the magnetic flux density $|B|$ from the FEMM simulations at fixed radial ρ distances from the inner-walls of the magnets (the boxed numbers ☐). 0mm corresponds to $\rho = 46.75\,\text{mm}$. The uncertainty of the distance to the walls due to the 32-sided polygon-shaped internal aperture is $\approx 0.2\,\text{mm}$. The continuous lines $(-)$ are from the standard simulations; the dashed lines $(--)$ are from the depolarized corners model. $\phi = 0°$ refers to the x-axis and $\phi = -90°$ to the y-axis. The vertical dash-dot lines $(-\cdot)$ indicate the angular positions of the centers of the pole and off-poles pieces.

demagnetization corners. The walls of the permanent magnets do not necessarily have to be the walls of the trap ρ_{trap}. This is discussed in Sec. 4.2, where space is required for thermally isolating the cooled permanent magnets from the UCN trapping space. For this reason, $|B|$ at 1, 2 and 3 mm from the magnet walls are also plotted.

The weakest $|B|$ at the walls of the trap defines the maximum trapping potential. This is expected to occur at the center of the off-pole pieces. There are strong peaks of $|B|$ at the boundary between two pieces thought to be due to the sharp edges of the magnetic material. As we move away from the trap wall, the effects of the depolarized corners become less pronounced. The slight increase of $|B|$ at the center of the off-pole pieces for the demagnetized corners comes from the model that gives the center of the off-pole pieces a slightly pointed shape.

The radial flux density $|B(\rho)|$ along the profiles towards the different pieces

(pole, off-pole and between) are indistinguishable from each other until about $\rho > 42\,\mathrm{mm}$, where the off-pole profile starts to drop to weaker $|B|$ values. These plots are shown in Fig. B.3 in the Appendix.

Measurements of the magnetic field of the modules are described in Sec. B.1 of the Appendix. The conclusions from the measurements are that the magnetization of most pieces of magnet are within $\approx \pm 5\%$, a reasonable variation from manufacturing. The typical field strengths $|B|$ at the walls, deduced by extrapolating from the FEMM calculations (without and with demagnetization) are $\approx 1.4\,\mathrm{T}$ for the pole, off-pole, and between pieces. Only one module was found to have two particularly weak magnet pieces giving a $|B|$ at the walls of slightly less than $\approx 1.3\,\mathrm{T}$. This was placed at the end of the assembled array (see next section) to reduce the effect it will have in the final system. To be conservative, a field at the walls of $1.3\,\mathrm{T}$ will be used for discussion. Unfortunately, the precision of the measurements do not allow the modeling of the demagnetization to be verified. The differences of the field at the walls between with and without demagnetization is only $\approx 0.01\,\mathrm{T}$.

4.2 The superconducting coils

The octupole magnet array provides confinement of UCNs in the xy (or transverse) plane only. For confinement in the z (axial or longitudinal) direction, a magnetic field gradient needs to exist in the z-axis. A convenient design is to form an Ioffe-Pritchard-type trap, where end-coils are used to close off the trap. If the octupole array is used vertically, i.e. the z-axis is parallel to the direction of gravity, then only the end-coil at the bottom is needed[4]. The comparison between a horizontal and vertical setup is discussed in the next section.

The size of the end-coils is a trade off between several factors. Naively, one might think that the only requirement is to have the solenoid diameter larger than the diameter of the trap so that the entrance to the trap is unobstructed. However, one must be careful with the radial component B_ρ from the coils that cancels and reinforce with the radial components from the octupole. Strong cancellation can lead to regions of weak $|B|$ which would reduce the minimum

---

[4]The end-coil at the top would still be desirable if focussing of charged particles are desired. This is discussed in Chapter 7.

$|B|$ value at the walls of the trap that defines the maximum trapping potential. Furthermore, the B-field from the end-coils can demagnetize the permanent magnet material of the octupole. This is particularly strong when the field is not perpendicular to the magnetization axis. End-coils with a large diameter are desired since this reduces the size of the radial component at the walls of the trap and other walls of the magnets. However, aside from cost considerations, end-coils with large diameters will have axial fields that extend further into the octupole array, reducing the effective volume available for trapping UCNs. Due to these reasons, coils with diameters larger than the outer diameter of the octupole array were required. In order to generate a sufficiently strong $|B|$ to match that of the octupole, superconducting coils were the best choice. At the time of writing this thesis, the coils have been manufactured and delivered so the design and dimensions are fixed.

The superconducting wire used in the coils consists of 20 NbTi filaments embedded in a Cu-matrix. The cross-section of just the wire is $1.06 \times 1.63 \, \text{mm}^2$ and with its Formvar insulation coating $1.14 \times 1.71 \, \text{mm}^2$. The fraction of Cu:NbTi in the wire is 8:1. The systems consists of three coils. Their names used in this thesis and their functions are given below. The magnetic field strengths stated are only suggested nominal field strengths. A discussion of more appropriate values is given in the text.

The bias field solenoid (0.3 T) — Removes the low-field regions from the octupole where depolarization of UCNs can occur (Sec. 5.7). The high strength is only needed for the extraction of charged decay products (Chapter 7). It can be weaker if this is not required.

The small end-coil (1.2 T or 1.7 T) — Confines UCNs in one axial direction with its $|B|$ gradient. It also provides a magnetic mirror for charged particles. This coil was designed (low turns, high current) to be ramped for filling and emptying of the trap, if the latter is indeed required. A field of 1.7 T should be used for the vertical and 1.2 T for the horizontal setups (see Sec. 4.4).

The large end-coil (0.3 T, 1.2 T or 3.7 T) — Confines UCNs in the other axial direction if the trap is used horizontally (1.2 T). If used vertically, then gravity provides confinement instead and the coil can be run at

0.3 T or less. If focusing of protons onto a small detector is required then 3.7 T—the maximum strength without causing demagnetization of the permanent magnets—can be used.

The specifications of the three coils are given in Table 4.2. The spools that support the wire are made from stainless steel type 309. Each coil will have a separate heat switch so that they can be run in persistent mode independently. These switches are placed in the recess of the bias-field coil to minimize space so that the maximum radius required for the whole assembly is 221 mm. The total length of the superconducting coil assembly (with spools) is 1356 mm.

Table 4.2: The specifications of the three superconducting coils. The central position is the center of each coil on the z-axis, with the center of the bias coil defined to be $z = 0$. The dimensions (length, r_{inner} and r_{outer}) are where the superconducting wire is located. The current densities are for a current of 300 A, considered to be the operating maximum, in the superconducting cables. The maximum B-field ("max. field") quoted for this current is given for the center of the coil at $\rho = 0$ mm. The value given is also for just that specific coil, i.e., the addition of B from the adjacent coils are not included.

coil	central pos. [mm]	length [mm]	r_{inner} [mm]	r_{outer} [mm]	num. of windings	current density [A mm^{-1}]	max. field [T]
small end	-575	130	156	182	1510	16.8	1.73
bias field	0	800	156	168	2208	8.7	1.19
large end	555	250	156	205	5656	17.3	5.04

The spacing and width of the coils in the z-axis have been designed so that there are no local minima of $|B|$, which can cause local trapping of charged particles due to the magnetic mirror effect (see Chapter 7). The output from the FEMM calculations of the superconducting coils is shown in Fig. 4.5 for all the coils operating at 300 A. The axial component B_z for $\rho = 0$ and ρ_{magnet}, and the radial component B_ρ for $\rho = \rho_{\mathrm{magnet}}$ and $\rho_{\mathrm{magnet\,outer}}$ for 300 A in all coils, are shown in Fig. 4.6 and Fig. 4.7. Also in these figures, useful B-field configurations, and the required current in the coils to produce them, are shown. It should be noted that $|B|$ at the center of a coil depends on the current in the adjacent coil(s). The reasons for a choice of the nominal field at each coil was already explained previously.
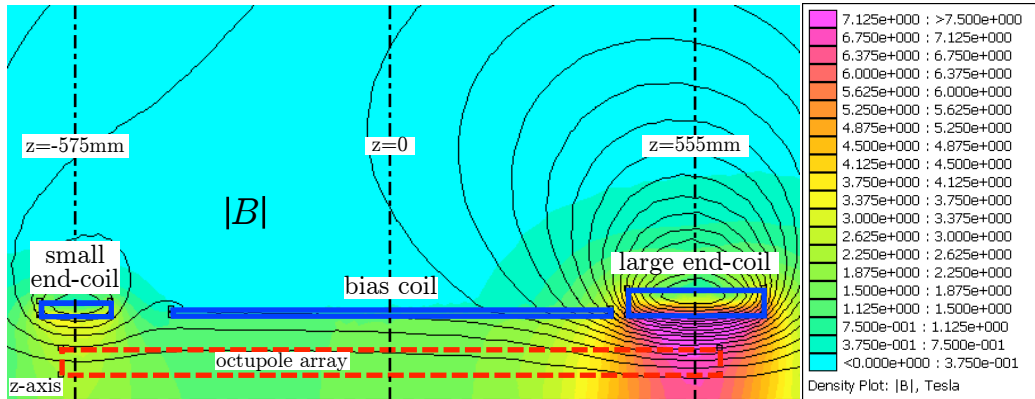
Figure 4.5: The output from the FEMM calculations of $|B|$ (shown shaded with legend on the *right*) and the B-field lines of the system of 3 superconducting coils. The problem is reduced to 2D by treating exploiting the symmetry of rotations about the z-axis, shown as the dash-dotted line $(-\cdot)$. The cross-sections of the three coils are shown by the rectangles in continuous blue lines $(-)$, and the location of the octupole array, not included in the calculations, is marked by the rectangular in red dashed lines $(--)$. The fields shown are with all the current in all 3 coils at $300\,\mathrm{A}$ (the corresponding current densities are shown in Table 4.2).

4.3   Demagnetization of the NdFeB material

The usual treatment of the demagnetization of a magnetic material considers only the directly opposing component of an external field $\vec{H}$ relative to the magnetization vector $\vec{M}$ to cause demagnetization. That is, if $\vec{H}\cdot\vec{M} = |\vec{H}||\vec{M}|\cos\varphi$, i.e. φ is the angle $\vec{H}$ makes with $\vec{M}$, then the coercivity of demagnetization varies for an angle φ by $H_{cJ}(\varphi) = H_{cJ}(0°)(\cos\varphi)^{-1}$. $H_{cJ}(0°)$ is the standard coercivity for directly opposing fields that is usually given. In this treatment, when $\vec{H}$ is perpendicular to $\vec{M}$ (i.e., $\varphi = 90°$), one expects no demagnetization.

However, this is only true for perfect grain orientation in a NdFeB material. Ref. [Kat05] studied the effects of inclined fields on magnets with $\mu_0 H_{cJ}(0°) = 1.76\,\mathrm{T}$ and $3.28\,\mathrm{T}$ made from sintered NdFeB formed by isostatic pressing [5]. It was found that $H_{cJ}(\varphi)$ remained constant to within the experimental uncertainty of $\approx 50\%$ for $\varphi = 0° - 45°$. It was only when the angle

---

[5]For comparison the materials used in our magnets have $\mu_0 H_{cJ}(0°) = 1.40\,\mathrm{T}$ and $1.60\,\mathrm{T}$, are also isostatic pressed, and produced by the same company.
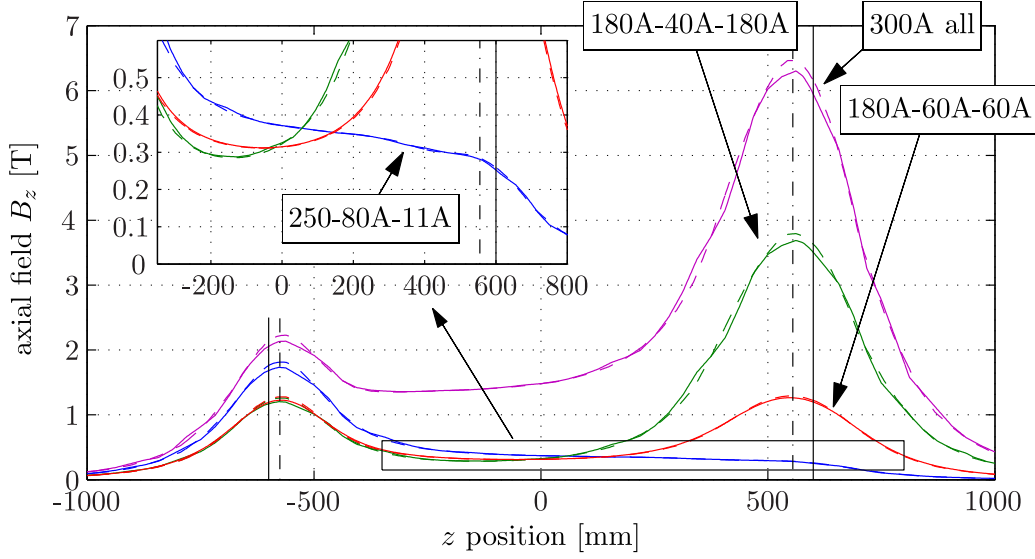
Figure 4.6: The axial component B_z calculated with FEMM for the superconducting coils for different useful current configurations. The values at $\rho = 0$ are shown with continuous lines ($-$) and at $\rho = \rho_{\text{magnet inner walls}}$ with dashed-lines ($--$). The vertical black dash-dotted line ($-\cdot$) shown the center of the end coil and extraction coil and the vertical black continuous lines ($-$) show the ends of the octupole array.

was increased to $\varphi = 90°$ did $H_{\text{cJ}}(\varphi)$ increase; but only to $H_{\text{cJ}}(90°) = 1.7 H_{\text{cJ}}$, far from the $\propto (\cos\varphi)^{-1}$ dependence. The results were the same for both materials.

For calculations of the demagnetization due to transverse fields, I will use a model described in Ref. [Ruo11] where an approximation of the φ dependence of $H_{cJ}(\varphi)$ was found to be:

$$H_{cJ}(\varphi) = H_{cJ}(0°)\left[1 + a_1\varphi + a_2\varphi^2 + a_3\varphi^3\right], \tag{4.1}$$

where $a_1 = +3.17\times10^{-4}\,\text{deg}^{-1}$, $a_2 = -3.38\times10^{-5}\,\text{deg}^{-2}$ and $a_3 = +1.37\times10^{-6}\,\text{deg}^{-3}$. It is stressed that this model underestimates the demagnetization effects compared to the measurements of Ref. [Kat05].

With this new understanding, we see that even without any B_ρ component, B_z can not exceed 2.4 T from the superconducting coils without demagnetizing the Vacodym 745HR material. B_ρ, which can take on both positive and negative values since the octupole array extends beyond the center of the end-coils,
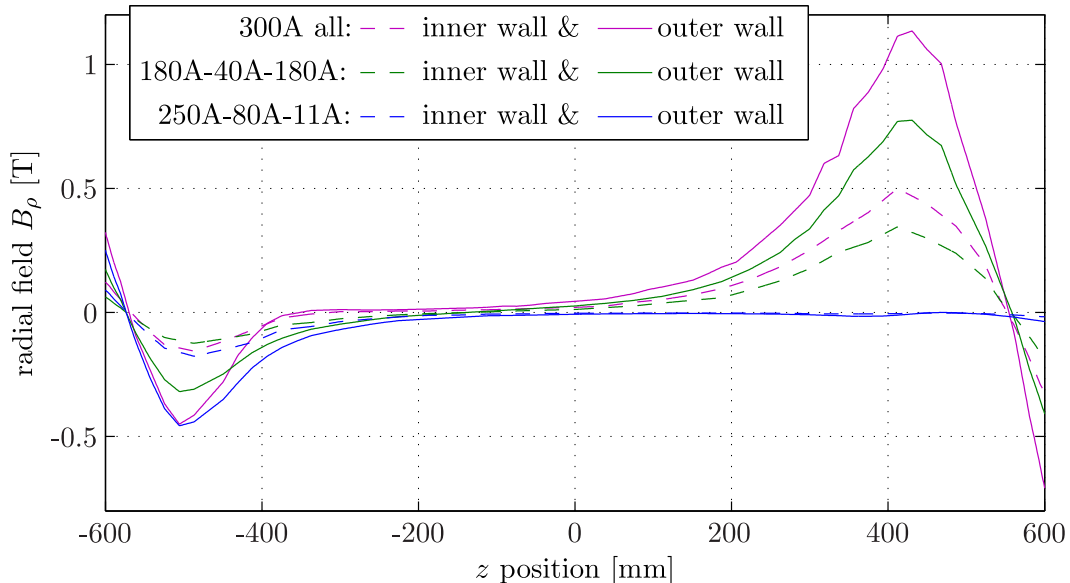
Figure 4.7: The radial component B_ρ calculated with FEMM for the superconducting coils in three different configurations for $\rho = \rho_{\text{magnet inner walls}}$ and $\rho_{\text{magnet outer walls}}$. The ends of the octupole array are at $z = -600\,\text{mm}$ and $600\,\text{mm}$.

is strongest for larger ρ values. This reinforces strongly with the H-field at the outer edges at half of the pole pieces (see Fig. 4.3). Demagnetization will thus be strongest near the outer edges of the magnet of these pole pieces.

Fortunately, the coercivity of the NdFeB material can be enhanced by cooling. Measurements in Ref. [Ben08] were made with Vacodym 764 for temperatures down to $80\,\text{K}$ for $\varphi = 0°$. They showed that H_{cJ} increases linearly as it is cooled with a gradient of $\mathrm{d}H_{cJ}/\mathrm{d}T = -0.58\,\%\,\text{K}^{-1}$. However, the magnetization reaches a peak before starting to fall at lower temperatures (due to the Spin Reorientation Transition phenomenon). The remanence magnetization, that is the magnetization with no external fields, was measured to peak at $\approx 100\,\text{K}$ (with a value 1.1 times than that at $300\,\text{K}$) [Ben08]. This behavior was found to be the similar in two other high remanence NdFeB materials as well.

A semi-empirical model of NdFeB material developed from the same group predicts that the magnetization peak shifts for different values of $|\vec{H}|$; when it is 0.5–$1.0\,\text{T}$ the peak is at $\approx 150\,\text{K}$ (see [LBCB09]). Ideally one should choose a temperature that coincides with the peak in magnetization to minimize the effects of temperature drifts on the trapping field. However, this is complicated

since the peak will vary depending on the piece, since $|\vec{H}|$ varies. Furthermore, the variations of the magnetization and coercivity have to be assumed to be the same for inclined fields, i.e. $\varphi \neq 0°$. For the discussion in this thesis, cooling the NdFeB material down to $\approx 120\,\mathrm{K}$, which gives an increase in the coercivity by a factor of ≈ 2.8 will be used. The most rapid change of magnetization when far from the peak for all reverse fields is $\approx 0.1\,\%\,\mathrm{K}^{-1}$. Therefore, temperature changes of the NdFeB material of $> 12\,\mathrm{K}$ are required to affect the field strength at the magnet walls by $> 15\,\mathrm{mT}$ or $1\,\mathrm{neV}$ of UCN energy. Since the depth of the trap will be defined at the end coils, and the temperature can easily be controlled to much less than this due to its large thermal mass, the effects of temperature fluctuations of the NdFeB material should be negligible.

In order to determine the amount of demagnetization that occurs in the NdFeB material when the superconducting coils are run, the H-field of the Halbach-type octupole is combined with the H-field from the superconducting coils. The inclination angle φ between the combined $\vec{H}$ and the magnetization vector $\vec{M}$ of each Halbach octupole piece was calculated and, using Eq. 4.1, the ratio of $|\vec{H}|$ to the demagnetization threshold, $|\vec{H}|/H_{cJ}(\varphi)$, was calculated for the entire volume of the octupole array. When $|\vec{H}|/H_{cJ}(\varphi) > 1$ demagnetization begins to occur. The spatial resolution of the calculations is around $0.5\,\mathrm{mm}$.

If the octupole array is not cooled, then running the superconducting coils even at low currents is enough to cause significant demagnetization. When they are cooled to $120\,\mathrm{K}$ an 2.8 times increase of the coercivity (at all φ) is assumed. Then, from the calculations, the small end coil and the bias field coil can be run at the full $300\,\mathrm{A}$ current without demagnetizing the permanent magnetic material. However, the current in the large end coil should not exceed $170\,\mathrm{A}$ if we wish to keep the maximum $|\vec{H}|/H_{cJ}(\varphi) < 0.9$ (or $I_{\mathrm{L-endcoil}} < 155\,\mathrm{A}$ for a more conservative $|\vec{H}|/H_{cJ}(\varphi) < 0.8$). The results of the demagnetization calculations for this configuration (300A-300A-170A) is shown in Fig. 4.8. If the small end-coil and the bias-coil are used with $I_{\mathrm{S-endcoil}} = 180\,\mathrm{A}$ (1.2 T nom.) and $I_{\mathrm{bias-coil}} = 40\,\mathrm{A}$ (0.3 T nom.) then the maximum current in the large end-coil is $I_{\mathrm{L-endcoil}} < 180\,\mathrm{A}$ in order to keep $|\vec{H}|/H_{cJ}(\varphi) < 0.9$ (or $I_{\mathrm{L-endcoil}} < 160\,\mathrm{A}$ to keep $|\vec{H}|/H_{cJ}(\varphi) < 0.8$). Having the maximum possible B-field at the large end-coil is used if protons are to be extracted and focussed onto a smaller detector. The B-field for the (180A-40A-180A) configuration corresponds to $|B| = 3.7\,\mathrm{T}$ at the center of the large end-coil.
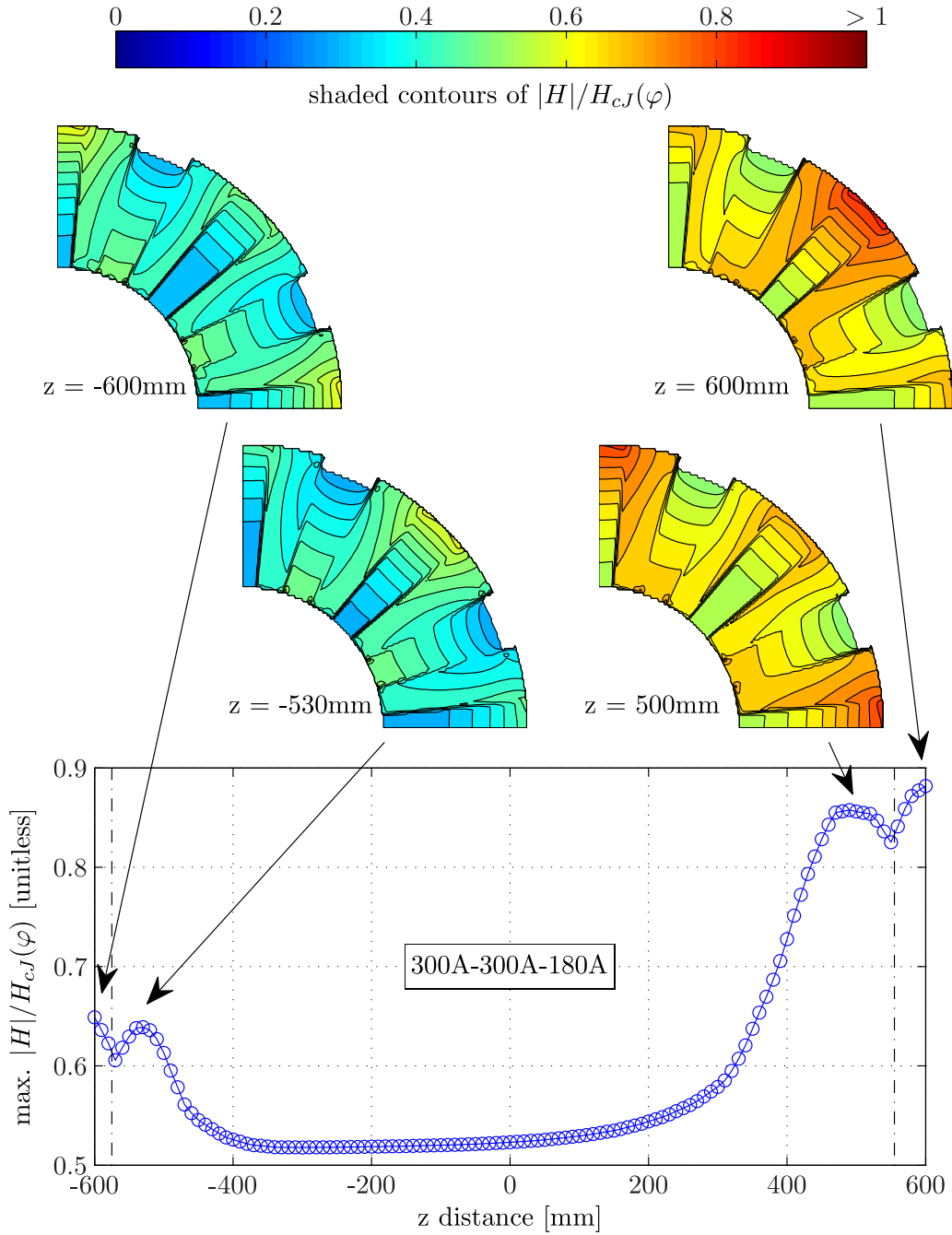
Figure 4.8: The demagnetization calculations of the NdFeB material of the octupole array due to the superconducting coils. See text for a detailed explanation of how $|\vec{H}|/H_{cJ}(\varphi)$, which is a measure of how close the material is to demagnetizing, is calculated. A value for $H_{cJ}(\varphi)$ increased by a factor of 2.8 times due to cooling was used. The *bottom* plot shows the maximum $|\vec{H}|/H_{cJ}(\varphi)$ value for various slices in the z-plane. The *top* are shaded contour plots of $|\vec{H}|/H_{cJ}(\varphi)$ for a quarter segment (in the same orientation as Fig. 4.1 and Fig. 4.3).

4.4   Combination of magnetic fields inside the trap

Here we wish to calculate the complete $\vec{B}$ inside trapping volume. When combining the magnetic fields from the superconducting coils and the octupole magnets, the end effects of the long octupole array need to be discussed. The calculations with FEMM in Sec. 4.1 are 2D and assumes the octupole is infinite in length. In order to calculate the magnetic field near the ends of the octupole array a 3D simulation is required.

4.4.1   3D calculations of the magnetic field from the octupole array

A software package called Radia [CEC97], a plug-in for Mathematica developed by the European Synchrotron Radiation Facility (ESRF), is used. In these calculations [Rosa, Fra09], the octupole array is simplified as consisting of 32 continuous trapezoidal pieces 1.2 m in length, i.e., the separate modules were not modeled. The slots and different material at the off-pole pieces were also not in the model. Discontinuous jumps in the calculations occur at the edge of the octupole array at $z = 600$ mm; therefore, the values shown avoid this region by 1 mm.

The calculations (see Fig. 4.9) show that $|B|$ at the walls of the octupole drops off near the ends of the 1.2 m long array. These calculations were confirmed by measurements [Fra09]. The decrease of $|B|$ is only significant at the last few centimeters and the size of the drop is different for different azimuthal ϕ angles, with the biggest drop is at the pole pieces. The center of the small and large end coils in the z-axis are inside the octupole array (centered at $z = -575$ mm and 555 mm, respectively) to avoid the effects of this drop. For the preliminary tests of UCN storage with the octupole array without the end coils (described in Chapter 6) the decrease in $|B|$ is not avoided.

There are also longitudinal components to the magnetic flux density B_z that start to develop at the end of the octupole array. A plot is shown in Fig. 4.10. The B_z components can be positive and negative, which can reinforce or cancel with solenoid field depending on the orientation of the current. They are also strongest around the off-pole pieces. The size of $|B_z|$ does not have
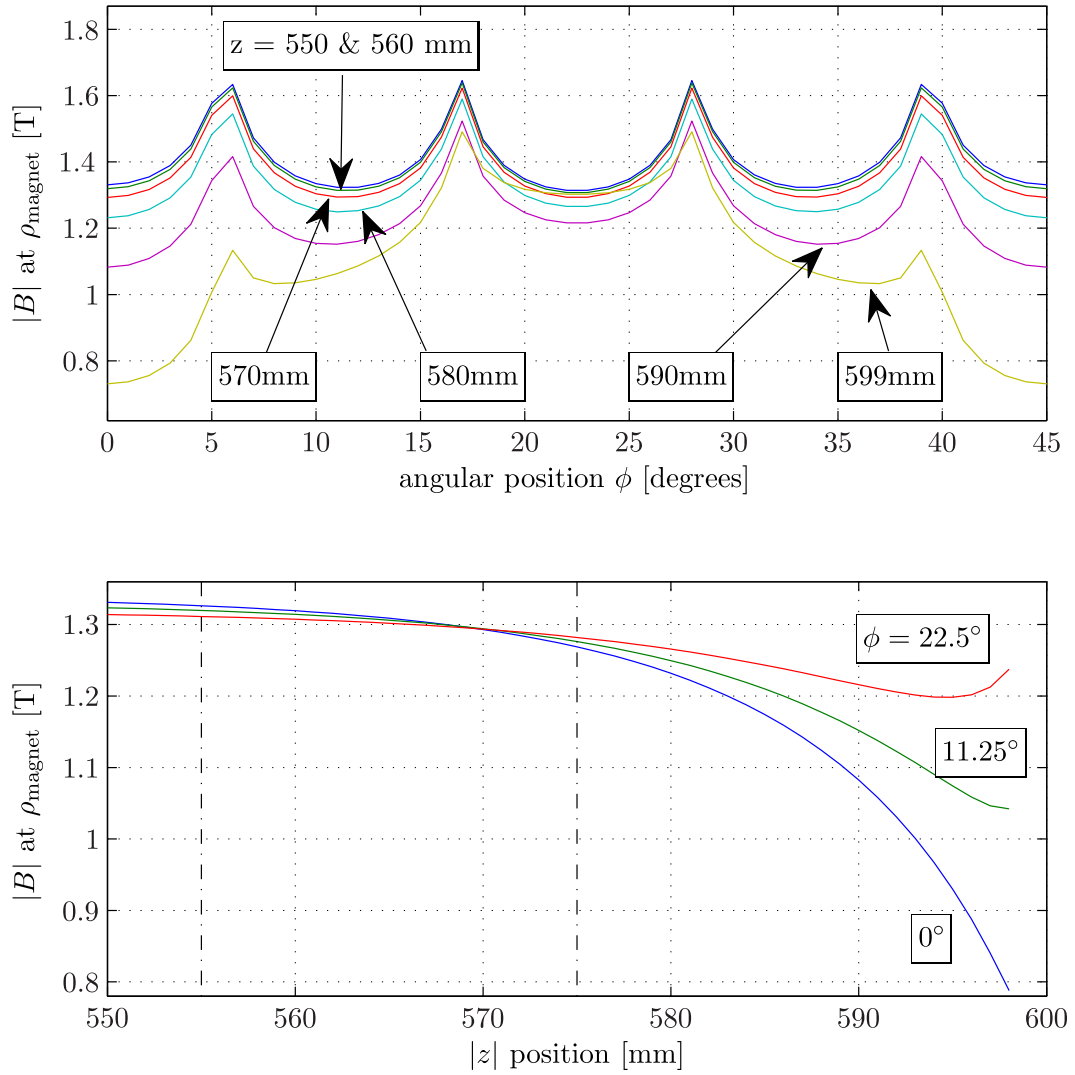
Figure 4.9: 3D calculations of the magnetic field at the ends of the 1.2 m octupole magnet array. *Top:* $|B|$ at the inner walls of the octupole array ρ_{magnet} for different continuous angular positions ϕ and different discrete longitudinal positions z. The end of the array is at $z = 600$ mm. *Bottom:* The change in $|B|$ at ρ_{magnet} for continuous z values and a few discrete ϕ values. The vertical black slashed-dotted lines $(-\cdot)$ show the central positions of the two end coils.
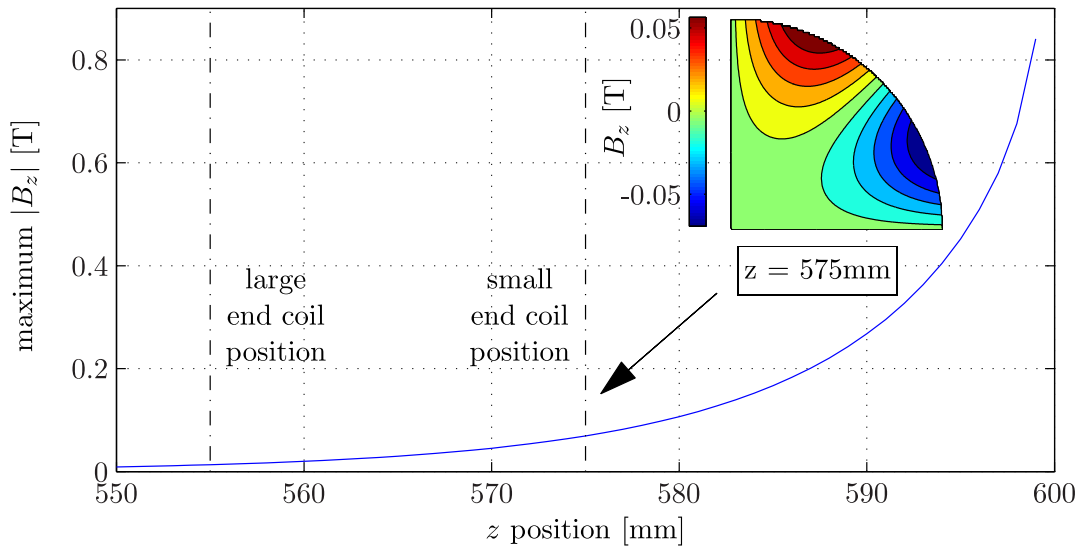
Figure 4.10: A plot of the maximum $|B_z|$ as a function of the axial position z. The strongest B_z fields occur around the off-pole pieces as shown in contour plot at $z = -575\,\text{mm}$. The vertical black slashed-dotted lines $(-\cdot)$ show the central positions of the two end coils.

a strong influence on the stored UCNs since the end coils are centered at $z = -575\,\text{mm}$ and $555\,\text{mm}$, and the maximum $|B_z|$ here is $\approx 0.07\,\text{T}$ only—much smaller than the end coil fields. However, near the edge of the octupole $z \approx 600\,\text{mm}$ the size of $|B_z|$ can be $> 0.8\,\text{T}$. This field will have an influence on the trajectories of the charged particles near the end of the array. If the charged particles are to be extracted completely out of the octupole array then a careful study of their interaction with the end fields of the array will need to be performed.

4.4.2   Combining $\vec{B}$ from superconducting coils and octupole array

An analysis is made by combining the magnetic field B from the superconducting coils and that from the octupole array with end effects included. This is done to ensure there is no strong cancellation resulting in regions of particularly low $|B|$ at the wall of the trap that defines the depth of the trap. This is shown in Fig. 4.11 for the $1.2\,\text{T} - 0.3\,\text{T} - 1.2\,\text{T}$ configuration. The minimum and maximum $|B|$ values at the walls of the magnet ρ_{magnet} and at $\rho_{\text{magnet}} - 2\,\text{mm}$ as
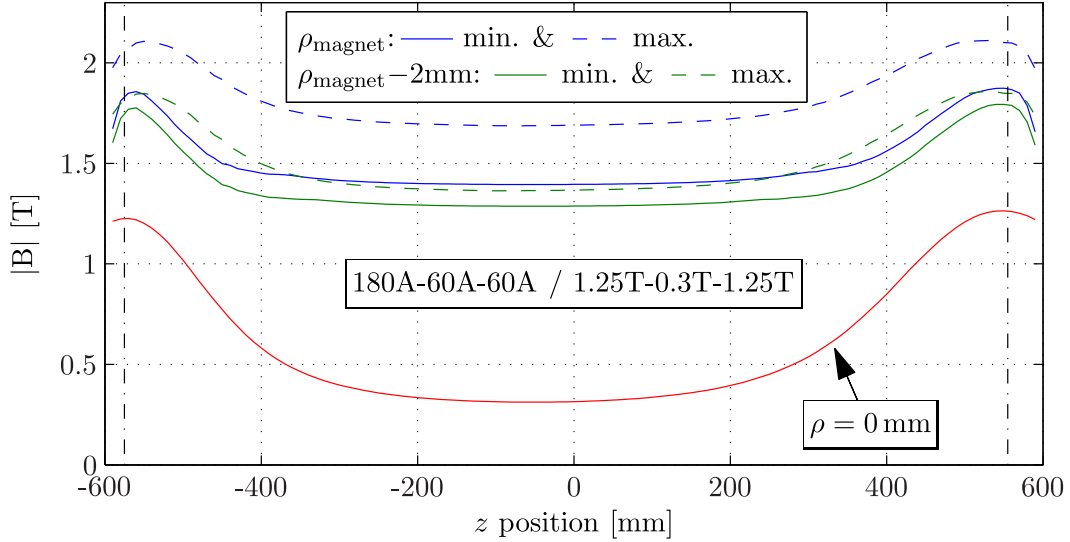
Figure 4.11: The magnetic field from the superconducting coils combined with the octupole array fields including the end effects for the $1.2\,\mathrm{T}-0.3\,\mathrm{T}-1.2\,\mathrm{T}$ configuration, which can be used for a horizontal trap setup. The center of the two end coils are indicated by the two black vertical slash-dotted lines $(-\cdot)$.

a function of z are also shown. The former determines the maximum trapping potential at the walls of the trap. The $|B|$ values at the central axis of the trap ($\rho = 0\,\mathrm{mm}$), which are due only to the superconducting coils, are also shown.

The line of minimum $|B|$ inside the trapping region close to the two end coils occurs at the pole pieces where cancellation of the B_ρ is largest, while the line of maximum $|B|$ occurs at the pole-pieces where B_ρ are reinforcing. For z values far from the coils, i.e. near the center of the bias coil, the line of minimum $|B|$ occurs at the off-pole pieces (see Fig. 4.4) since this is where $|B|$ at ρ_{magnet} is weakest. Outside the trapping region, near the ends of the octupole array, the minimum $|B|$ value drops off very rapidly due to cancellation with the strong B_z components. The separation between the lines of maximum and minimum $|B|$ are closer together around the end coils due to the stronger B_z component that is vectorially added to $(B_\rho^2 + B_\phi^2)^{1/2}$ from the octupole.

The cancellation of B_ρ does not determine the minimum $|B|$ at the walls of the trap. This is because the strongest radial component from the end coils (see Fig. 4.7) occurs at z-distances of $\approx 7\,\mathrm{cm}$ and $\approx 12\,\mathrm{cm}$ from the center of the small and large endcoils, respectively. The axial field strength B_z at these distances are still sufficiently strong to boost the total $|B|$ to above the $|B|$

value far from the end coil that comes from the octupole and bias fields only. For the $1.2\,\mathrm{T} - 0.3\,\mathrm{T} - 1.2\,\mathrm{T}$ horizontal configuration, the weakest value of $|B|$ at the walls of the trap occurs at $z = 0\,\mathrm{mm}$.

In order to determine the total potential energy, gravity has to be included as well (recall $V_{\mathrm{grav.}} = 102\,\mathrm{neV}\,\mathrm{m}^{-1}$ and $V_{\mathrm{mag.}} = \pm 60\,\mathrm{neV}\,\mathrm{T}^{-1}$). This is discussed in the next section.

Chapter 5

HOPE: Experimental concepts

This chapter will focus on the experimental concepts involved in performing a neutron lifetime experiment with a magnetic bottle. Emphasis will be given on how to control the systematics, especially the cleaning of the UCN spectrum. Possible designs for the experiment are also given.

5.1 Potential energy in the trap

The total energy E_n of a neutron at a point $\vec{r} = (x, y, z)$ in space is given by the sum of kinetic, gravitational and magnetic potential energies. Using the convention of Chapter 1:

$$E_n = E_{\mathrm{n}}(\vec{r}) + E_{\mathrm{pot}}(\vec{r}) = E_{\mathrm{n}}(\vec{r}) + V_{\mathrm{grav}}(\vec{r}) + V_{\mathrm{mag}}(\vec{r})$$
$$= E_{\mathrm{n}}(\vec{r}) + m_n\, g\, h \pm |\mu_n|\, |B(\vec{r})| \,. \quad (5.1)$$

In the last term: the plus sign ('+') refers to the *low field seeking* and the minus sign ('−') to the *high field seeking* state. The direction of h is equal to the longitudinal z-axis of the magnetic trap when it is used in a vertical configuration. When the use of V_{grav} ($102\,\mathrm{neV\,m^{-1}}$) for confinement is combined with V_{mag} ($60\,\mathrm{neV\,T^{-1}}$), this configuration is called a *magneto-gravitational* trap. In this thesis, the minimum E_{pot} inside the magnetic trap will set as $E_{\mathrm{pot}} = 0$, unless explicitly stated otherwise.

The potential energy E_{pot} of the trap with the octupole array vertically and the superconducting coils in the $1.7\,\mathrm{T} - 0.3\,\mathrm{T} - 0.3\,\mathrm{T}$ configuration is shown
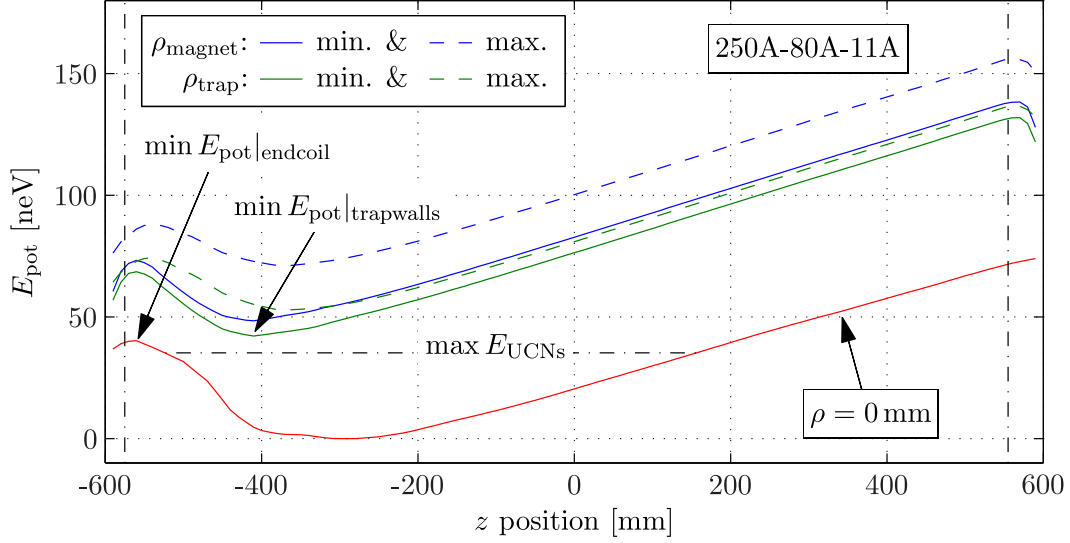
Figure 5.1: The potential energy E_{pot} as a function of the z-position for the low-field seeking UCNs in the vertical setup with the superconducting coils at $1.7\,\mathrm{T}$-$0.3\,\mathrm{T}$-$0.3\,\mathrm{T}$. The lines of minimum and maximum E_{pot} at ρ_{magnet} and at $\rho_{\mathrm{trap}} = \rho_{\mathrm{magnet}} - 2\,\mathrm{mm}$ are shown. The E_{pot} along the central z-axis ($\rho = 0\,\mathrm{mm}$) is also shown. The vertical black dash-dotted lines ($-\cdot$) show the center positions of the two end coils. The horizontal black dashed line ($--$) shows roughly where the well-trapped UCN spectrum should be cleaned to. For this configuration $\min E_{\mathrm{pot}}|_{\mathrm{endcoil}} = 40\,\mathrm{neV}$ (at $z = -560\,\mathrm{mm}$) and $\min E_{\mathrm{pot}}|_{\mathrm{trapwalls}} = 42\,\mathrm{neV}$ (at $z = -410\,\mathrm{mm}$), see text for explanation.

in Fig. 5.1. The minimum of E_{pot} in space forms a trap for the low-field seeking UCNs. The minimum E_{pot} in the trap occurs at $\rho = 0\,\mathrm{mm}$ and is at $z \approx -300\,\mathrm{mm}$. This is defined as the zero in potential energy in the plot. The shaded-contours of E_{pot} in both vertical and horizontal slices are shown in Fig. 5.2. From these plots, it is worth defining two important quantities that are used for discussions later: the minimum E_{pot} at the sidewalls of the trap, denoted by $\min E_{\mathrm{pot}}|_{\mathrm{trapwalls}}$; and the minimum E_{pot} at the endcoil, denoted by $\min E_{\mathrm{pot}}|_{\mathrm{endcoil}}$.

The effects of V_{grav} is much smaller for the horizontal setup since the diameter of the trap is small compared to the length. A shaded contour plot of E_{pot} for this setup is shown in Fig. 5.3. The effect of gravity causes the position of $\min E_{\mathrm{pot}}|_{\mathrm{endcoil}}$ to be shifted $22\,\mathrm{mm}$ lower from $\rho = 0$ and its value is $1.8\,\mathrm{neV}$ higher. The gain in E_{trap} by rotationally aligning the edge of a pole piece (where $|B|$ is strongest) to be the bottom edge of the trap is only $0.4\,\mathrm{neV}$.
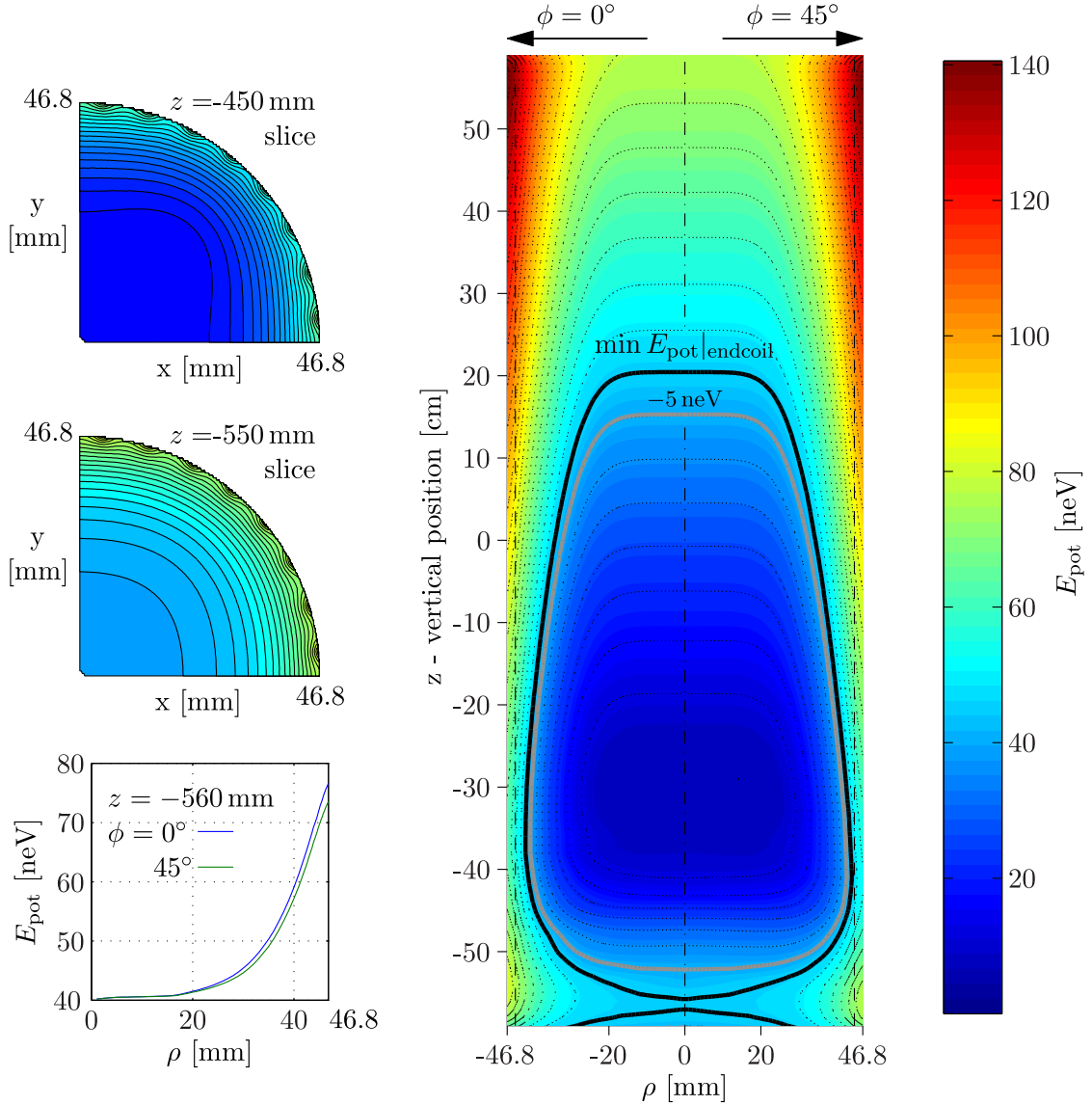
Figure 5.2: Shaded-contours of the potential energy E_{pot} for the vertical octupole array and the superconducting coils in the $1.7\,\mathrm{T} - 0.3\,\mathrm{T} - 0.3\,\mathrm{T}$ configuration (same as in Fig. 5.1). The thin dotted contours lines ($\cdots$) are spaced $5\,\mathrm{neV}$ apart. The plot on the *right* is a slice through a vertical plane with $\phi = 0°$ on the left-side and $\phi = 45°$ on the right-side. The difference between the two sides are caused by cancellation or reinforcement with B_ρ from the superconducting coils. Contour lines are shown for $E_{pot} = \min E_{pot}|_{endcoil} = 40\,\mathrm{neV} \equiv E_{trap}$, which defines the depth of the trap; and for $E_{trap} - 5\,\mathrm{neV}$, a suggested energy to clean the spectrum to. The two black vertical dashed lines ($--$) show the radius of $\rho_{trap} = \rho_{magnet} - 2\,\mathrm{mm}$. The top two plots on the *left* show shaded-contours plots for slices in the horizontal plane ($\phi = 0 \to 90°$) for different z positions to demonstrate the asymmetry in E_{pot} near the end coil. The bottom plot is of E_{pot} at the plane of the end coils.
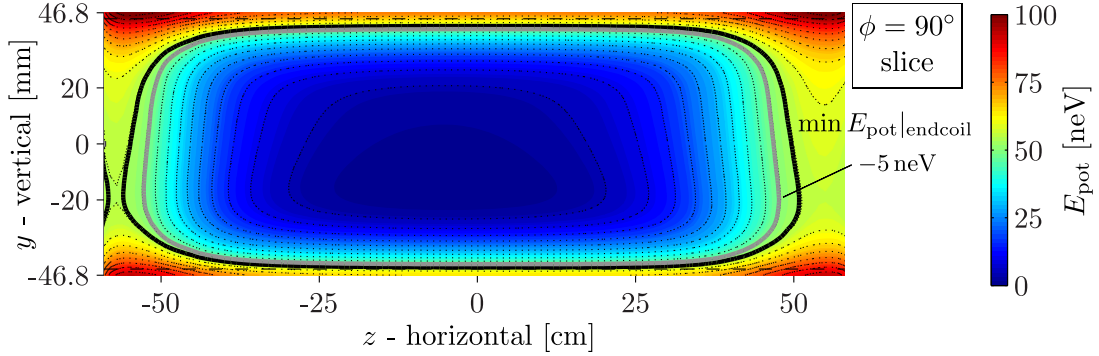
Figure 5.3: Shaded-contours of the potential energy E_pot for the horizontal octupole array and the superconducting coils in the 1.2 T- 0.3 T-1.2 T configuration (same as in Fig. 4.11). The thin dotted contours lines ($\cdots$) are spaced 5 neV apart. The asymmetry at the two end coils can be reduced with a more careful choice of the currents. This plot is not rotationally symmetric about the $\rho = 0$ axis due to gravity and cancellation and reinforcement of B_ρ between the magnets and superconducting coils. The plot is shown is a slice at the $\phi = 0°$ plane which is aligned with the vertical plane. For this horizontal setup $\min E_\mathrm{pot}|_\mathrm{endcoil} = E_\mathrm{trap} = 54\,\mathrm{neV}$. The horizontal dashed lines ($--$) at $\rho = \pm44.6\,\mathrm{mm}$ show the position of $\rho_\mathrm{trap} = \rho_\mathrm{magnet} - 2\,\mathrm{mm}$ (see text for explanation of the terms).

The material boundary of the trap will be chosen to be a good UCN reflector with a neutron optical potential greater than the potential from the magnetic field—for instance, stainless steel with $V_\mathrm{SS} \approx 180\,\mathrm{neV}$ placed at $\rho_\mathrm{trap} = \rho_\mathrm{magnet} - 2\,\mathrm{mm}$ is proposed as the material sidewalls of the trap. With this it will be possible to extract and detect depolarised or "warmed" UCNs (more is discussed in Sec. 5.7). To optimize the monitoring the depth of the trap should be defined by the endcoils, i.e. $E_\mathrm{trap} = \min E_\mathrm{pot}|_\mathrm{endcoil} < \min E_\mathrm{pot}|_\mathrm{trapwalls}$. If not UCNs with energy $\min E_\mathrm{pot}|_\mathrm{trapwalls} < E_n < \min E_\mathrm{pot}|_\mathrm{endcoil}$ will make many collisions with the material side walls of the trap without having the chance to escape and be detected.

UCNs with energy less than $\min E_\mathrm{pot}|_\mathrm{trapwalls}$ will not interact with any material. The maximum total energy of UCNs in the trap can be controlled by spectrum "cleaning". From Fig. 5.1 it can be seen that the volume UCNs can access increases with the UCN energy. Therefore, placing a UCN absorber at the surface of the desired volume will eliminate UCNs in the trap up to that energy. Alternatively, one can have a lower field at the end coil during
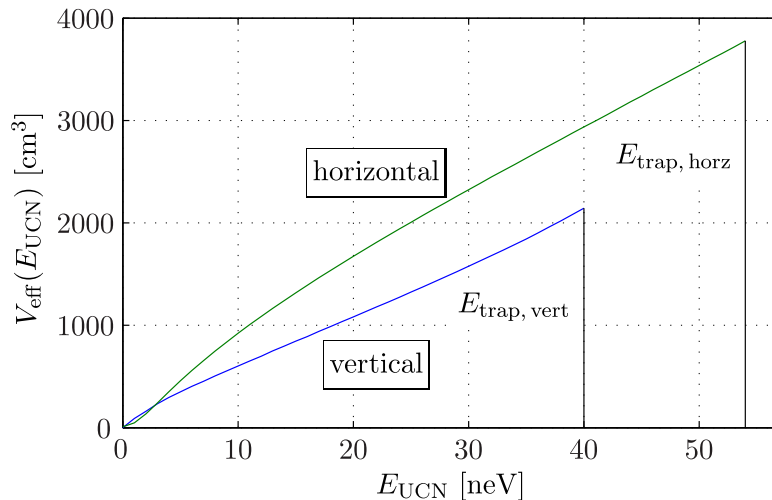
Figure 5.4: $V_{\mathrm{eff}}(E_n)$ from Eq. 5.2 for the horizontal and vertical trap setup. The E_{pot} values used are that shown in the shaded-contour plots of Fig. 5.2 and 5.3. The depth of the trap for the two setups are $E_{\mathrm{trap,horz}} = 54\,\mathrm{neV}$ and $E_{\mathrm{trap,vert}} = 40\,\mathrm{neV}$.

cleaning and then ramp this up slightly before storage. The effectiveness of different cleaning procedures is discuss in Sec. 5.4.

5.2 The effective volume

As mentioned in the previous section, and as can be seen in Fig. 5.1, UCNs with an increasing energy can occupy a greater volume of space. Because of this effect a quantity called the effective volume can be defined. Following the definition from Ref. [GRL91], UCNs with energy between E_n and $E_n + \mathrm{dE_n}$ will have an effective volume $V_{\mathrm{eff}}(E_n)$ is given by:

$$V_{\mathrm{eff}}(E_n) = \mathrm{Re}\left[\int_V \sqrt{\frac{E_n - E_{\mathrm{pot}}(\vec{r})}{E_n}}\,\mathrm{d}V\right], \qquad (5.2)$$

where $dV = \rho\,dz\,d\rho\,d\phi$. By taking the real component $\mathrm{Re}[...]$, only regions where $E_n > E_{\mathrm{pot}}$ contribute to the integral [1]. Plots of $V_{\mathrm{eff}}(E_n)$ for the vertical and horizontal trap are shown in Fig. 5.4.

---

[1] This is in essence the same as the changing integration bounds of Eq.(4.9) in Ref. [GRL91].

The average effective volume $\bar{V}_{\text{eff}}$ is the V_{eff} values averaged over the UCN spectrum. It is given by:

$$\overline{V}_{\text{eff}} = \int_{E_n=0}^{E_{\text{trap}}} \frac{dN}{dE_n} V_{\text{eff}}(E_n) dE_n \bigg/ \int_{E_n=0}^{E_{\text{trap}}} \frac{dN}{dE_n} dE_n \ , \qquad (5.3)$$

where dN/dE_n is the differential UCN energy spectrum in the trap. The form of dN/dE_n produced in the superfluid helium source is expected to be $\propto \sqrt{E_n}$. However, it is expected to change due to energy-dependent losses in the source and from transportation to the experiment. A measurement of the UCN spectrum from a superfluid helium source at $0.8\,\text{K}$ with vertical window-less extraction (in a system not too different from the SUN2 source) performed in Ref. [Mat08, Mat09] found that $dN/dE_n \propto E_n$ describes the extracted spectrum for $E_n < 60\,\text{neV}$. The measured results are also reproducible by Geant4 calculations.

The calculated average effective volumes $\overline{V}_{\text{eff}}$ in the vertical and horizontal setups are shown in Table. 5.1. This was done for both the $dN/dE_n \propto \sqrt{E_n}$ and $dN/dE_n \propto E_n$ spectra. There is only a small difference in the $\overline{V}_{\text{eff}}$ values between the two spectra. This shows that the exact knowledge of the spectrum is not crucial in these calculations. For the vertical trap, the calculations assume E_{pot} is ϕ symmetric, so that the variations of $|B|$ due to the reinforcement and cancellation of B_ρ near the walls of trap are neglected (to reduce computational time). For the horizontal trap, gravity breaks the approximate symmetry about ϕ and so the full calculation is performed. The spatial resolution used in the calculations are: $1\,\text{mm}$ for $\rho < 41\,\text{mm}$ (region of slowly changing $|B|$) and $0.2\,\text{mm}$ for $\rho > 41.2\,\text{mm}$; $1\,\text{cm}$ for z; and $1°$ for ϕ (used in the horizontal calculation only).

Table 5.1: The average effective volume $\overline{V}_{\text{eff}}$ calculated with Eq. 5.3 for the horizontal and vertical trap setup for two different UCN spectra.

	$dN/dE_n \propto \sqrt{E_n}$	$dN/dE_n \propto E_n$	E_{trap}
vertical $\overline{V}_{\text{eff}}$	$1,300\,\text{cm}^3$	$1,400\,\text{cm}^3$	$40\,\text{neV}$
horizontal $\overline{V}_{\text{eff}}$	$2,500\,\text{cm}^3$	$2,700\,\text{cm}^3$	$54\,\text{neV}$

The result from the calculation shows that the total number of UCNs ex-

pected to be confined with the trap in the horizontal setup compared to the vertical setup, given by $(\overline{V}_{\text{eff, horz}} E_{\text{trap, horz}})/(\overline{V}_{\text{eff, vert}} E_{\text{trap, vert}})$, is around 2.5× more. While this is significant, it is believed that the extra control of systematics offered by the vertical setup out-weighs the gain in statistics. This is discussed in detail throughout this chapter.

Estimating the actual number of UCNs expected to be stored in the trap is difficult. For an accumulate and empty source like SUN2, the expected number in the trap after the source is opened and an equilibrium density is reached is given by:

$$N_0 \approx \int_{m_n g h_{\text{trap}}}^{E_{\text{trap}}+m_n g h_{\text{trap}}} \rho_{0\,\text{source}}(E_n) V_{\text{source}}\, \mathrm{e}^{-T_{\text{empty}}/\tau_{\text{guides}}}$$

$$\times \frac{V_{\text{eff, trap}}(E_n - m_n g h_{\text{trap}})}{V_{\text{eff, trap}}(E_n - m_n g h_{\text{trap}}) + V_{\text{source}} + V_{\text{guides}}} dE_n \ , \quad (5.4)$$

where: h_{trap} is the height from the UCN source to the $E_{\text{pot}} = 0$ of the magnetic trap; $\rho_{0\,\text{source}}(E_n) dE_n$ is the density of UCNs in the source with energy between E_n and $E_n + dE_n$, i.e., the differential density of UCNs; V_{source} is the volume of the source; V_{guides} is the volume of the UCN guides connecting the source to the trap; T_{empty} is the time used for emptying the source; $\bar{\tau}_{\text{guides}}$ is the storage time of the guides averaged over the energy of UCNs in the guides taking into account the gravitational potential, with $\bar{\tau}_{\text{guides}} \ll \bar{\tau}_{\text{source}}$ and $\bar{\tau}_{\text{guides}} \ll \bar{\tau}_{\text{trap}}$ assumed. Depending on the values one takes, N_0 can range over 2 orders of magnitude. There are also losses at the guides during the ramping of the lower end coil and due to the heating the ramping. We expected $N_0 \approx 10^3 - 10^5$

5.3 Filling of the trap

Due to the conservation of energy, populating a UCN trap requires either reducing potential over a small region at the boundary of the trap for a short period of time, or it requires neutrons that have energies greater than the trapping potential to dissipate sufficient energy while they are inside the trapping region so that their total energy falls below E_{trap}.

The latter is performed in Ref. [Bro01, Huf00] where cold neutrons enter a 3D quadrupole Ioffe-Pritchard-type trap filled with superfluid helium. The CN then down-scatter to $E_n < E_{\text{trap}}$ via excitations in the superfluid and become

trapped. Such an experimental design integrates the UCN production inside of the magnetic trap since it reduces transportation losses. However, the existence of superfluid helium permeating the trap during the storage of UCNs for a neutron lifetime measurement requires very stringent control of UCN losses. This is because UCNs can be up-scattered by the excitations in the superfluid helium or be absorbed by ^{3}He contaminants. To sufficiently suppress these losses, reaching temperatures below $250\,\mathrm{mK}$ and limiting $R_{^3\mathrm{He}:^4\mathrm{He}} < 5 \times 10^{-13}$ are required.

The dissipation of the energy can also be performed by "*doppler reflections*"[2]. This was employed, for instance, in Ref. [Ezh05] where a "UCN elevator" is lowered from the top of a gravitational-magnetic trap. If the speed of lowering is slow compared to the UCN velocities, i.e., satisfying the adiabatic condition, then the kinetic energy the UCNs gain from the reduction in their gravitational potential energy can be lost from doppler reflections from the bottom receding surface of the elevator. Doppler heating reflections from the side walls are cancelled out by an equal rate of doppler cooling reflections (again, adiabatic condition). This idea is important in the current experiment since one of the proposed cleaning schemes—the insertion a reflecting piston from the bottom of a vertical trap—relies on this principle.

Another idea of causing a neutron dissipating energy in a trap so that it can be trapped, as discussed in Ref. [Zim00], is by inducing a spin-flip transition of a high-field seeker to a low-field seeker in a large magnetic field with r.f. radiation. However, such a technique has not yet been implemented for filling a magnetic trap.

5.3.1   Horizontal sliding trap extraction

An early idea for the HOPE project, proposed in Ref. [Zim05], was to integrate the UCN source and trap—similar to that done in Ref. [Huf00]—with the use of a superfluid helium converter inside an Ioffe-type magnetic trap. However, to avoid interactions of UCNs in the trap with the superfluid helium after filling, the converter was to be contained in a separate cylindrical volume with a UCN end window. For filling, the magnetic trap would be in a position so

---

[2]This is the term used for the increase or decrease in UCN velocity when it reflects of a preceding or receding material surface (in the lab frame).

that it surrounded the converter volume. The end window would be hidden from UCNs by being in the high field region of the back end coil. At the end of filling, the CN beam would be switched off and the magnetic trap would be slid back, away from the converter vessel. The magnetic wall from one of the end coils would then pull the UCNs along with the magnetic trap, squeezing them through the thin window so that they are extracted to vacuum. See Ref. [LZ09] for a schematic.

Losses of UCN are always expected to occur during passage through a thin-window—especially if the UCNs make repeated passages. A exploratory calculation was made to try to quantify the losses to see if the sliding thin foil technique could work. Some initial results from these calculations were published in Ref. [LZ09]. The calculations were developed further for this thesis. The details are given in Sec. B.2 of the Appendix. The conclusion is that with a $0.2\,\mathrm{mm}$ thick titanium foil and the trap sliding at $0.2\,\mathrm{m\,s^{-1}}$ around 25% of UCNs produced in the converter with energy $< 36\,\mathrm{neV}$ (due to the gain of $18\,\mathrm{neV}$ from leaving the superfluid helium) can be populated in the horizontal trap with $E_{\mathrm{trap}} = 54\,\mathrm{neV}$, under the approximations used for the calculations. Perhaps optimizing the sliding velocity (by having it vary) and having a thinner foil with a supporting grid can help improve this. However, in reality there are other losses not taken into account in the calculations. Given the mechanical requirements of moving a large cryogenic setup each time the trap needs to be filled—combined with the added complications of finding suitable solutions for the CN beam dump and shielding, scheme for extracting and detecting charged particles, and monitoring of depolarized UCNs—it was decided that for this extraction efficiency it was not worthwhile.

5.3.2   Ramping end coil for filling

Another way of filling a trap is to lower the potential barrier over a small region temporarily. This allows UCNs with energy less than the trapping potential E_{trap} (of the closed trap) to enter the trap for that period of time. This can be done by ramping of an end-coil.

There is a limit to how quickly one can ramp the current up and down of a superconducting coil. If the magnetic field changes rapidly large eddy currents will be induced in the non-superconducting material (copper cladding

and stainless steel coil supports) leading to a sufficient ohmic heating that can cause the superconducting coils to quench. We were told by the manufacturers of the coils that the limit of the ramp time would be restricted by the power supply only. It will be $\approx 10\,\mathrm{s}$ for a standard $15\,\mathrm{V}$ power supply.

For an accumulation-and-empty UCN source, such as the SUN2 superfluid helium source, UCNs are accumulated in the source for several hundreds of seconds. When it is time to fill the trap, the valve(s)[3] are opened. The UCNs will then leave the source until an equilibrium density is reached in the trap. When this is reached (or just before) the ramping of the end coil will begin. During both filling and ramping of the endcoil, UCNs with $E > \min E_{\mathrm{pot}}|_{\mathrm{endcoil}}(t)$ during the ramping are free to enter and leave the trap and thus they will experience a loss rate constant of $\tau_{\mathrm{tot}}^{-1} + \tau_{\mathrm{source}}^{-1} + \tau_{\mathrm{guides}}^{-1}$, where τ_{tot}^{-1} is the loss rate in the closed magnetic trap, i.e., $\approx \tau_{\beta}$. The storage time in the converter vessel τ_{source} should be on the order of $100\,\mathrm{s}$. The largest contribution to the losses during the filling is from the guides and gaps at the gate valves $\tau_{\mathrm{guides}}^{-1}$. For instance, storage times of only $\tau_{\mathrm{guides}} \approx 15\,\mathrm{s}$ are measured in $70\,\mathrm{mm}$ diameter electropolish stainless steel guides [GRL91] (for $\lesssim 180\,\mathrm{neV}$).

The bottle neck in the emptying time of the SUN2 source (and thus filling time of the trap) occurs at the small opening of the mechanical cold valve to the converter volume. This can not be made much bigger due to the radiative heating of the converter. From the preliminary experiments on the SUN2 source, the emptying time for a $60\,\mathrm{cm}$ long converter volume and $\approx 10\,\mathrm{mm}$ diameter opening was $\approx 12\,\mathrm{s}$ (for $\approx 10\text{--}230\,\mathrm{neV}$, due to the converter and vertical extraction potentials). However, for a longer converter volume, colder converter temperatures and lower UCN energy range of interest ($\approx 10\text{--}70\,\mathrm{neV}$ at the converter) this could be much longer. A possibility to reduce the emptying time of the source is to place some diffuse reflecting surfaces inside the converter volume (e.g. see the experiment of Ref. [Zim10]).

Implementation in the HOPE magnetic trap

A possible setup of how the trap can be filled by ramping up the small end coil is depicted schematically in Fig. 5.5. It is shown for a vertical configuration

---

[3]Additional UCN valves, beyond the cold flap valve in the superfluid converter, may exists for safety and separation of the vacua between the source and experiment.

but is equally applicable for a horizontal setup. In this case, instead of the gravitational gradient, the top end coil is required to be ramped up. This setup contains a side gate valve that can be connected to the UCN source (it can also be connected to a UCN detector, see Fig. 5.14). This side gate valve should be vacuum tight in order to separate the superfluid ^{4}He converter and the magnetic trap when it is closed. There is also a gate valve at the bottom used to give access into the magnetic trap when the small end coil is closed. This is closed during the filling phase. The distance between the valves and the trap should be as short as possible to reduce the volume that dilutes the UCN numbers

After filling of the trap the side valve should be closed. This stores the UCNs close to the trap and current wires wrapped around the guides produce a small magnetic field that can prevent them from depolarizing (not more than a few milli-Tesla is needed). The small end coil can then be ramped up. The final value of the magnetic field produced by the coil should be so that the minimum potential energy at the end coil min. $E_{\text{pot}}|_{\text{endcoils}} = E_{\text{trap}} < \text{min.}\, E_{\text{pot}}|_{\text{sidewalls}}$, i.e., the potential at the end coil defines the depth of the trap. This is so that above-threshold UCNs can escape from the bottom of the trap before touching the side walls.

One of the biggest disadvantages of filling the trap this way is the heating of the UCNs. Since the UCNs spend time around the increasing $|B|$ of the end coil, the low-field seekers will experience a gain in E_{mag} and thus their total energy E_n—measured relative to a point at $z = -30\,\text{cm}$, far from the end coil—will increase. This will cause otherwise well-trapped UCNs to become above threshold UCNs.

A calculation of the heating due to the ramping of a coil was done in Ref. [Fie05]. A vertical UCN guide with inner diameter of $\approx 7\,\text{cm}$ passes through the bore of an electromagnet, which closes the "trap" at the bottom. The field is ramped from $0 \to 1.5\,\text{T}$. Ramping times of $0.1\,\text{s}$, $1\,\text{s}$, and $3\,\text{s}$; and $E_n = 25\,\text{neV}$, $40\,\text{neV}$, and $70\,\text{neV}$ were simulated with a Monte-Carlo. Even the longest ramp down is shorter than our expected time, but even with the $3\,\text{s}$ the adiabatic condition was close to being reached so that the increase in energy were leveling-off. The relative gain in energy due to ramping is $\approx 20\%$ for $25\,\text{neV}$ and $\approx 10\%$ for $40\,\text{neV}$. The larger heating of slower UCNs is due to their smaller V_{eff} due to gravity so that they spend more time around the coil.
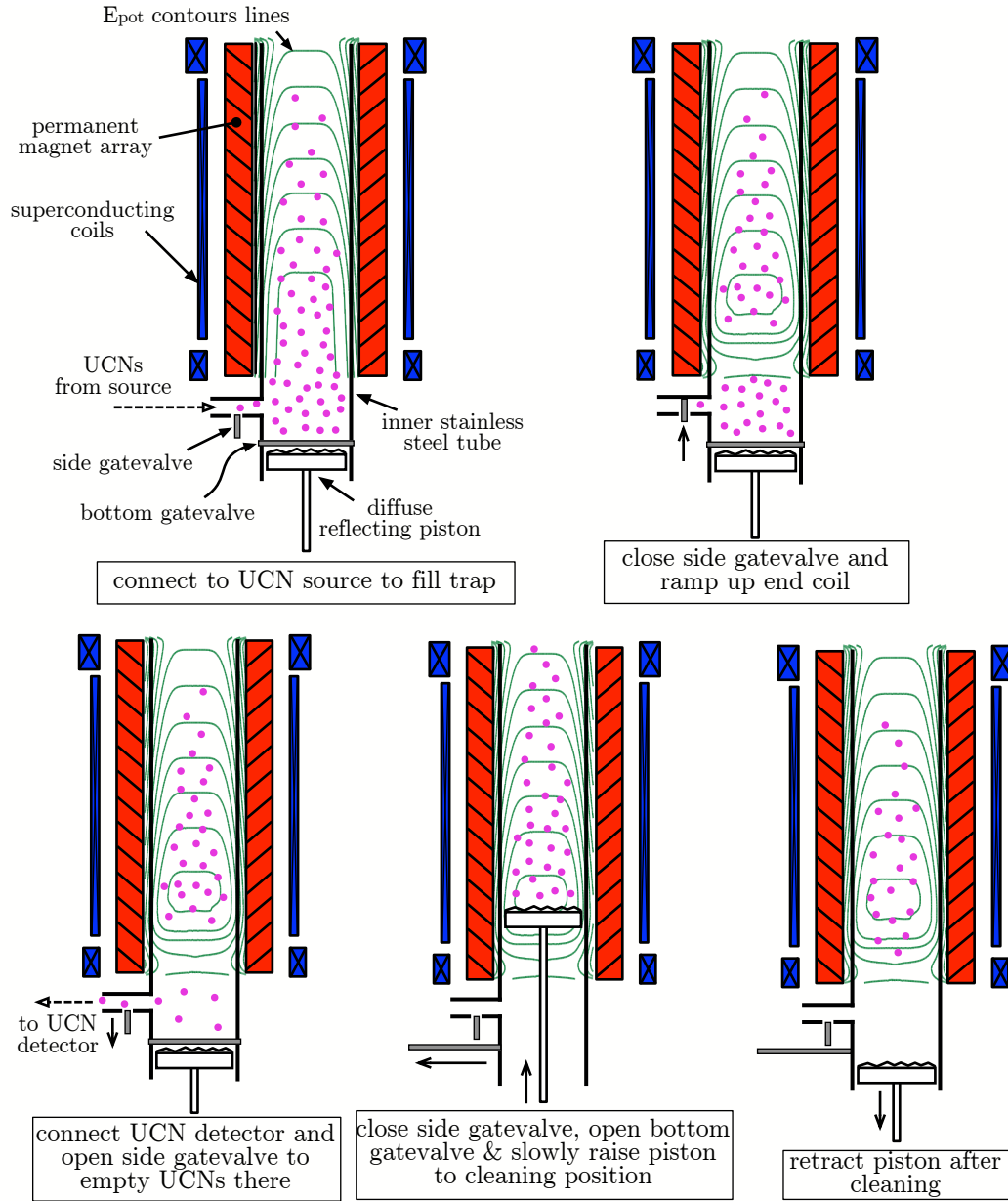
Figure 5.5: A proposed setup of filling the magnetic trap by ramping of the end coil and then using a diffuse reflecting piston for cleaning. Only the low-field seeking UCNs are shown. See text for more details of the operation. The other components that are used at the bottom and top of the trap are shown in Fig. 5.14. This diagram is not to scale.

The heating in our setup is expected to be even greater since since the end coil is ramped to $1.7\,\mathrm{T}$ and the diameter of the coil is much larger ($\approx 32\,\mathrm{cm}$ compared to $\approx 8\,\mathrm{cm}$) so that the field extends out further.

A technique is proposed in Sec. 5.5 where a UCN reflecting piston used for cleaning of the spectrum can also be used to reduce this heating. The piston is inserted before the end coil is ramped up to keep them away from the increasing $|B|$.

5.4   UCN spectrum cleaning

The UCNs delivered to the trap will have a population of UCNs with energy $E_n > E_{\mathrm{trap}}$. These "*above-threshold*" UCNs can take a long time before escaping the trap if either the UCNs do not efficiently explore the trap or the region defining the lowest trapping potential E_{trap} is small. If they have survival times comparable to τ_β, they will be hard to distinguish from the well-trapped UCNs and will cause a systematic shift in the observed τ_{tot}, and thus the extracted τ_β. An effective cleaning technique needs to ensure that all above-threshold UCNs explore the trap on a short time-scale so that they are removed from the trap.

An additional effect requiring consideration is the removal of high-field seeking UCNs that become trapped at the bottom end coil after the field there is ramped up. For instance, these were observed in Ref. [Dau11]. These also need to be removed in a cleaning procedure. This requires some reflective or absorbing material, i.e., a piston or a ring, to pass through the plane of the ramped-up end coil.

How marginally trapped orbits exist in a UCN trap and various techniques of removing them are first described in this section. Then, the effective removal area $A_{\mathrm{rem\,eff}}$ of a UCN remover is defined. This allows the effectiveness of using a material UCN absorber of different shapes or ramping down of the small end coil to be compared quantitatively. Finally, several ideas for cleaning procedures are proposed. Their advantageous, disadvantageous, and how they can be implemented will be discussed.

5.4.1   Motion in the transverse plane

Marginally trapped UCNs are a serious problem for neutron lifetime experiments in traps with high symmetry; such as for Ioffe-Pritchard type traps or other traps with a high degree of symmetry. This is due to a lack of mixing between the "momentum modes" that are possible: p_ρ, p_ϕ and p_z[4]. To illustrate this point, considering only the motion in the $\rho\phi$ plane for a cylindrical trap with an "ideal" multipole radial field far from the end coil(s). The force from the magnetic field gradient $\vec{F}(\vec{r}) = -|\mu_n|\nabla|\vec{B}(\vec{r})|$ is directed towards the central axis of the trap only. A constant of the motion is the angular momentum $p_\phi \equiv L$ given by:

$$L = m_n \rho^2 \dot{\phi} = m_n \rho\, v_\phi \,. \tag{5.5}$$

Occasionally, the linear angular velocity $v_\phi = \rho\dot{\phi}$ will be used as well. Another constant of motion is the total transverse energy (energy of the motion in the $\rho\phi$ plane):

$$E_{n,\,\rho\phi} = \frac{m_n}{2}\left(\dot{\rho}^2 + \frac{L^2}{m_n^2\rho^2}\right) + |\mu_n|.|B| = \frac{m_n}{2}(v_\rho^2 + v_\phi^2) + |\mu_n||B| \,. \tag{5.6}$$

The two equations of motions [5] are:

$$\ddot{\rho}(t) = -\frac{\mu_n}{m_n}\frac{\partial B}{\partial \rho} + \frac{L^2}{m_n^2\rho^3} \Rightarrow \dot{\rho}(t) = \pm\sqrt{\frac{2}{m_n}\left(E_{n,\,\rho\phi} - |\mu_n||B(\rho)|\right) - \frac{L^2}{m_n^2\rho^2}} \tag{5.7a}$$

$$\ddot{\phi}(t) = 0 \Rightarrow \dot{\phi}(t) = \frac{v_\phi}{\rho} = \frac{L}{m_n\rho^2} \,. \tag{5.7b}$$

On the right-hand side of Eq. 5.7a, the two solutions of $\dot{\rho} = 0$ give the two turning points of the motion at $\rho_{\min}$ and $\rho_{\max}$. When the angular momentum takes on its maximum value of $L_{\max} = \sqrt{2m_n\rho_{L_{\max}}^2\left(E_{n,\,\rho\phi} - |\mu_n||B|\right)}$ for a given $E_{n,\rho\phi}$, the two roots coincide $\rho_{\min} = \rho_{\max} \equiv \rho_{L_{\max}}$, and the trajectory is that of a circle. The $\rho_{\max}$ value for a given $E_{n,\,\rho\phi}$ occurs when $L = 0$, linear motion passing through the center of the trap. It is only for this case does the energy convert fully to potential energy $E_{n,\,\rho\phi} = |\mu_n||B(\rho_{\max})|$.

---

[4]The definition of these are: $p_\rho = |\vec{p}\cdot\hat{\boldsymbol{\rho}}|$, $p_\phi = |\vec{p}\cdot\hat{\boldsymbol{\phi}}|$ and $p_z = |\vec{p}\cdot\hat{\boldsymbol{z}}|$, where $\vec{p}$ is the momentum vector and the second vector of each equation are the unit vectors of the cylindrical coordinate system.

[5]The treatment of the classical central force problem are found in most textbooks. The ones used in this work were Ref. [GPS00, TM04].
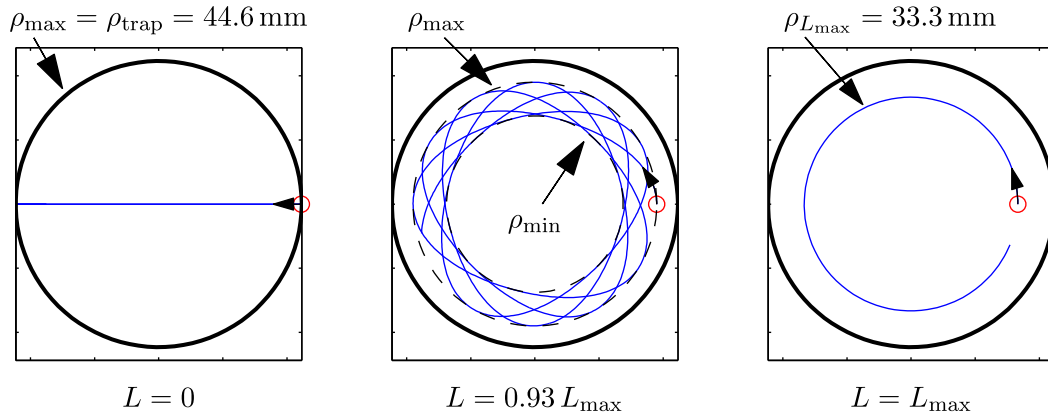
Figure 5.6: The trajectories in the $\rho\phi$-plane for UCNs with $E_{n,\rho\phi} - |\mu_n|B_{\text{bias}} = 56\,\text{neV}$ in a radial field of $B(\rho) = \sqrt{(\beta\rho^3)^2 + B_{\text{bias}}^2}$ (octupole with bias field) at three different angular momentum values L.

Unfortunately, an analytic solution for $\rho(t)$ of Eq. 5.7a exists only for $|B(\rho)| \propto \rho$ (quadrupole) and $|B(\rho)| \propto \rho^2$ (sextupole)—but not for $|B(\rho)| \propto \rho^3$, the octupole radial field [GPS00]. In order to determine the motion of a UCN the equations of motion needs to be solved numerically. A field of $|B(\rho)| = \sqrt{(\beta\rho^3)^2 + B_{\text{bias}}^2}$ with $\beta = 13,530\,\text{T m}^{-3}$, corresponding to $1.2\,\text{T}$ at the $\rho_{\text{trap}} = 44.6\,\text{mm}$ ($2\,\text{mm}$ from the magnet walls), and an axial bias field $B_{\text{bias}} = 0.3\,\text{T}$ was used. A plot of the trajectories for $E_{n,\rho\phi} - |\mu_n|B_{\text{bias}} = 56\,\text{neV}$, the energy relative to the minimum field region, for three different values of L are shown in Fig. 5.6. For the $L = 0$ trajectory, this energy corresponds to ρ_{max} just reaching ρ_{trap}, i.e., this is the maximum energy for which no wall collisions are guaranteed to occur (a well-trapped UCN). At this energy for the maximum angular moment $L = L_{\text{max}}$ the circular orbit trajectory has $\rho_{L_{\text{max}}} = 33.3\,\text{mm}$.

A plot of $\rho_{L_{\text{max}}}$ as a function of other $E_{n,\rho\phi} - \mu_n B_{\text{bias}}$ is given in Fig. 5.9. A UCN with $E_{n,\rho\phi} > \min E_{\text{pot}}|_{\text{trapwalls}} = |\mu_n|B(\rho_{\text{walls}})$ can have $\rho_{L_{\text{max}}} < \rho_{\text{trap}}$ and thus never make collisions with the side walls. From the calculations, it was found that with the previous field configuration this is possible for $E_{n,\rho\phi} - |\mu_n|B_{\text{bias}}$ up to $162\,\text{neV}$.

5.4.2 Existence of marginally trapped UCNs

First consider the octupole array in a horizontal configuration where no UCN remover is placed in the trap. The velocity along the z-axis v_z when far from

the endcoils is constant. If v_z is small then it will take a long time for the UCN to reach the ends of the trap. A reflection from the fields near end coil, due its structure (see Fig. 5.2), can cause "mode-mixing"—where a UCN is caused to take on different $E_{n,z}$ and $E_{n,\rho\phi}$ values[6]. This is how marginally trapped UCNs can exist: a UCN with $E_{n,\rho\phi} > E_{\text{trap}}$ and small v_z—hence large L—will be stable in this trajectory since near the center of the trap. However, it will eventually reach the ends of the trap where it can potentially make a mode-mixing reflection. When this occurs, it can start colliding with the sidewalls or escape the trap, thus become lost. These trajectories are called "*quasi-stable*". Of course, after a reflection from the end coils, there is also a probability of it being in another quasi-stable trajectory that would further prolong the existence of the above-threshold neutron in the trap.

It should be noted that even if L for a UCN with $E_{n,\rho\phi} > E_{\text{trap}}$ is not large enough for it to avoid sidewall collisions completely, it will make only glancing reflections with the side walls, and, if only specular reflections occur here, they will continue to exist for long times also. Therefore, having reflective side walls that only produce specular reflections will cause marginally trapped UCNs whenever $E_{n,\rho\phi}$ is large, and not just when L is large. This is an analogous criticism for material traps with high symmetry and smooth walls, i.e. made from liquids or oils.

The size of the effect on the measured storage time requires knowledge of the population and survival times of the marginally trapped UCNs. In order to treat the problem fully, a Monte-Carlo simulation tracking the UCN trajectories in the magnetic and gravitational potentials and their reflections off the neutron optical potentials of the side walls are required. This turns outs to be a difficult task for traps with high symmetry [Yan06].

A typical treatment of UCNs is to consider them to be isotropic. But this requires the UCNs to make frequent mode-mixing reflections so that their momenta become isotropic. If quasi-stable trajectories exist in a trap then, by definition, UCNs will stay in such trajectories for long times without making mode-mixing reflections. Indeed, one expects an accumulation of these trajectories due to their long survival times. Therefore, the isotropic UCN

---

[6]Note that a diffuse reflection, where the probability of the final angle relative to the normal of the surface θ_f is given by $P(\theta_f, \phi) \, d\Omega = \cos\theta_f \, d\Omega$ (Lambert's cosine law), is not the only type of reflection that can cause mode-mixing.

approximation is not valid if quasi-stable trajectories exist.

A demonstration of the problem of marginally-trapped UCNs was demonstrated in the Huffman trap. With no ramping of the end coils or quadrupole coils for cleaning, the existence of above-threshold UCNs shifted the observed storage time to a value of only $\tau = 621^{+18}_{-17}\,\mathrm{s}$ (with the fit starting only $200\,\mathrm{s}$ after the end of filling) [Dzh05].

In order to perform effective cleaning, above-threshold UCNs should make frequent mode-mixing reflections so they explore the trap efficiently. This can be done by eliminating all marginally trapped trajectories in the trap or their survival times should be made as short as possible. The techniques for doing this, caused "chaotic cleaning", are described later on in the section. But first, a parameter called the effective area of removal $A_{\mathrm{rem,\,eff}}$ will be defined. After above-threshold UCNs explore the trap efficiently, they still need to be removed from the trap since the sidewalls of the trap will have a high V_{opt}. The quantity $A_{\mathrm{rem,\,eff}}$ determines the effectiveness of a remover. While it is only valid for an isotropic UCN gas, it is still useful for comparing between different schemes. An isotropic calculation can then compared with a Monte-Carlo simulation of the trajectories to verify the validity the former approximation.

5.4.3 The effective removal area $A_{\mathrm{rem,\,eff}}$

It is desirable to have at the end coils $\min E_{\mathrm{pot}}|_{\mathrm{endcoil}} < \min E_{\mathrm{pot}}|_{\mathrm{walls}}$ so "warmed" UCNs can escape the trap. It is only the region near center of the end coil that defines E_{trap}. In order to use the end coil for UCNs to escape the trap during cleaning, it needs to be ramped down temporarily to allow the region for UCNs to escape to increase. However, this causes a loss of well-trapped UCNs as well. The same argument can be made for a flat horizontal absorber. Due to the radial field, only the region near the central $\rho = 0$ defines the energy before a UCN can start making contact. With a material absorber its shape can be chosen so that it is adapted to the E_{pot} contour surfaces of Fig. 5.2. For instance, a ring shaped absorber like that shown in Fig. 5.14 offers a very large surface area for cleaning at a specific energy.

In order to quantify the discussion on the effectiveness of a removal technique, it is useful to define a parameter called the effective removal area $A_{\mathrm{rem,\,eff}}$. This parameter is related to a real physical area but, like the effective volume
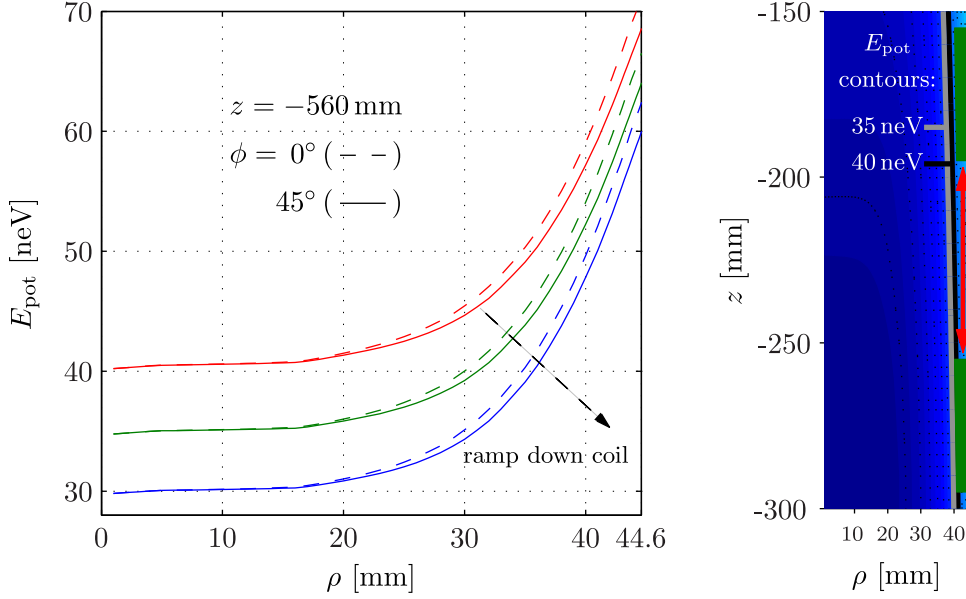
Figure 5.7: *Left*: The change in $E_{\rm pot}$ at the plane of the bottom endcoil in the vertical setup when it is ramped down; calculated by combining the 3D Radia calculations of the octupole and the 2D FEMM calculations of the superconducting solenoids. The profiles at $\phi = 0°$ and $45°$ are shown for three different end coil currents that produce $\min E_{\rm pot}|_{\rm endcoil} = 40\,{\rm neV}$, $35\,{\rm neV}$ and $30\,{\rm neV}$.*Right*: Zoomed-in of the $E_{\rm pot}$ contour plot in Fig. 5.2 around the position where a ring-shaped absorber can be inserted from the top. The z and ρ axis are set to the same scale. The ring-shaped absorber (green block) with a height of $4\,{\rm cm}$ and moved up by $10\,{\rm cm}$ is shown.

$V_{\rm eff}$ of Eq. 5.2, is reduced due to the compression of phase space from $E_{\rm pot}$ gradients in the trap. So it depends on the UCN energy E_n and the $E_{\rm pot}$ distribution in the trap. The definition of $A_{\rm rem, eff}$, based on the equations in Ref.[GRL91], is given by:

$$A_{\rm rem, eff}(E_n) = {\rm Re}\left[\int_{S_{\rm rem}} \sqrt{\frac{E_n'}{E_n}}\, \bar{\mu}(E_n') dS_{\rm rem} \right] ; \qquad (5.8)$$

where $E_n' = E_n - E_{\rm pot}(dS_{\rm rem})$ is the kinetic energy of the UCNs at $dS_{\rm rem}$ due to the change in $E_{\rm pot}$. The integration is over the surface of the remover $S_{\rm rem}$ (absorbing material or the plane of the end coil); and $\bar{\mu}$ is the average absorption (or escape) probability for isotropic UCNs. Taking the real component ${\rm Re}[...]$, only regions where the UCNs can reach contribute to the sum,
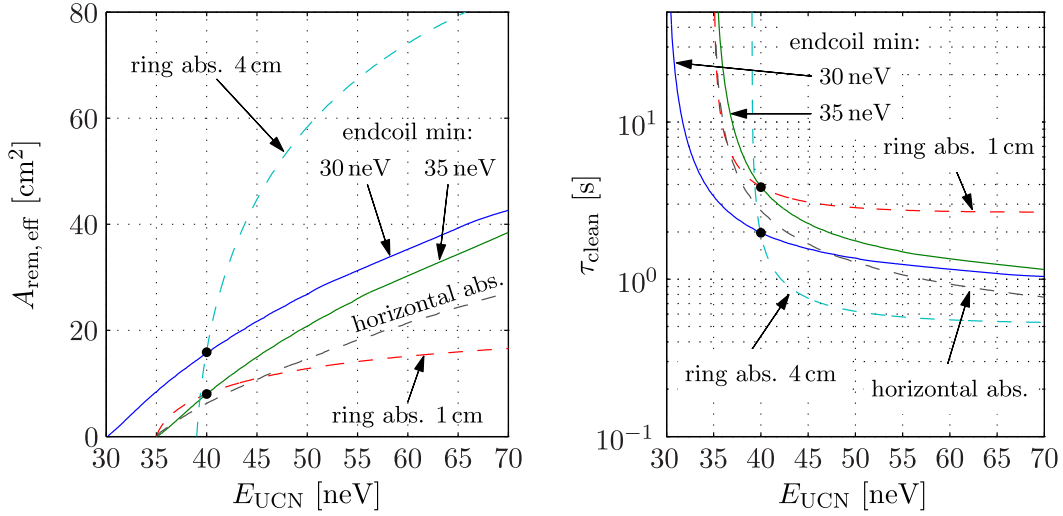
Figure 5.8: The effective remover area $A_{\mathrm{rem,eff}}$ and cleaning time τ_{clean} calculated from Eq. 5.8 and 5.9 for: the bottom end coil ramped down to $\min E_{\mathrm{pot}}|_{\mathrm{endcoil}} = 35\,\mathrm{neV}$ (–) and $30\,\mathrm{neV}$ (–), ring-shaped absorbers with an inner radius $\approx 40\,\mathrm{mm}$ and a height of $1\,\mathrm{cm}$ at an equipotential surface with $E_{\mathrm{pot}} = 35\,\mathrm{neV}$ (--) and a height of $4\,\mathrm{cm}$ at $E_{\mathrm{pot}} = 39\,\mathrm{neV}$, and a flat horizontal absorber at $35\,\mathrm{neV}$ (--). The black points ($\bullet$) shown where two sets of the curves intersect at $E_{\mathrm{trap}} = 40\,\mathrm{neV}$ where the cleaning time is most important.

i.e., when $E_n' > 0$. Expressions for $\bar{\mu}$ are given in Ref.[GRL91] for the weak absorber approximation, or more recently in Ref.[Bro12] for other cases.

The cleaning time τ_{clean}—mean time taken for a UCN with energy E_n to be removed—if an perfectly isotropic UCN gas is assumed is then given by (also following Ref. [GRL91]):

$$\tau_{\mathrm{clean}}(E_n) = \frac{4\sqrt{m_n}\,V_{\mathrm{eff}}(E_n)}{\sqrt{2E_n}\,A_{\mathrm{rem,eff}}(E_n)} \ . \tag{5.9}$$

Calculations of $A_{\mathrm{rem,eff}}(E_n)$ and $\tau_{\mathrm{clean}}(E_n)$ for ramping down the bottom end coil [7] in the vertical setup (shown in Fig. 5.7) for $\min E_{\mathrm{pot}}|_{\mathrm{endcoil}} = 30\,\mathrm{neV}$ and $35\,\mathrm{neV}$ are shown in Fig. 5.8. As can be seen, $\tau_{\mathrm{clean}}(E_n) \to \infty$ since $A_{\mathrm{rem,eff}} \to 0$, as expected. This is the reason why the coil must be ramped up after the cleaning procedure. The most important value of the cleaning time is at $E_{\mathrm{trap}} = 40\,\mathrm{neV}$. When the endcoil is ramped to $\min E_{\mathrm{pot}}|_{\mathrm{endcoil}} = 30\,\mathrm{neV}$,

---

[7] $\bar{\mu} = 1$ is used in the calculations.

$A_{\mathrm{rem,\,eff}}$ is two times larger than when $\min E_{\mathrm{pot}}|_{\mathrm{endcoil}} = 35\,\mathrm{neV}$ (hence τ_{clean} is two times shorter). However, the former results in only ≈ 0.75 times the number of well-trapped UCNs remaining, if assuming all UCNs up to $\min E_{\mathrm{pot}}|_{\mathrm{endcoil}}$ are lost during cleaning.

For comparison, the $A_{\mathrm{rem,\,eff}}(E_n)$ and $\tau_{\mathrm{clean}}(E_n)$ values of two ring-shaped polyethylene absorber designs are also shown on Fig. 5.8. One has a height of $1\,\mathrm{cm}$ placed so that its inner surface is on an equipotential surface with $E_{\mathrm{pot}} = 35\,\mathrm{neV}$; the other a height of $4\,\mathrm{cm}$ on an equipotential surface with $E_{\mathrm{pot}} = 39\,\mathrm{neV}$. Both have an inner radius of $\approx 40\,\mathrm{mm}$ and a thickness of around $5\,\mathrm{mm}$ (to minimise loss of β-electrons if they are to be counted). The standard flat horizontal absorber placed at a height so that the center is at $35\,\mathrm{neV}$ is also shown.

The $1\,\mathrm{cm}$ ring absorber is shown since it matches the end coil $\min E_{\mathrm{pot}}|_{\mathrm{endcoil}} = 35\,\mathrm{neV}$ cleaning time at $E_n = 40\,\mathrm{neV}$. However, such a small absorber does not take advantage of the fact that a material absorber can be very large. To demonstrate how effective a larger absorber can be, calculations are shown for the $4\,\mathrm{cm}$ high absorber ring at $E_{\mathrm{pot}} = 39\,\mathrm{neV}$. Such a design offers the same $A_{\mathrm{rem,eff}}$ at $E_n = 40\,\mathrm{neV}$ as the end coil ramped down to $\min E_{\mathrm{pot}}|_{\mathrm{endcoil}} = 30\,\mathrm{neV}$; and extra losses in the latter is only ≈ 0.6 times the number of well-trapped UCNs than the former.

A $4\,\mathrm{cm}$ high and $5\,\mathrm{mm}$ thick absorber inserted from the top needs to be inserted to around $z = -300\,\mathrm{mm}$ and would need to be raised by $\approx 10\,\mathrm{cm}$ so that the absorber's surface ends up $> 1\,\mathrm{mm}$ from the subsequent UCNs (see Fig. 5.7)

One of the challenges of using a thin ring absorber like this is the reproducibility of the its position after movement with different filling. This is especially important if a fill-and-empty procedure is used for extracting τ_β. It is worthwhile reiterating that $A_{\mathrm{rem,eff}}$ and τ_{clean} above is only valid if the UCNs are isotropic. Also, the heating of the UCNs when the end coil is ramped up after being at a lower $\min E_{\mathrm{pot}}|_{\mathrm{endcoil}}$ for cleaning has not been discussed.

5.4.4 Ramping of bias field for cleaning

The cleaning technique used in the Huffman quadrupole Ioffe-Pritchard trap was to ramp down the quadrupole field $|B(\rho)| = \beta\rho$. For a quadrupole trap

$\rho_{\max}\beta^{1/3}$ is a constant, so decreasing β causes $\rho_{\max}$ to increase. It was found that if the field is ramped to $\beta_f/\beta_i = 0.296$, then even the trajectories with $L_{\max}$ for all $E_n > E_{\text{trap}}$ would collide with the absorptive sidewalls. However, this causes a loss of around 50% of well-trapped UCNs as well [Yan06].

In the HOPE trap it is not possible to ramp the radial field due to the permanent magnets. However, the bias field coil can be increased to $1.2\,\text{T}$ so that the depth of the trap can be decreased, since $|B(\rho)| = \sqrt{(\beta\rho^3)^2 + B_{\text{bias}}^2}$. From Eq. 5.7a, $E_{n,\rho\phi}(\rho_{L_{\max}})$ can be derived to be:

$$E_{n,\rho\phi}(\rho_{L_{\max}}) = \frac{\mu_n}{2} \frac{5(\beta\rho_{L_{\max}}^3)^2 + 2B_{\text{bias}}^2}{\sqrt{(\beta\rho_{L_{\max}}^3)^2 + B_{\text{bias}}^2}} \ . \tag{5.10}$$

A plot of this for different B_{bias} values is shown in Fig. 5.9. It can be seen that ramping the bias coil to $2.8\,\text{T}$—beyond the strongest $1.2\,\text{T}$ of the coil specification—is required to increase $\rho_{L_{\max}}$ to ρ_{trap}. This is the best case scenario. It assumes that the energy gained by the UCN from the ramped field is the maximum possible $|\mu_n|\Delta B_{\text{bias}}$. This does not occur since $\rho_{L_{\max}} = 33.3\,\text{mm}$ in the original $B_{\text{bias}} = 0.3\,\text{T}$ field and the increase at this ρ is $< \Delta B_{\text{bias}}$. Therefore, UCNs gain energy less than $\mu_n\Delta B_{\text{bias}}$ and so will have smaller $\rho_{L_{\max}}$.

Since the UCN storage volume of the Huffman experiment is filled with $300\,\text{mK}$ superfluid helium, material reflectors/absorbers could not be inserted for a cleaning procedure due to the heat input. However, with the UCNs extracted to vacuum and with free access from below and above the trap in the vertical setup, various schemes for this is possible.

5.4.5 Using a specular reflecting paddle

Instead of increasing $\rho_{\max}$ in the trap, one can restrict the maximum $\rho_{\max}$ that can exist in the trap with a reflecting material paddle [BP05]. From Fig. 5.6 and 5.9 it can be seen that a UCN with energy equal to $\min E_{\text{pot}}|_{\text{trapwalls}}$ has a minimum $\rho_{\max} = \rho_{L_{\max}} = 33.3\,\text{mm}$. Therefore, if a reflecting paddle is inserted into the trap extending to $\rho = 33.3\,\text{mm}$, then UCNs with $E_{n,\rho\phi} > \min E_{\text{pot}}|_{\text{trapwalls}} = 56\,\text{neV}$ for all values of L will reflect off it and have its $E_{n,\rho}$ and $E_{n,\phi}$ modes of motion mixed. Of course, UCNs in trajectories with large $E_{n,\rho}$ but small $E_{n,\phi}$ might take a long time to find the paddle since they rotate slowly. To increase the exposure of the paddle, it can be placed on an angle
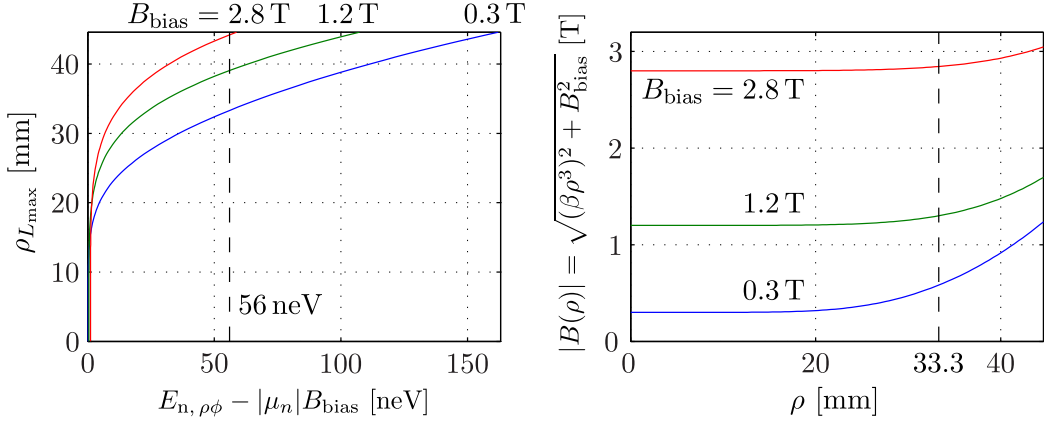
Figure 5.9: *Left:* The radius of the circular trajectory at maximum angular momentum $\rho_{L_{max}}$ as a function of $E_{n,\rho\phi} - |\mu_n|B_{bias}$, the UCN energy above the minimum energy in the trap, given by Eq. 5.10. The different B_{bias} values are the standard value used $(0.3\,\text{T})$, the maximum of the bias coil $(1.2\,\text{T})$, and the minimum value required for field ramp cleaning $(2.8\,\text{T})$. *Right:* The radial field profile $|B(\rho)|$ for the octupole with $1.2\,\text{T}$ at $\rho = 44.6\,\text{mm}$ combined with the three B_{bias} values. This shows how E_{trap} decreases. Both vertical dashed line $(--)$ shows $E_{trap} = 56\,\text{neV}$ when $B_{bias} = 0.3\,\text{T}$.

relative to $\hat{\boldsymbol{\rho}}$ so that it covers a range of ϕ values (See Ref. 5.10).

In the experiments using an incremental version of the trap with only the octupole array (see Chapter 6), it was shown having a low loss material in the trap (fomblin grease was used) did not decrease the storage time by too much. Therefore, the temporary insertion of a reflecting paddle, and later on a piston, should not cause significant UCN loss from material absorption.

When sliding out the paddle, UCNs that under go a diffuse reflection can be doppler shifted. To reduce this effect, the paddle should be as specular reflecting as possible. However, on all surfaces, there is some probability of non-specular reflection. In the Lambert model of non-specular reflection (see Sec. 1.1.5), a reflection is either completely specular or completely diffuse. In measurements of UCN transport in electro-polished stainless steel guides, a probability of diffuse reflection $P_{diffuse} \approx 5-20\%$ was found to best explain the data with the Lambert model[GRL91].
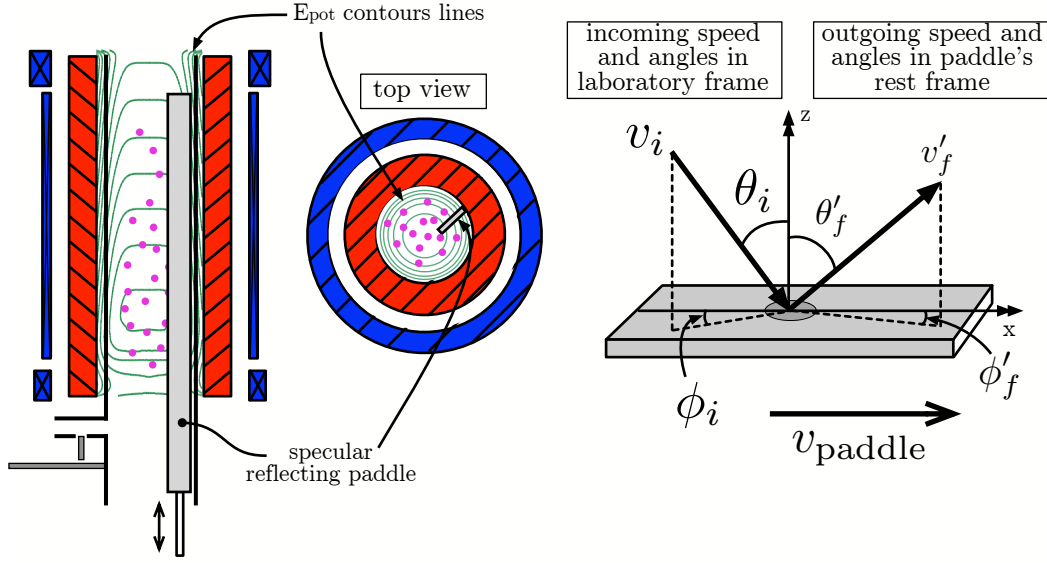
Figure 5.10: *Left*: A schematic of what is meant by the specular reflecting paddle for chaotic cleaning. *Right*: The coordinate system, angles, and velocities referred to in the calculation of the heating of UCNs due to diffuse reflections off the paddle when it is slid out of the trap.

Heating due to sliding out of paddle

To simulate the size of the heating effect numerical integrations assuming an isotropic UCN gas were performed. The technique is similar to that described in Sec. B.2 for the extraction efficiencies through a thin foil of a sliding trap. Initially a paddle covering $\rho > 33$ mm lying on the $\phi = 0$ plane with P_{diffuse} is inserted into the vertical trap to $z = 20$ cm from the bottom. The iteration step-size of the integration is fixed to the paddle being slid out by 1 cm. So, if v_{paddle} is the speed of the sliding paddle, then the time elapsed during a step is $\Delta t = 1$ cm/v_{paddle}. The number of diffuse reflections off a small element dS_{paddle} of the paddle for UCNs with energy E_n is calculated by:

$$dR = n(E_n) \, P_{\text{diffuse}} \, \Delta t \left(\frac{\sqrt{2E_n}}{4\sqrt{m_n} V_{\text{eff}}(E_n)} \right) \left(\frac{E_n - E_{\text{paddle}}}{E_n} \right) dS_{\text{paddle}} \; ; \qquad (5.11)$$

where the first term in brackets is from Eq. 5.9 for the reflection rate; the second term in brackets is from Eq. 5.8 for the effective area of the paddle, with E_{paddle} being the E_{pot} value at dS_{paddle}, which varies with ρ and z; V_{eff} is the effective volume calculated in Sec. 5.2; and $n(E_n)$ is the UCN spectrum.

The size of an element of $dS_{\text{paddle}} = (d\rho = 0.2\,\text{mm}) \times (dz = 1\,\text{cm})$. This expression for the reflection rate is only valid for an isotropic UCN gas.

To perform the calculations, the initial spectrum of UCNs $n(t = 0, E_n)$ are placed in equally spaced bins in velocity space with width dv (thus in energy-space, the bin-widths dE_n vary in size). For each UCN velocity bin, the diffuse reflection rate dR at $\rho + d\rho$ and $z + dz$ on the paddle and the amount of doppler heating/shifting after a reflection are calculated. This produces a new UCN spectrum that is then put through the next iteration of the calculation. The amount of heating depends on the details of the diffuse reflection process.

An ideal diffuse reflection from a stationary surface in the Lambert model gives a probability of emission into an element of solid angle $d\Omega$ is $\propto \cos\theta\, d\Omega$; where θ is the polar angle of a spherical coordinate system with its origin at the point of reflection. For a stationary surface, the problem is ϕ symmetric and the emission into an angle θ is $\propto 2\pi \cos\theta \sin\theta\, d\theta$. Furthermore, for a stationary surface the velocity/energy of the incoming and reflected particles are the same (elastic collisions) and there is no dependence on the incoming angles so that the surface can be considered as an emitter of particles.

However, if the surface is moving these conditions break down. Consider the motion of the paddle with a speed v_{paddle} in the direction towards the positive x direction (see Fig. 5.10) [8]. Let v_i, θ_i and ϕ_i be the initial speed and angles of the incoming UCN in the laboratory frame. And the speed of the UCN seen in the paddle's rest frame is denote v_i'. Then these quantities are related by:

$$v_i'(v_i, v_{\text{paddle}}, \theta_i, \phi_i) = \sqrt{(v_i \sin\theta_i \cos\phi_i - |v_{\text{paddle}}|)^2 + (v_i \sin\theta_i \sin\phi_i)^2 + (v_i \cos\theta_i)^2}\ ,$$

$$(5.12)$$

where $v_i = \sqrt{2\left[E_n - E_{\text{paddle}}(\rho, z)\right]/m_n}$, due to the slowing down of the UCNs before they reach the paddle. Since an isotropic UCN gas is assumed, the probability distribution of the angles θ_i and ϕ_i is $\propto \cos\theta_i \sin\theta_i\, d\theta_i\, d\phi_i$.

In the paddle's frame Lambert's law is obeyed, thus the probability of emission into the angles θ_f' and ϕ_f' relative to the surface in this frame is $\propto \cos\theta_f' \sin\theta_f'\, d\theta_f'\, d\phi_f'$. The final speed of the UCN back in the laboratory

---

[8]We consider only transverse motion of the paddle. Therefore, there is no y component of the velocity.

frame v_f is thus given by:

$$v_f(v_i, v_{\text{paddle}}, \theta_i, \phi_i, \theta'_f, \phi'_f) = \Big[(v'_i \sin \theta'_f \cos \phi'_f + |v_{\text{paddle}}|)^2$$

$$+ (v'_i \sin \theta'_f \sin \phi'_f)^2 + (v'_i \cos \theta'_f)^2 \Big]^{\frac{1}{2}}, \quad (5.13)$$

where v'_i from Eq. 5.12 is to be inserted. The final angles in the laboratory frame θ_f and ϕ_f are not important in the problem since the UCNs are assumed reach an isotropic state in a time-scale before their next diffuse reflection. What's important is the final speed v_f relative to the initial speed v_i, both in the laboratory frame. The size of this doppler shift depends on both the incoming angles and outgoing angles. Averaging the dependence on θ_i, ϕ_i and θ'_f, ϕ'_f requires integrating Eq. 5.13 with the Lambert model.

Performing the full numerical calculation is very computationally intensive. It requires a "for-loop" for: t, the time during the motion; E_n; ρ and z, since E_{pot} at the surface of the paddle $E_{\text{paddle}}(\rho, z)$ varies; and both θ_i, ϕ_i and θ'_f, ϕ'_f, since the doppler shift in velocity after reflection depends on the angles before and after reflection. This makes for a 8-dimensional problem. To reduce the needed computational time significantly, only an extreme case of heating is considered.

Recall in this problem that the velocity of the paddle v_{paddle} is towards the positive x direction. We consider four cases of reflection: (a) if $-90° < \phi_i < 90°$ and $90° < \phi'_f < 270°$, then the UCN is sure to be cooled $v_f < v_i$; (b) if $90° < \phi_i < 270°$ and $-90° < \phi'_f < 90°$, then the UCN is sure to be heated $v_f > v_i$; (c) if $-90° < \phi_i < 90°$ and $-90° < \phi'_f < 90°$, then the UCN can be heated or cooled, depending of the sizes of ϕ_i, θ_i, ϕ'_f, and θ'_f; similarly, for case (d) if $90° < \phi_i < 270°$ and $90° < \phi'_f < 270°$, then the UCN can be heated or cooled. All four cases occur with equal probability due to the approximation of an isotropic UCN gas and ideal diffuse reflection. Due to limitations of available computing power, integration over ϕ_i and ϕ'_f can not be performed. The approximation that cases (b), (c) and (d) all result in the worst case heating, when $\phi_i = 180°$ and $\phi'_f = 0°$, is assumed. That is, 3/4 of diffuse reflections off the paddle results

in:

$$v_f(v_i, v_{\text{paddle}}, \theta_i, \theta'_f) = \left(\left[\sqrt{(v_i \sin \theta_i + |v_{\text{paddle}}|)^2 + (v_i \cos \theta_i)^2} \, \sin \theta'_f + |v_{\text{paddle}}| \right]^2 \right.$$
$$\left. + \left[\sqrt{(v_i \sin \theta_i + |v_{\text{paddle}}|)^2 + (v_i \cos \theta_i)^2} \, \cos \theta'_f \right]^2 \right)^{\frac{1}{2}} . \quad (5.14)$$

For case (a)—the other 1/4 where doppler cooling must occur—no doppler shifting $v_f = v_i$ is assumed. This is the same as assuming the worse case heating for this case also.

The first set of calculations were done with the UCN spectrum split in to 500 equally-spaced bins in velocity-space. Initially, exactly 1 UCN is placed at $35\,\text{neV}$[9]. The polar angles θ_i and θ'_f are separated in 50 equally-spaced bins. Different values for the speed of the paddle $v_{\text{paddle}} = 0.05$, 0.1 and $0.2\,\text{m s}^{-1}$ and the diffuse probability $P_{\text{diffuse}} = 0.05, 0.1$ and 0.2 were used. The results are shown in Fig. 5.11 and Fig. 5.12. Each of these calculations took around 3 days to complete. Another calculation using the expected distribution of UCNs from $0 \rightarrow 35\,\text{neV}$ was also done for the case of $v_{\text{paddle}} = 0.1\,\text{m s}^{-1}$ and $P_{\text{diffuse}} = 0.1$. The spectrum uses the V_{eff} values from Fig. 5.4, and assumes $dn/dE_n \propto \sqrt{E}$ constant phase space density. It was divided into 1000 equally-spaced bins in velocity-space. The initial total number of neutrons in the spectrum $\int_0^{35\,\text{neV}} (dn/dE_n) dE_n = 1$. This calculation took 6 days to complete. The result is shown in Fig. 5.12.

The calculations with the mono-energetic UCNs show that when the paddle speed increases, one gets less heated UCNs since the paddle spends less time in the trap, but the heating, i.e., the size of the shift, is more severe. This is as expected. When the probability of ideal diffuse reflection is increased, the number of heated UCNs increases approximately proportional to it. The energy was chosen to be $35\,\text{neV}$ since this is the proposed UCN energy to clean the spectrum. If their energy is increased to above $E_{\text{trap}} = 40\,\text{neV}$ they can take a very long time to be removed since there is no efficient cleaning procedure in place after the paddle is removed from the trap.

The proportion of the initial $35\,\text{neV}$ UCNs that end up with $E_n > 40\,\text{neV}$ is 5×10^{-4}, 9×10^{-3} and 5×10^{-2} for $v_{\text{paddle}} = 0.05$, 0.1 and $0.2\,\text{m s}^{-1}$, respectively.

---

[9]Or $dn/dE_n = 11\,\text{neV}^{-1}$ for between $35\,\text{neV} \rightarrow 35\,\text{neV} + 0.09\,\text{neV}$.
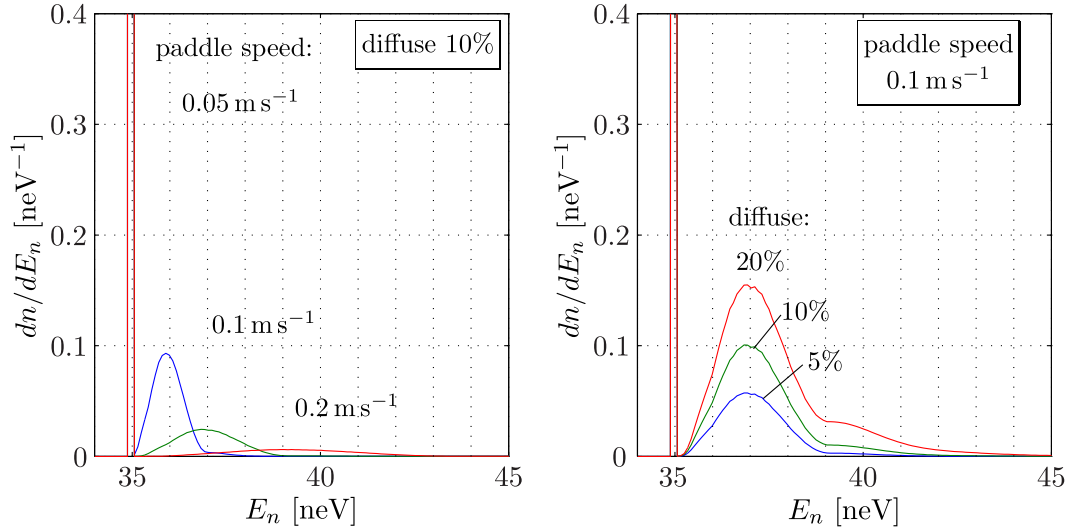
Figure 5.11: *Left*: The heating of mono-energetic 35 neV UCNs with a fixed 10% probability of ideal diffuse reflection off the paddle and a varied paddle speed. A pessimistic scenario of doppler heating was assumed to reduce the computation time (see text). *Right*: The same as *left* but with the paddle speed fixed at $v_{\text{paddle}} = 0.1 \, \text{m s}^{-1}$ and the probability of ideal diffuse reflection varied.

This can be seen more clearly in the logarithmic plot. For the full spectrum calculation with $v_{\text{paddle}} = 0.1 \, \text{m s}^{-1}$ and $P_{\text{diffuse}} = 0.1$, the proportion of the initial UCNs with energy $0 \to 35 \, \text{neV}$ that gets heated to $> 40 \, \text{neV}$ is 5×10^{-4}. For this fraction of above-threshold UCNs, the systematic shift in the observed storage time $\Delta\tau_{\text{tot}} = \left(\tau_\beta^{-1} + \bar{\tau}_{\text{clean}}^{-1}\right)^{-1} - \tau_\beta \approx 0.2 \, \text{s}$, if $\bar{\tau}_{\text{clean}}$ is assumed to be in the range between 600-1200 s, which are the values that have the largest effect on $\Delta\tau_{\text{tot}}$.

This is on the threshold of being a problem. Of course, as discussed above, this can be reduced with a slower paddle speed. While a worst case scenario is used for the heating, there are uncertainties associated with the calculations. The amount of heating is only a model for non-specular reflections on a transverse sliding paddle. In reality, it is not an abrupt transition between ideal specular and ideal diffuse reflections. There exists intermediate-case reflections where some mixing of the incoming and outgoing angles occur. Also, using the paddle does not mean the UCNs are completely isotropic.

To reduce this heating, one should use a material with as low P_{diffuse} as possible. However, diffuse reflections are required to mix the motion into the
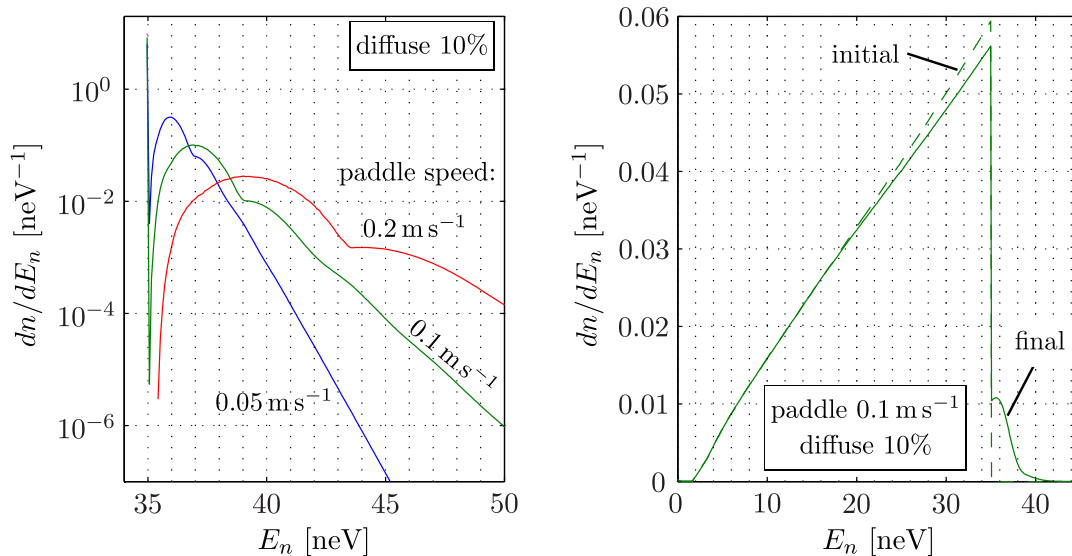
Figure 5.12: *Left*: Same as the plot on the left of Fig. 5.11 for a 10% fixed probability of ideal diffuse reflections off the paddle, but shown with a logarithmic vertical scale. The peaks (diminishing rapidly in amplitude) from discrete number of diffuse reflections off the paddle can be seen more clearly, as well as the probability of a heated UCN ending up with $E_n > E_{\text{trap}} = 40\,\text{neV}$. *Right*: The paddle heating calculation using the full UCN spectrum up to $35\,\text{neV}$ for $dn/dE_n \propto \sqrt{E}$ (constant phase space). The same worst-case heating (described in the text) as the other calculations was used. The speed of the sliding paddle $v_{\text{paddle}} = 0.1\,\text{m\,s}^{-1}$ and 10% probability of ideal diffuse reflections were used.

$E_{n,z}$ mode. From the simulations using mono-energetic isotropic $35\,\text{neV}$ UCNs, the average time between diffuse reflections off the paddle when is inserted up to $z = 80\,\text{cm}$ (in a vertical configuration) is only $\approx 20\,\text{s}$ [10]. Therefore, it is necessary to increase the diffuse reflections on the side walls when using the paddle.

The amount of heating from these calculations makes it hard to rule out the sliding out of the paddle as a possible significant systematic effect due to the unknowns in the calculations. More effort must be used to understand the heating process. This can be done with more sophisticated calculations on a computing cluster, and backed up by separate experiments which verifies

---

[10]It is due to this low rate of diffuse reflection with the paddle that the peaks corresponding to discrete number of diffuse reflections are well-defined in the log-plot of Fig. 5.12. If the collision rate is high, these peaks should smear out to a continuous distribution.

the model used in the calculations. Perhaps, more importantly, the effect of the heating can be indirectly measured in the experiment itself by varying the sliding speed of the paddle. This should change the amount of heating and thus an effect on τ_{tot} can be searched for. However, this would increase the required experiment time.

Advantages of the specular reflecting paddle

The main advantage of using the UCN paddle is that it leaves the access from the bottom of the trap to be free. For instance, if the end coil is used as the UCN remover. The escaping UCNs can be monitored during cleaning. Ideas for implementing this is shown in Sec. B.3 of the Appendix. This would allow a direct monitoring of the cleaning process, which would be very useful for understanding and verifying simulations of the cleaning procedure. Alternatively, instead of using the bottom end coil, an absorber ring can be inserted from the bottom of the trap. Since this absorber can be completely pulled out of the trap, it won't block the charged particles. Its thickness can be made greater, which would then reduce the precision of reproducing its z position since the E_{pot} contour planes are closer to the transverse plane. Such an absorber ring is needed anyway to clean out the high-field seekers trapped at the end coil's field gradient.

Another advantage of access from the bottom is that it gives good pumping on the trapping volume, especially if the top of the trap will be partially blocked with a detector. This is important since a proposed setup is to use the trap on the SUN2 source without a thin window so that the superfluid ^{4}He converter is exposed. A changing pressure of ^{4}He during the stored time can cause a systematic shift in τ_{tot} from UCNs up-scattering off the gas[11] (Ref. 5.8), and it can cause the charged particles to lose energy (see Sec. 7.5), thus effecting the detection efficiency.

5.4.6   Using a diffuse reflecting piston

Another technique of inducing mode-mixing is to insert a highly diffusive reflecting piston at the bottom of the trap for cleaning. The idea is that, although marginally-trapped trajectories with large L still exist, their longest surviving

---

[11]Since it is highly pure ^{4}He, absorption is negligible.

time is limited by the fact that they must fall and reflect from the bottom surface,and thus have their modes-mixed. The piston should be inserted to a height of around $z = -30\,\mathrm{cm}$ to ensure that all UCNs will reflect off it. A big advantage of the piston is that after cleaning it can be retracted without heating the remaining well-trapped UCNs in the trap. The insertion of the piston does not result in a loss of UCNs if the top of the trap is left open. For a vertical trap with no bottom end coil, all UCNs will gain $(102\,\mathrm{neV\,m^{-1}})\Delta h$ in total energy, where Δh is change in the vertical height of the piston. This assumes the motion of the piston is slow relative to the exploration time of the UCNs—satisfying the adiabatic condition. For insertion to $z = -30\,\mathrm{cm}$, the UCNs will gain a maximum of $\approx 20\,\mathrm{neV}$ (Δh from the center of the end coil).

If the E_{pot} contours of Fig. 5.2 are plotted for UCNs with $35\,\mathrm{neV}$ increased by $20\,\mathrm{neV}$, there will only be extra wall collisions with the side walls of the trap between $z = $ -20 and -30 cm. The extra collisions with the stainless steel side walls should not cause a great loss of well-trapped UCNs since their kinetic energy at the surface would not exceed $\approx 15\,\mathrm{neV}$.

Monte-Carlo simulation of the cleaning time

To study how long the above-threshold UCNs can survive for with this cleaning procedure, a Monte Carlo study using a simplified version of the trap was performed. The sidewalls of a vertical trap were assumed to be lossless and with specular reflections only, i.e., no loss or mode-mixing regardless of the $E_{n,\rho\phi}$ value. This is a pessimistic case. A lossless and 100% diffusive reflecting surface is placed at $z = 0$ and a UCN absorber placed at z_{cutoff}. When a UCN reflects off the bottom surface a $v_z(0)$ value is calculated from a randomly generated θ value obeying Lambert's cosine law, where $\cos\theta\,d\Omega = 2\pi\sin\theta\cos\theta\,d\theta$. If $v_z(0)^2/2 < g\,z_{\mathrm{cutoff}}$, where $g = 9.8\,\mathrm{m\,s^{-1}}$, the UCN does not reach the absorber and the time it takes for the UCN to return to the bottom reflector, $2v_z(0)/g$, is added to the survival time of the UCN. If $v_z(0)^2/2 > g\,z_{\mathrm{cutoff}}$, then the UCN reaches the absorber and $v_z(0) - (v_z(0)^2 - 2gz_{\mathrm{cutoff}})^{1/2}/g$ is added to the survival time. The probability of absorption is calculated using the equations for a polyethylene absorber in Ref. [Bro12] (also explained Sec. 1.1.5) using v_z at z_{cutoff}. If the UCN is absorbed then the simulation is terminated. If it is reflected, then a specular reflection is assumed to have occurred and the time
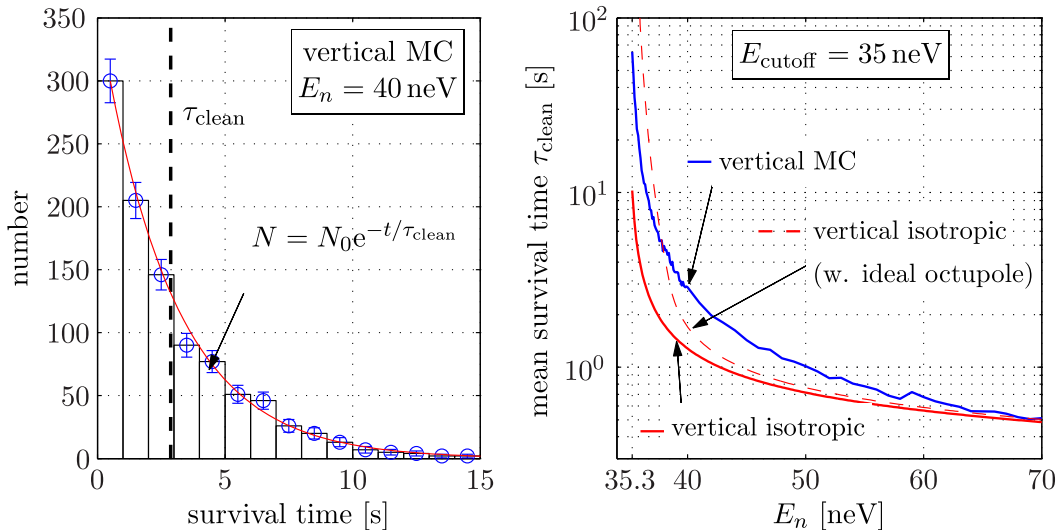
Figure 5.13: *Left:* An example of the distribution of the survival times of 1000 UCNs in the Monte-Carlo simulation with the simplified trap. It is for the absorber at $E_{\text{cutoff}} = 35 \, \text{neV}$ and for UCNs with $E_n = 40 \, \text{neV}$. An exponential decay with a time constant given by the mean of the survival times τ_{clean} describes the distribution well. *Right:* The mean survival time or cleaning time $\tau_{\text{clean}}(E_n)$ for the vertical Monte-Carlo simulations in the simplified trap (see text) is compared to that expected from an isotropic UCN gas for the same configuration and with an added ideal radial octupole field.

taken for the UCN to reach the reflector at the bottom of the trap is calculated and added to the survival time.

Using this technique, the survival time can be calculated for individual above-threshold UCNs with a energy E_n. The result from this simulation is shown in Fig. 5.13 for the absorber at a height $m_n g z_{\text{cutoff}} = 35 \, \text{neV}$. An example of the distribution of 1000 survival times is shown for when $E_n = 40 \, \text{neV}$. The distribution was found to be modeled well by an exponential decay (as expected), and the mean survival time, also called the cleaning time τ_{clean} can be calculated (also shown in the figure). The presence of the radial octupole field does not affect the results of this simulation. In fact, the true octupole field can cause some mode-mixing, thus improving the cleaning time. The field from the superconducting solenoids is neglected. But since the piston is inserted to a distance that is still far from the bottom end coil, this is a good approximation.

From the results it can be seen that as $E_n \to E_{\text{cutoff}}$, $\tau_{\text{clean}} \to \infty$. This is as

expected since these UCNs only find the remover for a very narrow range of θ, also, since their $E_{n,z}$ at the absorber is small, the probability of reflection is large. These cleaning times can be compared with those from Eq. 5.9 for an isotropic UCN gas. The values of the calculations also shown in Fig. 5.13. In general, τ_{clean} from the Monte-Carlo are 2–3 times longer. One must be careful before making the isotropic approximation of the UCN gas. The plots discussed above are for without the radial octupole field that reduces the effective volume and area of the absorber. A calculation for the vertical case with ideal octupole radial field is shown for comparison. One can see the increase in τ_{clean} for low E_n due to the reduction in the effective absorber area $A_{\text{rem,eff}}$.

These calculations show that a 100% diffuse reflecting piston at the bottom of a vertical trap is an effective cleaning procedure, even if the cleaning time $\tau_{\text{clean}} \approx 3\,\text{s}$ at $E_{\text{trap}} = 40\,\text{neV}$ for the Monte-Carlo simulation rather than the $1\,\text{s}$ from the isotropic assumption. This calculation re-illustrates the need to insert an absorber to $E_{\text{pot}} < E_{\text{trap}}$ (a value of $5\,\text{neV}$ less seems to be reasonable) and then retract it again to avoid the long τ_{clean} values. The radial octupole field does increase the cleaning time due to the reduction of $A_{\text{rem,eff}}$, but this can be easily solved by using a ring-shaped absorber to increase this to as large as necessary (see Fig. 5.8 and surrounding text). Furthermore, since no heating of the UCNs will occur when lowering the diffuse reflecting piston again, the idea of using a ring-shaped absorber with very large $A_{\text{rem,eff}}$ at $E_{\text{pot}} = 39\,\text{neV}$ can be applicable [12].

The duration of cleaning time required depends on the number and the energy distribution of the above-threshold UCNs in the trap after filling, as well as the desired precision of the τ_β measurement. For the final trap setup, a proper Monte-Carlo would require the inclusion of the full magnetic fields and the UCN trajectories would need to be tracked. Performing the Monte-Carlo simulation with the simplified trap estimates that it is around $2-3$ times longer than the isotropic approximation. Looking at the τ_{clean} values in Fig. 5.8, using a total cleaning duration of $\approx 100\,\text{s}$ should be sufficient. Some initial experiments testing the cleaning using a similar configuration are described in Chapter 6.

---

[12]Having the maximum E_n so close to E_{trap} after cleaning is dangerous when using the paddle for cleaning due to the heating when sliding it out.

5.5 A proposed experimental setup

In Fig. 5.5 the basic setup describing the filling and cleaning phase of an experimental run is shown. In order to perform other tasks such as: monitoring of filling, inserting a piston or paddle, inserting an absorber, monitoring depolarized and warmed UCNs, emptying the trap or detecting the decay products, more components are needed. One possible setup at the top and bottom of the trap is shown in Fig. 5.14. The design attempts to keep the experiment versatile, for example, by allowing unrestricted access to the trapping volume from below. This is to allow the cleaning procedures discussed in the last section, as well as other new procedures, to be implemented with minimal changes.

In this setup, discussing in terms of the diffuse reflecting piston, the bottom gate valve should be closed during the filling to hide the piston. This is important as there will be gaps between the outer edge of the piston and the inner stainless steel tube/UCN guide since the piston needs to slide later on. And the filling time is likely to take $\gtrsim 50\,\mathrm{s}$ due to the emptying time of the SUN2 source. After the end coil is ramped up, the side valve should be connected to UCN detector B using the linear motion guide switcher 2. The side valve should also be opened. This is so the low-field seekers trapped between the bottom gate valve and the end coil, as well as the high-field seekers, can be cleared. The former, even when pushed into the trap by the piston, will not remain trapped since their energy will be too high. Detecting both of these types of UCNs with a detector allows the filling process to be monitored (discussed in Sec. 5.5.1). After waiting a sufficient time for these to be cleared, the bottom gate valve can be opened and the piston inserted.

If the speed of the piston being inserted is slow compared to that of the UCNs (e.g. $\approx 0.05\,\mathrm{m\,s^{-1}}$ so that the whole movement takes $\approx 10-20\,\mathrm{s}$ would be sufficient), then doppler reflections off the moving the piston will raise the UCN gas, like the UCN elevator in the Ezhov experiment [Ezh09]. The top of the trap should be left unobstructed[13] to give space for the UCNs to rise so that there are no losses there. When the piston is retracted, if this is also done

---

[13]The bottom surface of the charged particle detector can be placed at $z = +50\,\mathrm{cm}$, for example, to give enough space for the UCN gas to raise. The decrease in probability of electrons reaching this higher plane is very small. In fact, it may be advantageous to have the charged particle detector even further out of the trap so that magnetic defocussing can occur. See Sec. 7.4 for a detailed discussion.
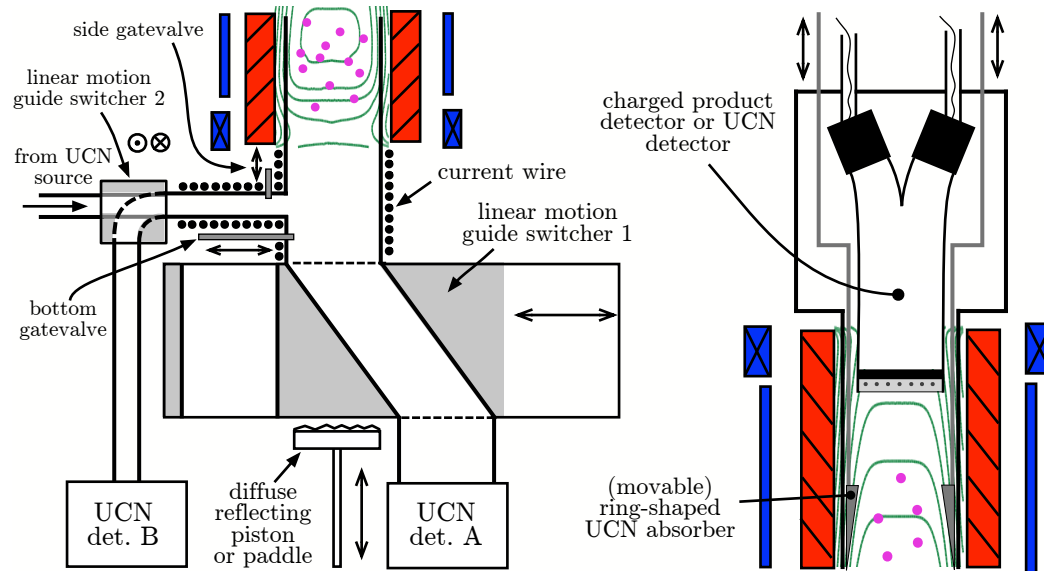
Figure 5.14: The schematic of a possible setup at the bottom and top of the experiment when the trap is vertical and a diffuse reflecting piston is used. *Left: The linear motion guide switcher 1* is used to connect either the piston or the *UCN detector A* to the bottom of the trap, used for monitoring warmed or depolarized UCNs during the holding time and for counting the surviving UCNs in the trap. This design reduces the sharp angles UCNs have to travel when they are filled and emptied from the trap. *The linear motion guide switcher 2* (whose motion is in and out of the page) is used to connect either the side gate valve to the UCN source or *UCN detector B*, which is used for monitoring the high field seekers and low-field seekers that are trapped between the bottom gatevalve and the end coil when it is ramped up. The current wires wrapped around the UCN guides are used to prevent the depolarization of UCNs. *Right:* At the top of the trap either a charged particle detector (the system proposed for electrons in Sec. 7.4 is shown) or a UCN detector can be used. The former is for in-situ detection of the decay products, and the latter for fill-and-empty mode. This UCN detector should be able to be lowered for monitoring the cleaning of above-threshold UCNs, and it should have a low UCN energy detection threshold. A proposed design is given in the text. A ring-shaped UCN absorber, which is used if the UCN detector from the top is not, is shown here. If the piston is used it must be inserted from the top, and if the paddle is used then it can come from the bottom. The thickness of the absorber, proposed to be around 5 mm thick, does not cause a significant loss of charged particles when left in the trap.

slowly, satisfying the adiabatic condition, then the doppler cooling reflections will lower the UCN gas back to its original height.

If the piston is used then the only possible option is to use an absorber inserted from the top for the removal of above-threshold UCNs. A ring-shaped absorber $\approx 5\,\text{mm}$ thick can be used for a large $A_{\text{rem, eff}}$ and to not obstruct the charged particle detector (see Fig. 7.8). Since the piston acts as an UCN elevator, the absorber ring, in principle, does not need to be inserted and retracted.

Having a piston with a diameter close to that of the inner stainless steel tube is useful for clearing the high-field seekers that may have become trapped at the bottom end coil's field when it was ramped up. These high-field seekers only escape the trapping volume when the piston is retracted out again (unless they are lost on the stainless steel side walls of the trap). Leaving the side valve open will offer the opportunity of detecting them in UCN detector B.

Reducing the gap between the piston and the inner stainless steel tube is also important for when the piston is inserted to its upper position for the cleaning process. If a well-trapped UCN enters this gap there is a high chance they will be lost due to making many reflections. However, since the gap exists in the high field region (due to the octupole field), the probability of UCNs reaching it is low.

After the cleaning is completed, the piston is retracted back and UCN detector A is connected to the bottom gate valve. The side valve should then be closed. This detector will be used to directly monitor warmed and depolarized UCNs that will escape the trap from the bottom end coil. It will also count the survivors when the end coil is ramped down for a fill-and-empty measurement.

Inserting the piston before ramping up end coil

When using the piston, there is the choice of inserting it before the ramping up of the end coil, just after the side gate valve to the UCN source is closed. Doing this can help reduce UCN losses during the ramping process. The first reduction comes from preventing the UCNs from exploring the gaps in the guides and closed UCN gate valves below the trap. Whether this is useful or not will depend on the shortest time the small end coil can be ramped and

the quality of the UCN valves versus the leak rate between the piston and the stainless steel tube/guides.

The other reduction comes from reducing the heating of UCNs due to the ramping, since the piston keeps UCNs away from the lower end coil. Recall that the vertical setup is only $40\,\text{neV}$ deep and the lower end coil needs to be ramped from $0.3\,\text{T}$ to $1.7\,\text{T}$ at the center of the coil. The amount of heating depends on the time the UCNs spend around the coil and the change in $|B|$ there. The position of the piston used for cleaning, inserted to $z = -30\,\text{cm}$ as proposed above, should be far enough from the increasing field of the small end coil so that heating is negligible.

One of the disadvantages of inserting the piston before ramping the end coil is that less UCNs will be monitored at UCN detector B. The low field seekers trapped below the lower end coil and the high-field seekers that could previously be monitored are now pushed into the trap by the piston, instead. If there is no gap between the piston and the inner stainless steel tube, then the high-field seekers will be lost on the stainless steel sidewalls during the cleaning process. Monitoring of the above-threshold, low-field seekers can still be done with the UCN monitor detector lowered from the top (described in Sec. 5.6.1).

5.5.1 Detection of high-field seekers

Here we describe the behavior of the high-field seekers during the experiment and discuss how they can be removed, or, even more desirably, be detected. While it is easy to place current wires around the UCN guides near the bottom of the trap to form a small solenoid for preventing the depolarization of UCNs, this is difficult to do all the way down to the converter volume of the source. During the filling phase, UCNs are free to move between the trap and the converter volume, hence they can depolarize. This will lead to losses of low-field seekers.

After sufficient filling of the trap, the side gate valve (see Fig. 5.14) is closed so UCNs will no longer be able to return to the converter volume and be depolarized. The end coil is then ramped up to confine the low-field seekers in the volume above it. There will be a few high-field seekers trapped at the plane of the end coil as it was ramped up. However, most high-field seekers

are free to move up and down past the end coil.

These high-field seekers can be monitored in UCN detector B by opening the side gate valve (and switching the linear guide switcher 2). After these UCNs are cleared, the piston can proceed to be raised to its upper position for cleaning. On its way up, the high field seeking UCNs trapped by the ramping of the end coil will be pushed up into the trap. These will either be cleaned along with the above-threshold UCNs by the absorber, or they will be detected in the UCN detector B. This can be done by leaving the side gate valve open and using a piston that is thicker than the diameter of the side port to this valve (to prevent the UCNs from leaking around the piston).

5.5.2   Detection of depolarized or warmed UCNs

During the holding time of a measurement, if a low-field seeking UCN in the trap undergoes depolarization to become a high-field seeker, it can exit the trap at the bottom end coil since the side walls are reflective. They will fall and be detected by the UCN detector A (see Fig. 5.14) so that they do not return to the trap. The details about the depolarization processes and efficiency of detecting them in other experiments are given in a Sec. 5.7.

Another process that can cause UCNs to leave the trap is the "warming" of UCNs. Such an effect, also called "quasi-elastic scattering" of UCNs, has been observed in material traps. The cause of warming in a magnetic trap could come from vibrations of the mechanical walls. It is for this reason that the $|B|$ value at the end coil is deliberately chosen to define E_{trap}, i.e., min. $E_{\text{pot}}|_{\text{endcoils}} = E_{\text{trap}} < $ min. $E_{\text{pot}}|_{\text{sidewalls}}$. This way these warmed UCNs can escape from the bottom end coil before they start interacting with the side walls. Once they escape, these warmed UCNs will be detected by the same detector as the depolarized UCNs. They can be differentiated by the use of a spin filter (e.g., a magnetized iron foil) infront of the detector.

The UCN guides below the bottom gate valve can have sequentially larger diameters (i.e. the diameter in the linear guide switcher is larger than the guides above, and the diameter of guides to the detector even larger that this). If this is done, any effects to the transport efficiency due to mis-alignments in

the repeated motion of the guide switcher is reduced[14].

5.6   Detection of UCN decay

5.6.1   Counting the survivors and monitoring the filling

UCN detector A (see Fig. 5.14) can also be used for counting the surviving UCNs in the trap when the end coil is ramped down. For a valid fill-and-empty neutron lifetime measurement the UCN spectrum dn/dE_n, the differential spectrum, is required to be constant between different fillings. It must also remain constant with holding time in the trap. This is required due to the energy-dependence of material losses. In magnetic trapping this affects the UCNs during the extraction and detection. This condition is more strict than just having the total initial number of UCNs in the trap constant. If the only loss of UCN is from β-decay then there should be no change in the UCN spectrum. Therefore, if the UCN spectrum is changing then it is a hint that there are other loss mechanisms in the trap, or there are variations of the UCN guiding and detection systems. In order to have information on the UCN spectrum after the holding time, the end coil can be ramped down slowly. Only the knowledge that the relative spectrum remains constant is required.

Normally a filling monitoring procedure will only count a total number of UCNs (i.e., $\int (dn/dE)dE$) which is related to the number low-field seeking UCNs confined in the trap. For instance, the total count in the monitor detector in the monitoring method proposed with UCN detector B in Fig. 5.14 will be the sum of the high-field seekers for an energy below the minimum well-trapped UCN energy up to the energy at which the ring-shaped absorber at the top is placed [15]. The integral of low-field seeking UCNs with energy below the minimum well-trapped UCN energy will also be counted.

This is a good monitoring procedure since the high-field seeking UCNs monitored have an energy range covering the actual energy range of the well-trapped low-field seekers. While this does not completely remove the possibility that some other UCN spectrum dn'/dE produces the same measured

---

[14]This can be done for the guides connecting the side gate valve to the UCN detector B also. But it is less useful here since the UCNs have to travel horizontally.

[15]Minus a few UCNs trapped in the high-field regions of the end coil.

integrated number, it does severely reduce the likelihood of this occurring. If one wishes to be even more stringent, then one needs to have information about the differential spectrum of the filling.

An idea to do this is to use a UCN detector lowered slowly from the top instead of the ring-shaped absorber. The design for such a detector would be a standard ^{3}He cold neutron gas proportional counter with a thin layer of polyethylene attached to the bottom surface. The optical potential V_{PE} = $-9\,$neV, so there is no lower energy threshold for UCNs to penetrate into the material. The proportion of the inelastic scattering cross-section to the total cross-section of UCNs in polyethylene (at room temperature) is > 90%, and almost all UCNs that undergo inelastic scattering will be increased to the cold and thermal neutron energy range so that it can easily penetrate the rest of the polyethylene and front window of the gas proportional counter. The detection efficiency will depend on the solid angle the detector makes with the bottom surface of the polyethylene—taking into account edge effects—and the neutron path lengths in the ^{3}He. This detector can also act as the UCN cleaner. By lowering this detector into the trap slowly, the differential energy spectrum of low-field seeking UCNs with energy just above max. E_n can be measured. So direct monitoring of the cleaning can take place even when the diffuse reflecting piston is used. If this detector is used then a charged particle detector can not be.

With this detector, the other monitoring technique of emptying the high-field seekers to UCN detector B can still be used. Therefore, the monitoring of the filling process will include all the high field seekers and the low-field seekers with energies below and above the well-trapped UCN energy range. This would be a very stringent monitoring procedure for a fill-and-empty measurement.

5.6.2 In-situ detection

In-situ detection means detecting the charged particle products from the neutron β-decays within a short time of when the decay occurred. A big advantage is that a decay curve is extracted for each filling so that the initial UCN spectrum, and thus initial number, does not need to remain constant between fillings. Different in-situ decay curves can be added together for improving the statistics of the fit, even if the spectra and detection efficiencies differ between

the different curves. The only necessary condition is that the UCN spectrum and charged particle detection efficiency remains unchanged during a single decay curve measurement.

This has advantages since many factors effect the intensity and spectrum from a UCN source. For example, at PF2: changes in the turbine speed or the reproducibility of the beam switcher position. For a superfluid source like SUN2: temperature of converter or freezing of air onto the extraction valves and guides. Effects common to both are subtle changes in the neutron flux from the reactor, which depends on not only the power but also where fission is taking place in the fuel element. The speed and operation of mechanical valves and shutter could vary. Due to the subtle nature of these changes, in-situ measurements are desirable in high-precision neutron lifetime measurements.

The magnetic field gradient from the end coils and the octupole magnets can reflect charged particles via the magnetic mirror effect. Therefore, collection of charged particles can occur. The efficiencies are estimated in Chapter 7. Various ideas for detecting the charged decay products are also presented in this section. The basic system is to place a detector at the top of the vertical trap since the charged products will have energies that can easily overcome the gravitational potential of the trap.

With charged particle detection, there is UCN energy-dependence of the detection efficiency still [LZ09]. To verify that the UCN spectrum indeed does not change while in the magnetic trap, as well as understanding the UCN source, performing fill-and-empty measurements is very worthwhile. This technique contains different systematic errors to the in-situ detection, so performing both measurements will provide a valuable check of unknown systematics.

5.7   Depolarization

One of the systematic losses unique to magnetic traps is depolarization of UCNs. Only low-field seeking UCNs remain confined in the trap—high-field seekers are attracted to the sidewalls, and make multiple reflections there and then exit through the end coils. Therefore, if a UCN converts from a low-field seeker to a high-field seeker (called "*Majorana spin-flip*" transitions) then it will no longer be well-trapped and will eventually become lost. To prevent this

from happening the adiabatic condition must be satisfied. This is where the Lamour precession frequency of the neutron in a magnetic field $|\vec{B}|$ must be much higher than the temporal variation of the $\vec{B}$-field seen by the neutron due to its motion, i.e.:

$$\frac{2\mu_n|\vec{B}|}{\hbar} \gg \frac{\mathrm{d}\vec{B}/\mathrm{d}t}{|\vec{B}|} = v\frac{\nabla|\vec{B}|}{|\vec{B}|} \tag{5.15}$$

where v is the velocity of the UCN. If $\vec{B}$ is the field from the octupole in the $\rho\phi$-plane only, then $\vec{B} = \beta\rho^3[\cos(\phi/4)\hat{\boldsymbol{\rho}} + \sin(\phi/4)\hat{\boldsymbol{\phi}}]$. For a UCN trajectory which passes through the center of the trap, where $\rho = 0$, the adiabatic condition is clearly maximally violated here since $|\vec{B}| \to 0$. If, however, a bias field is added in the z-direction, then $\vec{B} = \beta\rho^3[\cos(\phi/4)\hat{\boldsymbol{\rho}} + \sin(\phi/4)\hat{\boldsymbol{\phi}}] + B_{\text{bias}}\hat{\boldsymbol{z}}$; and for a trajectory passing through the center of the trap (i.e., with v_ρ only):

$$\frac{\nabla|\vec{B}|}{|\vec{B}|} = \frac{15\beta^2\rho^4(B_{\text{bias}}^2 - 2\beta^2\rho^6)}{(\beta^2\rho^6 + B_{\text{bias}}^2)^{7/2}} \ . \tag{5.16}$$

For this case, the radial position where the maximum of $\nabla|\vec{B}|/|\vec{B}|$ occurs is shifted. And, depending on the size of B_{bias}, it does not have to violate the adiabatic condition. The worst scenario is for a UCN with energy of the maximum trapping depth $E_n = E_{\text{trap}}$ and with angular moment $L = 0$, since these pass the region of maximum depolarization with the fastest speed v_ρ. We restrict our discussion to such a trajectory.

The depolarization probability of a single passage through such a region can be calculated using the Landau-Zener[16] transition formula [Zen32] which is given by $e^{-\pi\omega\tau}$, where $\omega = \mu B_{\text{bias}}/\hbar$ and $\tau = B_{\text{bias}}/(dB/dt) = B_{\text{bias}}/(v \cdot d|B|/d\rho)$. This is applicable for a small region where the potential changes linearly. Such an approach was used to estimate the effects in the trap of Ezhov [Ezh05]. A more complete calculation is given in Ref. [Bro00] where the full Hamiltonian of a neutron in a time-varying magnetic field is numerically integrated along the neutron's trajectory. We follow such an approach here and extend it to the case of a radial octupole.

---

[16]It was in fact published independently in 1932 by Lev Landau, Clarence Zener, Ernst Stueckelberg, and Ettore Majorana. I cite only the Zener paper due to it being the only one published in English.

The Hamiltonian using the standard Pauli spin matrices is:

$$H(t) = \mu_n \vec{\sigma} \cdot \vec{B} = \mu_n \begin{pmatrix} B_{\text{bias}} & \beta\rho(t)^3 \\ \beta\rho(t)^3 & -B_{\text{bias}} \end{pmatrix}, \tag{5.17}$$

where by standard convention the static bias field is chosen to be $B_{\text{bias}}\,\hat{\boldsymbol{z}}$ and the time-varying field $\beta\rho(t)^3\,\hat{\boldsymbol{x}}$, with $x(t) \equiv \rho(t)$, since only linear motion is considered. The time evolution of a general state $\chi(t) = \begin{pmatrix} \chi_+(t) \\ \chi_-(t) \end{pmatrix}$, where $\chi_+(t)$ and $\chi_-(t)$ are the normalised eigenspinors of $H(t)$, is given by Schrodinger's equation $i\hbar\,\partial\chi/\partial t = H\chi$:

$$\frac{d\chi_+}{dt} = \frac{-i}{\hbar}\left(B_{\text{bias}}\chi_+ + \beta\rho(t)^3\chi_-\right) \tag{5.18a}$$

$$\frac{d\chi_-}{dt} = \frac{-i}{\hbar}\left(\beta\rho(t)^3\chi_+ - B_{\text{bias}}\chi_-\right). \tag{5.18b}$$

This set of coupled first order ODE can be integrated numerically. The solution of $\rho(t)$ for the case where $B(\rho) \propto \rho$ (quadrupole) and $B(\rho) \propto \rho^2$ (sextupole) is analytically straight-forward. But when $|B(\rho)| = \beta\rho^3$, the analytic solution to the second-order nonlinear ODE $\ddot{\rho}(t) = -3\mu_n\beta m_N^{-1}\rho(t)^2$ (the same as 5.7a but without the angular momentum term) requires the Weierstrass elliptic function—an implementation of which is complicated. Hence, $\rho(t)$ in Eq. 5.18 is calculated numerically first, then the solution is approximated by a 3rd degree polynomial. This gives a simple analytic expression for $\rho(t)$, which differs from the numerical solution by $< 0.5\%$ over the time where non-negligible depolarization occurs ($t \approx 2$–$12\,\text{ms}$ or $\rho \approx 5$–$35\,\text{mm}$). This reduces the computation time needed, compared to when interpolation of $\rho(t)$ is used at every step of the integrator, from around $6\,\text{hours}$ (estimated) down to $2\,\text{hours}$ (depending on the numerical accuracy).

The integration is performed using a Runge-Kutta (4,5) integrator. The neutron is started at the center of the trap $\rho = 0$ with the maximum radial speed. The initial state $\chi(0)$ was chosen to be in a pure eigenspinor state χ_+ only. The output from the integrator are the discrete t_i, $\chi_{+,i}$ and $\chi_{-,i}$ values at each time step, the spin-flip probability $|\langle\chi(t)|\chi_-(t)\rangle|^2$ is then later calculated. The numerical accuracy of the integrator, controlled by a parameter specifying the maximum relative numerical error for all components was increased until the solutions converged.

The calculations were performed for an octupole field with $1.2\,\mathrm{T}$ at $44.6\,\mathrm{mm}$ ($2\,\mathrm{mm}$ away from magnet walls) and bias fields of $B_{\mathrm{bias}} = 1\,\mathrm{mT}$ to $0.3\,\mathrm{T}$. The variation of $|\langle \chi | \chi_- \rangle|^2$ as a function of $\rho(t)$ for $B_{\mathrm{bias}} = 0.1 - 0.3\,\mathrm{T}$ is shown in Fig. 5.15. If the spin-flipped component is assumed to lose coherence quickly, since it is pushed out away to the walls of the trap by the field gradient, then the total probability for a UCN undergoing a spin-flip transition after a time t_f is given by:

$$P_{\mathrm{spin-flip}} = \int_{t=0}^{t_f} |\langle \chi(t) | \chi_-(t) \rangle|^2 dt \Big/ t_f \;. \qquad (5.19)$$

This is calculated using a summation of the discrete values. The code was tested and found to reproduce the depolarization result quoted in the quadrupole trap of Ref. [Bro00][17].

Table 5.2: The results of the depolarization calculations made for a UCN with $L = 0$, $v_z = 0$ and $E_n = E_{\mathrm{trap}}$ for an octupole field with $1.2\,\mathrm{T}$ at $\rho_{\mathrm{trap}} = 44.6\,\mathrm{mm}$ and bias field $B_{\mathrm{bias}} = 1\,\mathrm{mT} - 0.3\,\mathrm{T}$. For comparison, the loss rate from β-decay is $\approx 1 \times 10^{-3}\,\mathrm{s}^{-1}$.

B_{bias} [T]	$v_\rho(0)$ [$\mathrm{m\,s}^{-1}$]	ρ at max. depol. [mm]	$P_{\mathrm{spin-flip}}$ one passage	average spin-flip transition rate [s^{-1}]
0.001	3.7	3.4	3×10^{-7}	2×10^{-5}
0.005	3.7	5.9	8×10^{-9}	5×10^{-7}
0.01	3.7	7.4	2×10^{-9}	1×10^{-7}
0.05	3.6	12.6	4×10^{-11}	2×10^{-9}
0.1	3.6	15.8	7×10^{-12}	4×10^{-10}
0.2	3.4	19.7	1×10^{-12}	6×10^{-11}
0.3	3.3	22.4	4×10^{-13}	2×10^{-11}

The probabilities of a spin-flip transition going from $\rho = 0 \to \rho_{\mathrm{trap}}$ are shown in Table 5.2. The motion takes $\approx 17\,\mathrm{ms}$ for all B_{bias} values and thus the average spin-flip transition rate can be calculated (also shown). The largest $P_{\mathrm{spin-flip}}$ (and rate) occurs for the lowest fields, as expected. It decreases very rapidly, faster than a $1/B_{\mathrm{bias}}^2$ dependence. When $B_{\mathrm{bias}} > 10\,\mathrm{mT}$ the average spin-flip transition rate of the straight going trajectory is $< 10^{-4}\,\tau_\beta$.

These calculations give the depolarization probability for one trajectory

---

[17]A value of $P_{\mathrm{spin-flip}} = 1 - 4 \times 10^{-9}$ per passage was quoted for a worst-case trajectory in quadrupole trap with a radius of $5.5\,\mathrm{cm}$, $3.1\,\mathrm{T}$ at the walls and bias field $B_{\mathrm{bias}} = 0.11\,\mathrm{T}$.
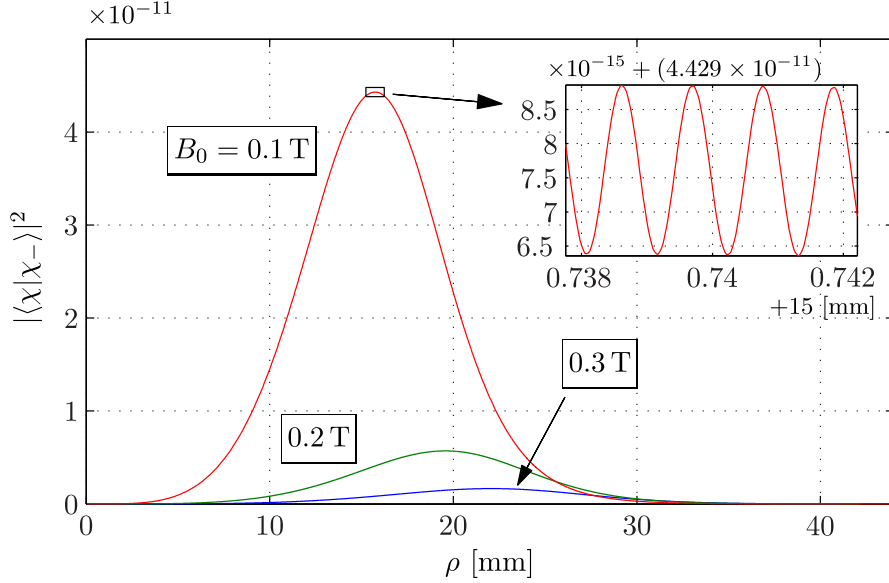
Figure 5.15: A plot of the spin-flip transition probability $|\langle\chi(\rho)|\chi_-(\rho)\rangle|^2$ plotted as a function of the radial distance ρ for a UCN with $E_{n,\rho\phi} = E_{\text{trap}}$ and with a trajectory passing directly through the central axis of the trap ($L = 0$). Three values of the bias field B_{bias} are shown. The results were calculated with a numerical integrator with the time-dependence of the trajectory $\rho(t)$ approximated with a 3rd degree polynomials. The *top-right* inset is a zoomed-in plot showing the famous Rabi oscillations of the spin-flip probability.

that is approximated by an analytical polynomial only. Performing the calculation for many trajectories, which in turn need to be numerically solved, would require a vast amount of computing power. The best is to set limits for depolarization losses in the experiment itself using direct and indirect searches.

An indirect search involves varying a parameter of the experiment, in this case B_{bias}, and measuring if an impact on the measured τ_β is observed. One requirement for a valid indirect search, which is sometimes overlooked, is each measurement needs to be at the same or better statistical precision and the range of the varied parameter should be as wide as possible. If charged particle detection is used then the configuration with $B_{\text{bias}} = 0.3\,\text{T}$ suggested from Chapter 7 will be a good high value; while for the lowest B_{bias} value it would be difficult for statistical reasons to go below $0.1\,\text{T}$ [18].

---

[18]From the extend simulations described in Chapter 7, the reduction of the number of electrons detected when going from $B_{\text{bias}} = 0.3\,\text{T}$ to $0.1\,\text{T}$ is 2.5 times, taking into account the increase in effective volume of the latter.

For a fill-and-empty experiment, however, one can use a much lower maximum value of B_{bias} for the indirect search. This is because the extraction and detection efficiency in this case is independent of B_{bias} and a lower B_{bias} would result in faster statistics. For example, a range from $5\,\text{mT} \rightarrow 0.1\,\text{T}$ would cover 3 orders of magnitude of expected depolarization losses for the worst-case trajectory and the depolarization rate at the maximum B_{bias} should be far lower than the statistical sensitivity achievable in an experiment. Some experimental results measuring indirectly the depolarization loss with B_{bias} in the milli-Tesla range is given in Chapter 6.

An indirect search only allows one to observe the effect of the parameter that is varied. If B_{bias} is varied as discussed above, then only depolarization due to the low field region will be studied. There could be depolarization at the magnetic field near the walls due to the variation of $|B|$ between the octupole pieces (due to the spikes in $|B|$ at sharp edges of the magnets or from demagnetized material, see Fig. 4.4), from field anomalies due to chips at the inner walls of the magnets[19], or from other unknown effects. This is why direct monitoring of depolarized UCNs is highly desirable.

UCNs that depolarize to become high-field seekers will be attracted to the side walls and end coils of the trap. If this happens for a well-trapped UCN at the low-field regions near the center of the trap, then when it comes into contact with the sidewalls, it can have a kinetic energy of $E_{\text{kin}} = E_{\text{trap}} + |\mu_n|(B_{\text{walls}} - B_{\text{bias}})$. Therefore, in order for the sidewalls to be effective in reflecting depolarized UCNs, so that they are given sufficient probability to find and escape from the end(s) of the trap, the neutron optical potential at the sidewalls should be $V_{\text{walls}} \gtrsim 2|\mu_n|B_{\text{walls}}$. For the current trap where $(B_{\text{walls}} - B_{\text{bias}}) < 1.3\,\text{T}$, using stainless steel at the side walls with $V_{\text{SS}} \approx 180\,\text{neV}$ is sufficient. If depolarization occurs near the sidewalls of the trap, they will gain only a small additional amount of kinetic energy when they collide with the sidewalls. Such UCNs will have a high collision frequency with the sidewalls at low energies though. If the trap is in a vertical configuration then the acceleration of gravity will pull these UCNs to the bottom end coil and help them be extracted. In a horizontal setup, if their initial v_z is low, then a diffuse

---

[19]Small loose grains of magnetic dust have been observed before. The NdFeB material is after all formed from pressed and sintered grains only. Modules with visible chips were placed at the ends of the array to reduce their effects.

reflection is required at the sidewalls for them to find the two ends of the trap.

Performing a Monte-Carlo study and tracking the depolarized UCN trajectories numerically to determine their extraction efficiency should not be difficult due to their short survival times in the trap. The experimental results with the Ezhov trap are worth discussing. A detection efficiency of ≈ 0.9 (Ref. [Ezh09]) relative to the detection efficiency of stored UCNs in the trap was measured by "forced depolarization" of the UCNs in the trap. This is when zero-field regions are deliberately created at the center of the trap with the outer bias field coil. The trap has $B_{\text{walls}} \approx 1\,\text{T}$ (the B_{bias} value not found in publications) so that depolarized UCNs will have between $60 - 120\,\text{neV}$ when they collide with the fomblin grease coated sidewalls of the trap ($V_{\text{fomblin}} \approx 110\,\text{neV}$). The opening at the bottom of the $10\,\text{L}$ (physical volume) trap is also small at $2\,\text{cm}$ compared to the diameter of the trap $20\,\text{cm}$. Therefore, in the HOPE experiment the extraction efficiency of depolarized UCNs is expected to be greater than this 90% value.

5.8   Interactions with residual gas

The rate of interactions of UCNs in a trap with residual gas is given by

$$\tau_{\text{gas}}^{-1} = n_{\text{gas}}\,\sigma_n\,v_{\text{rel}}\,, \tag{5.20}$$

where n_{gas} is the number density of the gas molecules, $\sigma_n = \sigma_{\text{cap}} + \sigma_{\text{scat}}$ is the total cross-section that is comprised of nuclear capture and scattering cross-sections, and v_{rel} is the velocity of the UCNs relative to the gas nuclei. Since the velocities of the UCNs are so much smaller than that of the gas molecules $v_{\text{gas}} \gg v_n$, we can make the assumption that $v_{\text{rel}} \approx v_{\text{gas}}$ and any scattering event causes the UCN to be come lost due to the large gain in energy. Therefore, Eq. 5.20 can be taken to be loss rate of UCNs caused by the residual gas and is UCN energy independent.

The nuclear capture cross-section σ_{cap} is $\propto 1/\bar{v}_{\text{rel}}$, so that the contribution to τ_{gas}^{-1} from this is v_{gas} independent. However, σ_{scat} does not depend on v_{rel} so that its contribution to τ_{gas}^{-1} is $\propto v_{\text{gas}}$. The velocity of the gas is given by the Maxwell-Boltzmann distribution. Under the current assumptions, it is

sufficient to use the average velocity $\bar{v}_{\text{gas}}$ given by:

$$\bar{v}_{\text{gas}} = \sqrt{\frac{8k_B T}{\pi m_{\text{gas}}}} \, , \qquad (5.21)$$

which depends on the gas temperature T and the mass of a gas molecule m_{gas}.

The expected vacuum levels reached in the UCN trapping volume is on the order of 10^{-7}–10^{-6} mbar. For levels of vacuum below around 10^{-4} mbar the residual gas composition is predominately hydrogen H_2 due to the differences in the pumping speed of a turbomolecular pump. For a pressure of 1×10^{-6} mbar, the molecular density $n_{H_2} = P/(k_B T)$ at 300 K is 2.4×10^{16} m^{-3}. The density of hydrogen nuclei ^{1}H is two times this, i.e., $n_{^1H} = 2\, n_{H_2}$. The capture cross-section of a hydrogen nuclei given at the thermal neutron velocity $\sigma_{\text{cap},\,^1H}(v_{\text{rel}} = 2200\,\text{m s}^{-1}) = 0.33$ barns. The free hydrogen nuclei total scattering cross-section $\sigma_{\text{scat, free}\,^1H} = 20.5$ barns (from Ref. [OEC12]). To convert this to the cross-section of ^{1}H bound in H_2, it is multiplied by a factor of $(m_n + m_{H_2})^2 / m_{H_2}^2 \approx 2.3$, so that $\sigma_{\text{scat},\,^1H\,\text{bound in }H_2} = 47$ barns. The average velocity of hydrogen molecules at 300 K is $\bar{v}_{H_2} = 1780\,\text{m s}^{-1}$. Therefore,

$$\tau_{H_2}^{-1}\left(1 \times 10^{-6}\,\text{mbar}, 300\,\text{K}\right) = 2\, n_{H_2}\left[\sigma_{\text{cap}}(2200\,\text{m s}^{-1}) \times 2200\,\text{m s}^{-1} + \sigma_{\text{scat},\,^1H\,\text{bound in }H_2} \times \bar{v}_{\text{gas}}\right]$$
$$\approx 4 \times 10^{-7}\,\text{s}^{-1} \quad (5.22)$$

If this is the only loss of UCNs besides τ_β^{-1}, then this leads to a shift in the observed total storage time of $\Delta\tau_{\text{tot}} \approx 0.3$ s.

In Ref. [Ser05] a systematic correction of 0.40 ± 0.02 s was applied to find τ_β for a vacuum of 5×10^{-6} mbar and a temperature of 113 K. This was deduced by deliberately worsening the vacuum (by switching to a turbomolecular pump with lower pumping speed) to 8×10^{-4} mbar and then measuring $P\tau_{\text{gas}} = 9.5$ mbar $\cdot$ s. There are several critiques that can be made for this technique: (a) it requires assuming that the gas composition remains the same for the two vacuum levels, which is strictly not true if one reduces the pumping speed (no mass spectrometer to analyse the gas content was used); (b) the pressures were measured with a gauge in the warm (T_1) while the trapping volume behind heat screens of a cryostat had its walls covered with fomblin oil cooled to -160°C (T_2). For the extrapolation technique to be valid the

correction factor $k(T_1, T_2)$, which relates the pressure at the gauge with the pressure the UCNs experience in the volume, needs to remain constant despite the change in vacuum; (c) in order to deduce just τ_{gas}^{-1} at different pressures, the wall loss rate τ_{walls}^{-1} must remain constant (however, with fomblin the wall losses are strongly temperature dependent); and (d) fomblin vapor, whose density should be higher near the walls of the trap is not taken into account if just the overall vacuum is worsened.

The warm stainless steel bore of the HOPE trap would avoid most of these problems. It provides a "clean" vacuum, devoid of vapors near the walls, and the pressure can be measured reliably without temperature gradient effects. A mass spectrometer should be used for verifying the gas composition for the different vacuum levels if τ_{gas}^{-1} is to be extrapolated. One decision that remains is how to deal with the ^{4}He in the vacuum if the SUN2 source is used without thin windows so that the trapping volume is exposed to the superfluid converter bath. While the vapor pressure of ^{4}He at $0.7\,\text{K}$ is $\approx 10^{-6}\,\text{mbar}$, there is going to be superfluid creeping so that there are parts that will be at a warmer temperature—and thus a higher vapor pressure. The pressure seen by the trap is difficult to estimate as it depends on the amount of creeping. In principle, the vapor emitted from this bath should be highly pure ^{4}He, which has $\sigma_{\text{cutoff}} = 0$ and σ_{scat} around 50 times smaller than for hydrogen. However, if a high pressure of it exists in the trapping volume then the sensitivity of the mass spectrometer will be decreased for the other gases. During the filling of the magnetic trap, it is difficult to effectively pump on the trapping volume (besides from the top), without experiencing loss of UCNs. However, if a valve to the source (e.g., the linear guide switcher, see Fig. 5.5) that will be closed after filling is also vacuum tight, then strong pumping can begin as soon filling is completed. If two turbomolecular pumps with pumping speeds $\approx 200\,\text{L\,s}^{-1}$ for helium and with diameters matched to the trapping volume (DN100) are used unobstructed from the top and bottom of the trap, then an initial helium pressure of $10^{-3}\,\text{mbar}$ can be pumped down to $< 10^{-6}\,\text{mbar}$ in a few seconds according to a theoretical calculation. If, however, a piston at the bottom or detector at the top covers the pumping access to the volume, then this time will increase.

Chapter 6

HOPE: Experimental results

6.1 The angled trap measurements

I wished to test the storage of UCNs with the Halbach-type octupole magnet array. An experiment was performed on the PF2-EDM beam with the z-axis of the octupole array on an angle of $\approx 30°$ relative to the horizontal so that gravity (with $\approx 55\,\mathrm{cm}$ of height difference) provided the potential for trapping at the upper end of the trap. The bottom end was closed off by a valve; an annular-shaped copper plate with an inner aperture of $6\,\mathrm{cm}$ that is open and closed with a teflon piston ($V_{\mathrm{PTFE}} = 123\,\mathrm{neV}$). It was found that the copper and teflon had to be covered by fomblin grease (Solvay Solexis RT-15), with $V_{\mathrm{fomblin}} \approx 110\,\mathrm{neV}$ and $f \approx 2 \times 10^{-5}$ [Ric91] in order to reduce losses from surface impurities or leakages through small gaps [1]. fomblin grease was also placed on the inner walls of the magnetic array for $8\,\mathrm{cm}$ from both ends to cover the regions where the magnetic field strength dropped off due to the finite length of the array (see Fig. 4.9). The magnet walls have a calculated $V_{\mathrm{Nd_2Fe_{14}B}} = 170\,\mathrm{neV}$ and $f = 170 \times 10^{-5}$, but are covered by glue. The bias field required to reduce the depolarization rate was provided by a solenoid made from winding 2 layers of copper wire with a diameter of $1.4\,\mathrm{mm}$ on to a DN250 ($250\,\mathrm{mm}$ diameter) vacuum tube. The length of the solenoid is longer than the $1.2\,\mathrm{m}$ octupole array by $\approx 5\,\mathrm{cm}$. The vacuum level reached during the experiment was $\approx 5 \times 10^{-5}\,\mathrm{mbar}$. A schematic of the experimental setup is shown in Fig. 6.1.

---

[1]Exactly which of these two effects was causing the losses was not pinned-down.
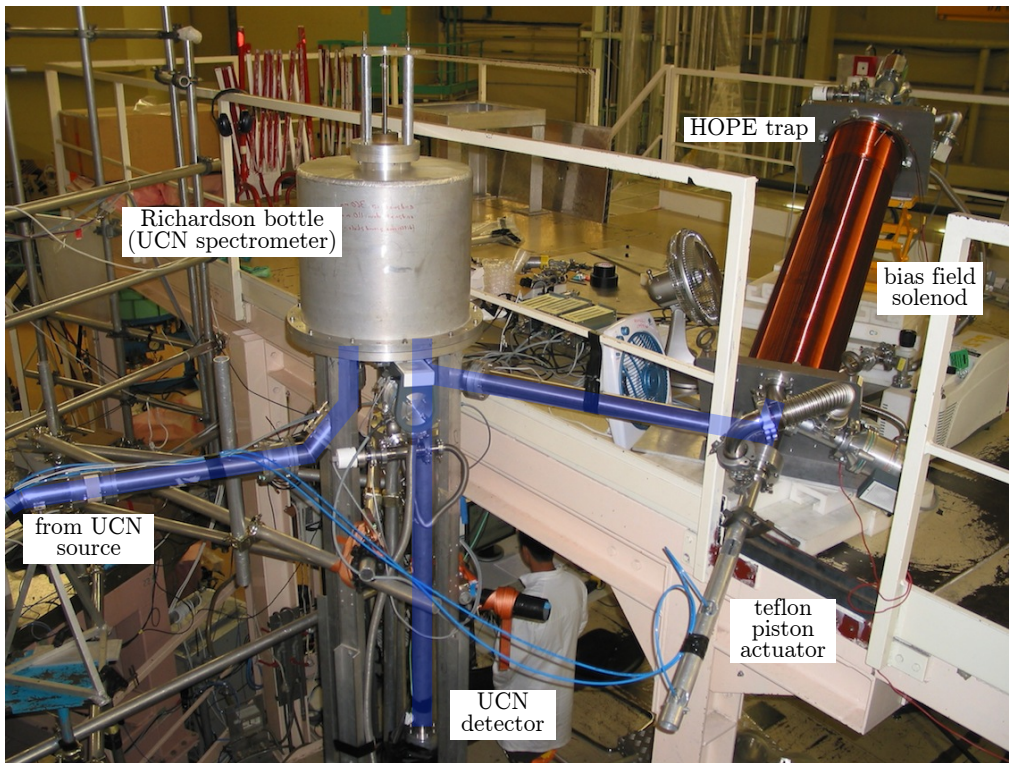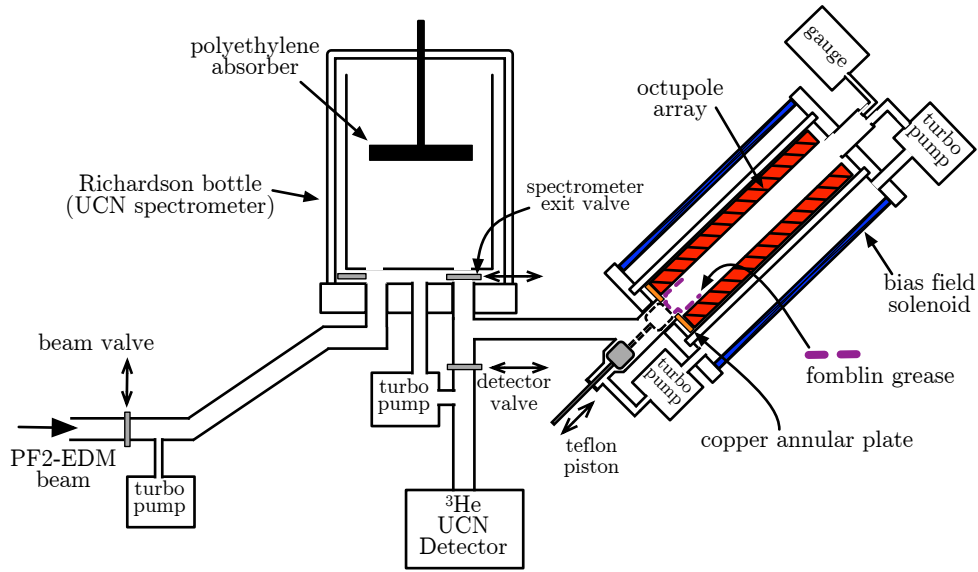
Figure 6.1: *Top*: Schematic of the 1st experiment demonstrating UCN storage with the octupole magnet array. A fill-and-empty experiment to measure the storage times with the octupole magnet array at an angle of $\approx 30°$ relative to the horizontal. Left opened at the top of the trap and closed at the bottom with a material (fomblin) shutter. The Richardson bottle UCN spectrometer was used for pre-cleaning of the spectrum. *Bottom*: A photograph of the experimental setup on the EDM platform of PF2. The UCN guides are highlighted in blue.

The Richardson bottle spectrometer [Ric91] was used for pre-cleaning the UCN spectrum in the "flow-through" mode—where the input and exit valves were left open during filling. The base of the Richardson bottle was $15\,\mathrm{cm}$ higher than the lower opening of the magnetic trap. The polyethylene absorber that defines the upper energy cut-off of the UCN spectrum in the bottle was used in three positions relative to the upper opening of the magnetic trap: 20 cm below (low position), at the same height (medium position) and 15 cm above (high position).

The detector was then shielded with boron and polyethylene. A filling time of $100\,\mathrm{s}$ and emptying time of $90\,\mathrm{s}$ were used for the measurements. In order to measure the background for each emptying $20\,\mathrm{s}$ before and the last $40\,\mathrm{s}$ of the emptying time (the emptying peak was $\lesssim 20\,\mathrm{s}$ wide) was used and corrected for in the data. The background rate was found to be always $< 0.5\,\mathrm{s}^{-1}$.

Table 6.1: The operation of the source gate valve, the detector gate valve and trap teflon piston during the two experiments.

	source valve	detector valve	teflon piston
filling time:	open	closed	open
holding time:	open	closed	closed
(after $5\,\mathrm{s}$ delay):	closed	open	closed
emptying time:	closed	open	open

The decay curves for the three absorber positions are shown in Ref. [Leu10]. The decay curves were found to be modeled well by a sum two exponential decays:

$$N(t_{\mathrm{hold}}) = N_{0,\,\mathrm{short}}\,\mathrm{e}^{-t_{\mathrm{hold}}/\tau_{\mathrm{short}}} + N_{0,\,\mathrm{long}}\,\mathrm{e}^{-t_{\mathrm{hold}}/\tau_{\mathrm{long}}}\ , \qquad (6.1)$$

where t_{hold} is the holding time, $N_{0,\,\mathrm{short}}$ and τ_{short} can be associated with the number and the cleaning time of above threshold UCNs, and $N_{0,\,\mathrm{long}}$ and τ_{long} the number and storage time of well-trapped UCNs. This is only a simple model of the data. In reality, the decay curves contain a continuum of $N_0(E_n)$ and $\tau(E_n)$ for both the above-threshold and well-trapped UCNs.

Using the Richardson bottle in a flow-through mode does not allow stringent control over the maximum UCN energy reaching the bottle. Only qualitative conclusions could be drawn from the measurements of the decay curves.
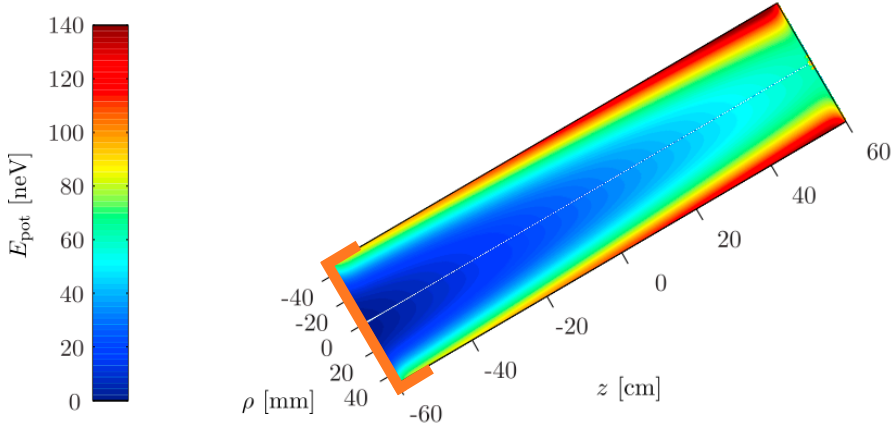
Figure 6.2: The calculated E_{pot} contour map of the angled ($\approx 30°$ to the horizontal) setup. The drop in $|B|$ at the ends of the array is included. A slice of the $\phi = 0°$ plane (with $\phi = 180°$ shown as the negative ρ values) is shown. The minimum E_{pot} occurs at $z = 0\,\text{mm}$, $\phi = 0°$ and $\rho = 7\,\text{mm}$. Where the fomblin grease is located (at the bottom and side walls of the trap) is shown as the solid line colored ■ $\approx 110\,\text{neV}$. As the UCN energy is increased, they start to escape from the opening at the top of the trap (starting $\approx 60\,\text{neV}$) before making collisions with the un-coated side walls of the trap (starting $\approx 80\,\text{neV}$).

One of the more useful observations is that with the absorber in the high position, it took very long for above-threshold UCNs to escape. The fitted τ_{short} gave an indication of this. But another analysis, called "time chopping", can be used. This is when a single exponential with a time constant $\tau_{\text{time-chop}}$ is used to fit the data. The first holding time for the fit $t_{\text{hold 1st}}$ is then increased to see the effect on $\tau_{\text{time-chop}}(t_{\text{hold 1st}})$. When a sufficient number of above threshold UCNs have escaped, $\tau_{\text{time-chop}}(t_{\text{hold 1st}})$ will stabilize to some value with the given statistical uncertainty.

For the decay curve with the high absorber, it took until $t_{\text{hold 1st}} \approx 400-500\,\text{s}$ for $\tau_{\text{time-chop}}$ to stabilize to a value of $\approx 820 \pm 40\,\text{s}$. For smaller statistical error bars, this is expected to take even longer. This can be explained by looking at Fig. 6.2. Due to the fomblin at the walls of the magnet near the end, the trap depth is defined at the top of the trap $E_{\text{trap}} = 60\,\text{neV}$. The region defining this is for a small circular region near the center of the trap and for above threshold UCNs with energy 60–80 neV this is the only region where they can escape.
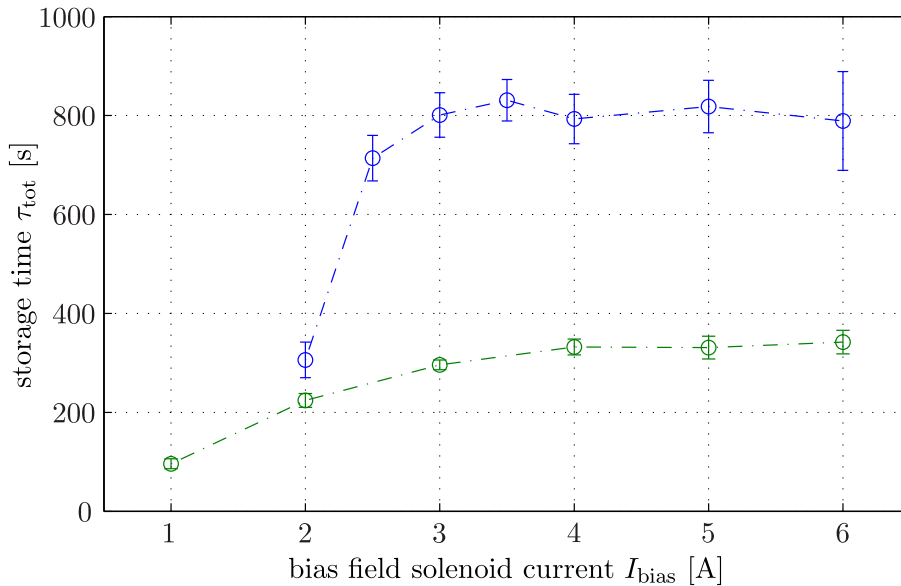
Figure 6.3: The dependence of the storage time τ_{tot} on the current in the bias field solenoid I_{bias} for two sets of data (see text). $I_{\text{bias}} = 3\,\text{A}$ corresponds to $|B| \gtrsim 1\,\text{mT}$ everywhere in the trap due to the complicated structure (see text). The slash-dotted lines $(-\cdot)$ are to guide the eyes only.

6.1.1 Depolarization measurements

An important series of measurements with different current in the bias solenoid I_{bias} were made. The results, shown in Fig. 6.3, come from two sets of data: one with the angled-trap configuration with the fomblin grease as shown in Fig. 6.1; the other was with fomblin just on the side walls. The former set of measurements was done with the absorber in the medium position and τ_{tot} was determined with points with holding times of $500-600\,\text{s}$ and 1200–$1800\,\text{s}$ (two points only). The latter set was done with the absorber in the high position and with holding times of $100\,\text{s}$, $350\,\text{s}$ and $600\,\text{s}$. The former exhibited a $\tau_{\text{tot}} \approx 800\,\text{s}$ and the latter $\approx 330\,\text{s}$, with both saturating at $I_{\text{bias}} \approx 3-4\,\text{A}$. Due to the short storage time of the $\tau_{\text{tot}} \approx 300\,\text{s}$ data, only short holding times could be used. Therefore, the cleaning time of above-threshold UCNs can not explain the shift since it was only the bias field being changed.

With the just bias field solenoid at $3\,\text{A}$ the measured and calculated $|B_z| \approx 4\,\text{mT}$ at the center of the coil axially and radially [Fra09]. At the edge of the octupole array (i.e, $z = -60\,\text{cm}$ and $+60\,\text{cm}$) $|B_z|$ from the solenoid is around

60% of this. Close to 95% of the maximum value is reached when ≈ 30 cm in from the 130 cm long solenoid [Rob09].

There is also a residual axial component of the B_z field in the magnet array. This was discovered with a Hall probe placed at $\rho = 0$ and inserted around 30-40 cm (due to physical restrictions) from either end of the trap. The B_z component from the finite length of the trap (see Fig. 4.10) does not appear at the central $\rho = 0$ axis and should disappear when $\gtrsim 10$ cm into the array. This residual $|B_z|$ was observed to have peaks (and zeros) spaced ≈10 cm apart [Fra09], with amplitudes of $|B_z| \approx 1-3$ mT (the residual fields deeper into the array could not measured). The direction of B_z changes from positive to negative in a non-periodic way (i.e., sometimes two peaks with B_z in the same direction are adjacent to each other; other times they are in the opposite direction). Due to the random switching of directions, spacing of the peaks, and the small size of B_z, it was concluded that this residual axial field comes from combining magnet modules with slightly different magnetization strengths due to manufacturing variations. Therefore, due to the complicated structure of the B_z components, we can only say that for $I_{\text{bias}} = 3$ A, $|B| \gtrsim 1$ mT everywhere in the trap. All subsequent measurements were made with $I_{\text{bias}} = 4$ A.

The calculated spin-flip transition rates τ_{depol}^{-1} for the worse case UCN trajectory (maximum energy UCN that passes repeated through $\rho = 0$ of the trap) are given in Sec. 5.7. For a bias field $B_{\text{bias}} = 1$ mT the average loss rate for this case was $\tau_{\text{depol}}^{-1} = 2 \times 10^{-5}$ s^{-1}. This would cause a shift in the observed storage time, if $\tau_{\text{tot}} = 800$ s to be $\Delta\tau_{\text{tot}} = 13$ s (and if $\tau_{\text{tot}} = 330$ s, $\Delta\tau_{\text{tot}} = 2$ s). There is insufficient statistics in the measured storage times to see this effect. In future experiments with the superconducting coils, the minimum bias field will be on the order of 100 mT.

6.2 Vertical trap with absorber piston

After the initial commissioning experiments, a second experiment was performed on the PF2-TES beam in June-July 2011. The octupole array was used vertically, while the bottom was closed off by the same fomblin grease ($V_{\text{fomblin}} \approx 110$ neV) coated copper plate and teflon piston as in the previous

experiment (shown in Fig. 6.5).

A horizontal polyethylene absorber paddle (65 mm in diameter) that can be inserted and retracted from the trap with an actuator is used for cleaning. Performing the cleaning this way is similar to one of the proposed final procedures that will be used. The absorber was used at different heights, up to energies close to E_{trap}. These measurements can be used to test the understanding of the cleaning process from the calculations in the previous sections.

The number of initial well-trapped UCNs in the trap allows the integrated spectrum of UCNs to be deduced. Using this, combined with the expected losses on fomblin from literature, the loss rate on material walls in the trap $\tau_{\mathrm{walls}}^{-1}$, which is by far the biggest loss, can be calculated and corrected for. After a smaller correction for τ_{gas}^{-1} the neutron lifetime τ_β can be deduced from the results and compared with the expected value.

6.2.1 Description

A schematic and photograph of the experimental setup are shown in Fig. 6.4. The bottom of the magnetic trap was $\approx 70\,\mathrm{cm}$ above the center of horizontal guide from the PF2 turbine. This is done to decelerate the UCNs that have to pass the aluminium foil ($V_{\mathrm{Al}} = 54\,\mathrm{neV}$) at the exit of the turbine [2]. All the UCN guides used were made from electropolished stainless steel and had an inner diameter of 70 mm. The detector used was a ^{3}He gas proportional counter (the same as that used in the experiments of Chapter 2) and it was located $\approx 1.5\,\mathrm{m}$ below the bottom of the trap. The detector spectrum cut-off was chosen to be similar to that shown in Fig. 3.8 for the UCN detector used in the SUN2 experiments. The background rate after shielding the detector with polyethylene and boron rubber was $\approx 0.2\,\mathrm{s}^{-1}$ (without the shielding it was $\approx 2\,\mathrm{s}^{-1}$). The side of the closed gate valves exposed to the magnetic trap side were covered with stainless steel foils. These valves were driven pneumatically with opening and closing times of $\approx 1-2\,\mathrm{s}$ (estimated). The polyethylene absorber in the trap was a circular disc with a diameter of 65 mm and a thickness of 5 mm. The position of the absorber moved by the actuator is reproducible to within a few millimeters. The two linear motion vacuum

---

[2]Initially, the bottom of the trap was only 10 cm above the center of the Al foil, but only ≈ 60 UCNs per fill was observed without the absorber. The trap was then raised to its final position.
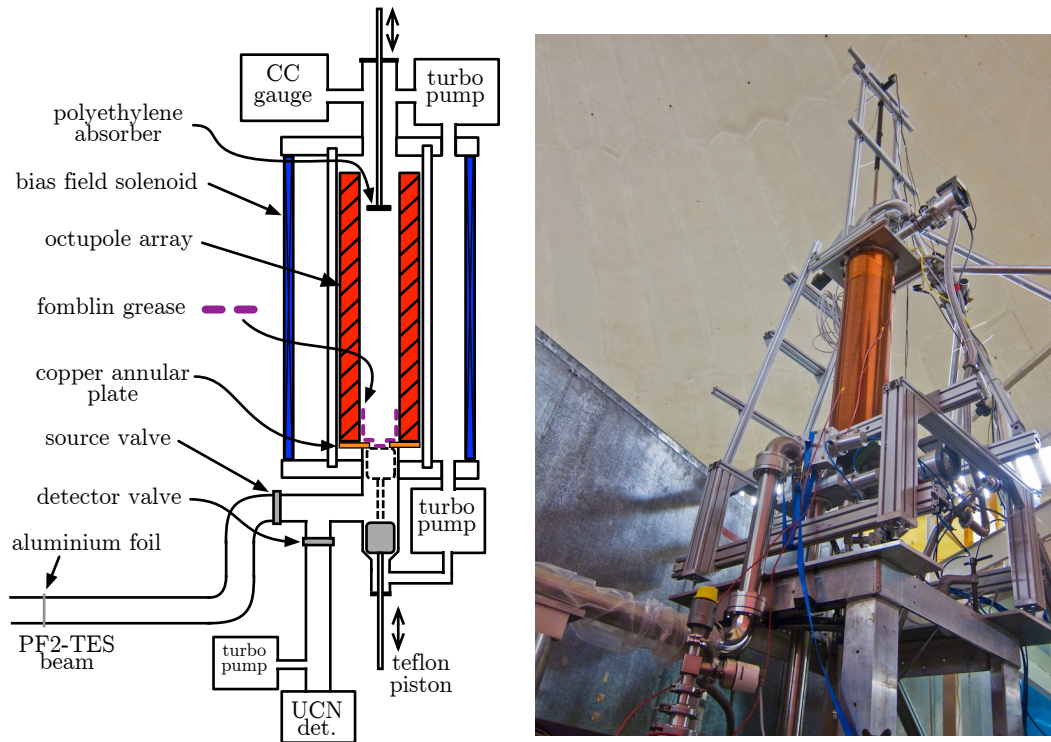
Figure 6.4: *Left*: Schematic of the vertical trap with absorber experiment. The octupole magnetic array is placed vertically, the bottom of the trap is closed with the fomblin covered copper plate and teflon piston valve, and from the top a moveable polyethylene absorber disc can be inserted and retracted from the trap. *Right*: Photograph of the setup sitting on top of the aluminium table of the PF2-TES beam.

feedthroughs (for the teflon piston and polyethylene absorber) are both double O-ring seals with an intermediate vacuum ($\approx 10^{-2}$ mbar achieved with an ACP pump) in between. The vacuum level in the trapping volume was estimated to be $\approx 5 \times 10^{-5}$ mbar. This was measured by closing the valves to the pumps in order to reduce pressure gradients in the vacuum space. No rises were observed when the piston or absorber were moved.

The movement sequence of the valves for filling, holding and emptying of the trap is the same as that shown in Table 6.1. The gate valve at the source is left open during the experimental sequence. The duration of the filling time was 100 s; the holding time was varied and was counted from when the teflon piston was first inserted, with the total motion taking < 2 s; and the
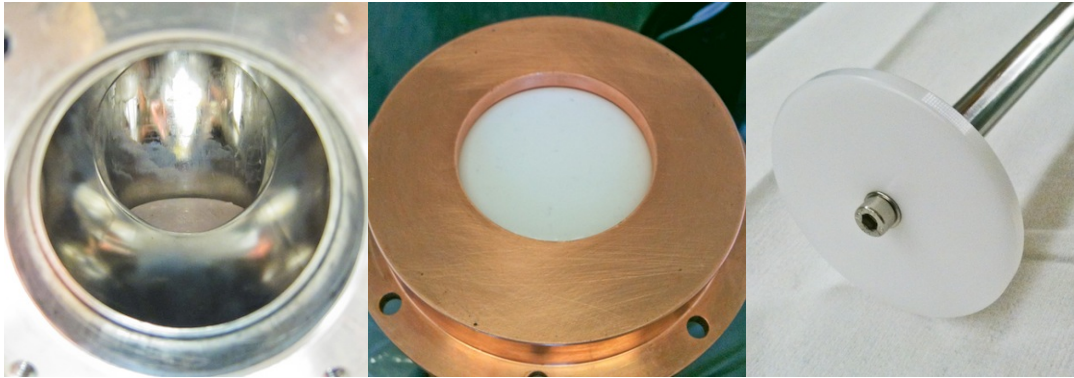
Figure 6.5: Photos of the teflon piston, copper annular plate and the polyethylene absorber. *Left*: A view of the teflon piston in the open position looking into the T-piece UCN guide directly below the trap from where the UCNs enter. The fomblin grease can be seen on the piston and smeared around the guides. *Middle*: The teflon piston in the closed position pushed against the copper annular ring. The opening is 60 mm in diameter and the piston is recessed 7 mm. The fomblin grease on the copper, teflon, and at the seal between the two is not shown. *Right*: The 65 mm diameter polyethylene absorber. The stainless steel screw was covered in vacuum grease so that it is also effective removing UCNs.

emptying time was 100 s long. When the absorber was used, at the start of the filling time, the absorber sits 10 cm above its final position [3]. It is then inserted during the first 10 s of the filling time. After a cleaning time of 80 s the absorber is retracted, taking also 10 s. The speed of the absorber movement is around $1 \, cm \, s^{-1}$.

The count rate in the UCN detector during a measurement sequence is shown in Fig. 6.6. The background in the UCN detector is determined during the 30 s before the emptying time (sometimes this is not possible if the holding time is too short) and the last 40 s of the emptying time. (The emptying time is 100 s long and the width of the emptying peak is $\approx 10 \, s$ long) A background rate of $\approx 0.2 \, s^{-1}$ [4] was corrected for in the data.

Three sets of data were taken: without the absorber ($E_{cutoff} = E_{trap}$), with

---

[3]For the data taken without the absorber, it is still inserted into the trap in order to have similar pumping area on the volume. This should keep the vacuum inside the trap the same with and without absorber.

[4]The background count rate during the emptying time and filling time within the statistics. For instance, from a set of data the former was found to be $0.22 \pm 0.03 \, s^{-1}$, while the latter $0.24 \pm 0.02 \, s^{-1}$. This indicates that it is ambient background or electronic noise.
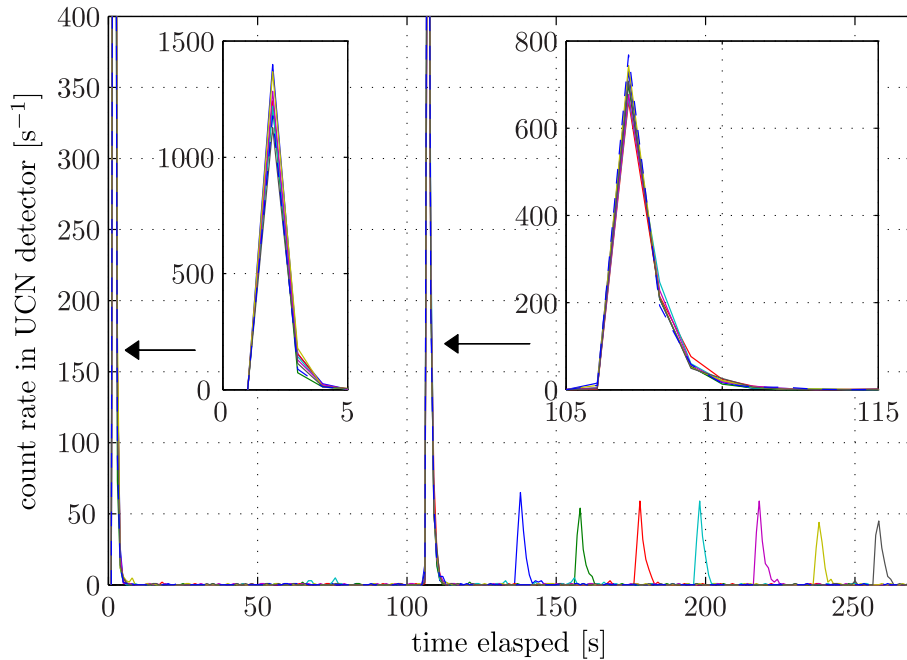
Figure 6.6: The count rate in the UCN detector during an experimental sequence shown in Table 6.1 with the setup in Fig. 6.4. The 1st spike in counts (with the zoomed-in inset) is from switching of the valves to the filling time positions. The 2nd spike (also with the zoomed-in inset) is from emptying the UCNs in the guides. The subsequent peaks in multi-colors are from UCNs emptied from the trap after varied holding times from different fill-and-empty procedures (each in a different color). The 2nd spikes was used to monitor the filling.

the absorber at $80\,\mathrm{cm}$ above the bottom of the trap ($E_{\mathrm{cutoff}} = 82\,\mathrm{neV}$), and with the absorber $65\,\mathrm{cm}$ above the bottom of the trap ($E_{\mathrm{cutoff}} = 66\,\mathrm{neV}$). When the absorber is used, it is inserted into its lowest position for $80\,\mathrm{s}$ of cleaning before being raised by $10\,\mathrm{cm}$, as mentioned above. The decay curves are shown in Fig. 6.7a, 6.7b and 6.8. The data is fitted with the double exponential decay model described in Eq. 6.1, as well as analyzed with the time chopping procedure. Each point used contains data combined from different fill-and-empty procedures. The data was collected over several days for each curve, and the order of the points was randomized as much as possible. The correction in the counts due to the change in the reactor power was around $\lesssim 3\%$, except for four points with $E_{\mathrm{cutoff}} = 66\,\mathrm{neV}$ that required a correction of 6% (see relevant caption in Fig. 6.7b).
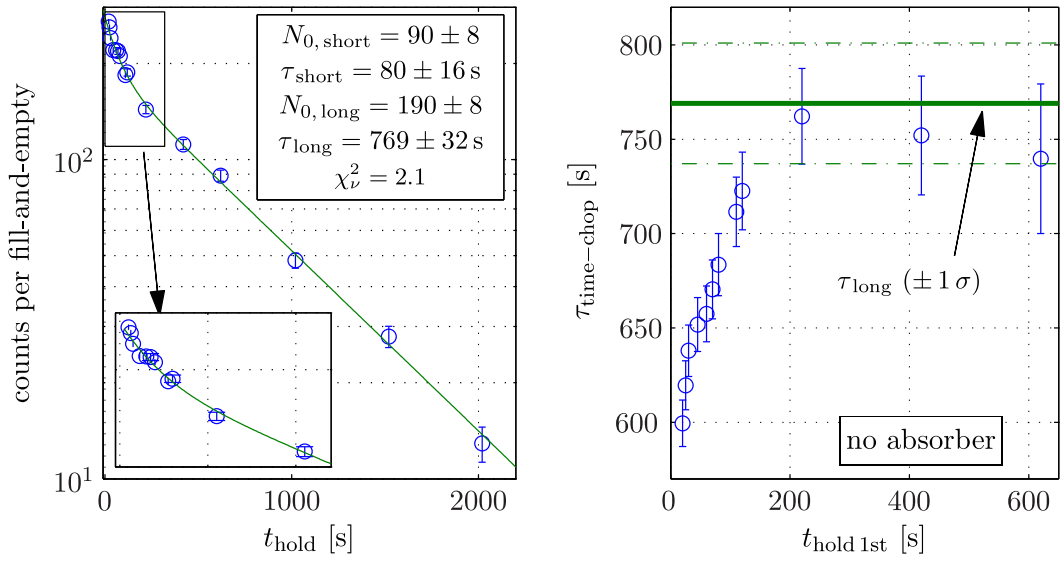
(a) No absorber used so that only the side walls of the magnets are used for cleaning. There is a total of 15 points: the first seven ($\leq 100\,$s) are summed from 13 fill-and-empties; and the last eight ($\geq 110\,$s) from 9.
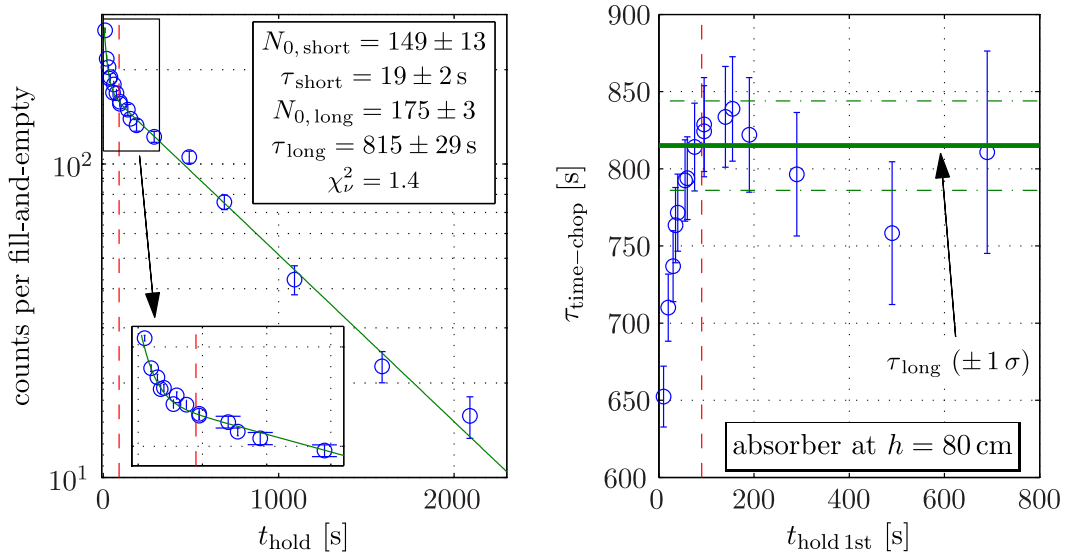
(b) Polyethylene absorber at a height of 80cm from the bottom of the trap. The absorber was left in place until 80s from the start of the holding time, indicated by vertical red dashed line ($--$). It was then retracted up by 10cm at a speed of $\approx 1\,$cm s^{-1}. There is a total of 19 points: the long holding times ($\geq 150\,$s) are combined from 6 fill-and-empties; some shorter holding times were combined from 13; and others were combined with 7. The latter points (at 20, 40, 60 and 80s) required a reduction of counts due to a change in the reactor power of 6%.

Figure 6.7: The decay curves for no absorber and with the absorber at 80 cm for the vertical trap setup of Fig. 6.4. The double exponential decay sum model is used on the *left*, and the time channel chopping on the *right*.
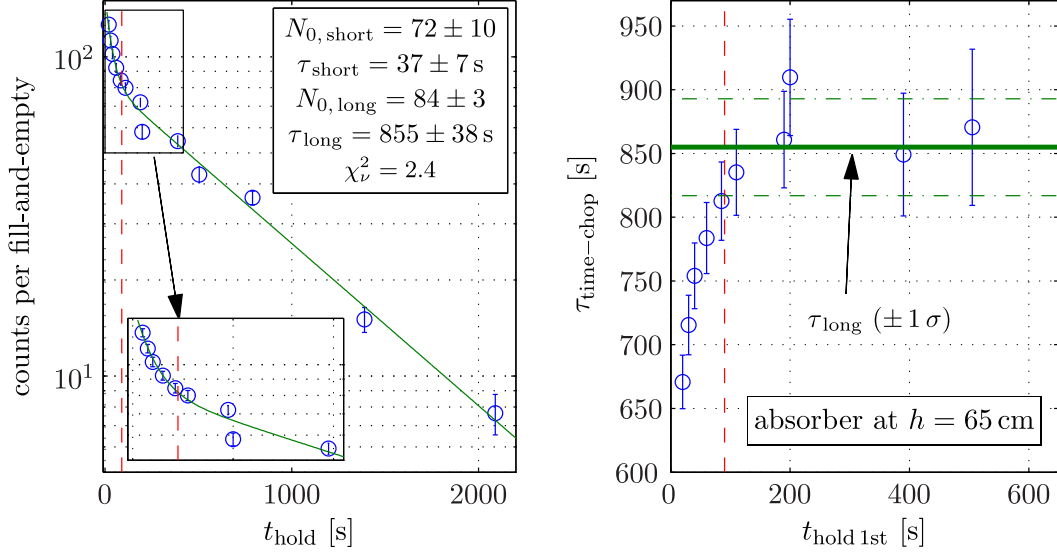
Figure 6.8: The decay curve for the vertical trap experiment with the absorber at a height of 65 cm from the bottom of the trap. The absorber was left in place for the same time and retracted by the same height and speed as for Fig. 6.7b. There is a total of 19 points: the long holding times (≥ 150 s) are combined from 6 fill-and-empties; the shorter holding times combined from between 6–7. The double exponential decay sum model is used on the *left*, and the time channel chopping on the *right*.

A plot of E_{pot} of the octupole array in the vertical position is shown in Fig. 6.9. The fomblin grease, with $V_{\text{fomblin}} \approx 110$ neV (precise value discussed later), extended up 8 cm of the sides of the trap as before. It is the E_{pot} value just above the top of the fomblin that defines the depth of the trap— UCNs start making collisions with the magnet walls that have a high UCN loss probability here. A number of factors make calculating the exact E_{trap} *a priori* difficult: the height of the fomblin grease is not well-defined since it was spread by hand, there are variations in $|B|$ at the walls due to the variations of the magnetization of the permanent magnets from manufacturing, and there are variations at different ϕ angular positions. The best estimate of E_{trap} actually comes from measurements with UCNs by looking at the number of well-trapped UCNs for different absorber positions (the UCN spectrum measurements). Since the energy at which UCNs start interacting with it E_{cutoff} is well-defined. Extrapolating to the number when no absorber is used, $E_{\text{cutoff}} = E_{\text{trap}}$ can be estimated. See Fig. 6.12. From this technique, it was found that $E_{\text{trap}} \approx 84$ neV,

within the expected limits of calculations.

6.2.2   Cleaning of above-threshold UCNs

The effectiveness of the absorber and sidewalls for cleaning above-threshold UCNs can be compared by calculating the effective loss area $A_{\mathrm{loss,\,eff}}$. Following Eq. 5.8, for a surface S and an isotropic UCN gas, this is given by[5]:

$$A_{\mathrm{loss,\,eff}}(E_n) = \mathrm{Re}\left[\int_S \sqrt{\frac{E_n'}{E_n}}\,\bar{\mu}(E_n')dS\right],\tag{6.2}$$

where $E_n' = E_n - E_{\mathrm{pot}}(dS)$ is the UCN kinetic energy at the small element dS of the surface. A calculation of this for the magnet side walls and the absorber at $80\,\mathrm{cm}$ and $65\,\mathrm{cm}$ is given in Fig. 6.10. The expression of the average loss probability per collision $\bar{\mu}(E')$ for the polyethylene absorber, with $V_{\mathrm{PE}} = -8.5\,\mathrm{neV}$[6] is given in Ref. [Bro12] as:

$$\bar{\mu}_{\mathrm{PE}}(E') = \frac{8E'^2 - 8\sqrt{E'}(E' - V_{\mathrm{PE}})^{3/2} - 12E'\,V_{\mathrm{PE}} + 3V_{\mathrm{PE}}^2}{3V_{\mathrm{PE}}^2}.\tag{6.3}$$

Not only is the starting height and E_{pot} on the magnet sidewalls not well known. The choice of $\bar{\mu}$ for the magnet side walls is also not so clear. The calculated $V_{\mathrm{Nd_2Fe_{14}B}} = 170\,\mathrm{neV}$, whose large value is due predominantly to the high iron (Fe) content, and $f_{\mathrm{Nd_2Fe_{14}B}} = 170 \times 10^{-5}$, so Eq. 6.6 is used for calculating $\bar{\mu}_{\mathrm{Nd_2Fe_{14}B}}$. However, on the inner walls of the magnets, there is a lot of glue (see Fig. 4.2). Glue has a high hydrogen content and has a density and composition similarly to that of the polyethylene (i.e. negative V_{opt}). Therefore, Eq. 6.3 can be used to esimate $\bar{\mu}_{\mathrm{glue}}$. The extreme cases where the walls are only $\mathrm{Nd_2Fe_{14}B}$ material or only glue are calculated and shown in Fig. 6.10.

Also shown in Fig. 6.10 are the cleaning times of above threshold UCNs τ_{clean} calculated with these $A_{\mathrm{loss,\,eff}}$ values. This is done for the two absorber positions and without the absorber. For the former cases, the effective area of

---

[5]Note the change of subscript from $A_{\mathrm{rem,\,eff}} \to A_{\mathrm{loss,\,eff}}$ and replacing $S_{\mathrm{rem}} \to S$ since this is now calculating general wall losses.

[6]It is independent of f or W since the main loss comes from when the UCN enters the material.
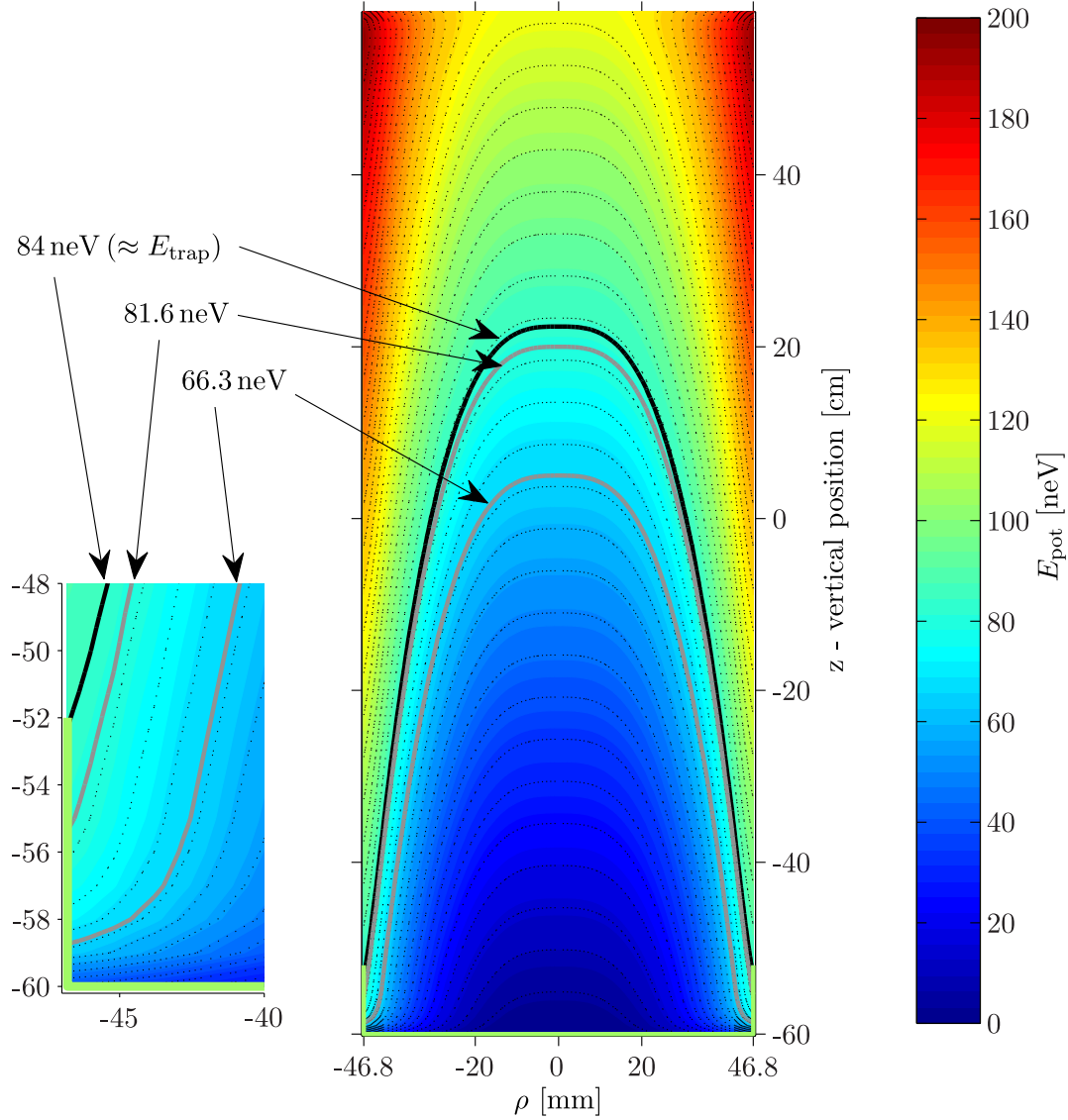
Figure 6.9: The calculated E_{pot} contours of the octupole array in a vertical position. The drop in $|B|$ at the end of array is due to the end effects of the array. A green line (■) is drawn to show where the fomblin grease at the bottom of the trap ($\approx 110\,\text{neV}$) is located. Negative ρ valves are for $\phi = 0°$ and positive valves for $\phi = 45°$. The contour line for the depth of the trap $E_{\text{trap}} \approx 84\,\text{neV}$ is shown in black (▬). Two other contour lines for E_{cutoff} when the absorber is $80\,\text{cm}$ and $65\,\text{cm}$ from the bottom of the trap are shown as grey lines (▬).
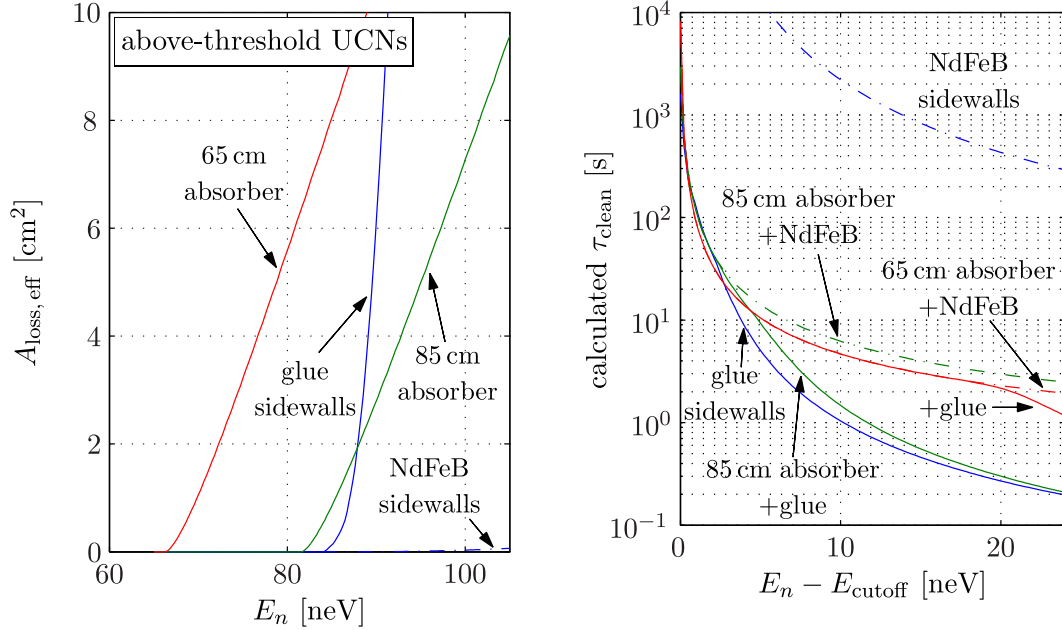
Figure 6.10: The effective loss area $A_{\text{loss, eff}}$ and cleaning times τ_{clean} for above-threshold UCNs. *Left*: $A_{\text{loss, eff}}$ calculated with Eq. 6.2 and the E_{pot} map from Fig. 6.9. In the side wall calculations, the loss probability for only NdFeB exposed at the inner walls or only glue are shown. The losses from the fomblin is assumed to be negligible. *Right*: τ_{clean} from Eq. 5.9 using calculations of the effective volume V_{eff} from Eq. 5.2. The curves are shown for either NdFeB or glue at the side walls.

the sidewalls are added to that from the absorber. This is done for both cases of sidewall material. The cleaning time τ_{clean}, given in Eq. 5.9 but repeated here, is:

$$\tau_{\text{clean}}(E_n) = \frac{4\sqrt{m_n}\, V_{\text{eff}}(E_n)}{\sqrt{2E_n}\, A_{\text{loss, eff}}(E_n)} \ , \tag{6.4}$$

where

$$V_{\text{eff}}(E_n) = \text{Re}\left[\int_V \sqrt{\frac{E'}{E_n}}\, \mathrm{d}V \right] . \tag{6.5}$$

The definition of V_{eff} is only valid for smooth continuous volumes. If the UCN energy is too high, then they can start "leaking" around the outer edge of the absorber. The volume is then divided into two, and the UCN density will not be continuous across this boundary. For the current diameter of 65 mm for the absorber, the V_{eff} calculations, and thus τ_{clean}, for the absorber at 80 cm

and 65 cm are valid only up to $E_n - E_{\text{cutoff}} = 25\,$neV and $30\,$neV, respectively, because of this effect.

There is some uncertainty over the energy E_{cutoff} at which $A_{\text{loss, eff}}$ starts to increase. For the sidewalls, the reasons, due to uncertainty in E_{trap}, were already explained. For the absorber, the uncertainty comes from the stainless steel screw head protruding from its bottom surface (see Fig. 6.5). An analysis of the systematic uncertainty caused by this uncertainty to the measured τ_{tot} is given later. It is found to be small, especially for the 65 cm high absorber measurement, as expected.

It can clearly be seen that the NdFeB material is not effective for removing above threshold UCNs at all. This is due to $V_{\text{Nd}_2\text{Fe}_{14}\text{B}}$ being much larger than E_n'. The glue, however, is effective. The observed τ_{short} values are an ensemble average of τ_{clean} over the above threshold UCN spectrum in the trap. It will be dominated by the UCNs with energies just above the respective E_{cutoff}. If the true $A_{\text{loss, eff}}$ and τ_{clean} values from the side walls are assumed to be somewhere between the two extreme cases (with NdFeB only or glue only), then the sizes of the observed τ_{short} are qualitative explained. The cleaning time without the absorber is the longest since the sidewalls are not too effective in cleaning. The cleaning time when the absorber is at 80 cm is shorter than for when it is at 65 cm due to the extra cleaning from the sidewalls. This gives confidence that we indeed understand the cleaning process in the trap.

The choice of the absorber height at 80 cm with $E_{\text{cutoff}} \approx 82\,$neV is not a wise choice for cleaning since it is so close to $E_{\text{trap}} \approx 84\,$neV. Recall from Sec. 5.4 that it is the τ_{clean} at E_{trap} that defines how effective cleaning is. From Fig. 6.10, it can be seen that for the absorber at 80 cm, $\tau_{\text{clean}}(E_{\text{trap}}) \approx 30\,$s. In contrast, with the absorber at 65 cm, $\tau_{\text{clean}}(E_{\text{trap}}) \approx 3\,$s. These numbers are with the isotropic UCN approximation.

The population of long surviving above-threshold UCNs will not be well-modeled by τ_{short} from the double exponential model. Instead, it will cause the extracted τ_{long} to be shifted towards shorter values. This then causes a systematic shift in the observed $\bar{\tau}_{\text{tot}}$ caused by marginally trapped UCNs. The measurement of $\bar{\tau}_{\text{tot}}$ and how τ_β is extracted from these are discussed next.

6.2.3 Well-trapped UCNs

UCNs with energy below E_{trap} interact only with the fomblin grease, which has a neutron optical potential $V_{\text{fomblin}} \approx 107\,\text{neV}$ and an energy-independent loss factor $f_{\text{fomblin}} = V/W \approx 2 \times 10^{-5}$ at room temperature. While the former is quite well known, the latter is not. A discussion of the best value deduced from the literature will be given later. For now, the analysis will leave f_{fomblin} as a free parameter by dividing by it in $A_{\text{loss eff}}$ and τ_{clean}^{-1}.

For the fomblin grease, which satisfies the conditions that $f = W/V \ll 1$ and $V > 0$, the loss probability for an isotropic UCN gas $\bar{\mu}(E')$ is given by:

$$\bar{\mu}_{\text{fomblin}}(E') = 2f_{\text{fomblin}} \left[\frac{V_{\text{fomblin}}}{E'} \sin^{-1} \left(\frac{E'}{V_{\text{fomblin}}} \right)^{1/2} - \left(\frac{V_{\text{fomblin}}}{E'} - 1 \right)^{1/2} \right] . \quad (6.6)$$

From these, the effective loss area $A_{\text{loss eff}}/f_{\text{fomblin}}$ can be calculated using Eq. 6.2. This is shown in Fig. 6.11 for the fomblin covered bottom (the copper and piston is simplified as being flat) and side walls. With these values, and the effective volume V_{eff} (Eq. 6.5) calculated from the E_{pot} plot of Fig. 6.9, the loss rate due the material walls for an isotropic UCN gas $\tau_{\text{walls}}^{-1}(E_n)/f_{\text{fomblin}}$ can be calculated from Eq. 6.4. This is also shown in Fig. 6.12.

Due to the UCN energy-dependence of τ_{walls}^{-1}, the total storage time of well-trapped UCNs τ_{tot}^{-1} will be energy-dependent as well, since it is given by:

$$\tau_{\text{tot}}^{-1}(E_n) = \tau_{\beta}^{-1} + \tau_{\text{walls}}^{-1}(E_n) + \tau_{\text{depol}}^{-1} + \tau_{\text{gas}}^{-1} . \quad (6.7)$$

The form of the decay curve will then be an integral of exponential decays with varying decay time constants:

$$N(t) = \int_0^{E_{\text{max}}} \frac{dN_0}{dE_n} \, e^{-t/\tau_{\text{tot}}(E_n)} dE_n . \quad (6.8)$$

However, in the current experiment, the variation of $\tau_{\text{tot}}^{-1}(E_n)$ is small over the UCN energy range used, since τ_{β}^{-1} is approximately 10 times larger than the other losses. Given, the counting statistics and the number of points of the data, only a single exponential decay constant, denoted by $\bar{\tau}_{\text{tot}}$ can be used to fit the data, so that:

$$N(t) \approx N_0 \, e^{-t/\bar{\tau}_{\text{tot}}} . \quad (6.9)$$
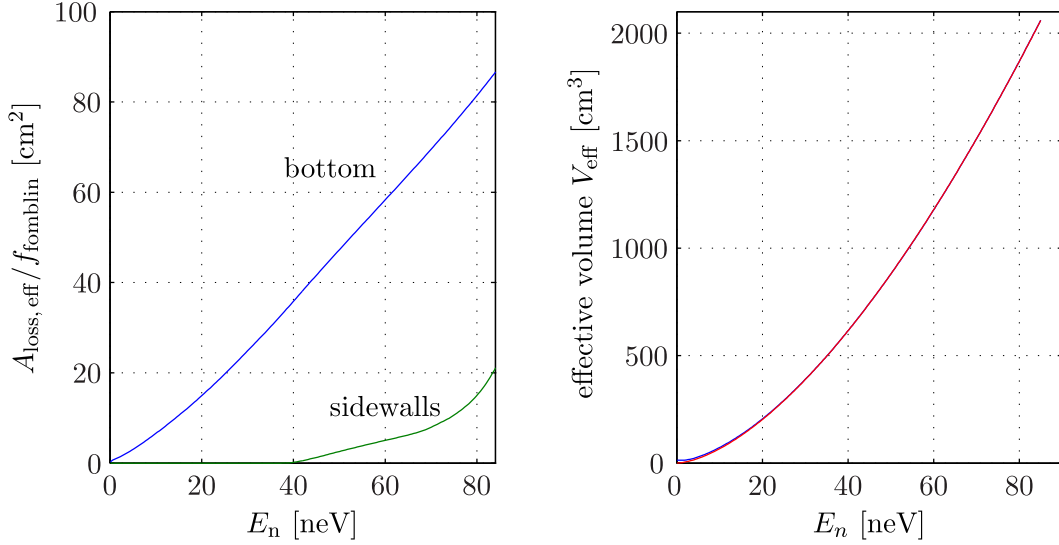
Figure 6.11: *Left*: The calculated effective loss area $A_{\text{loss, eff}}$ (Eq. 6.2) for well-trapped UCNs with the fomblin grease at the bottom and side walls of the trap in the vertical setup. *Right*: The effective volume V_{eff} (Eq. 5.2) of well-trapped UCNs with no absorber. The calculated values are shown with the blue line (–). This is well-described by the analytical function $V_{\text{eff}} = \left(1.65\,\text{cm}^3\,\text{neV}^{-1.6}\right) E_n^{1.6}$ as shown by a red line, which is indistinguishable.

The value of $\bar{\tau}_{\text{tot}}$ can be estimated by the ensemble average of $\tau_{\text{tot}}^{-1}(E_n)$ over the UCN energy spectrum $n_0(E_n)$:

$$\bar{\tau}_{\text{tot}}^{-1} \approx \int_0^{E_{\max}} n_0(E_n)\,\tau_{\text{tot}}^{-1}(E_n)\,dE_{\text{tot}} \bigg/ \int_0^{E_{\max}} n_0(E_n)\,dE_n \ . \qquad (6.10)$$

However, $\bar{\tau}_{\text{tot}}$ is extracted from non-linear regression. The parameters-of-best-fit come from finding $\bar{\tau}_{\text{tot}}$ and N_0 that satisfy minimizing the χ^2 value. That is, minimizing:

$$\frac{\partial^2}{\partial \bar{\tau}_{\text{tot}}\,\partial N_0} \sum_i \left(\frac{N_0 \exp(-t_i/\bar{\tau}_{\text{tot}}) - \int_0^{E_{\max}} n_0(E_n)\,\exp(-t_i/\tau_{\text{tot}}(E_n))dE_n}{\sigma_i} \right)^2 = 0 \ ,$$

$$(6.11)$$

where the summation is over the data points measured on the decay curve. Showing the approximation of Eq. 6.10 from this is difficult. In fact, it will depend on the size of the variations of $\tau_{\text{tot}}(E_n)$ and the initial differential spectrum dN_0/dE_n.
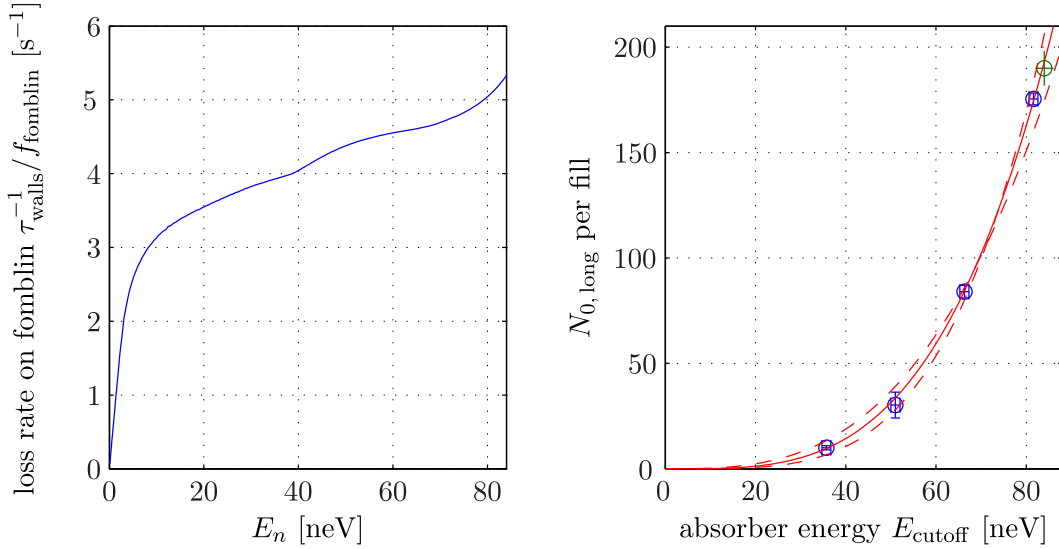
Figure 6.12: *Left*: The energy-dependent loss rate constant of UCNs on the fomblin grease at bottom and side walls of the trap $\tau_{\mathrm{walls}}^{-1}$. This is calculated with Eq. 5.9 and from $A_{\mathrm{loss, eff}}$ and V_{eff} from Fig. 6.11. *Right*: A plot of $N_{0,\mathrm{long}}$ from the double exponential decay model versus the cut-off energy of the absorber E_{cutoff} for four different absorber heights. This is used to determine the integrated UCN spectrum. The line-of-best-fit (red line)was found to be $N_{0,\mathrm{long}} = (3.5 \pm 1.5) \times 10^{-5}\, E_{\mathrm{max}}^{(3.50 \pm 0.16)}$ ($\chi_\nu^2 = 0.3$). The green point ($\bigcirc$) comes from the decay curve measured without the absorber, where E_{cutoff} is not well-defined (see text). It is not used in the fit of the curve. The two other curves shown with red dashed lines ($--$) are best-fits with $\propto E_n^3$ and $\propto E_n^4$, the range of the systematic uncertainty used for the spectrum.

To test the validity of this approximation, data points using Eq. 6.8 with Poisson statistical errors added were generated and fitted with a single exponential decay. The fitted $\bar{\tau}_{\mathrm{tot}}$ and the ensemble average from Eq. 6.10 were compared for different shapes of the UCN spectrum dN_0/dE_n (discussed later), different forms of $\bar{\tau}_{\mathrm{walls}}^{-1}$ from calculations (Fig. 6.12), and different spacing and number of points on the decay curve. Simulated the size of the statistical errorbars in the current measurements, the two $\bar{\tau}_{\mathrm{tot}}$ agreed within the statistics of the fit. When the generated statistic errorbars were set to zero, it was found that the difference between the two were $\approx 0.1\,\mathrm{s}$. And when $\bar{\tau}_{\mathrm{walls}}^{-1}$ was increased by a factor of 10, the difference was $\approx 1\,\mathrm{s}$. Therefore, within the statistical accuracy of obtaining $\bar{\tau}_{\mathrm{tot}}$ from data fitting of this experiment, it can be well-approximated by the ensemble average. This is important since

from Eq. 6.10, it is evident that:

$$\bar{\tau}_{\text{tot}}^{-1} \approx \tau_\beta^{-1} + \int_0^{E_{\max}} \frac{dN_0}{dE_n} \tau_{\text{walls}}^{-1}(E_n) \, dE_n \bigg/ \int_0^{E_{\max}} \frac{dN_0}{dE_n} \, dE_n$$

$$\approx \tau_\beta^{-1} + \bar{\tau}_{\text{walls}}^{-1} \, . \tag{6.12}$$

And so the wall losses can be defined as an ensemble average $\bar{\tau}_{\text{walls}}^{-1}$, which can be calculated from the measured form of $n_0(E_n)$ and the calculated τ_{walls}^{-1}. After this is done, τ_β can be extracted.

6.2.4   UCN spectrum in the trap

The initial spectrum in the trap can be deduced with the $N_{0,\text{long}}$ values from the double exponential sum model. If we assume that the cleaning was sufficient so that $m_n g h_{\text{cutoff}} \equiv E_{\text{cutoff}} = \max E_n$, where h_{cutoff} is the height of the absorber from the bottom of the trap, then $N_{0,\text{long}}$ gives the initial ($t = 0$) integrated spectrum:

$$N_{0,\text{long}} = N_0(E_n < E_{\text{cutoff}}) = \int_0^{E_{\text{cutoff}}} \frac{dN_0}{dE_n} \, dE_n \, . \tag{6.13}$$

Of course, there is a time-evolution of the spectrum to the times when $N_{0,\text{long}}$ is measured due to the energy-dependent wall losses τ_{walls}^{-1}. Similar to that done in the last section, computer generated data from Eq. 6.8 with the calculated τ_{walls}^{-1} is used to estimate the systematic shift in the fitted N_0 value due to spectral shaping. It was found that if only points at $t > 300 \, \text{s}$ are used, then there's a shift in N_0 of < 0.002 counts per fill. And if only points with $t > 1000 \, \text{s}$ are used, then the shift is around 5 times larger. Therefore, the systematic shift due to spectral shaping in the determination of the integral spectrum is negligible in these measurements.

A plot of the $N_{0,\text{long}}$ values are shown in Fig. 6.12. In addition to the two measurements with the absorber at $65 \, \text{cm}$ and $80 \, \text{cm}$, there were two more measurements made at $35 \, \text{cm}$ and $50 \, \text{cm}$. However, due to the low counts, the latter two provide only a good estimate for $N_{0,\text{long}}$ and not for τ_{long}. A fit of the four points with a power function gives $N_0(E_n < E_{\text{cutoff}}) = (3.5 \pm 2.5) \times 10^{-5} E_{\text{cutoff}}^{(3.50 \pm 0.16)}$ with $\chi_\nu^2 = 0.2$. A uncertainty of $\pm 1 \, \text{neV}$ was added to the E_{cutoff} of each of point in the fit to model the uncertainty of the position of the paddle due to its position and the protruding stainless steel.

The additional $N_{0,\text{long}}$ value from the measurements with no absorber is also shown in the plot. However, this is not used for the fit since the cleaning of above-threshold UCNs is not very efficient for this measurement and it is difficult to assign the E_{cutoff} value, since E_{trap}, as discussed previously, is not clearly defined. Indeed, finding the best value of E_{trap} comes from observing where this point fits on the trend of data. The point shown on the plot is placed at $E_{\text{cutoff}} = 84\,\text{neV}$ gives a good estimate for E_{trap}.

The form of the integrated spectrum $N_0(E_n < E_{\text{max}}) \propto E_n^{(3.50\pm0.16)}$ can be explained if the differential spectrum from the source is dN_{source}/dE_n is approximately $\propto E_n^{0.9}$. From Ref. [GRL91], the differential spectrum $dN_0/dE_n \propto V_{\text{eff}}(E_n)(dN_{\text{source}}/dE_n)$. For a vertical cylindrical trap with material sidewalls $V_{\text{eff}} = 2E_n\pi\rho_{\text{trap}}^2/(3m_n g)$, i.e., it is proportional to E_n since UCNs can reach up to the fixed radius of the trap ρ_{trap} and the vertical gravitational potential is linear in E_n. However, for a magnetic potential with $|B| \propto \rho^3$, the maximum radial position a UCN can reach is $\propto E_n^{1/3}$. Hence, the expected form of the effective volume for a vertical ideal octupole trap is $V_{\text{eff}} \propto E_n^{5/3}$. As shown in Fig. 6.11 the calculated V_{eff} values are very well approximated by $V_{\text{eff}} \propto E_n^{1.6}$ for $E_n > 20\,\text{neV}$. The deviations at lower energy and from the $E_n^{5/3}$ dependence most likely comes from the decrease in $|B|$ at the end of the octupole array.

Therefore, if the differential spectrum from the source is $dN_{\text{source}}/dE_n \propto E_n^{0.9}$, then this results in $N_0(E_n < E_{\text{max}}) \propto E_n^{(3.50\pm0.16)}$. The spectrum from the turbine is expected to be $dN_{\text{source}}/dE_n \propto E_n^{1/2}$ from constant phase space density. However, there are absorption losses in the Al foil, which is higher for UCNs with lower E_n. As mentioned in Sec. 5.2, a spectrum of $dN_{\text{source}}/dE_n \propto E_n^{1/2} \propto E_n$ was measured for a superfluid helium source [Mat08, Mat09]. The observation here is closer to the latter case. The systematic uncertainty in the form of the differential spectrum is taken into account in the extraction of τ_β.

6.2.5 Extracting the neutron lifetime with systematic corrections

The value of the storage time of the well-trapped UCNs $\bar{\tau}_{\text{tot}}$ will be chosen to be τ_{long} from the double exponential decay model. The values of τ_{long} compare well from the storage times to the time channel chopping analysis within the statistical errors (see Fig. 6.7a, 6.7b and 6.8).

The observed total storage time rate constant is made up of:

$$\bar{\tau}_{\text{tot}}^{-1} = \tau_{\beta}^{-1} + \bar{\tau}_{\text{depol}}^{-1}(E_n) + \bar{\tau}_{\text{walls}}^{-1}(E_n) + \tau_{\text{gas}}^{-1} + \bar{\tau}_{\text{abv. thres}}^{-1} \; . \qquad (6.14)$$

For these measurements $\bar{\tau}_{\text{depol}}^{-1}$ is negligible within the statistical errors. The loss on the fomblin surfaces $\bar{\tau}_{\text{walls}}^{-1}$ is the largest loss (besides τ_{β}^{-1}) and can be calculated if the differential spectrum (see previous subsection) is known and an isotropic UCN gas assumed. Both of these are UCN energy-dependent. The loss rate due to residual gas can be calculated if the gas pressure and composition is known (see Sec. 5.8). This correction is much smaller than the statistical errors also. The shortening of the observed $\bar{\tau}_{\text{tot}}^{-1}$ caused by ineffective cleaning of long-surviving marginally trapped UCNs is modeled by $\bar{\tau}_{\text{abv. thres}}^{-1}$. The size of this depends on the additional $N'_{0, \text{short}} e^{t/\bar{\tau}_{\text{clean}}}$ decaying exponential component to $N(t)$. Since $\bar{\tau}_{\text{clean}}$ is comparable in size to τ_{β}, and due to finite statistics, it is difficult to fit for $\bar{\tau}_{\text{abv. thres}}^{-1}$. It is also difficult to calculate this *a priori*. Its general effect is to shift the τ_{β} extracted from the data so that what is observed is in fact $\tau_{\beta}'^{-1} = \tau_{\beta}^{-1} + \tau_{\text{abv. thres}}^{-1}$.

$\tau_{\text{abv. thres}}^{-1}$ will be large if the population of above threshold UCNs just above E_{trap} is large. This is potentially the case for the no absorber and $80\,\text{cm}$ absorber measurements due to the inefficient cleaning at E_{trap}. It is this effect we wish to study. A plot of the values of $\bar{\tau}_{\text{tot}}$ is shown in Fig. 6.13. There is perhaps a systematic shift beyond the statistical errors of $\bar{\tau}_{\text{tot}}$ suggesting that the cleaning is not that efficient for the no absorber measurement, as expected.

A calculation of $\bar{\tau}_{\text{walls}}^{-1}$ comes from Eq. 6.4, which requires $V_{\text{eff}}(E_n)$, $A_{\text{loss, eff}}(E_n)$, and dN_0/dE_n. The former two quantities are calculated based on the potential energy E_{pot} of the trap, which includes the magnetic field distribution, the physical dimensions of the trap, and the fomblin grease properties. The latter is divided into V_{fomblin} and f_{fomblin}. The calculation of $\bar{\tau}_{\text{walls}}^{-1}/f_{\text{fomblin}}$ is shown in Fig. 6.12. To extract $\bar{\tau}_{\text{walls}}^{-1}$, this is averaged over the UCN differential spectrum (Eq. 6.12). The estimated systematic errors in the calculations are:

- *The energy-independent loss factor of fomblin*: The only measurement (known to the author) of f for fomblin grease (Solvay Solexis RT-15) was done in Ref. [Ric91], where an energy-independent loss factor $f = V/W = 1.85\,(10) \times 10^{-5}$ was found. The loss factor is strongly temperature-dependent with f changing by $\approx 3\,\%\,\text{K}^{-1}$ at room temperature. The

measurement was performed at 21°C ("room temperature" at PF2). The temperature in our measurements was $\approx$ 23°C (also "room temperature at PF2). Many more measurements have been made with fomblin oil. A review of the results is given in Ref. [PNHN08]. At room temperature, there are around 5–6 measurements which lie in the range between $f = 6.7\times10^{-6} \rightarrow 2.5\times10^{-5}$. They usually do not agree within the statistical error. Hence, relying on one measurement for fomblin grease is not a good idea. Instead, for the fomblin grease, I will take $f_{\text{fomblin}} = (1.6\pm0.9)\times10^{-5}$. This covers the range of values measured for fomblin oil, a good estimate of the systematic errors in these measurements, and it includes the one value measured for fomblin grease taking into account temperature variations of $\approx \pm10$°C.

- *The neutron optical potential of fomblin (the real part)*: The value of V_{fomblin} for the oil has been much more studied and is often quoted as 106.5 neV [LG02]. For the grease, a value of 107.5^{+1}_{-2} neV was quoted in Ref. [GRL91]. The two agree within the experimental limits. For the calculations, a conservative value of 107 ± 5 neV is used for estimating the systematic error.

- *The physical volume of the trap*: The bottom of the trap is not exactly flat, as can be seen in Fig. 6.5. The recess towards the piston has a diameter of 60 mm and is 7 mm deep, and thus a volume of 20 cm³. There might be variations in the physical dimensions of the magnets as well. A systematic error of ±100 cm³ was chosen, which would take into account this recess and variations in the diameter of the magnet bore of ±0.6 mm, as well.

- *UCN spectrum*: The integrated spectrum $N_0(E_n < E_{\text{cutoff}}) \propto E_{\text{cutoff}}^{(3.50\pm0.16)}$ extracted directly from the data implies that the differential spectrum from the source $n_{\text{source}} \propto E_n^{0.9}$. This falls in the possible range expected from a UCN source. For a conservative estimate of the systematic error from the knowledge of the spectrum, we let the integrated spectrum vary by $N_0(E_n < E_{\text{max}}) \propto E_{\text{cutoff}}^{(3.5\pm0.5)}$ (see the variation due to this systematic error in Fig. 6.12). This range covers the case of $n_{\text{source}} \propto E_n^{0.5}$.

- *Strength of the permanent magnets*: A was seen in the magnetic field

measurements of Sec. 4.1, the magnetization (or magnetic field strength at the walls) of the magnets can be as much as 5% lower than that calculated. The strength of the magnets used in the calculations was found by varying it until the value of $E_{\text{trap}} \approx 84 \, \text{neV}$ (obtained from the UCN integral spectrum measurements) matched up for 8 cm of fomblin grease up the side walls. Since the $A_{\text{loss, eff}}$ from the sidewalls is small compared to the bottom, changing the strength of the magnets does not have a large effect. Variations of the strength at the walls also has a slight variation of the effective volume V_{eff}. A conservative variation of $\pm 10\%$ in the magnetization strength of the magnets is assumed for the error calculations.

- *Residual gas loss*: The calculation of the gas losses in pure hydrogen H_2 from Eq. 5.22 over estimates the value of τ_{gas}^{-1} from Ref. [Ser05, Ser08]. A shift of $\Delta\bar{\tau}_{\text{tot}} \approx 1 \, \text{s}$ is expected for $5 \times 10^{-6} \, \text{mbar}$ at $113 \, \text{K}$ instead of the $0.40 \pm 0.02 \, \text{s}$ quoted. A gas composition of $\approx 30\%$ hydrogen and $\approx 70\%$ helium (both natural abundances) would be needed to explain this small τ_{gas}^{-1}. Using this equation for pure hydrogen for the vacuum conditions of the current experiment, $5 \times 10^{-5} \, \text{mbar}$ at $300 \, \text{K}$, gives $\tau_{\text{gas}}^{-1} = 6 \times 10^{-6} \, \text{s}^{-1}$ or $\Delta\bar{\tau}_{\text{tot}} \approx 5 \, \text{s}$. Using the measured $P\tau_{\text{gas}} = 9.5 \pm 0.5 \, \text{mbar} \cdot \text{s}$ at $113 \, \text{K}$ from Ref. [Ser08] (after scaling for the temperature and pressure) gives $\tau_{\text{gas}}^{-1} \approx 3 \times 10^{-6} \, \text{s}^{-1}$. A conservative value for $\tau_{\text{gas}}^{-1} = (4.5 \pm 1.5) \times 10^{-6} \, \text{s}^{-1}$, with a systematic error that cover the range from both these values, will be used.

The evaluation of the effect of these systematic errors comes from varying the parameters and seeing the effect on the calculated τ'_β. The sizes of the systematic and statistical errors are shown in Table 6.2. The values of the extracted τ'_β are shown in Fig. 6.13.

The values of τ'_β determined from the analysis on the experimentally measured $\bar{\tau}_{\text{tot}}$ all agree with the recommended values of τ_β from the Particle Data Group (Ref. [Ber12, Nak10]). This is mainly due to the large error bars of the current experiment. Half of which comes from the statistics of the experimental data, and the other half comes from a conservative estimate of the systematics. The dominant systematic by far is from the energy-independent loss factor of fombin f_{fomblin}.
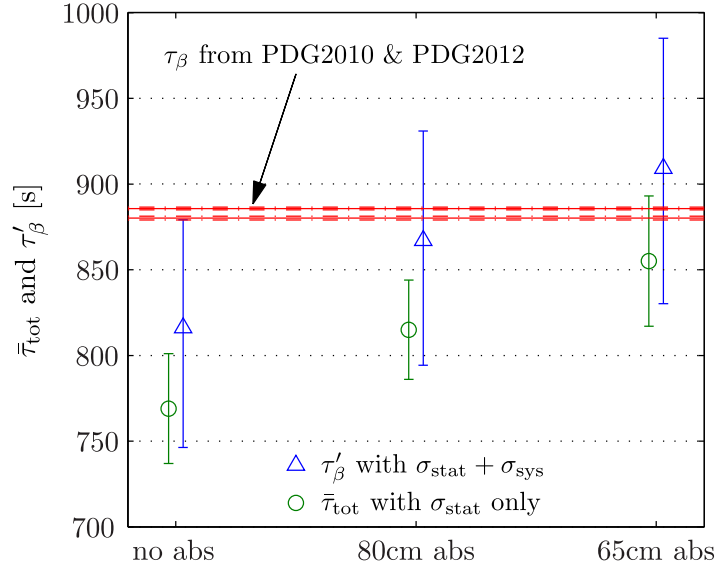
Figure 6.13: The observed $\bar{\tau}_{\text{tot}}$ with statistical error bars for the measurements with no absorber, 80 cm absorber, and 65 cm absorber as measured from the bottom of the vertical magnetic trap. Just to the right of these are the extracted values of τ'_β, where $\tau_\beta'^{-1} = \tau_\beta^{-1} + \tau_{\text{abv. thres}}^{-1}$, where $\tau_{\text{abv. thres}}$ is a parameter that models the effect of above-threshold, marginally trapped UCNs. A table of the systematic errors are shown in Table 6.2 and discussed in the text. The largest correction is from wall losses on the fomblin grease $\bar{\tau}_{\text{walls}}^{-1}$. The (conservatively) estimated systematic errors are added together linearly with the statistical error bars. Differences between the values for different absorber positions could be due to the ineffectiveness of the cleaning procedure, causing an increase of $\tau_{\text{abv. thres}}^{-1}$ from right to left. The recommended values and error bars (too small to be seen in the plot) for τ_β from the Particle Data Group's reviews in 2010 and 2012 ([Nak10] and [Ber12]) are also shown.

Table 6.2: A table of the loss rate constants from Eq. 6.14 for the three measurements. The statistical uncertainty and the estimated systematic errors are given also. A description of the latter are given in the text. This allows the extraction of τ_β and associated errors. This is plotted in Fig. 6.13.

	no abs.	80 cm abs.	65 cm abs.	
$\bar{\tau}_{\mathrm{tot}}$:	**769 s**	**815 s**	**855 s**	
$\bar{\tau}_{\mathrm{tot}}^{1}$:	1.300	1.227	1.170	$\left[\times 10^{-3}\,\mathrm{s}^{-1}\right]$
$\bar{\tau}_{\mathrm{walls}}^{-1}$:	7.0	7.4	7.5	$\left[\times 10^{-5}\,\mathrm{s}^{-1}\right]$
τ_{gas}^{-1}:	0.45	0.45	0.45	$\left[\times 10^{-5}\,\mathrm{s}^{-1}\right]$
$\tau_{\beta}^{\prime -1}$:	1.227	1.150	1.092	$\left[\times 10^{-3}\,\mathrm{s}^{-1}\right]$
$\tau_{\beta}^{\prime}$:	**815 s**	**870 s**	**916 s**	
statistical error:				
$\sigma_{\mathrm{stat}}(\tau_{\beta}^{\prime -1})$	±5.4	±4.4	±5.2	$\left[\times 10^{-5}\,\mathrm{s}^{-1}\right]$
$\sigma_{\mathrm{stat}}(\tau_{\beta}^{\prime})$	**36 s**	**33 s**	**44 s**	
systematic error:				
fomblin f	+3.9/−4.1	+3.9/−4.3	+4.3/−4.3	$\left[\times 10^{-5}\,\mathrm{s}^{-1}\right]$
fomblin V	+1.9/−2.4	+2.5/−2.7	+3.1/−2.3	$\left[\times 10^{-6}\,\mathrm{s}^{-1}\right]$
effective volume	+0.02/−7.8	+0.4/−6.1	+1.3/−5.4	$\left[\times 10^{-6}\,\mathrm{s}^{-1}\right]$
magnetic field	+0.1/−4.7	+2.0/−6.1	+3.6/−6.2	$\left[\times 10^{-7}\,\mathrm{s}^{-1}\right]$
UCN spectrum	+2.4/−11	+4.4/−11	+9.9/−7.1	$\left[\times 10^{-7}\,\mathrm{s}^{-1}\right]$
residual gas	±1.5	±1.5	±1.5	$\left[\times 10^{-6}\,\mathrm{s}^{-1}\right]$
$\sigma_{\mathrm{sys}}(\tau_{\beta}^{\prime -1})$	+4.3/−5.4	+4.4/−5.5	+5.0/−5.4	$\left[\times 10^{-5}\,\mathrm{s}^{-1}\right]$
$\sigma_{\mathrm{sys}}(\tau_{\beta}^{\prime})$	**+29 s/−36 s**	**+33 s/−42 s**	**+42 s/−45 s**	

After correcting for all the systematic effects and error, the $\tau_\beta^{\prime}$ values from no absorber, 80 cm absorber and 65 cm absorber measurements all agree with each other, i.e., the size of $\bar{\tau}_{\mathrm{abv.\,thres}}$ is too small to be observed. Measurements with higher statistical precisions would be needed in order to start clearly observing the effects of poor cleaning.

For the measurement with the absorber at 65 cm, the calculated $\tau_{\mathrm{clean}} \approx 3\,\mathrm{s}$ at $E_{\mathrm{trap}} \approx 84\,\mathrm{neV}$ for an isotropic UCN gas. The cleaning with the absorber in place was $> 80\,\mathrm{s}$. Therefore, it is quite certain that the cleaning for this measurement is very efficient so that $\tau_{\mathrm{abv.\,thres}}^{-1} \approx 0$, hence $\tau_{\beta}^{\prime} \approx \tau_{\beta}$, within the error bars of the experiment. The best estimate of the neutron lifetime from this experiment is $\tau_\beta = 921 \pm 44_{\mathrm{stat}} \pm 50_{\mathrm{sys}}\,\mathrm{s}$.

This is a reasonable result from approximately 1 week of measurement

time on the TEST beam of PF2 where only $\approx$ 80 well-trapped UCNs are filled in the trap for E_n < 66 neV. (This is increased to $\approx$ 170 UCNs for E_n < 82 neV.) Improvements can still be made by using better UCN gate valves and raising the trap even higher. The number of points on the decay curve can be reduced too. The other UCN beams at PF2 offer $\approx$ 20 times more UCNs with a "softer" spectrum as well. Unfortunately, during the 1st experiment, although performed on the EDM beam of PF2, the Richardson spectrometer was used between the source and the trap; therefore, no realistic estimate of UCN numbers can be concluded from this. Future superthermal UCN sources, such as the SUN2 source, would help future improve the statistical precision.

Chapter 7

HOPE: Charged particle detection

7.1 Motivation

A measurement of the neutron lifetime can be made by detecting the electrons and protons produced after the β-decay of a neutron:

$$n \rightarrow p^+ + e^- + \bar{\nu}_e \; . \tag{7.1}$$

Since it is a three-body decay, the products have a continuous energy distribution with means and endpoints of: $360\,\mathrm{eV}$ and $750\,\mathrm{eV}$ for the protons; $300\,\mathrm{keV}$ and $780\,\mathrm{keV}$ for the electrons; and $500\,\mathrm{keV}$ and $780\,\mathrm{keV}$ for the anti-neutrinos. The distribution for the protons and electrons are shown in Fig. 7.1. The anti-neutrino, due to the difficulties in detection, will not be considered in the discussion.

The rate of detected charged particles $\dot{N}_{\mathrm{det}}(t)$—if ignoring the time it takes for them to reach the detector, which is much shorter than τ_β—is given by:

$$\dot{N}_{\mathrm{det}}(t) = \epsilon_{\mathrm{det}} \tau_\beta^{-1} N(t) \; , \tag{7.2}$$

where ϵ_{det} is the detection efficiency (discussed later), and $N(t)$ is the number of UCNs remaining in the trap. The change in the number of UCNs in the
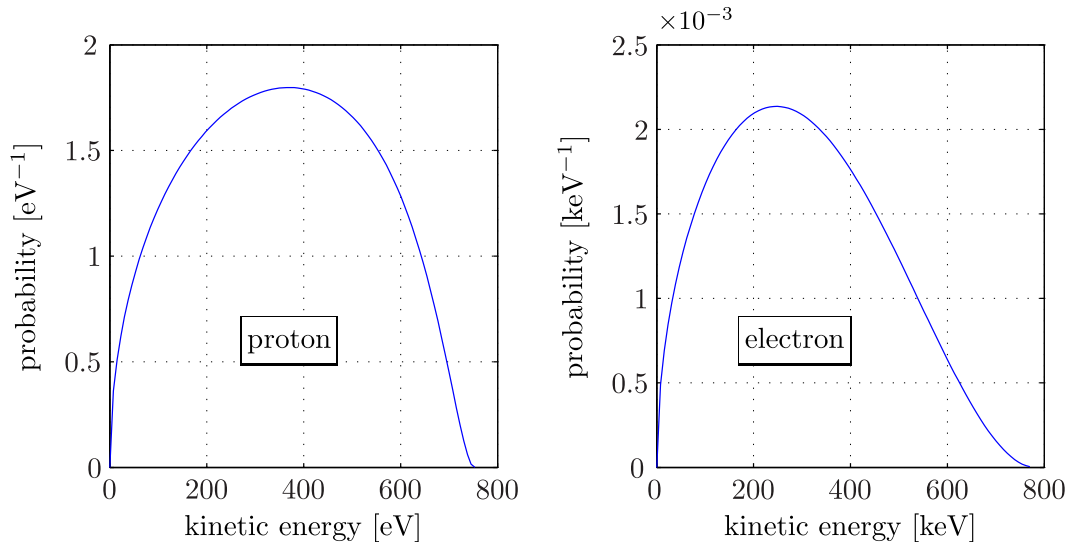
Figure 7.1: The energy spectrum of the protons and electrons produced from neutron β-decay. The expressions for the spectra are taken from Ref. [Sim10]. The electron antineutrino angular correlation $a = -0.103$ (the present world average) in the former; and the Fermi function $F(E) = 1$ in the latter.

trap depends on the total storage time $\bar{\tau}_{\text{tot}}^{-1}$ so that:

$$\dot{N}_{\text{det}}(t) = \epsilon_{\text{det}} \tau_\beta^{-1} N_0 \exp(-t/\bar{\tau}_{\text{tot}}) \, , \tag{7.3}$$

where N_0 is the initial number of UCNs in the trap. Therefore, the time-dependence of the count rate of charged particles $\dot{N}_{\text{det}}(t)$ depends not on τ_β^{-1} but on $\bar{\tau}_{\text{tot}}^{-1}$. The same as for a fill-and-empty or "*count the survivors*" measurement.

The main advantage of detecting the charged decay products in-situ, as discussed in Sec. 5.6, is that $\dot{N}_{\text{det}}(t)$ can be continuously measured for every fill of the trap. In principle, $\bar{\tau}_{\text{tot}}$ can also be extracted from every fill as well. It is also possible to sum up the data from different decay curves and extract $\bar{\tau}_{\text{tot}}$ from this—even if N_0 or the starting time $t = 0$ has varied between the different curves. These variations just change the multiplication factor in the fit and not $\bar{\tau}_{\text{tot}}$ itself. The detection efficiency ϵ_{det} and the differential spectrum of UCNs needs to remain constant over the duration of a decay curve measurement though.

The argument can be made that there is a reduction of experimental time

compared to the fill-and-empty procedure for obtaining the same statistical precision. However, this will depend on the efficiency of the charged particle detection and how many points on the decay curve one measures with the fill-and-empty procedure. The standard number in other experimemts is around 2–3 only. However, from in-situ detection the time can be recorded for every count (called "event mode data"). Thus, the time bin widths and cuts in time can be varied in the post-experiment data analysis. This gives more tools for searching for unknown systematic effects.

The in-situ detection of the charged products for a neutron lifetime experiment was performed in Ref. [Huf00]. Here, the scintillation light produced in the superfluid helium permeating the magnetic trap is used for the detection. A detection efficiency of $31\pm4\%$ was estimated in an early version of this experiment. In our experiment, we plan on extracting the charged particles before detecting them. In this section, results from the simulations of the trajectories of the protons and electrons in the trap are presented. This is done to show that extraction of charged particles is possible with this trap. The technical difficulties and systematic errors that may be present when detecting the electrons or protons are compared and discussed. Finally, ideas for the detection system are mentioned.

7.2   General behavior of charged particles

The final products have much higher energies than the UCNs due to the mass difference between the initial neutron and the final products, hence the gravitational potential of $\approx 100\,\mathrm{neV\,m^{-1}}$ and $0.06\,\mathrm{neV\,m^{-1}}$ for the proton and electron, respectively, is negligible. So if the top of a magneto-gravitational trap is left open (i.e., there is no magnetic mirror here) then the protons and electrons will escape from there. Similarly, the potential energies of the protons' and electrons' magnetic moments with the magnetic field gradient of the trap $E_{\mathrm{mag}} = |\mu|.|B|$ are only $90\,\mathrm{neV\,T^{-1}}$ and $60\,\mathrm{\mu eV\,T^{-1}}$, respectively. Therefore, like gravity, this is negligible. By far the largest interaction comes from interaction of the electric charge with the magnetic field (and possibly electric fields).

The non-relativistic equations of motion (in SI units) of a charged particle at position $\vec{x}$ with charge q, mass m and velocity $\vec{v} = d\vec{x}/dt$ in a magnetic field

$\vec{B}$ and electric field $\vec{E}$ is given by:

$$\frac{d^2\vec{x}(t)}{dt^2} = \frac{q}{m}\left(\vec{E} + \vec{v} \times \vec{B}\right) .$$ (7.4)

This is sufficient to describe the general motion of the particle in external electromagnetic fields (neglected the emission of radiation). The simulations of the trajectories of charged particles in the magnetic trap come from numerically integrating this equation. Here I describe some special cases to help understand the general motion. These properties can be found in many references, including Ref. [Jac98], which is perhaps the most notable.

In a constant magnetic field and no electric field, the longitudinal motion $v_\parallel$, defined as the velocity parallel to $\vec{B}$, remains unchanged. The motion in a plane transverse to $\vec{B}$ is circular with a radius r:

$$r = \frac{mv_\perp}{qB} = \frac{\sqrt{2mE_\perp}}{qB} ,$$ (7.5)

where $E_\perp \equiv mv_\perp^2/2$. The charged particle follows a helical trajectory, with the sign of the helicity of the motion determined by the sign of the charge q. When the charged particles are near the center of the trap, where they see predominately the bias field along the z-axis, this is the motion they are expected to take. The radius is large when the energy in the transverse mode is large. When all the energy is in $E_\perp$, the mean and maximum radius in a $0.3\,\mathrm{T}$ for protons are both $\approx 1\,\mathrm{cm}$; and for electrons, it is around 30% smaller.

Now suppose $|\vec{B}|$ is not constant, but increases in strength slowly (adiabatically) along the z-direction. The charged particle initially sits in the field B_bias with an initial velocity components $v_{\parallel 0}$ and $v_{\perp 0}$. It follows a helical trajectory towards the direction of increasing field so that at some point later it is in a field of B with velocity components $v_\parallel$ and $v_\perp$. If the variation in B is small over the scale of the motion of the charged particle, then two adiabatic invariants of the motion are:

$$Br^2 \quad \text{and} \quad m^2v_\perp^2/B ,$$ (7.6)
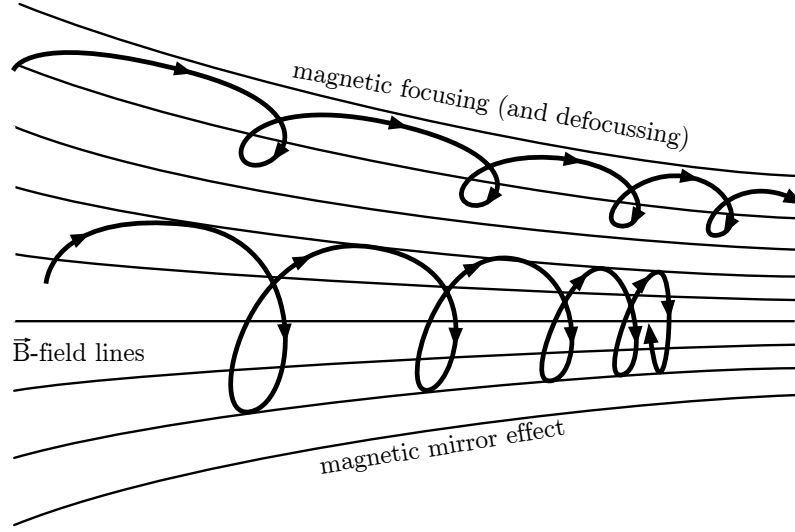
Figure 7.2: A sketch illustrating how a magnetic field strength can be used to reflect particles, due to the magnet mirror effect, and for focussing them to an small area (or defocussing when the motion is in reverse).

where $v_\perp$ is the transverse velocity. Then, from the latter,

$$\frac{v_{\perp 0}^2}{B_{\text{bias}}} = \frac{v_\perp^2}{B} . \tag{7.7}$$

However, since there is no electric field present, the total kinetic energy is conserved:

$$\frac{1}{2}m(v_{\perp 0}^2 + v_{\parallel 0}^2) = \frac{1}{2}m(v_\perp^2 + v_\parallel^2) \Rightarrow v_\perp^2 = v_{\perp 0}^2 + v_{\parallel 0}^2 - v_\parallel^2 . \tag{7.8}$$

Therefore,

$$v_\parallel^2 = (v_{\perp 0}^2 + v_{\parallel 0}^2) - v_{\perp 0}^2 \frac{B}{B_{\text{bias}}} . \tag{7.9}$$

As B increases, the particle's velocity parallel to $\vec{B}$ will decrease. At some stage $v_\parallel^2 = 0$ when $B = B_{\text{mirror}}$. After this point, $v_\parallel$ will reverse direction so that it becomes reflected. This is called the *magnetic mirror effect*. The field required to reflect a particle B_{mirror} depends on the ratio of the parallel and transverse kinetic energies, i.e., $B_{\text{mirror}}/B_{\text{bias}} = 1 + v_{\parallel 0}^2/v_{\perp 0}^2$. Also, since Br^2 is an adiabatic invariant, the helical gyration radius will decrease as B increases by $r/r_0 = \sqrt{B_{\text{bias}}/B}$.

When the charged particles are near the sides of the trap, the magnetic field is dominated by the octupole. The charged particles will gyrate and follow the field lines towards the side walls of the trap. Fortunately, due to the increasing field strength of the octupole, the magnetic mirror effect can reflect them back towards the center of the trap, preventing from being lost. Of course, whether the mirror reflection occurs or not depends on the field strength at the wall and the ratio between the longitudinal and transverse energy. Another region where the magnetic mirror effect is important is at the end coil if it is ramped up. Due to the increasing $|B|$ when approaching the end coils, the charged particles can reflect off there.

The magnetic mirror effect can not reflect all charged particles that are produced. If it is produced near a magnetic pole of the octupole and has its initial velocity directed towards the wall (i.e. $v_\parallel$ is large) or if it is produced close to the center of the trap and has an initial velocity directed towards the end solenoid, then it will not be magnetically reflected. This is where a Monte-Carlo simulation can be used to give an indicate of how often this will occur to give us an idea of the collection efficiency. Furthermore, the discussion so far has relied on the adiabatic (slowly changing magnetic field) approximation. If the trajectory simulations integrate directly the equation of motion, Eq. 7.4, then non-adiabatic effects will be taken into account as well.

From the discussion above, it may seem like the ideal scheme is to have one end coil ramped up—usually the small end coil used for filling the trap since it is hard to place a detector here—and the other ramped down so that the charged particles can escape and be detected. However, if it is protons that are to be detected, then it is expensive to have a detector covering the entire cross-section of the trap ($\approx 9\,\text{cm}$ diameter or $65\,\text{cm}^2$). This is especially true since a detector with low noise, e.g. the silicon drift detector (SDD) of aSPECT, is required due to the low expected rate of protons. To focus the charged particles on to a smaller area, the large end solenoid can be used so that the focussing field here is $B_\text{focus} > B_\text{bias}$. If the multipole field is neglected, as well as the effects from the smaller gyration radii, then the area over which the charged particles exists is reduced by a factor of $(B_\text{bias}/B_\text{focus})^2$. If the bias field $B_\text{bias} = 0.3\,\text{T}$, then a focussing field B_focus of $\approx 0.9\,\text{T}$ is needed to focus from the trap's circular cross-section with a diameter of $9\,\text{cm}$ to one of $3\,\text{cm}$ (so that they fit on a 3×3 array of aSPECT SDDs that have a dimension of

$1\,\text{cm} \times 1\,\text{cm}$). Similarly, to focus onto a region with diameter of $1\,\text{cm}$ (one SSD detector), $\approx 0.9\,\text{T}$ is required. Note these estimates neglect the octupole radial field.

However, if $B_{\text{focus}} > B_{\text{bias}}$ then the threshold for a magnetic mirror reflection $1 + v_{\parallel}^2/v_{\perp}^2$ will be lower, so that a greater number of charged particles won't be able to reach the detector. This can be overcome by using electric fields. If a series of ring electrodes concentric to the z-axis of the magnetic trap and placed at successively higher voltages as they get closer to the large end coil and detector, then the energy of the charged particles in the z-direction, and thus $v_{\parallel}$, can be increased. The highest voltage required to overcome the magnetic mirror occurs when all the initial kinetic energy of the particle is in the transverse mode $E_{\perp}$. For this case the potential required is $U_{\text{extract}} = (B_{\text{focus}}/B_{\text{bias}} - 1)E_{\perp}$. For a proton, which can have a maximum energy of $750\,\text{eV}$, and for $B_{\text{focus}}/B_{\text{bias}} = 2.7\,\text{T}/0.3\,\text{T}$, the voltage needed is $U_{\text{extract}} = 6\,\text{kV}$. An acceleration voltage of $\approx 10\,\text{kV}$ is required for efficient detection of the protons anyway. This technique is not possible for the electrons, however. Their maximum energy is $780\,\text{keV}$. Therefore a voltage of $U_{\text{extract}} = 7\,\text{MV}$ is needed. This is technically not feasible to achieve.

If the large end coil is ramped up for focussing protons, then the electrons can remain for very long times in the trap. These trapped electrons can cause ionization in the residual gas of the vacuum. The ions produced, initially with low energies, will be accelerated by the ring electrodes and produce similar signals to the protons in the detector. This will cause a false proton count and thus produce a time-dependent systematic effect in the counts. An estimate of the ionization rate is given in Sec. 7.5.

Another use of electric fields in this configuration is to have them perpendicular to the B-field lines. When this is done, a charged particle will experience the "$E \times B$ force", which is a force that is perpendicular to $\vec{E}$ and $\vec{B}$ regardless of the velocity $\vec{v}$. The effectiveness of the force depends on the time spent near the electric field, therefore it is more effective for the protons. A design to aid in the extraction of the protons—by placing an electric octupole field offset from the magnetic octupole so that a $\vec{E} \times \vec{B}$ is always pointed towards the detector—is discussed in the next section.

Finally, also worth mentioning is the *inverse magnetic mirror effect*, where a particle moves from a stronger B-field towards a region of weaker field. This is
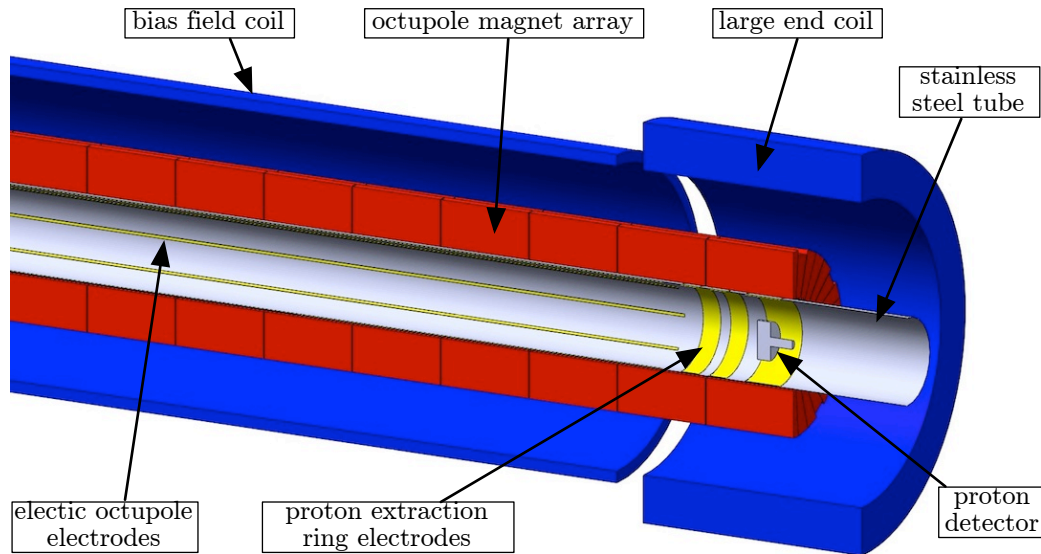
Figure 7.3: A proposed setup for detecting protons by focussing them on to a small detector. The large end coil needs to be ramped up so that $B_{\text{focuss}} > B_{\text{bias}}$ (see text). To over come this magnetic mirror effect, ring electrodes are used to increase the axial velocity $v_\parallel$ of the protons. The electric octupole electrodes are used to apply a $E \times B$ drift force towards the detector. This helps for extracting protons with most of its energy in the transverse mode. The inner stainless steel of the trapping volume is shown. The material electrically insulating electrodes from the tube is not shown.

also sometimes called "*defocussing*". In this case, the energy in the transverse mode gets shifted to the longitudinal mode so that $v_\parallel$ is increased. A larger $v_\parallel$ reduces the reflection off the front windows or surfaces of the charged detector, especially important for electrons. This increases the detection efficiency and reduces the problems of trapped charged particles. This can be done by having large end coil at a lower field strength than the bias coil.

7.3 Detection of protons

7.3.1 Proton trajectory simulations

Simulations were made tracking the trajectory of the protons in a uniform axial bias field B_{bias} and infinitely long, ideal radial octupole field with $1.3\,\text{T}$ at the inner walls of $46.8\,\text{mm}$ radius. The end coils were not included. The non-
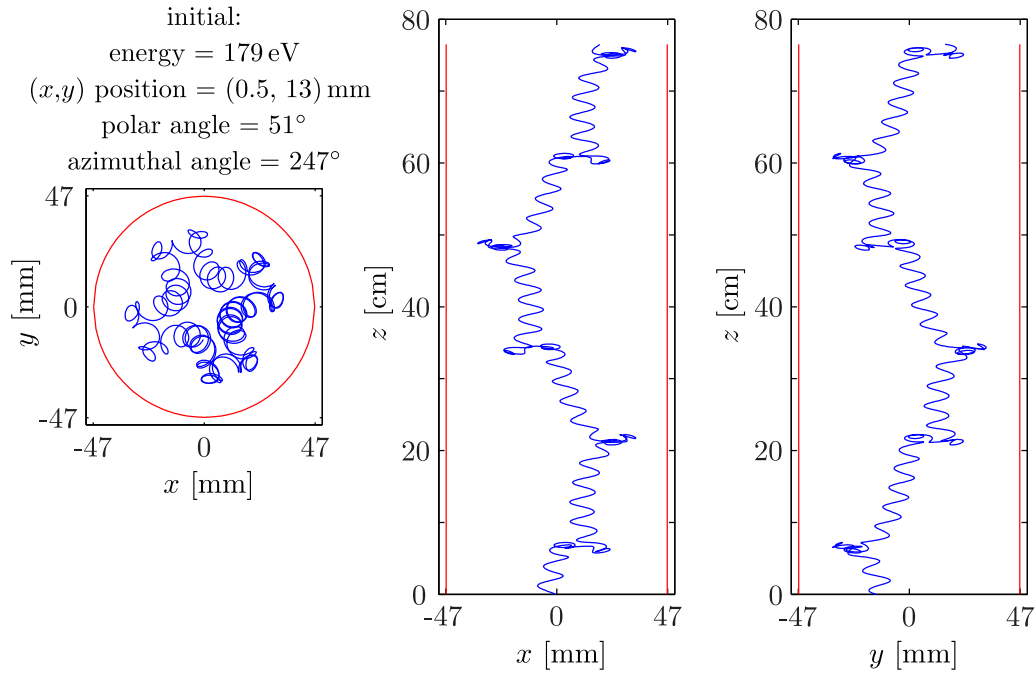
Figure 7.4: A proton trajectory from the simulations in a infinitely long octupole trap (see text for full description). The red solid lines (−) at $\rho = 46.8$ mm show where the side walls of the trap are placed. The trajectory is started in the $z = 0$ plane. The rest of the initial parameters are listed in the figure. The polar angle is measured from the positive z-direction and the azimuthal angle from the x-axis.

relativistic equation of motion from Eq. 7.4 was solved with a variable step-size Runge-Kutta (4,5) numerical integrator[1]. The relative tolerance parameter of the integrator was set to 10^{-4}, which produced integration step sizes of between 1–5 ns. Due to computing power limitations, the protons trajectories were followed for a maximum of 10 μs only. If the radius of their position exceeded that of the trap during the simulation time, then they are considered to have hit the wall (contributing to the "*hit wall*" percentage) and the simulation would be stopped. The conservation of energy was checked and found to be always better than 0.5%. An example of a trajectory is shown in Fig. 7.4.

In order to deduce properties about the ensemble of protons, their initial position, energy and direction were generated via Monte-Carlo techniques. Since β-decay is UCN energy independent, the initial position of the protons

---

[1]It is the routine from Ref. [DP80] implemented in MATLAB by Mathworks®.

are proportional to the density of the UCNs. If mechanical equilibrium is assumed, then, as discussed in Sec. 5.2, the total number of UCNs with energy up to E_{trap} at a radial position ρ due to the compression of phase space by the magnetic octupole is approximately given by:

$$N(\rho) \propto (E_{\text{trap}} - k\rho^3)^{3/2} \, \rho \, , \tag{7.10}$$

where $k = 1.3 \, \text{T}/(46.8 \, \text{mm})^3 = 1.5 \times 10^{-5} \, \text{T} \, \text{mm}^{-3}$. The distortion of E_{pot} from the bias field, since $|B(\rho)| = \sqrt{k\rho^3 + B_{\text{bias}}}$, is neglected. The number of UCNs at small ρ is reduced due to the reduction of the element $dV = \rho \, d\rho \, d\phi \, dz$. This approximation for the radial density for the UCNs is sufficient for the accuracy required for the simulations. From this distribution an initial radial position is generated, and combined with a random angle, the initial x and y coordinates can be found. The protons always start at the $z = 0$ plane. The problem is z-symmetric since the octupole is assumed to be infinitely long and there is no compression of phase space of the UCNs due to gravity (i.e., these approximations describe a horizontal trap, the originally intended configuration for the detection of the protons). The UCN is considered at rest when it decays. The initial proton energy is generated from the distribution of Fig. 7.1 and the initial direction is isotropic. Any effects on the initial proton energy due to the UCN velocity is negligible.

The effect of having the bias field $B_{\text{bias}} = 0.2 \, \text{T}$, $0.3 \, \text{T}$ and $0.4 \, \text{T}$ is shown in Fig. 7.5. Recall the definition of a "hit wall" proton being one that makes contact with the side walls of the trap within the $10 \, \mu\text{s}$ duration of the simulation time.

It can be seen that the hit wall percentage falls very quickly with increasing B_{bias}. The axial z positions and times at which the UCNs hit the wall, as well as their initial radial position, are shown in the plot. It can be seen that the majority of UCNs that hit the wall do so almost immediately ($< 1 \, \mu\text{s}$). Hence, their initial position and velocity determines to a large extent whether they will hit the wall or not. It can also be seen the majority hit the wall very close to their starting positions ($< 10 \, \text{cm}$). Therefore, the hit wall protons have most of their energy in the transverse mode and they have very little chance of reaching the end of the trap where they can be extracted and detected. The final plot on the figure is of the initial radial position $\rho(0)$ of the hit wall

protons. It can be seen, regardless of B_{bias}, protons created near the walls of the trap have a large, and roughly the same probability, of hitting the wall, as expected. The extra hit wall protons for small B_{bias} comes from the regions of smaller $\rho(0)$.

A proton not hitting the wall within $10\,\mu s$ does not imply it will become detected. From the plots of the axial position distribution with time, it can be seen that a lot of them remain around the $z = 0$ plane where they were created. However, they need to reach the end of the trap where detection (or extraction) occurs. To force them to travel axially, an octupole formed by electric fields can be used. By placing 8 long thin electrodes against the walls of the trap [2]. The electrodes can be placed at alternating high and low potentials so that an electric octupole with field lines always perpendicular to the magnetic octupole are produced. This provides an $E \times B$ drift force always directed towards one end of the trap, stopping protons from remaining fixed in the same axial plane.

To test the effectiveness of the electric octupole drift electrodes, simulations like those described above, were made with the added electric field for $B_{\text{bias}} = 0.3\,\text{T}$. The potential at the electrodes were placed at $U_{\text{octupole}} = \pm 1000\,\text{V}$, $\pm 3000\,\text{V}$ and $\pm 5000\,\text{V}$, where the $\pm$ denotes the positive and negative alternating potentials at adjacent octupoles[3]. The results of the simulations are shown in Fig. 7.6. The results with an ideal electric octupole and those with the electrodes simulated in FEMM were compared and found to be similar. The effects of increasing U_{octupole} is clearly evident in pushing the protons towards the positive z-direction. It occurs with only a modest increase in the hit wall percentage. Such an electrode system would be particularly useful for long traps.

The calculations shown here were done to demonstrate that the magnetic octupole combined with a sufficiently strong bias field is viable for confining protons. The efficiencies of the magnetic mirror reflection on one end of the

---

[2]The electrodes can be implemented by conductive copper strips on a thin film of Kapton®, a polyimide material from DuPont™. Copper is a standard coating and can be etched away to form the desired pattern. The electrodes would be electrically isolated from the conductive stainless steel inner tube by the kapton which has a resistivity of $1.4 \times 10^{17}\,\Omega\,\text{cm}$ at room temperature.

[3]Of course, half of the electrodes could also be grounded while the potential at the charged electrodes twice as large, i.e. using $0\,\text{V}$ and $+2000\,\text{V}$ on alternating electrodes is equivalent to $\pm 1000\,\text{V}$.
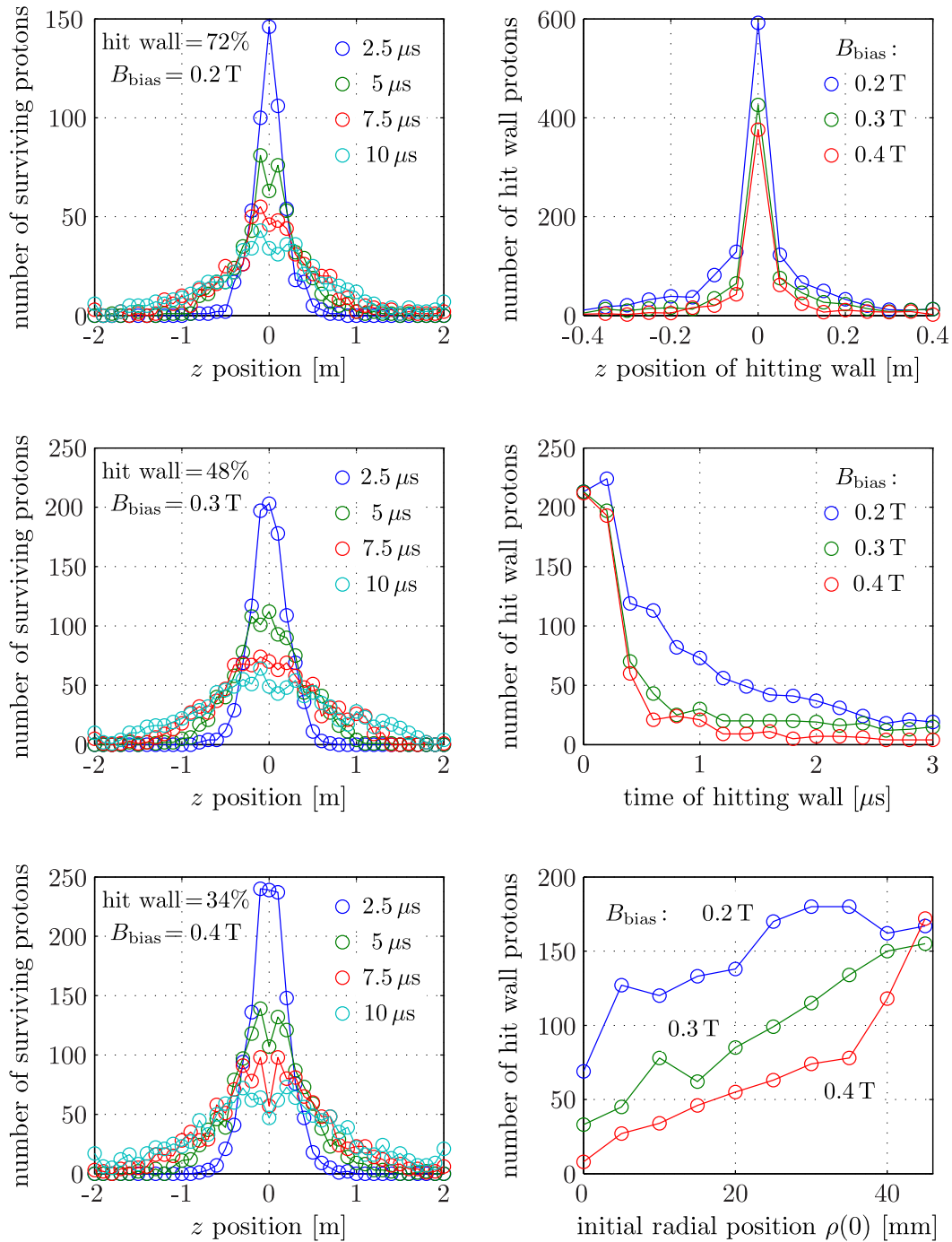
Figure 7.5: The properties of an ensemble of protons for different bias fields B_{bias} from the simulations. Each simulation contains 2000 protons. See the text for more details about the magnetic field configuration used in the simulations, the definition of a "hit wall" proton, the initial distribution and properties of the protons, and the conclusions derived from these plots.
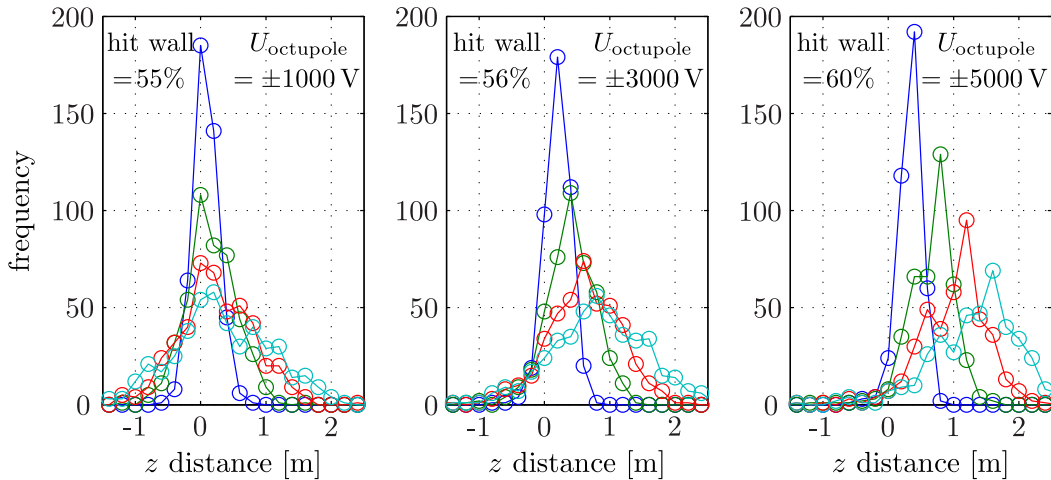
Figure 7.6: The effect of using the electric octupole $E \times B$ electrodes at increasing potentials. $U_{octupole}$ are the alternating voltages of the electrodes. Each simulation contains 1000 proton trajectories.

trap, and the extraction, focussing and detection on the other, are not included in these simulations. Nevertheless, the hit wall percentage does give a rough estimate for the probability for a proton to reach the extraction end of the trap. This is because most of the lost protons hit the wall in the first few microseconds and the simulations includes this time, and the protons that don't can be pushed towards one end of the trap with the electric octupole.

7.3.2   Using a MCP detector for proton detection

The Silicon Drift Detector (SDD) used in the aSPECT spectrometer experiment, as mentioned earlier, is great for the low proton acceleration required and its low noise characteristics (see Ref. [Sim07, Sim10] for more details about the detector). However, due to its small size, a field higher than B_{bias} at the large end coil is required for focussing the protons. This then would create a trap for the electrons which can produce ions in the residual vacuum and cause false counts in the detector—especially since acceleration electrodes are used for extracting the protons. An $E \times B$ cleaning electrode (similar to that used in aSPECT) could be used but it would affect the protons as well. To avoid the need for a focussing field, a proton detector with a larger surface could be used. A good separation from the electronic noise only occurred for

an incoming energy greater than $\approx 20-30\,$keV. Even for these high energies, the separation from noise is not as good as the SDD of aSPECT.

Due to the low count rates expected in the τ_β experiment, there is a stringent requirement on having a low noise and low background detector system. One way of significantly filtering out the false electronic noise and background counts would be to detect both the protons and electrons, the unique signature of a β-decay, in the detection system. This can be achieved with different detectors for the two different particles. Or it can be done with a single detector since the electrons should arrive $\approx 0-10\,\mu$s before the protons due to their higher velocities.

The detection of electrons by MCP detector was explored briefly. Spectra were taken with mono-energetic electrons with energies at $5\,$keV, $10\,$keV and $13\,$keV at the PAFF source. It was found that as the electron energy increases, the peak shifts to lower channels so that at $13\,$keV it was almost no longer resolved from noise. This was confirmed by measurements with a ^{90}Sr source, which has a β-spectrum with an average energy of $196\,$keV and an end-point of $546\,$keV. Hence, doing a coincident system in a single MCP detector is not possible. An idea of using a coincident system with separate detectors for the protons and electrons by using the MCP as a front detector and a plastic scintillator behind—forming a what's called "telescope" system— was also briefly explored. The protons can be detected by the MCP and the electrons, if the energy is large enough, can penetrate and pass-through the MCP completely and have sufficient remaining energy to be detected by the back detector. However, a measurement of the transmission of electrons from the ^{90}Sr source through the MCP-MA25 detector, which has two plates with a combined thickness of 0.5mm (material presumably similar to glass) and an metallic anode (unknown thickness), showed that no electrons were able to pass through. It might still be possible with a different design, for instance, a single MCP plate combined with a very thin plate or perhaps wires as anodes, though.

7.4 Detection of electrons

7.4.1 Electron trajectories

Simulations like those for the protons were done for the electron trajectories
also. It uses the same code that integrates the non-relativistic equation of
motion (Eq. 7.4) with a Runge-Kutta (4,5) integrator. The same magnetic
field configuration—infinitely long, ideal magnetic octupole with a bias field—
was also used. Due to the higher velocities of the electrons, smaller time
step-sizes of the integrator are needed. With the relative tolerance parameter
of the integrator set to 10^{-5}, step-sizes of $0.2-2\,\mathrm{ps}$ were used. The trajectories
were tracked for a total duration of $80\,\mathrm{ns}$ unless the electron was found to hit
the wall. The energy conservation of the electrons—like for the protons—are
found to be always better than 0.5%. The electrons trajectories resembled
those of the protons (an example of which is shown in Fig. 7.4), except the
gyration radii when in the same bias field were slightly smaller, as expected
from Eq. 7.5. It should be stressed that these calculations are non-relativistic.
For electrons with energies of $\approx 700\,\mathrm{keV}$, relativistic effects start to play a role,
but should not effect the final results by more than a few percent [Mär10].

Using Eq. 7.10 for the radial distribution of UCNs in the trap (mechanical
equilibrium and constant phase space density), the electrons starting at the $z =$
0 plane, and energies from the spectrum of Fig. 7.1, simulations of ensembles
of electrons were made. As defined previously, the "hit wall" percentage is
the probability an electron strikes the side walls of the trap before the end
of the total tracking time of $80\,\mathrm{ns}$. This is shown for varying bias fields B_{bias}
in Fig. 7.7, as well as plots of the distributions of the axial z-distances of the
electrons at different times; the axial positions and times of where and when
the electrons collide with the side walls; and the initial radial positions $\rho(0)$ of
an electron that collides with the side walls. Each set of simulations contains
2000 trajectories.

The behavior of the electrons are similar to that of the protons except that
it occurs on a shorter time-scale. The larger the bias field B_{bias}, the lower the
hit wall percentage. However, this percentage is lower for the same B_{bias} for the
electrons than for the protons. This is likely to be due to the smaller gyration
radius of the former. The collisions with the side walls occur within the first
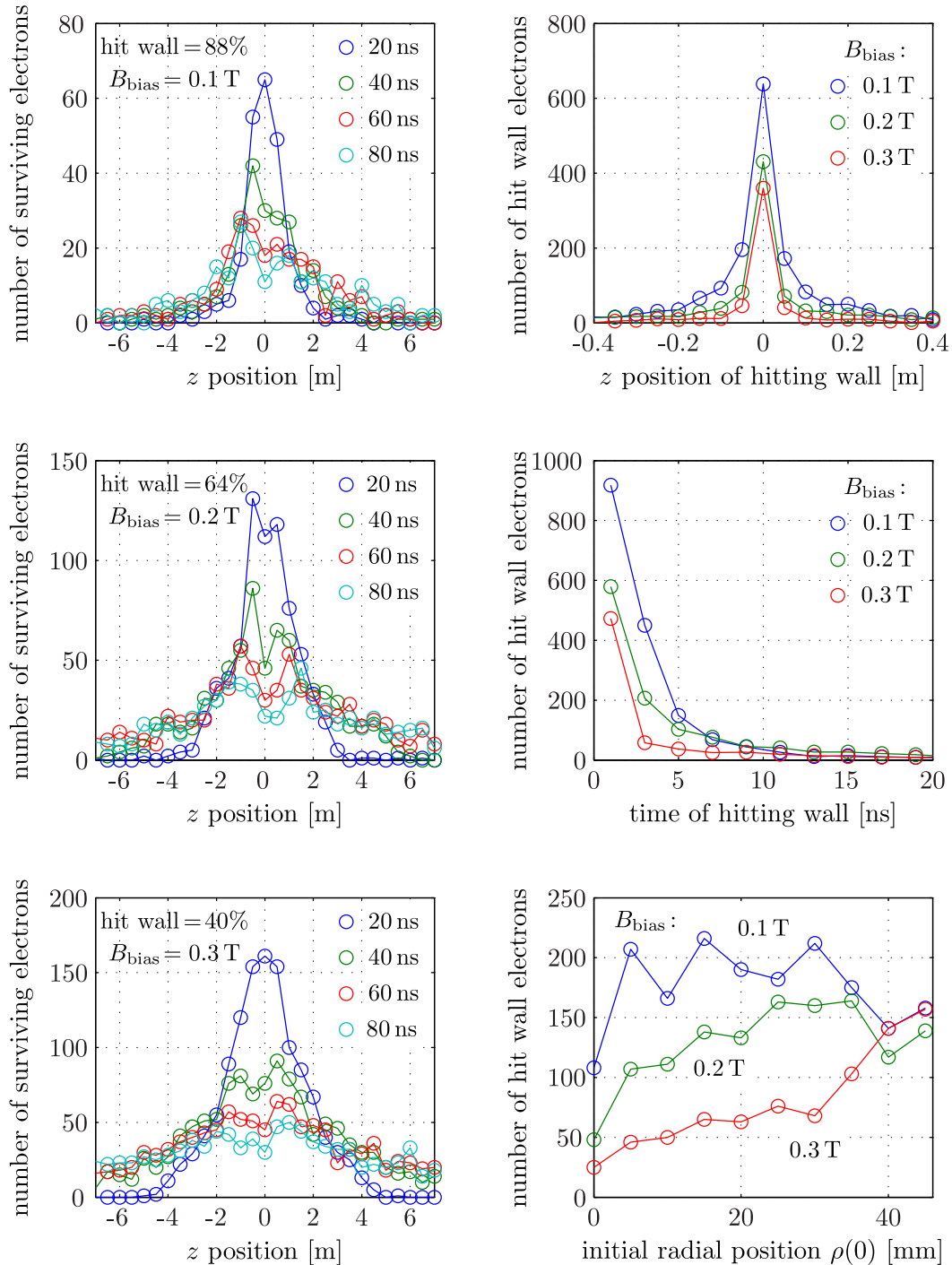
Figure 7.7: The properties of an ensemble of electrons for different bias fields B_{bias} from the simulations. Similar to the plots of Fig. 7.5. Each set of simulations contains 2000 trajectories. The behavior is generally similar besides the hit wall percentages being a bit lower for the same B_{bias} and the movements occurring on a shorter time-scale. The starting conditions are the same as for the proton simulations besides the energy. Note that relativistic effects are not included.

5 ns and at axial distances < 10 cm from their initial $z = 0$ positions. Due to the higher velocities, the electric octupole that was successful at providing a $E \times B$ force for protons to move them away from their initial $z = 0$ positions is not effective for the electrons. For the electrons the simulations tracked them over greater distances traveled. It can be seen that after 80 ns over 80% of the electrons that did not collide with the side walls moved an axial distance of more than 1 m.

The radial distribution of electrons in the trap can be used to estimate the loss of electrons due to the ring-shaped UCN absorber placed inside the trap (for cleaning the UCN spectrum) that is proposed in Sec. 5.4. Shown in Fig. 7.8 are plots of the distribution of electrons after the 80 ns of simulation time. This distribution is reached very quickly—less than 20 ns—after the start of the simulations. Also shown in the figure is the distribution of the maximum radial position ρ_{max}, the maximum radial position of the complete electron trajectory. The ρ_{max} distribution allows the worst-case loss of electrons due to collisions with the ring absorber to be estimated. If ρ_{max} is larger than the inner radius of the ring-shaped absorber, then there is a chance the electron can collide with it. It is a pessimistic estimate since it depends on how long the absorber is and how frequently (the spacing in the z axis) the electron makes it to ρ_{max}. For an infinitely long 5 mm thick ring absorber $\approx 8\%$ of electrons will collide with it. For shorter lengths, e.g., the proposed length is between $1 - 4$ cm, this percentage will be less.

These extensions were extended by Ref. [Rosb] to include a full magnetic field map from the superconducting coils from 3D calculations with the magnetic mirror of the small end coil. These calculations do not include full relativistic effects. The distribution of UCNs in the trap included the phase space compression by gravity and thus variations in $z(0)$. The probability of extracting the electrons to a detector inside the trap was calculated to be $\approx 50 - 60\%$ for $B_{\mathrm{bias}} = 0.3$ T. The values from these extended simulations agree with the predictions from the "hit wall" percentage to within around 10%.

A good way to confirm the calculations would be the detection of electrons from a β-source. Variations of the transmission of electrons for different initial radial positions and for different axial distances could be tested. Unfortunately, these tests are not possible without the superconducting bias field coil. If a bias field of only a few milli-Tesla is used, then the hit wall percentage is close
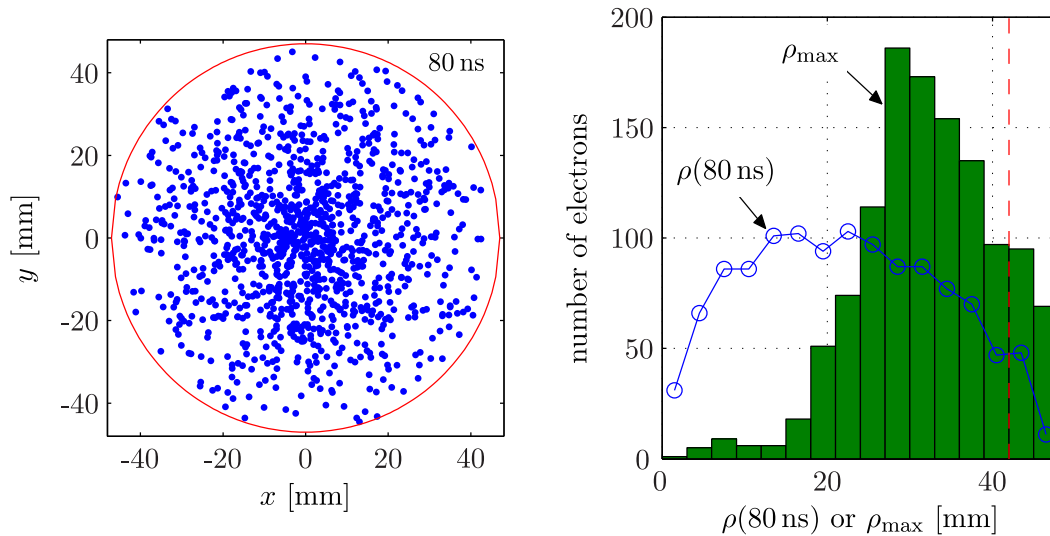
Figure 7.8: *Left*: A plot of the position of the electrons in the xy-plane after 80 ns of simulation time for the $B_{bias} = 0.3\,\mathrm{T}$ simulation. The red circle (—) shows the side walls of the trap. *Right*: The radial distribution of the electrons after 80 ns $\rho(80\,\mathrm{ns})$ (shown as the blue line and circles $-\!\ominus\!-$) and the largest radial position of the electron during the entire simulation time (of 80 ns). The horizontal scale extends to the side wall of the trap. The vertical red dashed line ($-\!-$) shows the radial position where an UCN absorber ring 5 mm thick (see Fig. 5.7) would extend to. The distributions shown for 80 ns were reached before 20 ns of simulation time and did not change between these times.

to 100%.

7.4.2   Electron detection system

The detection of the electrons is technically simpler than the protons due to their higher energies. For instance, in the PERKEO series of experiments [Abe97, Bop88, Mär09], which measures the electron asymmetry in neutron β-decay, two detectors made from plastic scintillators 5 mm thick—required to stop up to the 780 keV end point energy—are used with multiple photomultiplier tubes (PMTs) connected to each scintillator to reduce electronic noise. However, these experiments count the electrons from a cold neutron beam decaying in a volume $\approx 1\,\mathrm{m}$ long. The observed electron rate in the detector is $\gtrsim 1 \times 10^4\,\mathrm{s}^{-1}$. For comparison, we expect less than $\lesssim 100\,\mathrm{s}^{-1}$ when the magnetic UCN trap is first filled. This rate reduces with time so that after a time of $4\,\tau_\beta$

it is $\lesssim 5\,\mathrm{s}^{-1}$. Therefore, the background and noise suppression requirements of our detection system will be different. The source of the background is also different.

In experiments that extract the charged particles from a decaying cold neutron (CN) beam, most of the background comes from prompt reactions caused by scattered cold neutrons. For experiments with UCNs, the apparatus can be well-shielded from the CN beam since the UCNs can be guided long distances and through large angles. An existing experiment that detect the electrons from decaying UCNs is the UCNA project [You01, Pat09, Liu10], which also measures the electron β-asymmetry. In this experiment, the background is predominantly composed of γ-photons, which should be similar to what we expect in our experiment.

The detection system chosen for the UCNA experiment is to have a thin Multi-Wire Proportional Chamber (MWPC), a gaseous detector, in front of a plastic scintillator detector [4], and using the two in coincidence mode. The MWPC detector is described in Ref. [Ito07].

The total system of MWPC and scintillator in coincidence and the cosmic veto system, a background rate of $< 0.5\,\mathrm{s}^{-1}$ was reached. A detector following this type of design is shown schematically in Fig. 5.14. A long adiabatic light guide is used so that the PMTs, chosen to be a model with high resistance to external magnetic fields and operable in vacuum, can be situated away from the large end coil. The adiabatic light guide will also mix the scintillation light from the plastic scintillator before reaching the two PMTs for a coincidence mode measurement.

Electron backscattering from the MWPC or the plastic scintillator is a major systematic effect in the measurement of the β-asymmetry. To reduce back-scattering the UCNA MWPC was made with thin front foils and wires on the foils as electrodes and heavy hydrocarbon quencher gas with a low atomic number Z was used. Furthermore, the magnetic field was adiabatically decreased from $1\,\mathrm{T}$ to $0.6\,\mathrm{T}$ at the detector so that the inverse magnetic mirror effect is used to realign the electron moment to the direction perpendicular

---

[4]Similar to PERKEO but the plastic scintillator in UCNA is only $3\,\mathrm{mm}$ thick since the electrons are expected to be lose energy in the front detector. Having thicker plastic than required to stop the electron with highest energy is redundant since it will only pick up additional background.

to the detector. With these efforts the amount of back-scattering events is suppressed to a probability of $\approx 10\%$. Back-scattering events do not cause a systematic error in a neutron lifetime counting experiment since the probability of it occurring remains constant with time. However, it can reduce the efficiency of the electron detection since if an electron is scattered back into the magnetic trap without registering an event in the scintillator, then it can become lost—from hitting the side walls of the trap or escaping through the small end coil—without returning back to the detector. Due to the short time-scales of the electron trajectories, if an electron does return to the MWPC several times the signals produced would not be separated in time.

Magnetic defocussing is more difficult in the current setup. Defocussing can be done while the electrons are still inside the octupole array by having the magnetic field at the large end coil less than B_{bias} and placing the detector here. However, since the physical dimensions of the side walls are fixed here, the defocussing will also push a lot of electrons towards the walls. Alternatively, the large end coil can be at the same magnetic field as B_{bias} and the detector can be placed outside the octupole array. However, the behavior of the electrons due to the fields at the ends of the octupole array is complicated and has not been studied yet. For instance, there are strong B_z components as large as $0.8\,\text{T}$ at the between pole pieces of the octupole that will reinforce and cancel the field from the large end coil. This will cause magnetic mirror reflections or push the electrons against the side walls. This effect was observed in the extended simulations of the electrons described previously. These calculations should be extended for extracting the electrons completely from the trap, and verified experimentally with β-sources.

Another improvement that can be made to the MWPC for our experiment is to have a greater spacing between the anode wires since spatial resolution is not required. The diameter of the gyrations in the xy-plane is around $1\,\text{cm}$, so a spacing of 2–$3\,\text{cm}$ between the wires should be sufficient. The wires can also be shorted together to form single anode to simplify the electronics. A prototype gas proportional chamber was started in Ref. [Cic10]. Initial tests with radioactive sources showed promising results.

The plastic scintillator is also not necessary since the total energy of the electron is not required. Instead of the scintillator, a single chamber but with 2 (or more) sets of alternating cathode-anode wire planes can be used in co-

incidence to suppress noise. Or, alternatively, two separate chambers in a telescope configuration separated by a very thin foil can also be used. This is useful for reducing the energy loss in the foils of a gas counter (made from Mylar foils $\approx 10\,\mu$m thick and reinforced by Kelvar fibres) and the dead layer of a plastic scintillator (measured to be $\approx 3\,\mu$m thick in Ref. [Pla08]).

7.5 Interactions of charged particles with residual gas

The charged decay products can interact with the residual gas in the vacuum of the trap. There are many different processes that can cause an inelastic collision between a proton or an electron with a gas molecule. Experiments that measure the proton spectrum to a high precision, such as aSPECT, are quite sensitive to these energy losses [Glü05]. While the current experiment is less sensitive, it is not completely immune. The charged particle detection efficiency varies with the charged particle energy and the vacuum level in the trap can change with time. Furthermore, if electric fields for proton extraction and acceleration are used in the experiment, then the free ions and electrons produced from ionization can be accelerated and cause false, time-dependent counts in the proton detector.

To estimate the size of the effect, the values for the stopping power $-dE/dx$, the energy loss per unit distance, can be used. Values calculated from the Bethe-Bloch formula (e.g., see Ref. [Leo87]) are given in Ref. [Ber93]. For electrons with energy below $\approx 1\,$MeV, the stopping power increases with decreasing energy. At room temperature and leaving the gas pressure P as a free parameter, the stopping power, approximately the same for both gases, is $-dE/dx \approx (4 \times 10^5\,\mathrm{keV\,m^{-1}\,mbar^{-1}})\,P$ for an electron energy of $10\,$keV and $\approx (3 \times 10^4\,\mathrm{keV\,m^{-1}\,mbar^{-1}})\,P$ for $800\,$keV. For example, for a pressure of $1 \times 10^{-6}\,$mbar, the energy loss is expected to be $\approx 0.4\,\mathrm{keV\,m^{-1}}$ and $\approx 0.03\,\mathrm{keV\,m^{-1}}$, respectively.

While the maximum lateral distance to the detector is $\approx 2\,$m, the actual flight path of the electrons can be much longer due to the complicated trajectories and reflections. However, at a vacuum level of $1 \times 10^{-6}\,$mbar, the energy losses of the electrons due to inelastic processes should not affect the detec-

tion efficiency sufficiently to cause problems. If, however, no thin foil is used separate the superfluid helium source and UCN trapping volume, then helium gas can enter during the filling. At the end of filling, some time is required to pump this helium. One should wait a sufficient period so that the energy loss due to the gas does not cause a significant time-dependent efficiency of detection of electrons.

For the protons, $1\,\mathrm{keV}$ is the lowest energy for which the stopping power value is available in Ref. [Ber93]. At this energy, $-\rho^{-1}\,dE/dx \approx 1\times10^6\,\mathrm{keV\,cm^2\,g^{-1}}$ for hydrogen and $\approx 2\times10^5\,\mathrm{keV\,cm^2\,g^{-1}}$ for helium. At room temperature and a gas pressure of P, this is equivalent to $-dE/dx \approx (8\times10^6\,\mathrm{keV\,m^{-1}\,mbar^{-1}})\,P$ for hydrogen and $\approx (3\times10^6\,\mathrm{keV\,m^{-1}\,mbar^{-1}})\,P$ for helium. While the stopping power appears to be decreasing with proton energy in the region just above $1\,\mathrm{keV}$, the behavior below this energy is more complicated. Ref. [Phe90, TS00] gives the cross-sections of processes such as rotational and vibration excitations of the hydrogen molecule that start to dominate below $1\,\mathrm{keV}$. Without doing a full analysis of these processes, the stopping power at $1\,\mathrm{keV}$ is only an estimate for that in the 0–$800\,\mathrm{eV}$ energy range. The energy loss of protons in the residual vacuum, especially when considering the relative loss, is much greater than for the electrons.

In order to estimate the ionization rate, the values for the ionization cross-section from Ref. [KD66, TS00] were used. The rate of ionization with cross-section σ_ion occurring, like Eq. 5.20, is given by $\tau_\mathrm{ion}^{-1} = n_\mathrm{gas}\,\sigma_\mathrm{ion}\,v_\mathrm{rel}$, where n_gas is the number density of the residual gas and v_rel is the relative velocity between the charged particles and the gas. The gas molecules at room temperature can be considered at rest, since even $100\,\mathrm{eV}$ protons move at a speed of $1.4\times10^5\,\mathrm{m\,s^{-1}}$. The values of $P\,\tau_\mathrm{ion}(E)$, where P is the pressure of hydrogen or helium (at $300\,\mathrm{K}$), for different charged particle energy is shown in Fig. 7.9. Also shown on the plot is the ionization in terms of the mean free distance $\bar{x}_\mathrm{ion} = (n_\mathrm{gas}\,\sigma_\mathrm{ion})^{-1}$. This quantity is perhaps more illustrative.

The energy loss of the charged particles due to the other inelastic processes will shift the electron and proton energy to lower values. However, it can be seen that for electrons, even at the worst-case energy ($\approx 0.1\,\mathrm{keV}$) the mean free distance $\bar{x}_\mathrm{ion}$ in a vacuum of $1\times10^{-6}\,\mathrm{mbar}$ is around $3\,\mathrm{km}$. For the protons, the worst-case occurs at the end-point energy of $750\,\mathrm{eV}$, with $\bar{x}_\mathrm{ion} \approx 200\,\mathrm{km}$ for the same vacuum. If one end of the trap is left open without a magnetic
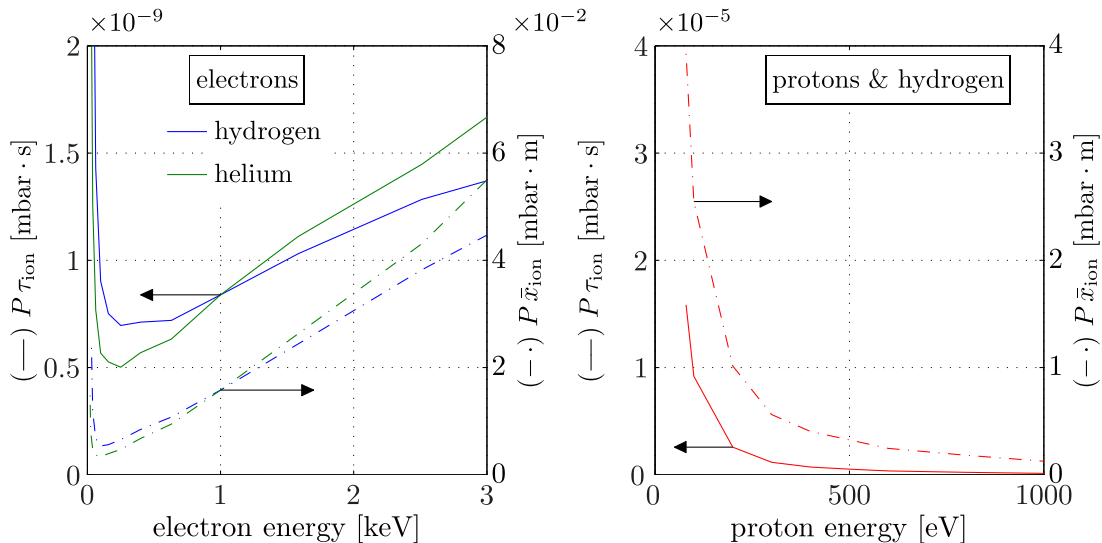
Figure 7.9: The mean time τ_{ion} (in solid lines —) and mean travel distance $\bar{x}_{\mathrm{ion}}$ (in slashed-dotted lines $-\cdot$) between ionization events for electrons and protons interacting with the residual gas a vacuum with pressure P. The horizontal arrows ($\leftarrow$ & $\rightarrow$) indicate which vertical scale the lines correspond to. For the electrons, the plot is only shown for small energies where the largest amount of ionization occurs.

mirror then ionization for both protons and electrons will not be a problem since they will escape or collide with material before that. The problem of ionization is thus only a problem when both end coils are ramped up so that the two magnetic mirrors form a trap for charged particles.

Using two end coils with a radial multipole is a common design for plasma sources [5]. The configuration is not a 100% efficient trap of charged particles. When the electrons are performing magnetic mirror reflections off the octupole side fields, they can have their modes of motion mixed. If they end up in a trajectory directed towards the magnetic poles or the end coils with sufficiently large $v_{\parallel}$, then they will collide with the side walls or escape the trap. However, if the electrons are near the center of the trap, away from the octupole side-walls, then they can reflect back and forth from the two end coils without experiencing mode-mixing and survive for long times in the trap. This is the operating principle of a "mirror machine"[Jac98]. However, scattering of the

---

[5]Specifically, it is used in Electron Cyclotron Resonance Ion Sources (ECRIS) to confine electrons and ions for long enough times so that sufficient energy can be inputted (via RF radiation) to produce a plasma.

electrons by the residual gas of the vacuum described previously can prevent them from staying in these trajectories for too long. This scattering process can be added to the electron trajectory calculations.

An additional possible effect not analyzed is the release of electrons (or ions) via secondary emission by a collision of an electron with the side walls of the trap. These secondary electrons (and ions) have low initial energies. However, if electric fields are used to accelerate the decay protons, the ions can undergo the same acceleration and be detected by the detector. This could be particularly problematic if ring electrodes at successively higher potentials are used for extracting the protons (see Fig. 7.3). The secondary charges emitted after the primary electron from β-decay can be amplified by this dynode structure like in a photomultiplier tube causing a noticeable build up of secondary charge.

Chapter 8

Summary and conclusion

Development of a new superfluid helium UCN source

During this thesis, a continuous flow ^{3}He cryostat and its associated equipment were constructed and tested. A liquefaction system using the cooling power of a commercially available 2-stage GM cryocooler was applied to liquefy ^{4}He at a rate of $80\,\mathrm{g\,hr^{-1}}$ at $4.2\,\mathrm{K}$, improving on a previous system with which only $55\,\mathrm{g\,hr^{-1}}$ was observed [SWZ06]. The extraction rate of superfluid helium through the superleak was measured to obey the linearity with heat input for different ^{4}He bath temperatures. The performance of the continuous ^{3}He circuit was also tested. The cooling power of the continuous flow ^{3}He pot was measured. A cooling power of $100\,\mathrm{mW}$ at $0.65\,\mathrm{K}$ (extrapolated) was observed.

A prototype converter vessel was then coupled to this cryostat. The cooling power of this preliminary setup was not sufficient to reach the projected base temperature of $\lesssim 0.7\,\mathrm{K}$. An accumulation-and-empty measurement with $T = 1.08\,\mathrm{K}$ gave an uncorrected, extracted, and detected $93,000$ UCNs. The total storage time was observed to be $\bar{\tau}_{\mathrm{tot}}(1.08\,\mathrm{K}) = 20.3 \pm 1.2\,\mathrm{s}$. Continuous UCN production measurements were also made covering a temperature range $T = 1.2 - 2.4\,\mathrm{K}$, above the superfluid transition temperature T_λ.

The highest directly observed UCN production rate was $P'_{\mathrm{UCN,\,cont.}}(1.16\,\mathrm{K}) = 2.5 \pm 0.2\,\mathrm{cm^{-3}\,s^{-1}}$ in the continuous measurements. This is amongst the highest observed values of P_{UCN} in superfluid helium. The value from the accumulation measurement is $P'_{\mathrm{UCN,\,accum.}}(1.08\,\mathrm{K}) = 1.9 \pm 0.2\,\mathrm{cm^{-3}\,s^{-1}}$. After applying corrections to P'_{UCN} due to loss in the converter volume, differences in neutron optical potentials, and an extraction factor $\approx 40\%$ [Zim10], the value agrees

with $P_{\text{UCN}} = 8 - 14\,\text{cm}^{-3}\,\text{s}^{-1}$ for the PF1b beam.

From the continuous measurements, the form of τ_{up}^{-1} was studied at much higher temperatures than in previous experiments. It was found that the UCN up-scattering due to single phonon absorption with simultaneous single phonon emission, $\tau_{\text{up},B}^{-1} \propto T^7$ (Eq. 1.21), was adequate in describing the form of the total up-scattering rate τ_{up}^{-1}. This is consistent with other experiments [Bak03, Yos92, Gol83].

Progress towards a neutron lifetime measurement with a new magnetic trap

The combined fields from the octupole array with the superconducting coils were studied to understand effects such as demagnetization of the permanent magnets, cancellation of the field at the walls of trap, the depth of the magnetic trap, and the effective volume. It was found that it is necessary to cool the magnets to prevent demagnetization, and that the cancellation between magnetic fields does not create field minima in the trap. Using the trap in a vertical, magneto-gravitational configuration gives $E_{\text{trap}} = 40\,\text{neV}$, while in a horizontal configuration $E_{\text{trap}} = 54\,\text{neV}$. These values are for a minimum bias field of $0.3\,\text{T}$. If charged product detection is not required, this can be increased by $\approx 10\,\text{neV}$. The number of UCNs expected to be filled in the trap in the vertical configuration is ≈ 0.4 times that of the horizontal configuration.

Using an end-coil designed to have short ramp times is planned to be used for filling and emptying the trap. Calculations were made for a technically more demanding option [Zim05, LZ09], but pursuing this has since been abandoned.

A quantity called the effective removal area was defined which allowed quantitative comparisons between different configurations for the removal of UCNs: ring-shaped absorber, a flat piston absorber, or ramping down of the end coil. A viable UCN chaotic cleaning procedure was identified. This involves inserting a piston with a highly diffuse-reflecting surface from the bottom of the trap. For this configuration, a Monte-Carlo (MC) simulation was compared with the calculations for an isotropic UCN gas. The analysis showed that the cleaning time $\tau_{\text{clean}}(E_n)$ (from MC) is ≈ 3 times longer than from assuming the isotropic approximation. The $\tau_{\text{clean}}(E_{\text{trap}}) \approx 3\,\text{s}$ (from the MC), when the absorber is inserted to $E_{\text{cutoff}} = E_{\text{trap}} - 5\,\text{neV}$. A big advantage of the

piston is that when it is retracted from the trap after cleaning, no heating of the UCNs will occur.

Another technique where a specular-reflecting paddle is inserted along the length of the trap is also proposed. The heating of the UCNs due to the diffuse reflections off the paddle while it is being slid out of the trap was calculated based on the isotropic UCN gas approximation. The calculations did not conclusively show that the heating can be considered negligible. Further calculations or experimental studies are required. Both the specular-reflecting paddle and diffuse-reflecting piston can be used in the trap to compare systematic errors.

Experimental tests of UCN storage with the octupole array were made at PF2 of the ILL using a material UCN valve to open and close the trap. A field of $\gtrsim 1\,\text{mT}$ everywhere in the trap, was sufficient to suppress depolarization losses in the low-field regions such that its effect on $\bar{\tau}_{\text{tot}} \approx 800 \pm 30\,\text{s}$ was no longer observable within the statistical error bars.

Another experiment with the same valve and a UCN absorbing piston was performed on the TES beam of PF2. The UCN spectrum cleaning—in a scheme similar to the proposed diffuse reflecting piston configuration—was performed in the trap. Using a measurement of the UCN spectrum, the loss due to material interactions was calculated and corrected for. From this, a value of the neutron lifetime $\tau_\beta = 916 \pm 44_{\text{stat}} \pm 45_{\text{sys}}\,\text{s}$ was obtained from $\bar{\tau}_{\text{tot}} = 855 \pm 44\,\text{s}$. The UCN spectrum was cleaned with the absorber to an energy $E_{\text{cutoff}} = 66\,\text{neV}$, while $E_{\text{trap}} \approx 84\,\text{neV}$ in this setup. The statistical precision was achieved after 2 days of measurement time. Two other measurements were made with $E_{\text{cutoff}} = 82\,\text{neV}$ and $E_{\text{cutoff}} = E_{\text{trap}}$ (i.e., no absorber was used). The results showed quantitative understanding of the wall losses of well-trapped UCNs within the statistical error and qualitative understanding of the cleaning of above-threshold UCNs.

Simulations were made tracking the trajectories of the protons and electrons in the magnetic field of an infinitely long octupole and bias field. It was found that using a bias field of $\gtrsim 0.3\,\text{T}$, around $40 - 50\,\%$ of the decay products can be kept from colliding with the side walls. Particles with a large part of their energy in the transverse mode tended to remain in the $z = 0$ plane. A system of octupole electrodes was shown to be effective for pushing protons in a preferred axial direction while causing little increase in losses. This gives

an estimate of the extraction efficient, which agrees within $\approx 10\%$ from other calculations.

For the detection of protons, a silicon drift detector is the main candidate. But electrodes for accelerating the protons to overcome the necessary focussing magnetic mirror are required. This will increase the times which electrons spend in the trap. Estimates of the energy loss of electrons and the mean distance travelled for an ionization event were given. Another source of ions can come from secondary emission from the electrons colliding with the walls of the trap. These can be problematic if there are electrodes in the trap accelerating them to high energies.

For electrons, the proposed detector a gas proportional counter with multiple electrodes or multiple chambers so that coincidence can be used to eliminate electronic noise. This system offers low background and noise sensitivity; and detecting electrons avoids the problem associated with acceleration electrodes. Inserting the detector inside the trap does not allow magnetic defocussing to be used. Extracting the electrons out of the trap is difficult due to the end field of the octupole array.

Upcoming prospects

Both projects are continued being developed currently. The SUN2 source has been moved to the new H172b monochromatic beam position at the ILL [Sch09]. A new cooling tower and UCN valve mechanism will be installed. The production volume with a length of 1 m will initially be used, but its aimed for final length is 3 m. The cryostat for cooling the superconducting coils of the HOPE magnetic trap is currently being fabricated. When it is delivered, many tests, such as electron detection with β-sources or spectrum cleaning and depolarization experiments with UCNs, will be performed. Once both the projects are ready, the HOPE magnetic trap can used with SUN2 to perform a high-precision magnetic neutron lifetime measurement with a next-generation UCN source.

Appendix A

Appendix for the SUN2 source

A.1 Development timeline

October 2008: • Begun assembly of the cryostat: coldhead mounted onto the top DN400 flange with O-ring seal; input Swagelok membrane valves installed; isolation vacuum gate valve installed; blind flanges put on pumping tubes, other access ports at the top, horizontal extraction vacuum, and bottom access port. • The isolation vacuum vessel was pumped down and leak tested $< 4 \times 10^{-8}\,\mathrm{mbar\,L\,s^{-1}}$.

March 2009: • The two horizontal gold-plated copper plates of the 1st and 2nd stage radiation screens were installed. • The 1K pot with an aluminium blind flange on the bottom and the pumping tube were also installed. • The internal cold traps were assembled and put into place. • The entire ^{4}He circuit and ^{3}He circuit, with a blind flange after the spiral capillary on the cold head, were leak tested to $< 1 \times 10^{-9}\,\mathrm{mbar\,L\,s^{-1}}$.

April 2009: • Aluminium foil $200\,\mu\mathrm{m}$ thick closing off the holes on the heat screens for the horizontal transfer tube but none covering the holes on the horizontal plates. (The biggest hole being the ^{3}He pumping tube. An estimated total area of $\approx 90\,\mathrm{cm}^2$ on the 1st and 2nd stage heat screens was uncovered.) • Lowest temperatures reached: $T_{1\mathrm{st\,stage}} = 35\,\mathrm{K}$ (measured with a PT100 only), $T_{2\mathrm{nd\,stage}} = 5.7\,\mathrm{K}$. • These temperatures correspond to a total heat load of $10\,\mathrm{W}$ and $3.5\,\mathrm{W}$ on the 1st and 2nd stage, respectively.

May 2009: • Covered ^{3}He pumping line with Al foil and other holes on heat screens • Lowest temperatures: $T_{2\mathrm{nd\,stage}} = 4.1\,\mathrm{K}$, $T_{1\mathrm{st\,stage}} = 35\,\mathrm{K}$ (PT100),

T_{1Kpot} = 2.5 K. • There's a problem keeping 1K pot warm. 2nd stage should also be cooler.

June 2009: • Super-insulation wrapped around sides of 2nd stage heat screen. • Freezing O-ring problem discovered on ^{4}He pumping line. • Test was made to rule out 1K pot capillary reaching down to the bottom of the 1K pot was cause of problems. • Lowest temperatures: $T_{\text{2nd stage}}$ = 2.8 K, $T_{\text{1st stage}}$ = 35 K (PT100) $T_{\text{1K pot}}$ = 2.4 K with ACP40 $T_{\text{1K pot}}$ = 2.2 K Edwards rotary vane in series with ACP40. (with 80 g hr^{-1} input flow. With no input flow T_{1Kpot} = 2.0 K) • P_{iso} = 4 – 7 × 10^{-6} mbar.

April 2010: • Capillary bent up inside 1K pot anyway. • Lowest temperatures: $T_{\text{2nd stage}}$ = 2.6 K, $T_{\text{1st stage}}$ = 34 K (PT100), $T_{\text{1K pot}}$ = 2.3 K. • But when pumping on direct 1K pot filling line, $T_{\text{1K pot}}$ = 1.6 K. • P_{iso} = 2 × 10^{-6} mbar. • Found the problem keeping 1K pot warm due to gas oscillations in the direct 1K pot filling line.

May 2010: • Direct 1K pot line blind flanged. The original input line has been adapted to a LN2 precooling circuit. • Cernox put on 1st stage heat screen. • ^{3}He pot installed with a blind copper flange. • Superleak installed. • Extraction capillary to the top of cryostat.

July 2010: • Running ^{4}He in ^{3}He circuit. • No thermal contact between ^{3}He input and 1K pot. • $T_{\text{2nd stage}}$ = 4.2 K when ^{3}He pot at 100 K. • Lowest: T_{2ndstage} = 3.3 K (increase due to ^{3}He pumping line, LN2 line or extraction capillary?), $T_{\text{1st stage}}$ = 35 K, T_{1Kpot} = 1.6 K, and $T_{^3\text{He pot}}$ = 1.6 K. • Extraction through superleak not possible (around 0.02 g hr^{-1} observed) without heating wire. • P_{iso} = 2×10^{-6} mbar.

July 2010: • Added heater to SL. • Lowest temperatures: $T_{\text{1st stage}}$ = 35 K. $T_{\text{2nd stage}}$ = 3.2 K, T_{1Kpot} reached new low of 1.4 K (due to compressor behind ACP40 for extra pumping power?), and $T_{^3\text{He pot}}$ = 1.4 K (also lower than before?) • Saw extraction through SL for different heating powers. • Saw hysteresis effect of SL extraction when going back to zero heating.

November 2010: • First test of LN2 precooling. Takes 1 – 1.5 hrs at this lower thermal mass and saves around 8 hours. Rate of LN2 flow for precooling limited by O-rings freezing on the exit ISO-K DN60 exit flange. With the precooling takes around 18 hours to get a state to liquefy ^{4}He and ^{3}He. • ^{3}He pumps set up but still running ^{4}He in ^{3}He circuit. • NV special OP line with only brazing and indium flange design installed. • Lowest temperatures:

$T_{\text{2nd stage}}$ = 3.2 K, $T_{\text{1st stage}}$ = 35 K, $T_{\text{1K pot}}$ < 1.4 K, and $T_{\text{3He pot}}$ = 0.92 K (with ^{4}He in ^{3}He & big root pumps). • P_{iso} = 7×10^{-6} mbar.

January 2011: • After thorough cleaning oil and grease off heat screens. $P_{\text{iso}} \approx 4 \times 10^{-7}$ mbar. • Running with ^{3}He in ^{3}He line. • Put in "weak coupling" between ^{3}He input and 1Kpot. • Thermal contact between ^{3}He input and 1Kpot not that great. When $T_{\text{1K pot}}$ = 1.8 K, $T_{\text{3He in}}$ = 2.9 K. • Lowest temperatures: $T_{\text{2nd stage}}$ = 3.4 K. (Why warmer? Coupling between ^{3}He in and 1K pot shouldn't make a difference. Horizontal SL extraction line moving around and increasing holes in radiation screen?), $T_{\text{1st stage}}$ = 37 K, $T_{\text{1K pot}} \leq$ 1.4 K, $T_{\text{3He pot}}$ = 0.4 K (with ^{3}He and big roots).

Feburary 2011: • Leak at SL NV removed. • Heater placed on blind ^{3}He pot. • Thermal contact between 1K pot and ^{3}He in improved and gave curve in Fig. 2.10. • Lowest temperatures: $T_{\text{2nd stage}}$ = 3.2 K (because of reason of above?), $T_{\text{1st stage}}$ = 39 K, $T_{\text{1K pot}}$ =< 1.4 K, and $T_{\text{3He pot}}$ = 0.4 K. • P_{iso} reached 2×10^{-7} mbar after pumping down to 5×10^{-6} mbar before starting compressor • Using $\dot{\rho}_{\text{4He}}$ = 50 – 60 g hr^{-1} and $\dot{\rho}_{\text{3He}}$ = 20 – 30 g hr^{-1}, takes around 24 hrs to cool to a state to liquefy ^{3}He and ^{4}He.

April 2011: • Put in heat exchanger (leak tested externally with LN2, ramping several times), horizontal extraction tube and UCN production volume end aluminium piece. • Put in horizontal extraction heat screens and "eiffel tower" structure. (The "eiffel tower" has boron stycast coated heat screens + graphite rods for mechanical support between cube to 1st stage and 1st stage to 2nd stage.) Thin Al foil heat screens for "eiffel towe" in the cube. Long copper rods cool eiffel tower screens directly. • Put in UCN extraction guide. It is thermally anchored on the upcoming copper block and at the bend to the 2nd stage heat screen and then 30 cm further down to the 1st stage heat screen. • Liquefaction still possible with $T_{\text{2nd stage}}$ = 7.8 K but only done at low temperatures (and thus low rates, see Fig. 2.6) since didn't want to cool down 1K pot again from 4.2 K. • Extraction through superleak almost impossible with 1K pot at 2.1 K. But with $T_{\text{1K pot}}$ = 1.95 K could extract at 20 – 30 g hr^{-1}. • The extracted ^{4}He cooled the production volume from 30 K down to 1.6 K in 30 – 40 mins. • A bypass capillary, passing through the extra cold trap and "weakly" anchored to the 2nd stage could cool the UCN production volume down to 30 K. • LN2 precooling took 2 hours to get 1st stage down to 140 K and 2nd stage to 120 K. • Thin Al flap foils was used to

reduce radiation down UCN extraction guide. •Horizontal extraction tube
and UCN production volume showed to be superfluid tight. •Lowest temper-
atures: $T_{\text{2nd stage}} = 6.5\,\text{K}$, $T_{\text{1st stage}} = 48\,\text{K}$, $T_{^3\text{He pot}} = 1.22\,\text{K}$, $T_{\text{volume}} = 1.3\,\text{K}$ (with
only a tiny amount of LHe in there). •$P_{\text{iso}} = 2 \times 10^{-7}\,\text{mbar}$.

This was the last cool down before running the experiment on PF1b due
to time constraints. While cooling problems already showed up here it was de-
cided to go ahead with the experiment since mostly successful. The production
volume cooled down very quickly when injected in LHe after SL. Bad thermal
contact with the heat screen was already suspected to be a problem. For next
cool down with the extra $0.5\,\text{m}$ long production volume and associated heat
screens, the bypass capillary would be changed to an extended capillary to
provide gas cooling of the extra heat screens. Another suspected problem was
conduction along the graphite rods in the "eiffel tower" structure.

May 2011: Cooldown on the beam of PF1b for UCN production experi-
ment. Due to cooling problems. Hard to estimate since never got to liquefy
using 2nd stage. Can estimate around 5-6 days for 2nd stage to reach near
lowest temperatures. Now due to the heat exchanger UCN production volume
and ^{3}He pot is correlated so hard to liquefy and operate ^{3}He pot without first
going below lambda and extracting superfluid through superleak to cool UCN
production volume. Now LN2 precooling can save a day or so since thermal
mass of heat screens large and takes a long time to cool. Once below T_λ in 1K
pot and extracting superfluid at $40\,\text{g}\,\text{hr}^{-1}$, can cool large thermal mass produc-
tion volume from $70\,\text{K}$ to $2\,\text{K}$ in $4\,\text{hrs}$. LN2 precooling with direct filling of 1K
pot filling can probably reduce the cooling time it takes to get to the lowest
possible temperatures in this setup to $4-5$ days.

A.2 ^{3}He pot pumping power

Here, I calculate the pumping speed of our pumping system on the ^{3}He bath.
The massflow rates ($\dot{\rho}_{^3\text{He}}$) of the closed ^{3}He circuit as a function of temperature
during the ^{3}He pot cooling power tests shown in Fig. 2.11 are re-plotted in
Fig. A.1. The flow meter is actually placed on the ^{3}He input line. If stable
conditions are assumed, this flow rate is equal to the output flow rate as well.
To convert the mass flows to a pumping speed S, which is given as a volumetric
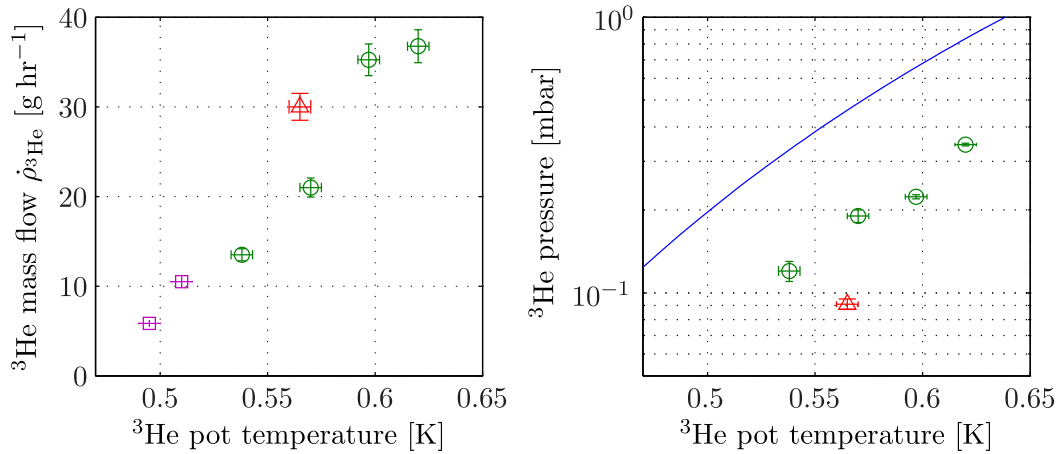
Figure A.1: The ³He mass flow $\dot{\rho}_{^3\mathrm{He}}$ and ³He pot pressure (measured at room temperature) for different the ³He pot temperatures measured in Sec. 2.2.5. The solid blue line (−) denotes the expected SVP pressure measured at room temperature above a ³He bath points. The purple squares (□) are measurements for which the pressure falls below the range of the Ceravac CTR100 gauge used. The green circles (○) are the standard points while the point marked by the red triangle (△) is the "anomalous" point.

flow q_V, the intake pressure at the ³He pumps are required.

At the time of the ³He pot cooling power tests described in Sec. 2.2.5, a Leybold Ceravac CTR100 with a "valid" range of $0.13-1330\,\mathrm{mbar}$ (with an accuracy of 0.2% and a resolution 0.003% of full scale [Oer]) was used at the top of the ³He pot. The measured values of the pressure as a function of $T_{^3\mathrm{He\,pot}}$ are shown in Fig. A.1. For the lower temperatures the pressure values were below the range of the gauge.

The pressure drop Δp across a pumping tube can be calculated using the conductance C, defined as $q_{pV} = \Delta p\, C$, where q_{pV} is the pump throughput. C can be estimated using the Knudsen equation, which for air at $20\,°\mathrm{C}$ [Umr98] is:

$$C = 135\frac{d^4}{L}\bar{p} + 12.1\frac{d^3}{L}\frac{1 + 192\,d\,\bar{p}}{1 + 237\,d\,\bar{p}} \qquad (\mathrm{A.1})$$

where C is given in $\mathrm{L\,s^{-1}}$, d and L are the inner diameter and length of the piping[1] in cm and $\bar{p}$ is the average pressure in the piping. For helium, C is multiplied by a factor of 0.92 for laminar flow or 2.65 for molecular flow

---

[1]This equation is only valid for $L \geq 10d$

[Umr98]. For our pressure range of $0.1-0.4$ mbar, we are somewhere between the two regimes. For the tests, approximately 3 m of DN150 and 10 m of DN100 piping is used. From Eq. A.1, the estimated conductances are $7500\,\text{m}^3\,\text{hr}^{-1}$ and $27,000\,\text{m}^3\,\text{hr}^{-1}$, respectively. The the expected maximum throughput of our pumping system, $q_{pV} = p \cdot 2000\,\text{m}^3\,\text{hr}^{-1}$, therefore, in our pressure range only a small drop in pressure is expected along the ^{3}He pumping tubes. These pressures can thus be used to estimate the pressure at the intake of the ^{3}He pumps.

The volumetric flow is calculated from the mass flow via $q_V = q_m MRT/p$, where $M = 3\,\text{g}\,\text{mol}^{-1}$ is the molar mass of ^{3}He and a temperature $T = 300\,\text{K}$ is used which assumes the gas has come into thermal equilibrium with the tube walls. The calculated volumetric flows are plotted against the different pressures and ^{3}He pot temperature in Fig. A.2. A nominal pumping speed of $\approx 1000\,\text{m}^3\,\text{hr}^{-1}$ is observed. An anomalous data point that showed too high flow rate and too low pressure for $T_{^3\text{He pot}} = 0.565\,\text{K}$ is shown as the red triangle ($\triangle$). This could perhaps be attributed the cryostat being not in an stabilized condition, e.g. the level of liquid ^{3}He was still changing.

The measured pressures at the top of the ^{3}He pot are only around 60% of the saturated vapor pressure (SVP) for the corresponding measured temperature. This is most likely caused by the pumping impedance (or low conductance) of the ^{3}He pumping tube. Although the diameter of the tube is 63 mm, there are many baffles along the length of the tube. Estimating the conductance is difficult. The mean free path of helium atoms in our pressure and temperature range is $\lambda \approx 0.1-1$ mm, i.e. small compared to the baffle structure dimensions. Formulas only exist for the case of viscous flow or molecular flow [Umr98]. Using these equations, a rough estimate of conductance of the total baffle system for air at 20°C gives a value of $30\,\text{m}^3\,\text{hr}^{-1}$ and $100\,\text{m}^3\,\text{hr}^{-1}$ for the molecular and viscous flow regimes, respectively. It is of course expected to be larger for helium at lower temperatures. Another way to estimate the conductance of the baffles is to look at the difference between the expected vapor pressure of a ^{3}He bath and the pressure measured by the gauge at the end of the baffles, which gives $C \approx 1300-560\,\text{m}^3\,\text{hr}^{-1}$. From this it seems possible that the baffles could be what is restricting the pumping throughput on the ^{3}He.
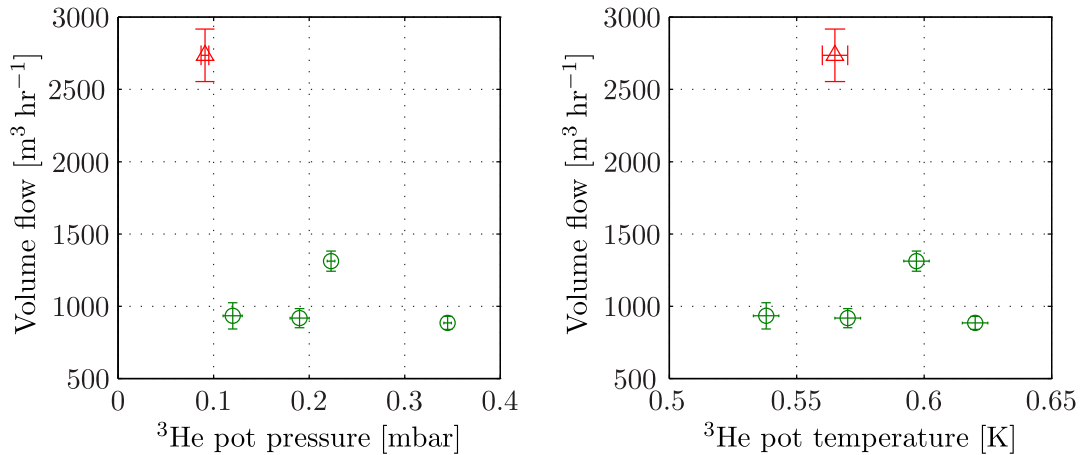
Figure A.2:   The volumetric flow q_V of ^{3}He at the intake of the large $2000\,\mathrm{m^3\,hr^{-1}}$ nominal roots pump plotted as a function of the ^{3}He pot pressure and as a function of the ^{3}He pot temperature. The ^{3}He pot pressure is measured with a Ceravac gauge after the radiation buffles of the pumping tube and at room temperature. This pressure is assumed to be the pressure at the pumps also.

A.3   Gas handling circuit

A legend to the P&ID diagram of Fig. 2.14 is shown in Fig. A.3. The convention used is a combination from the PH-DT-DI Gas Project at CERN (Organisation Européenne pour la Recherche Nucléaire), which in turn is "based generally on the philosophy described in the ISA S5.1 standard" [CER], and from those used in Ref. [Umr98] ("extracted from DIN28401").

Some numbered notes to Fig. A.3:

(1) All the valves mounted on the gas rack are membrane valves. There are also various angled valves and gate valves used.

(2) All are passive, adjustable spring-based overpressure relief valves. The value set is to protection damage to pumps, compressors, the 1K pot and ^{3}He pots.

(3) Only one angled valve is explicitly mentioned to highlight the fine control of pumping on the 1K pot. More are used but are put under the generic valve catagory.

(4) Oerlikon CERAVAC capacitance diaphragm gauges are used for measuring the lower helium pressures on the rack and in the cryostat.

(5) Recording implies that the values are read and stored on the computer slow control program.

(6) Swagelok PGI-series analog pressure gauges are used on the rack for the higher pressures measurements.

(7) Massview MV-102 or MV-104 flow meters; described in Sec. 2.3.1.

(8) Adixen ACP25 or ACP40 multi-roots pump are normally used unless explicitly specified.

(9) A KNF N143AN.12E double membrane compressor is used. The space between the top and bottom membrane is evacuated (via the "between membranes" line). The top membrane performs the compression work while the bottom membrane provides a temporary seal, preventing the escape of ^{3}He, if the top membrane bursts or leaks.
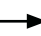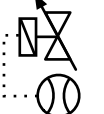
Symbol	Description	Symbol	Description
	generic valve [1]	PI	pressure indicator w/ digital display [4]
	overpressure relief valve [2]	PIT	pressure indicator w/ digital display & recording [4],[5]
	angled valve [3]	PI	pressure indicator w/ analog display [6]
	needle valve		vacuum gauge w/ digital display & recording [5]
	open to air		mass flow meter [7]
	stainless steel flexible tubes		generic pump [8]
	pressure reducer & regulator		single membrane compressor
	digital flow meter and controller		double membrane [9] compressor
			roots pump
	Liquid N_2 cold trap		scroll pump

Figure A.3: Legend to the P&ID diagram in Fig. 2.14. The numbered notes are given in the text in this section.

A.4   Additional photos

In this section some additional photos of the SUN2 cryostat setup on PF1b are presented.
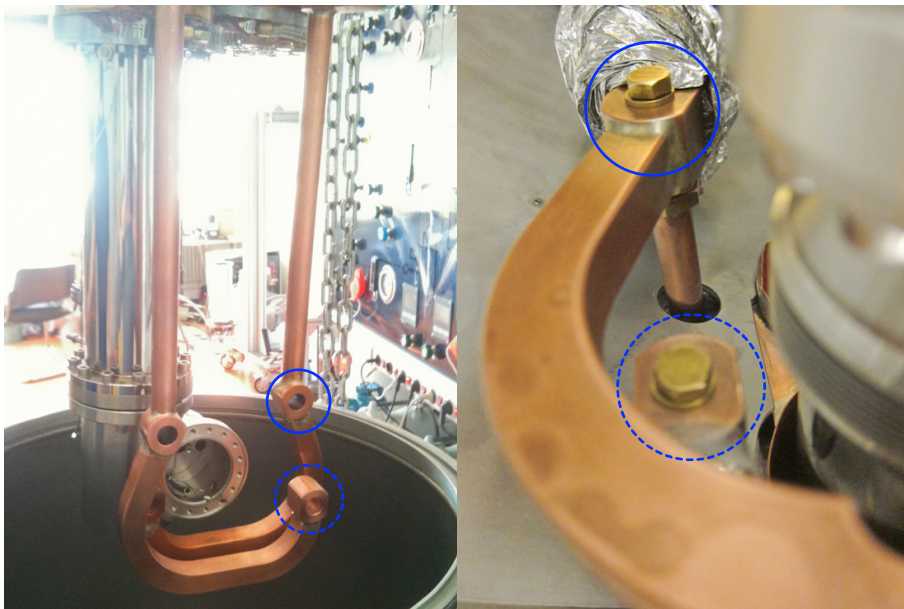
Figure A.4: Photos of the copper rod system used for the thermal contact between the horizontal gold-plated copper plates, which are directly attached to the cold head, and the horizontal transfer tube heat screens. *Left*: The rod on the left and the attached "U-shaped" piece at the front are for the 1st stage screens connections; the other are for the 2nd stage. *Right:* The connection of the copper rods of the horizontal transfer tube heat screens connected to the conical holes on the "U-shaped" pieces. The same holes on the left and right are indicated with respective solid (—) and dotted (– –) blue circles.
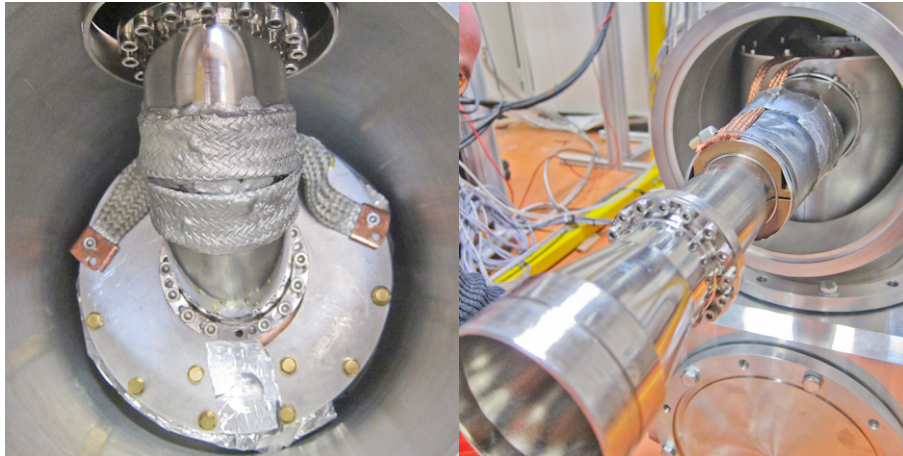
Figure A.5: The thermal anchors on the vertical UCN extraction guide. *Left:* Silver coated copper braiding is used to anchor the elbow (to ensure direct views into the volume are from areas as cold as possible) to the top of the "turret" 2nd stage heat screen inside the DN200 cross piece above the cube. The copper block on the vertical part of the extraction guides is already anchored. *Right:* Copper braiding hose clamped onto a copper ring which in turn is attached to the guides is used for the thermal contact. Super-insulation is later wrapped around horizontal section to reduce heating from radiation.

A.5 Determining the level of the superfluid converter

A.5.1 Using discrete sensors

In order to have a rough idea of the height of the superfluid inside the production volume, it was decided to use three Cernoxes (maximum number restricted by the number of electrical feedthroughs available) at different heights. The locations of these sensors and their names are shown in Fig. A.7.

A standard technique of determining if a sensor is submerged in a cryogenic liquid is to make a resistance measurement (related to a temperature measurement) using an excitation current that is high enough to produce self-heating in gas but not when immersed in liquid [Eki06]. However, this becomes more difficult for superfluid baths since one needs to differentiate between the sensor submerged in the bulk liquid or just covered by film-flow. With ≈ 2–$3\,\mathrm{L}$ of superfluid at $\approx 1.95\,\mathrm{K}$, fairly close to T_λ, the excitation current and thus power
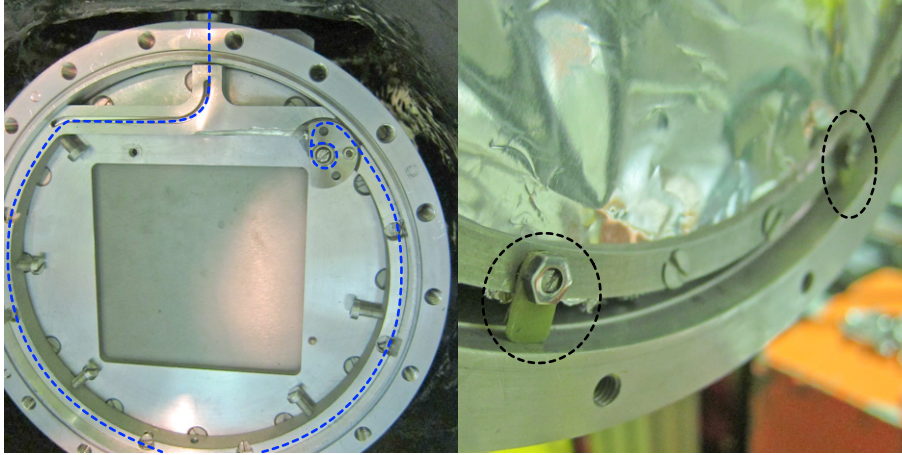
Figure A.6: *Left:* The UCN flap valve mechanism (Sec. 3.1.4) as viewed from the back. The blue dotted line (−−) indicates where the stainless steel cable that is connected to the linear motion vacuum feedthrough at the top of the DN200 cross is located (it is hidden since it runs through a track inside of the ring-shaped aluminium piece. This cable is used to rotate the pulley and axle that opens and closes the UCN flap valve. The end of the cable is fixed onto the pulley with a loop made with soft solder. *Right*: The plastic feets, made from PCB board, used to help support the weight of the 1st stage heat screen at the front production volume.

was increased from $1\,\mathrm{pW} \rightarrow 9\,\mu\mathrm{W}$ over the course of around $5\,\mathrm{mins}$ on all three sensors. The behavior of the "temperatures" read at the three sensors is shown in Fig. A.8. This processed was repeated twice.

During this measurement, neither of the top two sensors would have been submerged in the bulk fluid. However, the curves peak at different heights for the "top" and "top $-2\,\mathrm{cm}$" sensors, indicating the amount of superfluid film flow affects the measurement. These measurements were not performed when the volume was more full—especially for when one or both of the top two sensors were submerged. Also, when the converter is at lower temperatures there should be more film-flow making this technique less effective.

A.5.2   Observing UCN and CN count rates

Another technique is to use the CN beam to observe the UCN production during filling. This is the most direct method of finding the ideal level since it is this parameter that we wish to maximize in the end for a source. The
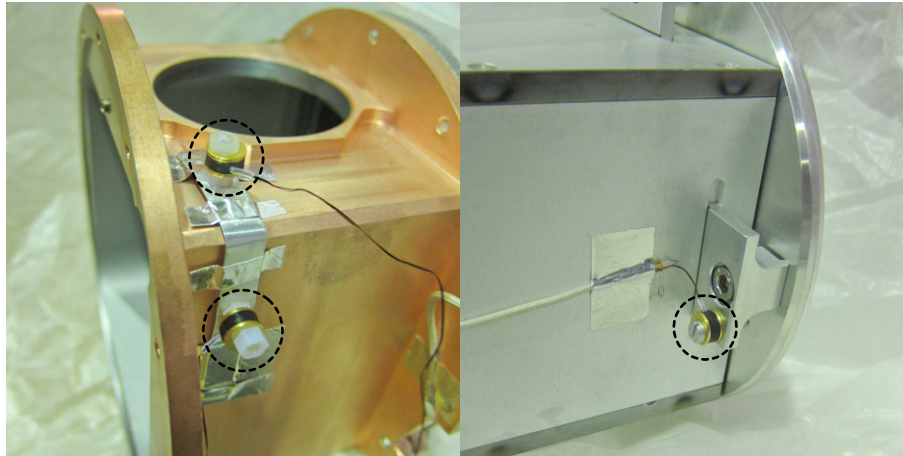
Figure A.7: The three Cernox sensors used inside the outer containment vessel of the production volume. The "top" and "top −2 cm" sensors, placed near the inner copper end piece, are shown on the *left*. They are thermally isolated from the thin aluminium strip and the copper with nylon screws and nuts. The "middle" sensor is shown on the *right*. It is located at the front end of the UCN production volume, attached to and in thermal contact with a customized claw clamp used to fix the front window of the inner production volume.

stabilized count rates in the UCN detector with the CN beam turned on and the count rate in the monitor detector during two periods of filling are shown in Fig. 3.4.

The UCN detector count rates shown are either $\dot{N}_c$, if the UCN valve is opened, or $\dot{N}_{\mathrm{det,\,leak\,\infty}}$ if the UCN valve is shut. These are given by (repeating from Sec. 3.4):

$$\dot{N}_{\mathrm{det,\,leak,\,\infty}} = \bar{\epsilon}_{\mathrm{leak}}\, P_{\mathrm{UCN}} V_{\mathrm{CN}}\, \bar{\tau}_{\mathrm{tot}}\, \bar{\tau}_{\mathrm{leak}}^{-1} \tag{A.2}$$

and

$$\dot{N}_c \approx P_{\mathrm{UCN}}\, V_{\mathrm{CN}}\, \bar{\epsilon}\, \frac{\bar{\tau}_{\mathrm{valve}}^{-1}}{\bar{\tau}_{\mathrm{wall}}^{-1} + \tau_{\mathrm{up}}^{-1} + \tau_{\mathrm{abs}}^{-1} + \tau_{\beta}^{-1} + \bar{\tau}_{\mathrm{valve}}^{-1}}\ . \tag{A.3}$$

The description of the terms won't be repeated here. For $\dot{N}_{\mathrm{det,\,leak,\,\infty}}$ the UCN valve can be hand-pulled shut or loosely shut with the pneumatic piston only. This leads to different $\bar{\tau}_{\mathrm{leak}}^{-1}$ and $\bar{\epsilon}_{\mathrm{leak}}$ values.

The idea of the measurements was to observe an increase in the count rate due to an increase in V_{CN}, the volume of converter the CN beam is incident upon. This was indeed observed during the initial part of the "first filling".
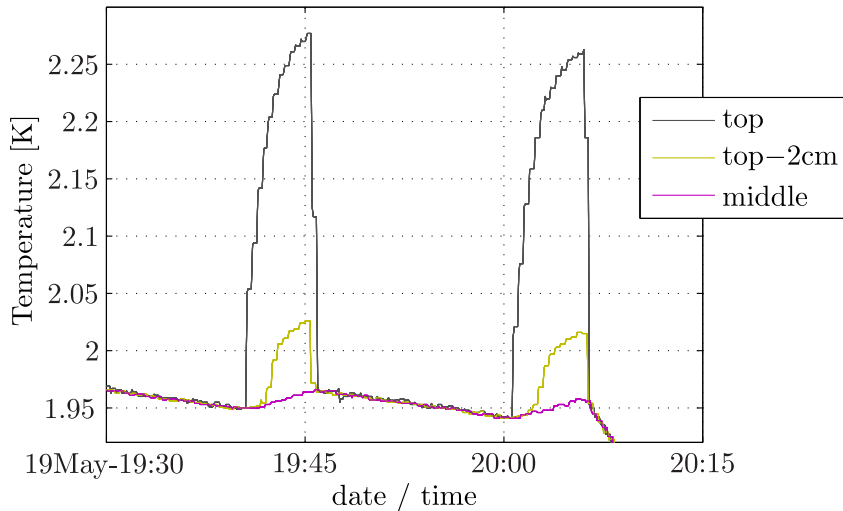
Figure A.8: The divergence of the temperature/resistance measurements from the 3 sensors placed at difference heights in the UCN production volume as the excitation power deposited in the senors were increased from $1\,\mathrm{pW} \rightarrow 9\,\mu\mathrm{W}$ (repeated twice). The deliberate over-heating is used to determine if superfluid exists at the sensor. This data was taken for when the production volume was a little bit less than half-filled.

However, unexpectedly, a drop in $\dot{N}_{\mathrm{det,\,leak,\,\infty}}$ was then observed while the volume was still being filled. This effect was observed again during the 2nd filling of the production volume. This time not only was the drop observed for the closed UCN valve count rates, but also for the open valve, i.e. $\dot{N}_c$. While there are questions over the reproducibility of the exact opening and closing of the flap valve, it is hard to imagine this effect coincidentally causing the drop for two different ways of closing the valve (both using the pneumatic piston and "hand-pulled shut") and for when the valve is opened as well. This behavior was not observed in the experiment of Ref. [Zim10], which also used a flap valve.

The reason for this drop in counts is not known. There is a hypothesis involving strong changes of the UCN extraction and transport efficiency with the size of the gap between the converter and the top of the UCN production volume. Another hypothesis is, since the change in the UCN rate is so much larger for the closed UCN valve then the open one, the buoyancy force as the beryllium plate is submerged in the converter, would affect the size of the leak
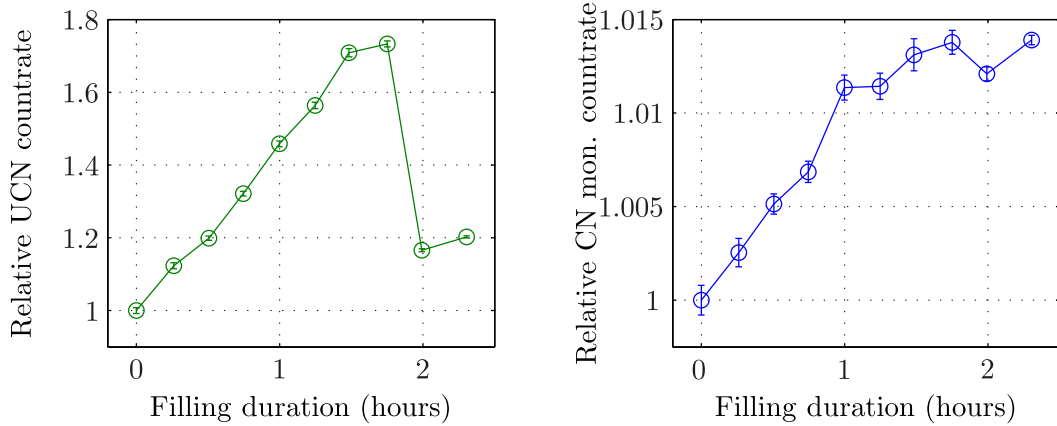
(a) First filling, data from 20/05/11 12:00 → 14:30, $T_{1\text{K pot}} \approx 1.35\,\text{K}$, $T_{\text{volume}} \approx 1.4\,\text{K}$, superleak heating $\approx 40\,\text{mW}$. UCN count rates measured with the flap valve "loosely" closed. Initial count rate in the UCN detector is $316 \pm 2\,\text{s}^{-1}$ and in the CN monitor detector is $31,500 \pm 30\,\text{s}^{-1}$.
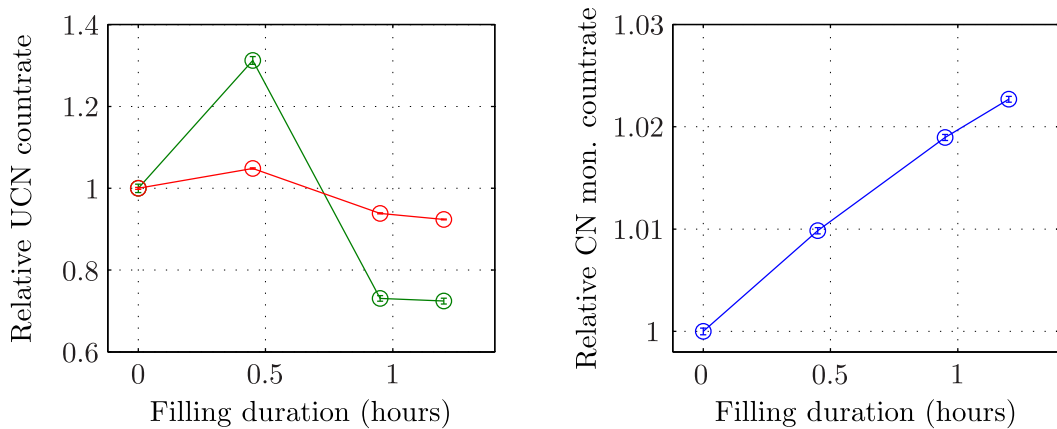
(b) Second filling, data from 22/05/11 15:10 → 16:35, $T_{1\text{K pot}} \approx 1.45\,\text{K}$, $T_{\text{volume}} \approx 1.2\,\text{K}$, superleak heating $\approx 40\,\text{mW}$. UCN count rates measured for flapvalve "hand pulled shut" (○) and flap valve open in the emptying position (○). Initial count rates in the UCN detector for "pulled shut" and open flap valve are $100 \pm 1\,\text{s}^{-1}$ and $4,247 \pm 9\,\text{s}^{-1}$, and the initial count rate in the CN monitor detector is $30,420 \pm 10\,\text{s}^{-1}$.

Figure A.9: Count rates in the UCN detector and CN monitor detector during the final periods of the two filling of the UCN production volume. For the two plots, the initial amount of superfluid already in the production volume is not well-known but it is not the same (see text). The count rates are normalized to the initial data point to emphasize the relative change observed with time. The solid lines exist for guiding the eyes only.

at the closed UCN valve much more than the open valve. However, both these hypotheses are just speculation at this point.

The initial quantity of converter is not the same between the two plots. The "1st filling" plot started with an estimated $4-6$ L in the production volume followed by a filling of $1-2$ L during the measurements. The "2nd filling" data occurred 2 days later and so a general boiling off of the superfluid was expected. The flow meter does not register mass flows below $5\,\mathrm{g\,hr^{-1}}$ and thus the upper limit of the boiled off amount of superfluid is ≈ 1.6 L. This gives an estimate of the volume of superfluid in the production volume at the start of the second filling plot. The plot spans a filling of $0.6-1.2$ L. After this plot and before the phase C set of UCN production data in Sec. 3.4, an additional $0.8-1.4$ L was added to the production volume (the 1K pot ran empty after this) and a roughly similar amount ≈ 1.0 L was pumped off over the next few days. Recall that ≈ 7.3 L is required to fill to the top of the $8\,\mathrm{cm} \times 8\,\mathrm{cm}$ inner production volume. A plot showing the CN monitor count rates and the gaseous flow out of the volume over the course of several days is shown in Fig. A.10.

For the CN monitor count rates, the reactor power, and thus CN flux, were 53.01 ± 0.01 MW and 52.96 ± 0.01 MW during the 1st and 2nd filling, respectively. Therefore, this does not explain the rise in the observed count rates. A more likely source is due to CN that would normally not reach the monitor detector, due to the small aperture, being scattered by the converter and into the detector. Once the level is above the aperture near the halfway point, an increase of converter height will increase the number scattered. The scattering is more likely to come from the shorter-wavelengths since the mean free path of 3 Å neutrons is only ≈ 70 cm in the converter, compared with ≈ 15 m for 8.9 Å neutrons.

From the rising of CN count rates during filling, it can be concluded the converter is above the half-height level. The fact that the CN count rates do not experience the same drop as UCN count rates indicates the latter is due to UCN transport effects. The reduction in the gradient as the level of the converter is higher is probably due to the lower cross-section of scattering of the CN beam to larger angles. A plateau, which should occur when the level is above the height of the CN beam, was not observed. Therefore, it is not certain from the CN count rates alone that the UCN production volume was completely filled. We can only state that since the converter was above
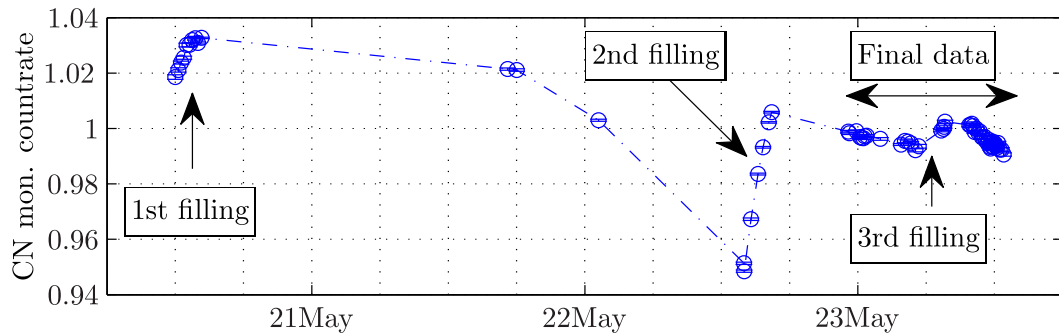
(a) The count rate in the monitor detector normalised to the mean of the points. The solid line (− ·) joining the discrete data points is used to guide the eyes only. The text labels mark when different periods of filling (via extraction through the superleak) of the production volume and when the UCN production data presented in the next section occurred.
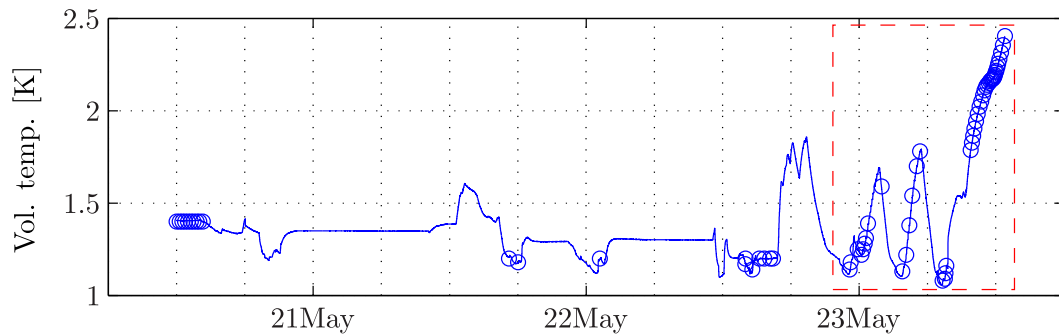
(b) The temperature of the superfluid converter; the discrete points (○) correspond to the data points in (a), while the solid line (−) shows the continuously measured temperature. The region enclosed by the red dotted rectangle (− −) is shown in detail in Fig. 3.10.
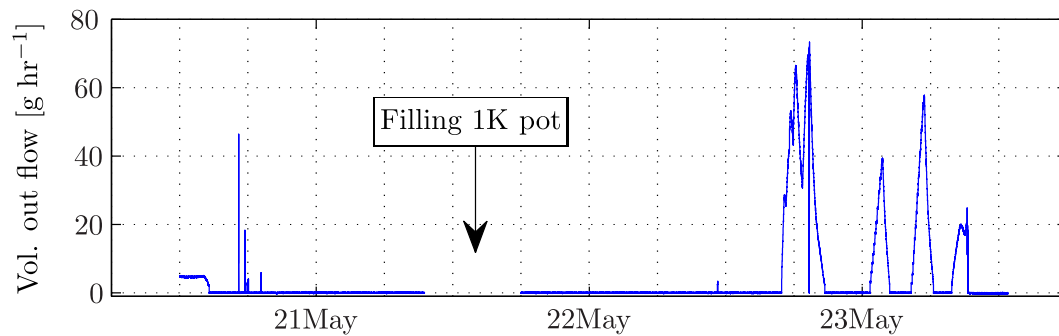
(c) The outgoing flow rate behind the ACP28 pump from the production volume. For the "final data" period an ACP15 pump was used in parallel but the flow rate through this is not known. The flow during the "filling 1K pot" period is also not known since the flowmeter was used to measure the pumping of the 1K pot.

Figure A.10: The count rates in the CN monitor detector to show its change over the course of several days. The corresponding temperature and flow rate exiting the production volume are also shown.

the half-height level at the start of the filling, and the initial rise in UCN production rate almost doubled (in the first filling), then the volume is close to being filled to first order approximations.

A.6   Timing of CN shutter, UCN valve and UCN time-of-flight

In this section, we deduce the timing of the CN shutter, UCN valve and UCN minimum time-of-flight from detailed plots of the CN monitor and UCN detector count rates during noteworthy periods of the accumulation-and-empty and continuous measurements. It should be kept in mind that the values for the CN monitor and UCN detector counts are the counts accumulated on the electronic counter card over the previous second. Also, the binary status of the CN shutter and UCN valve are the internal values of the Labview program that are outputted to the data file every second, along with the count values.

The time-of-flight of CNs are assumed to be negligible in this setup. So when the CN monitor detects counts, these are assumed to be at the instant when the CN shutter was opened (within the 1 s width of the time bins, of course). From Fig. A.11a and A.11b, we see that when the value of the CN shutter changes (from zero to a non-zero value, or vise versa), there is a delay of at least one full second, and then only sometime within the next second is the CN shutter actually physically opened or shut. This full second delay is a result of the Labview program, after changing the internal value of the CN shutter status, waiting until the start of the next 1 s cycle before sending the command to switch the relay that controls the pneumatic system of the CN shutter. That is to say, the command to switch the relay occurs at the start of the loop, which repeats itself every 1 s, rather than the end.

The time-of-flight of the UCNs from the vessel to the UCN detector might not be negligible. The speed of 250neV UCNs are $\approx 7\,\mathrm{m\,s^{-1}}$ while the distance travelled will be longer than the length of guides ($\approx 3\,\mathrm{m}$) since most trajectories are not direct. The UCN time-of-flight can be deduced from the continuous measurements where the UCN valve was left on and CN beam switched on. In this way there is no uncertainty over the opening time of the UCN valve. From Fig. A.11b, ≈ 100 UCNs were counted in the same time bin that first picked-up

CN counts. This rate is far greater than the prompt CN background in the UCN detector (see Sec. 3.4.4). This implies that the fastest UCNs reaching the detector take $< 1\,\mathrm{s}$.

From this we can deduce from Fig. A.11a that for the time bin when the UCN counts jumps from the ≈ 100, the $\dot{n}_\infty$ rate, to the > 400 value the UCN valve was opened sometime during this time bin. Since we don't know exactly when within this time bin the UCN valve was actually open, we can take the central value and assign an uncertainty of half the width of the time bin. The behavior of the UCN valve is similar to the CN shutter in that there is a full second delay after the changing of the internal status of the UCN valve in the Labview program before the valve was physically opened or shut.

Applying this uncertainty to the $1.08\,\mathrm{K}$ measurement, the CN beam was on at full intensity while the UCN valve was opened for $0.5 \pm 0.5\,\mathrm{s}$ and for $1\,\mathrm{s}$ with the CN beam at $\approx 60\%$ intensity. This is equivalent to $1.1 \pm 0.5\,\mathrm{s}$ at full intensity.

A.7 Heating from the CN beam and UCN valve opening

The temperatures in the production volume for an accumulation-and-empty with CN left on measurement and for the lowest temperature $1.08\,\mathrm{K}$ accumulation-and-empty measurement are shown in Fig. A.12. Both when the CN beam was turned on and when the UCN valve was opened caused an increase in the converter temperature. The raises in temperatures are more pronounced for the lower converter temperatures, as expected. When the UCN valve was shut, the temperature started to fall again. Quantitative data is difficult to extract from these plots, but the heating is probably more when the UCN valve was opened. Also, no abrupt changes in the temperatures could be seen for the continuous measurements where the UCN valve was left open (and the volume temperature was rising) and then CN beam switched on and off.
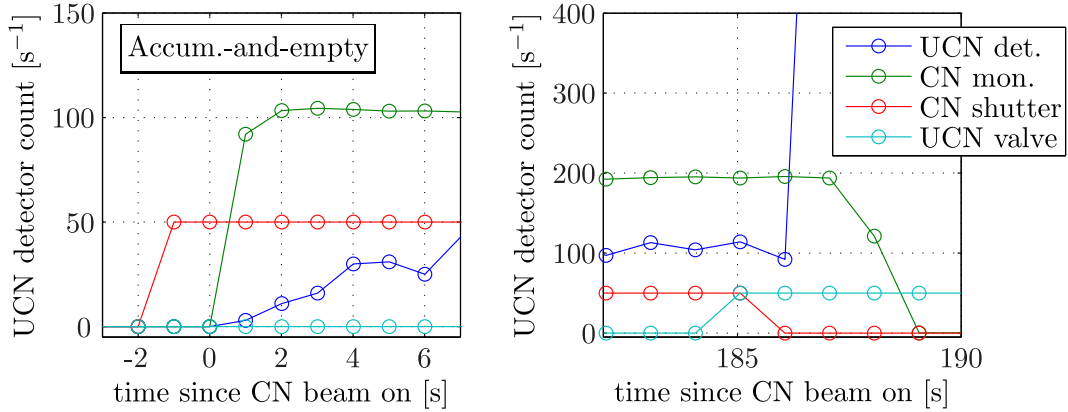
(a) At the start of accumulation (*left*) and emptying (*right*) for the 1.08 K accumulation-and-empty experiment. This data is used to deduce the time the CN beam was left on with and continually producing UCNs when the UCN valve was opened to empty the accumulated UCNs.
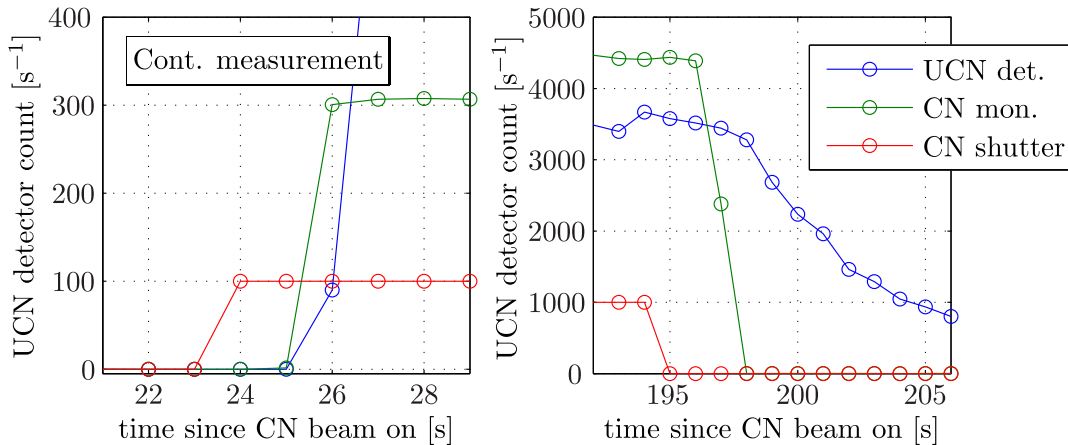
(b) When the CN beam was switched on (*left*) and then off again (*right*) for the continuous measurement during phase A at 1.3 K.

Figure A.11: The counts in the UCN detector and CN monitor zoomed-in for when the CN beam was turned on and off for the two types of measurements. The status (open or shut) of the CN shutter and UCN valve on the data acquisition computer is also shown. The vertical scale is for the UCN detector counts only. The CN monitor counts are re-scaled. The status values of the CN shutter and UCN valve, which are binary values (0 or 1, with 0 being "closed" for both), are also re-scaled.
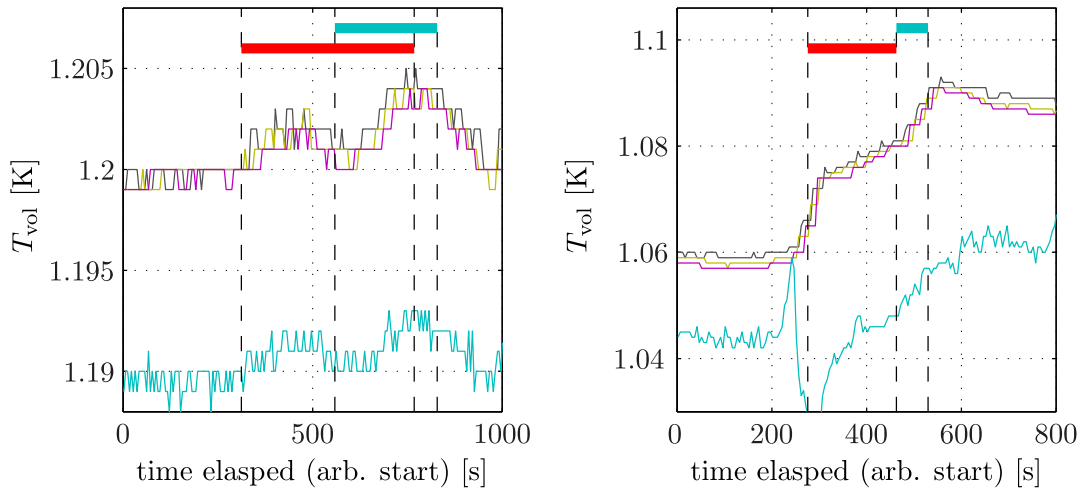
Figure A.12: The effects of the CN beam and UCN valve on the converter temperature. The plot on the *left* is from the 1.2 K accumulation-and-empty with the CN beam left on made at 16:25, 22-05; and on the *right* is from the 1.08 K accumulation-and-empty measurement made at 07:20, 23-05. The continuous black (–), amber (–) and magenta (–) coloured lines represent the temperatures at the "top", "top –2 cm", and "middle" senors in the production volume, respectively. The ^{3}He pot temperature, also shown, is the continuous cyan (–) line. The thick horizontal bars in red (■) indicated when the CN beam was on and in cyan (■) when the UCN valve was opened. The first, fast jump in production volume temperature on the *right* is caused by the jump in the ^{3}He and is unrelated to the CN beam (it also occurs before the CN beam was turned on).

Appendix B

Appendix for the HOPE magnetic trap

B.1   Magnetic field measurements

The details of the magnetic field measurements of the Halbach-type octupole permanent magnet modules from Sec. 4.1 are described in this section. For the measurements, a 3-axis hall probe was used with a Lakeshore 460 3-channel gaussmeter [Lak04]. The tip of the probe is cubic in shape and the 3 hall sensors are located on the bottom and two side-faces. The dimensions are shown in Fig. B.1. The aluminium probe holder used for the measurements is also shown in the figure. The "stem" of the "mushroom" shaped probe holder slots inside the circular aperture of a magnet module; while the lip of the "cap" fits across the outer stainless steel jacket of a module. The probe is inserted into a slot, which defines the radial position of the probe and aligns it parallel to the z-axis of a module. The tip is adjusted and fixed so that it sits centered in the z axis.

For the consistency measurements, the rotation orientation of the probe relative to the holder is fixed so that one of the transverse Hall sensors is perpendicular to the $\vec{\rho}$ vector. This we shall call the B_ρ sensor. The other transverse probe will be called the B_ϕ sensor. The probe holder is then rotated from piece to piece for the different measurements. Due to the change of orientation of the B-field lines, the following information is used from the gaussmeter at the various positions to determine the apparent $|B|'$: at the
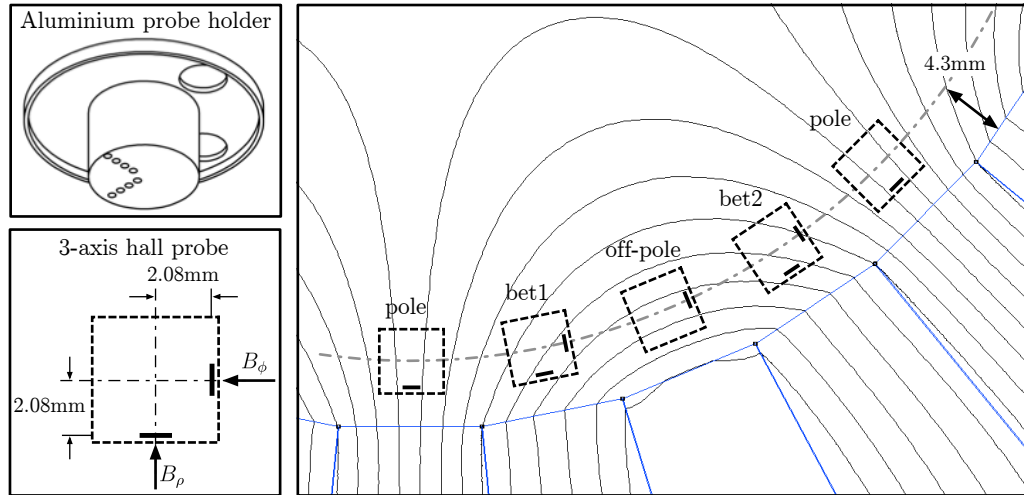
Figure B.1: *Top-left:* the "mushroom" shaped aluminium hall probe holder used for the magnetic field measurements. *Bottom-left:* the dimensions in the xy-plane of the tip of 3-axis hall probe used for the measurements. The two hall probes are labelled B_ρ and B_ϕ due to the orientation of the probe used with the magnetic trap for the consistency checks. *Right:* the positions of the 3-axis hall probe relative to the octupole magnetic field for the measurements of Fig. B.2. For the pole measurement, only the value from the B_ρ probe is used; for the off-pole measurements, only B_ϕ is used; for the bet1 and bet2, the value used for $|B| = \sqrt{|B_\rho|^2 + |B_\phi|^2}$. The distance of the central-axis of the hall probe from the magnet walls is shown also.

pole position $|B|' = |B_\rho|$; at "bet1" $|B|' = \sqrt{|B_\rho|^2 + |B_\phi|^2}$; at off-pole $|B|' = |B_\phi|$; and at "bet2" $|B|' = \sqrt{|B_\rho|^2 + |B_\phi|^2}$. The $|B|'$ values for all the magnet pieces of each module are shown in Fig. B.2.

Combining the measurements from the two probes, B_ρ and B_ϕ, is only valid if the field does not vary significantly at their two positions. This is not the case for a radial octupole field close to the magnet walls. Only the "pole" measurements give a good estimate of the value of the true $|B|$ at the magnet walls since the field is perpendicular to the B_ρ hall sensor and the sensor is close to the walls (≈ 2.2 mm away). For the "off-pole" measurements there is a deviation from the perpendicular position for the B_ϕ and the probe is far from the magnet walls. This is why these give the weakest $|B|'$. For the "bet1" and "bet2" measurements, there is the same angle between the field at the B_ρ sensor, and they are both the same distances from the magnet walls. However, there is a greater angle between the field and the B_ϕ sensor for
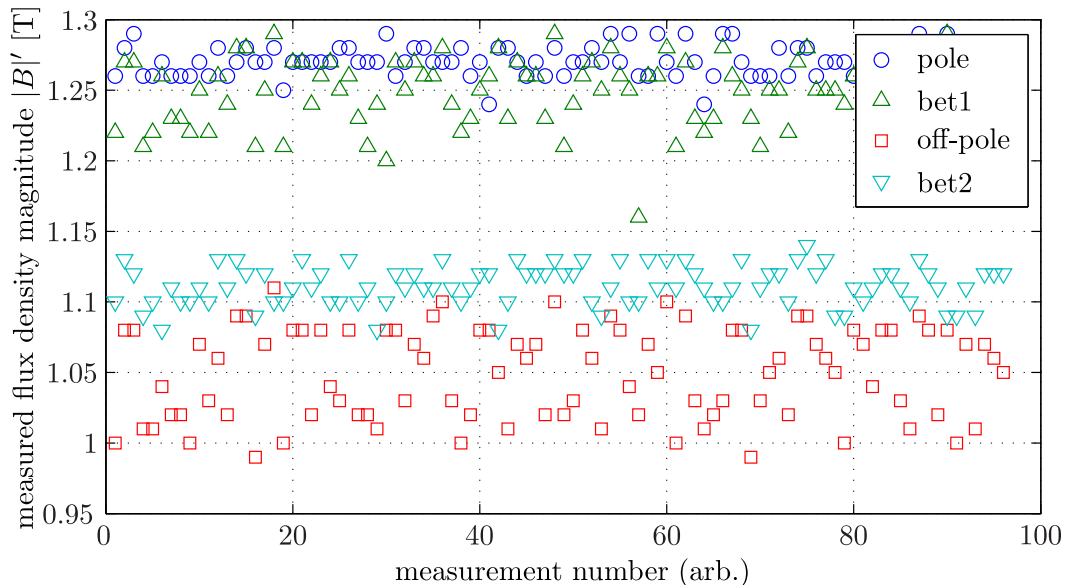
Figure B.2: Consistency measurements of all the 384 permanent magnetic pieces of the 12 octupole modules. Only the relative value of $|B|'$, the measured magnitude of the flux density, at the same position ("pole", "bet1", "off-pole" and "bet2") can be compared. The differences are caused by the different angle the B-field makes with the hall sensor used in the measure. This is described in details in Sec. B.1. The anonymously low "bet1" measurement was verified by radial $|B|$-profile measurements and was found not to be a problem.

the "bet2" measurements. This is why these measurements are weaker than "bet1". Because of these differences, $|B|'$ can only be used to compare the relative strength within the same type of measurements.

Measurements of the magnetic field strength as a function of the radial position $|B(\rho)|$ were also made. The 11 ρ-profile measurements used the 8 holes at different radial distances in the aluminium probe holder. At each measurement the probe was rotated until the maximum value was obtained at one of the transverse probes. This ensured that the field lines were perpendicular to the probe at that position and a true $|B|$ value measured. Since the holes in the probe holder only fix the ρ-distance at the center of the probe, rotating the probe causes a slight shift in the ρ position. This was taken into account. The estimated uncertainty in the ρ distance is estimated to be $\approx 0.2\,\mathrm{mm}$ for these measurements and is a due to a combination of the precision of the placement the holes, wobbling of the probe and the angle of the probe used for the

maximum measured field.

The positions where perhaps a weaker magnet was identified by the consistency measurements were checked with the $|B(\rho)|$ measurements. A comparison with the $|B(\rho)|$ of the same type was made. A plot of an average value measurement of each type are shown in Fig. B.3. These were fitted with an ideal octupole (i.e. $|B(\rho)| = k\rho^3$) and the $|B(\rho)|$ curves (*top-left* of that figure) from the FEMM calculations with a linear multiplicative or scale factor a. This was done for both the standard and the depolarized corners model version. The results from the fits are shown in Table. B.1. The uncertainties used for the fit were estimated to be $\pm 0.01\,\mathrm{T}$ in $|B|$ and $\pm 0.2\,\mathrm{mm}$ in the radial position of the probe.

Table B.1: The results from fitting the 11 ρ-profile measurements of $|B|$ with an ideal octupole $|B(\rho)| = k\rho^3$, and the results from FEMM calculations of the standard ("std.") and depolarised corners ("depol.") geometry with a scaling factor, denoted by a. The octupole strength constant k is given in units of $[\mu\mathrm{T\,mm^{-3}}]$ and the $|B_{\mathrm{wall}}|$ values in [T]. The uncertainty from the fits in k are all between $0.01 - 0.02\,\mu\mathrm{T\,mm^{-3}}$; in $|B_{\mathrm{wall}}|$ between $0.01 - 0.02\,\mathrm{T}$; and $a = 0.01$.

position	ideal octupole			FEMM std.			FEMM depol.		
	k	$|B_{\mathrm{wall}}|$	χ^2_ν	a	$|B_{\mathrm{wall}}|$	χ^2_ν	a	$|B_{\mathrm{wall}}|$	χ^2_ν
pole	1.38	1.41	0.2	0.95	1.35	0.3	0.96	1.35	0.3
	1.43	1.46	0.2	0.99	1.39	0.2	0.99	1.40	0.2
	1.39	1.42	0.2	0.96	1.35	0.4	0.99	1.35	0.4
off-pole	1.42	1.45	2.0	0.98	1.36	1.4	0.98	1.36	1.6
	1.48	1.51	0.8	1.02	1.40	0.6	1.02	1.41	0.6
	1.39	1.42	3.0	0.97	1.32	2.3	0.97	1.33	2.6
	1.38	1.42	1.8	0.96	1.31	1.2	0.96	1.33	1.4
	1.45	1.48	1.6	1.00	1.37	1.2	1.00	1.39	1.3
between	1.45	1.49	0.1	1.00	1.42	0.3	1.01	1.42	0.2
	1.43	1.46	0.4	0.99	1.39	0.7	0.99	1.40	0.6
	1.47	1.50	0.5	1.02	1.43	0.7	1.02	1.44	0.6

The closest position of the hall sensor for these measurement do not allow the fits with the three different curves to be discerned; although separating between the FEMM standard and FEMM with depolarized corners modeled is more important. In order to be conservative, the lower of the values should be used for discussion. The fitting with the off-pole curves by far give the
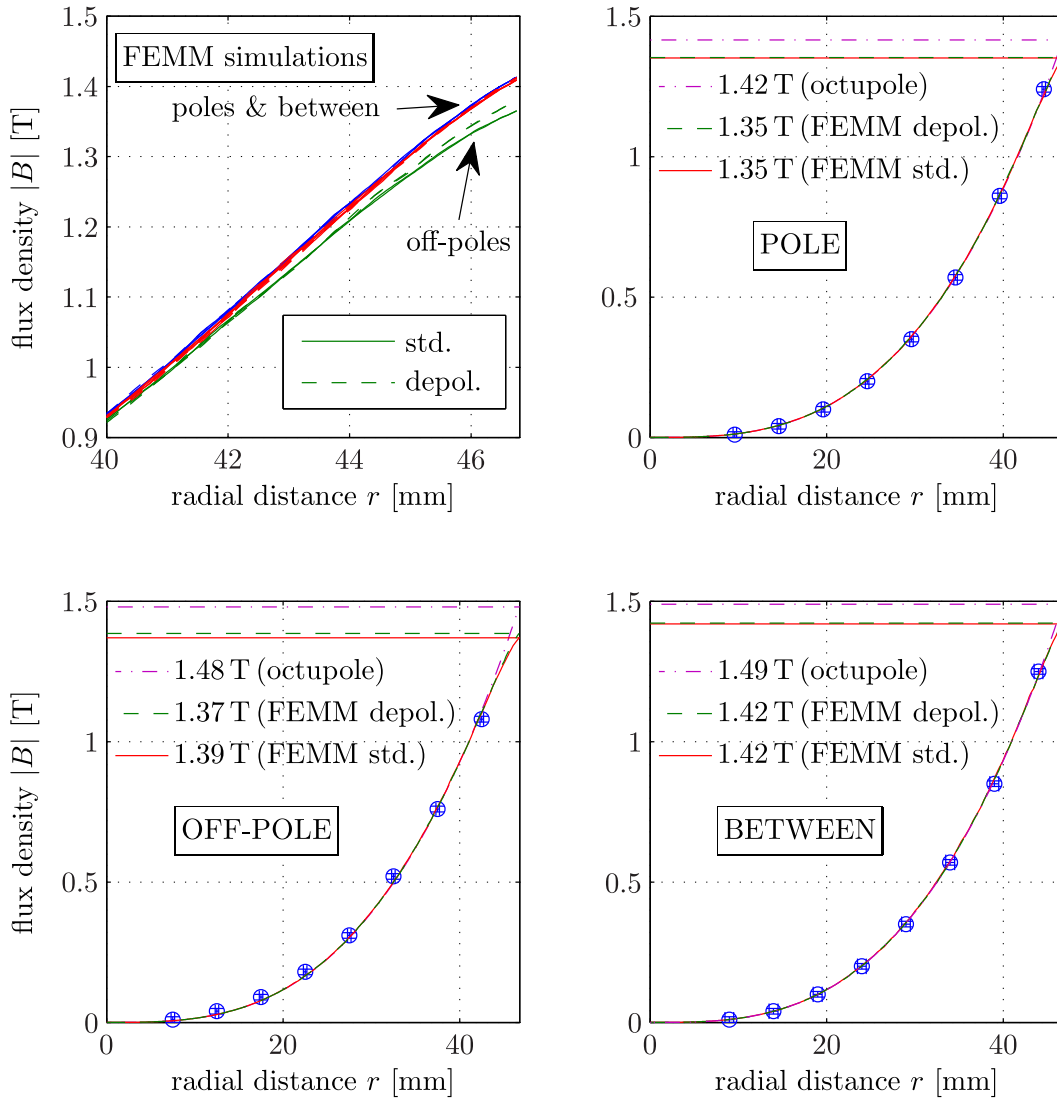
Figure B.3: *Top-left:* calculated $|B|$ value along different $\vec{\rho}$-profiles centered on pole, off-pole and between pieces of the Halbach octupole near the walls of the magnets. The continuous lines (–) are for the standard FEMM calculations and the dashed-lines (– –) are with depolarized corners (see Sec. 4.1.1). The lines (continuous and dashed) for poles and between are indistinguishable on the scale shown. *Top-right, bottom-left and bottom-right:* measured $|B|$, shown as blue circles (○), for different radial distances ρ along profiles centered on a pole, off-pole and between piece. More radial profile measurements were made but only one of each is shown. The magenta dashed-dot line (– ·) are the best-fits with an ideal octupole; the red continuous line (– –) and green dashed line (– –) are fits with the FEMM standard and FEMM depolarised corners calculated curves (of the *top-right*) with a multiplicative factor (see text). The horizontal lines and values on the plots are the $|B|$ at the magnet walls from these fits.
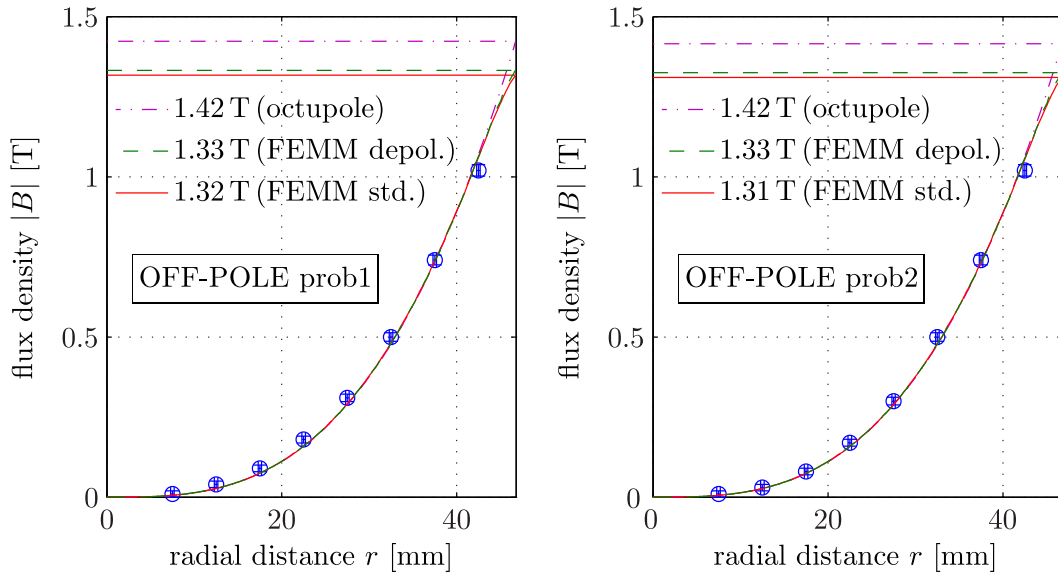
Figure B.4: The two off-pole $|B(\rho)|$ measurements with large χ_ν^2 (2.6 and 1.4) and the weakest a and $|B_{\text{wall}}|$ from Table B.1. These are both on the same octupole module which is placed at the end of the array to reduce the effects of the weaker fields.

poorer fits. The two off-pole measurements with $\chi_\nu^2 = 2.6$ and 1.4 are shown in Fig. B.4. These also give the lowest a and $|B_{\text{wall}}|$ values—the latter of which is expected to be weakest at the off-pole pieces already. What is worrying is that the fits probably over-estimate $|B_{\text{wall}}|$ since the last points falls below the fitted curves. Fortunately these two weaker off-pole pieces are from the same octupole module and so it is deliberately placed at the end of the array where the weaker field is less important due to the end-coils. Further magnetic field measurements of the array should be performed to carefully check the field after combining the modules.

B.2   Moving thin foil extraction

The calculations of the horizontal slide trap extraction technique described in Sec. 5.3 is presented here. Some results have been published in Ref. [LZ09] but the code has since been improved for this thesis. The general conclusion of the calculations remain the same.

The calculations are based on a simple iterative loop where the time during

the sliding trap extraction process t is incremented by Δt after each step. Initially all the UCNs are started in the converter volume with a superthermal spectrum $dn/dv \propto v$. The UCNs are placed in velocity bins of equal width with the width chosen to be 1/10th of that of the velocity of the moving trap's magnetic walls v_{trap} in order to model the doppler reflections from the magnetic end walls. The magnetic field gradients in the trap are neglected so that the octupole and end coil fields are modeled by step-potentials. All the material except for the thin foil are assumed to be lossless. The dimensions used for the calculations are: radius of the trap $r_{\text{trap}} = 4.7\,\text{cm}$, radius of converter vessel $r_{\text{vessel}} = 3.5\,\text{cm}$, radius of thin foil $r_{\text{foil}} = 2\,\text{cm}$, and length of the trap $L_{\text{trap}} = 80\,\text{cm}$ (an approximate "effective length"). The volume of the trap V_{trap} and converter vessel V_{vessel} available to the UCNs are incremented and decremented by $\pi r_{\text{trap}}^2 v_{\text{trap}} \Delta t$ and $\pi r_{\text{vessel}}^2 v_{\text{trap}} \Delta t$ after every step. Initially $V_{\text{trap}} = 0$ and $V_{\text{vessel}} = \pi r_{\text{vessel}}^2 L_{\text{trap}}$.

The UCNs in the converter vessel and trap are assumed to be always in mechanical equilibrium. Under this assumption the number of UCNs colliding off a surface with area A, velocity between $v + dv$, within a time Δt is given by: $(dn/dv)\,vA\,\Delta t/(4V_{\text{trap/vessel}})$, i.e., it depends on the current number of UCNs in the trap and converter vessel and their respective volumes during each time-step of the calculation. For UCNs that make a collision with the thin foil, the probabilities of transmission and loss are calculated using the equations from [Zim05]. The thickness of the foil is $0.2\,\text{mm}$ for the different types of materials used: aluminium (Al), titanium (Ti) and vanadium (V). The real and imaginary parts of the neutron optical potentials are those from the reference.

Transmission and losses are calculated for UCNs traveling from V_{trap} to V_{vessel}, and V_{vessel} to V_{trap}. In former case, the kinetic energy E_{kin} of the UCNs are increased by the neutron optical potential of superfluid helium $18.6\,\text{neV}$; and in the latter case this energy is subtracted. This last effect is the main difference between the calculations from Ref. [LZ09] and this thesis. Previously, the increase of $18.6\,\text{neV}$ was only applied to the final spectrum of UCNs in the trap by shifting it. In the current calculations, the increase in energy during the increments causes the UCNs to have a higher collision rate and thus increase their probability of making passages through the foil. This increases their probability of returning back to the converter vessel or being lost.

UCNs in the converter vessel that make a collision with the front magnetic wall with an area πr_{vessel}^2 will have an increase in the UCN velocity of $2v_{\text{trap}}$ along the movement axis due to the doppler reflections. In the trap, only UCNs that collide off a surface with area πr_{vessel}^2 were calculated to have a doppler redshift even though $r_{\text{vessel}} > r_{\text{vessel}}$. This is done to simplify the calculations by assuming that reflections off the front and back annular regions of the magnetic wall with area $\pi(r_{\text{vessel}}^2 - r_{\text{trap}}^2)$, which causes a doppler blueshift and redshift, respectively, will approximately cancel each other out. No doppler shift is expected to occur at the sidewalls of the trap.

Due to the gain in energy from leaving the superfluid helium converter, UCNs immediately after passing through the foil and into the trap will have kinetic energy $E_{\text{kin}} > 18.6\,\text{neV}$. However, due to the receding back magnetic wall, they can undergo doppler redshift reflections and end up with kinetic energy $E_{\text{UCN}} < 18.6\,\text{neV}$. This is the reason for the tail of UCNs with $E_{\text{UCN}} < 18.6\,\text{neV}$ in the final energy spectrum for foils with a negative neutron optical potential (titanium and vanadium). Note that in V_{trap}, since there is no magnetic potential or helium, the total energy $E_{\text{UCN}} = E_{\text{kin}}$.

Another change in the code is the prevention of the number of UCN leaving a volume to be greater than the number currently in that volume at a time step. This can happen if the collision rate $vA\,\Delta t/(4V_{\text{trap or vessel}})$ is much greater than the number of UCNs. This occurs for a few time steps at the beginning and end when V_{trap} and V_{vessel} are small. The effect of this new correction makes only a very small difference in the overall process since it only occurs for a few time steps at the start and end.

Calculations were performed for aluminium (Al), titanium (Ti) and vanadium (V) foils at different trap sliding speeds. The number of UCNs in the converter vessel n_{vessel} and trap n_{trap} as a function of the time during the procedure is shown in Fig. B.5. The final UCN energy spectrum in the trap is shown in Fig. B.6.

The choice of UCN energy range to use in the simulations and how to define the extraction efficiency are tricky. In the vessel volume, E_{trap} is very high due to the optical potential of the material walls. However, in the magnetic trap, for the standard $1.2\,\text{T}$-$0.3\,\text{T}$-$1.2\,\text{T}$ configuration of the superconducting coils used for the horizontal trap setup (see Sec. 5.1) then $E_{\text{trap}} = 54\,\text{neV}$ only. Also, due to the gain in kinetic energy of $18.6\,\text{neV}$ when leaving the helium, only
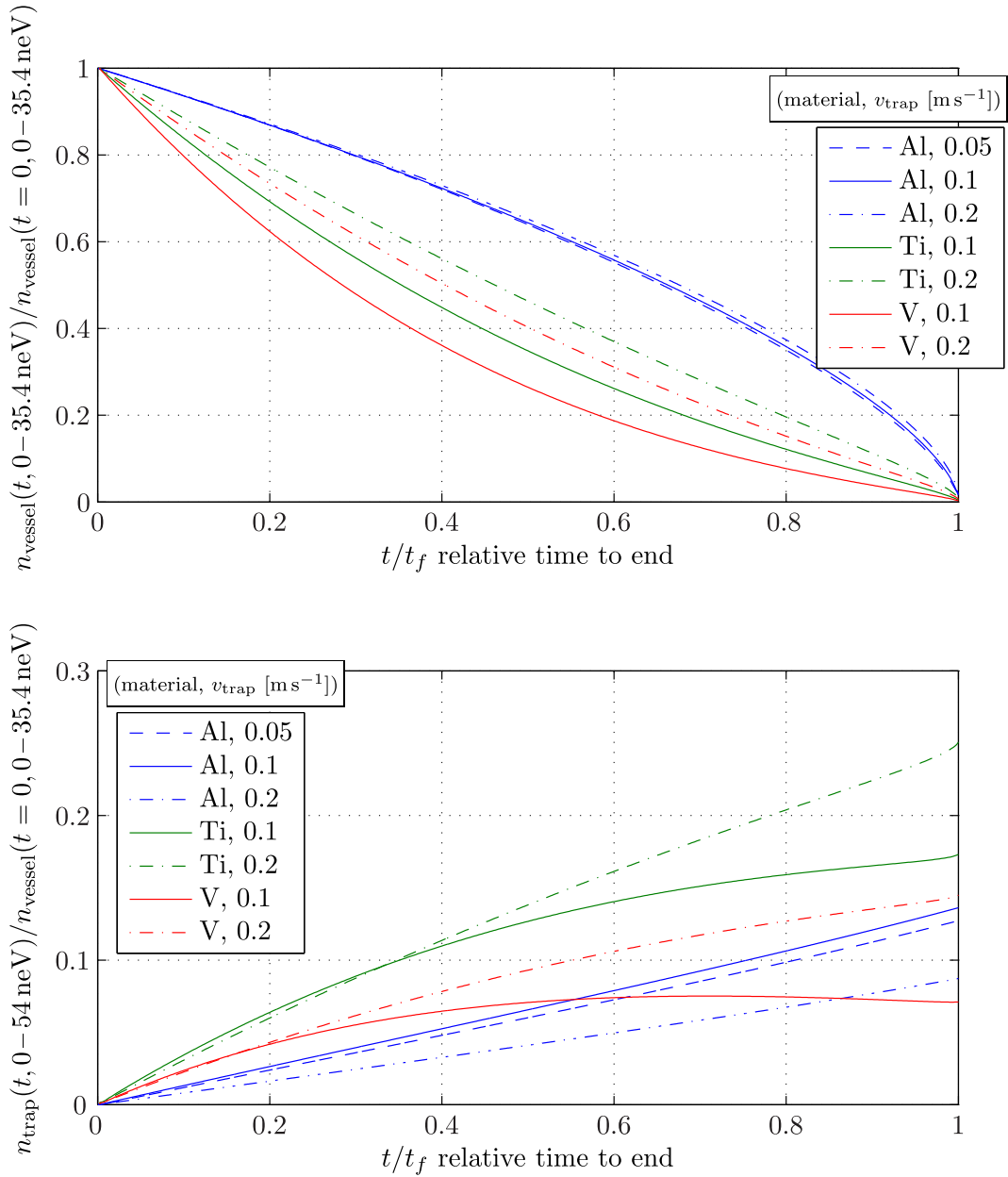
Figure B.5: The number of UCNs in the production vessel V_{vessel} with $E_{\text{kin}} = 0-35.4\,\text{neV}$ (*top*) and in the magnetic trap V_{trap} with $E_{\text{kin}} = 0-54\,\text{neV}$ (*bottom*) as a function of the relative time t/t_f from the simulations with different foil material and trap sliding speeds v_{trap}. Both numbers are normalized to the initial number of UCNs in the vessel with $E_{\text{kin}} = 0-35.4\,\text{neV}$. The details are given in the text.
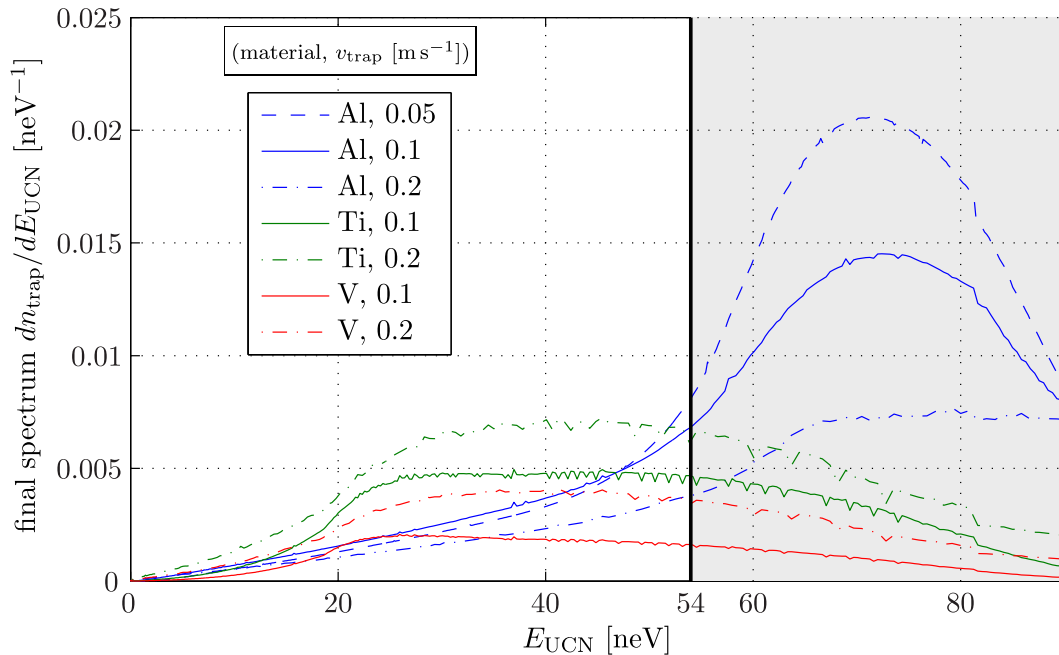
Figure B.6: The final spectrum of UCNs in the trapping volume V_{trap}. For a horizontal magnetic trap $E_{\text{trap}} = 54\,\text{neV}$, so only energies below this are relevant. Nonetheless, the higher energies are also plotted (shaded in grey ▨) to give an indication of the sliding trap extraction process if E_{trap} was higher.

UCNs in the vessel with $E_{\text{kin}} < 35.4\,\text{neV}$ will have an energy $E_{\text{UCN}} < E_{\text{trap}}$ when it first enters the volume. However, UCNs with $E_{\text{UCN}} > E_{\text{trap}}$ in the trap, if they survive for long enough times, can end up with $E_{\text{UCN}} < E_{\text{trap}}$ due to doppler cooling reflections.

In these calculations, UCNs in the magnetic trap with $E_{\text{UCN}} < 100\,\text{neV}$ are left in the trap so that they have a chance to doppler cool and end up with $E_{\text{UCN}} < E_{\text{trap}} = 54\,\text{neV}$. This could be realized in a physical setup by temporarily putting a piston or a foil in the magnetic trap. This would help increase the final number of UCNs that can remain magnetically stored in the trap. Temporarily raising E_{trap} in the trapping volume is necessary for any UCNs to be extracted successfully if an aluminium foil is used. This is because aluminium has a neutron optical potential, coincidentally, $V_{\text{Al}} = 54\,\text{neV}$, so only UCNs with $E_{\text{UCN}} > 54\,\text{neV}$ can make it into the magnetic trapping volume. In Fig. B.6, while only UCNs with $E_{\text{UCN}} < 54\,\text{neV}$ can remain trapped, the spectrum is plotted for a higher energy range. This is done to show that the

use of an aluminium foil is much more useful if the final trapping volume is much higher. For a E_{trap} = 54 neV, only the doppler cooled tail of UCNs remain in the trap.

The final number of UCNs remaining in the V_{trap} and with $E_{\text{UCN}} < 54$ neV give how efficiency the sliding trap extraction is. These values, $n_{\text{trap}}(t_f, 0-54\,\text{neV})$, are shown in Fig. B.5. These values are divided by the number of UCNs with $E_{\text{kin}} < 35.4$ neV initially in V_{vessel}, $n_{\text{trap}}(t = 0, 0-35.4\,\text{neV})$. This is taken as the normalization for determining the extraction efficiency. For this, it can be seen that the best material and sliding velocity is with a titanium foil (Ti) with $v_{\text{trap}} = 0.2\,\text{m}\,\text{s}^{-1}$, which gives an efficiency of $\approx 25\%$.

B.3   Alternative monitoring designs

In Fig. 5.14 a possible experimental design for when a reflecting piston is inserted after the bottom end coil is ramped up is shown. The main design for below the trap is so the high-field seekers (and some low-field seekers) can be counted so that the filling can monitored. However, if the piston is to be inserted before ramping up the bottom end coil—the main advantageous being a reduced heating of UCNs due to the increasing magnetic field—then a different setup is required to monitor the high-field seekers. Two possible designs are presented in Fig. B.7 of this section. The schematic diagrams show the required positions of the side gate valve, linear guide switcher, piston, and UCN reflecting plate (for one of them) when monitoring the high-field seekers leaking around the gap between the piston and inner stainless steel tube when it is inserted. These setups can also be used if a reflecting paddle is used and the monitoring of the cleaned UCNs escaping the bottom end coil (see Sec. 5.4) is desired.

The main idea behind these setups is to guide UCNs escaping from the trap to a UCN detector, called "UCN detector B", when a piston or paddle is inserted into the trap. The standard detector that is used for counting the survivors in the trap, "UCN detector A", can't be used since the linear motion guide switcher below the trap can not be moved while something is inserted into the trap from below.

In the first idea, an angled guide with a hole for the shaft supporting the
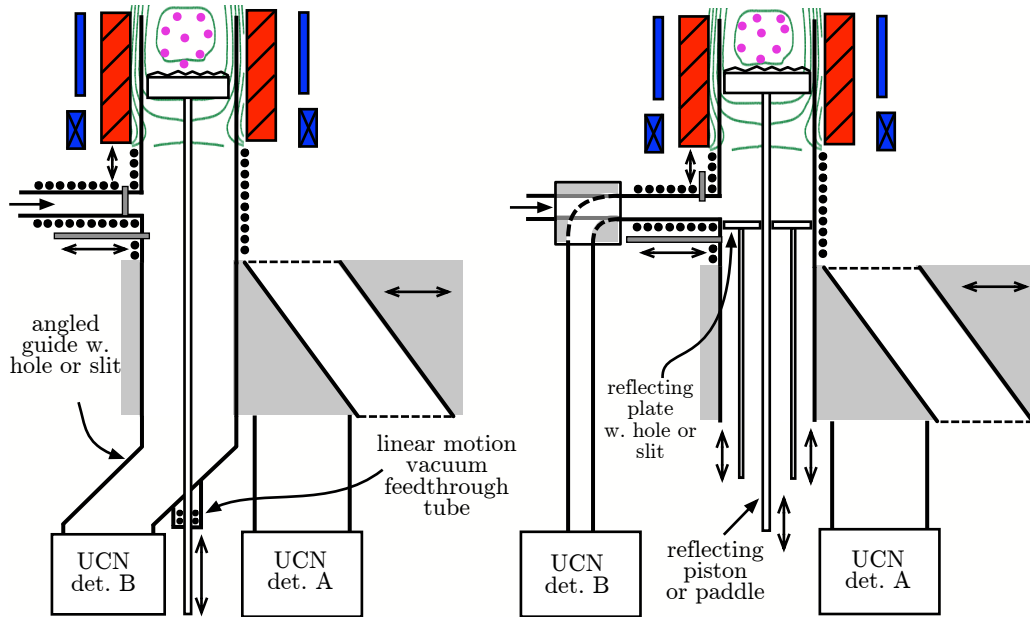
Figure B.7: Two possible setups for monitoring the high-field seekers leaking around the gap between the piston and the stainless steel tube if the piston is inserted before the ramping up of the end coil. Both are valid for monitoring the cleaned UCNs escaping the bottom end coil when the paddle is used. The unlabeled elements correspond to those in Fig. 5.14. The new components and their purpose are described in the text of this section.

piston or a slit for the paddle to pass through is used. The gap at this hole or slit should be made as small as possible. The linear motion feedthrough (shown as two O-rings) should exist on a small tube welded onto the angled guide. For a piston, this tube needs to be as wide as the shaft of the piston and can be short. For a paddle it needs to be as wide as the paddle and as long as the paddle. The angled guide connects to UCN detector B below the trap. In this setup, the second UCN guide switcher is not needed.

In the second idea, an independently movable reflecting plate—again, which has a small hole for the shaft of the piston or a slit for the paddle—is used to reflect UCNs to the side gate valve to UCN detector B via the second linear UCN guide switcher. The gap between the reflecting plate and the inner stainless steel tube should be as small as possible also. This reflecting plate can also be used to clear the high-field seekers trapped at the lower end coil when it is ramped when the paddle is used. In both these ideas, it is unclear

how an absorber ring inserted from below—if needed—can be implemented.

Bibliography

[Abe97] H. Abele, et al., *A measurement of the beta asymmetry A in the decay of free neutrons*, Physics Letters B **407** (1997), no. 3–4, 212 – 218.

[Abe06] ———, *Characterization of a ballistic supermirror neutron guide*, Nuclear Instruments and Methods in Physics Research Section A: Accelerators, Spectrometers, Detectors and Associated Equipment **562** (2006), no. 1, 407–417.

[Abe08] H. Abele, *The neutron. Its properties and basic interactions*, Progress in Particle and Nuclear Physics **60** (2008), no. 1, 1–81.

[Age89] P. Ageron, *Cold neutron sources at ILL*, Nuclear Instruments and Methods in Physics Research Section A: Accelerators, Spectrometers, Detectors and Associated Equipment **284** (1989), no. 1, 197–199.

[AM76] M. Atkins and P. V. E. McClintock, *Isotopic purification of ^4He*, Cryogenics **16** (1976), no. 12, 733–734.

[AMK85] P. Ageron, W. Mampe, and A. I. Kilvington, *The temperature dependence of ultra-cold neutron confinement times*, Zeitschrift für Physik B Condensed Matter **59** (1985), no. 3, 261–263.

[Ang09] A. Anghel, et al., *The PSI ultra-cold neutron source*, Nuclear Instruments and Methods in Physics Research Section A: Accelerators, Spectrometers, Detectors and Associated Equipment **611** (2009), no. 2–3, 272–275.

[Api] Apiezon, *Vacuum grease properties*, `http://www.apiezon.com/apiezon-vacuum-greases-properties-table.htm`.

[Arz12] S. Arzumanov, et al., *Analysis and correction of the measurement of the neutron lifetime*, JETP Letters **95** (2012), no. 5, 224–228.

[Atc10] F. Atchison, et al., *Diffuse reflection of ultracold neutrons from low-roughness surfaces*, The European Physical Journal A **44** (2010), no. 1, 23—29.

[Bak03] C. A. Baker, et al., *Experimental measurement of ultracold neutron production in superfluid ^4He*, Physics Letters A **308** (2003), no. 1, 67–74.

[Bak06] ———, *Improved experimental limit on the electric dipole moment of the neutron*, Physical Review Letters **97** (2006), no. 13, 131801.

[Bak10]   ———, *CryoEDM: a cryogenic experiment to measure the neutron electric dipole moment*, Journal of Physics: Conference Series **251** (2010), no. 1, 012055.

[Ben08]   C. Benabderrahmane, et al., *Development of cryogenic undulator CPMU at SOLEIL*, Proceedings of EPAC08, Genova, Italy **02** (2008), no. T15, 2225–2227.

[Ber93]   M.J. Berger, et al., *ESTAR, PSTAR, and ASTAR: Computer programs for calculating stopping-power and range tables for electrons, protons, and helium ions (version 1.2.3)*, `http://physics.nist.gov/Star` [2012, Aug 20]. National Institute of Standards and Technology, Gaithersburg, MD., 1993.

[Ber12]   J. Beringer, et al. (Particle Data Group), *The review of particle physics*, Physical Review D (Particles, Fields, Gravitation, and Cosmology) **86** (2012), no. 010001, .

[Bop88]   P. Bopp, et al., *The superconducting neutron decay spectrometer PERKEO*, Nuclear Instruments and Methods in Physics Research Section A: Accelerators, Spectrometers, Detectors and Associated Equipment **267** (1988), no. 2–3, 436 – 447.

[BP05]   J. D. Bowman and S. I. Penttila, *On the measurement of the neutron lifetime using ultracold neutrons in a vacuum quadrupole trap*, Journal of Research of the National Institute of Standards and Technology **110** (2005), 361–366.

[Bro00]   C. R. Brome, *Magnetic trapping of ultracold neutrons*, Ph.D. thesis, Harvard University, 2000.

[Bro01]   C. R. Brome, et al., *Magnetic trapping of ultracold neutrons*, Phys. Rev. C **63** (2001), no. 5, 055502.

[Bro09]   Bronkhorst High-tech B. V., *Instruction manual, operation instructions digital mass flow/pressure instruments parameters and properties*, `http://www.massflow-online.com/`, 2009.

[Bro12]   D. Brose, et al., *Absorber materials for low-energy neutrons—theoretical and experimental studies*, Nuclear Instruments and Methods in Physics Research Section A: Accelerators, Spectrometers, Detectors and Associated Equipment **664** (2012), no. 1, 353 – 357.

[CEC97]   O. Chubar, P. Elleaume, and J. Chavanne, *Radia v4.1*, `www.esrf.eu/Accelerators/Groups/InsertionDevices/Software/Radia`, 1997.

[CER]   CERN - European Organization for Nuclear Research , *PH-DT-DI gas project*, `http://detector-gas-systems.web.cern.ch/`.

[Cic10]   J. Cicéron, *Développement d'un système de détection pour les produits de désintégration beta des neutrons*, Master's thesis, INP Toulouse ENSEEIHT, 2010.

[Coc07]   A. Coc, et al., *Coupled variations of fundamental couplings and primordial nucleosynthesis*, Physical Review D **76** (2007), no. 2, 023511–12.

[Dau11] M. Daum, et al., *First observation of trapped high-field seeking ultracold neutron spin states*, Physics Letters B (2011), no. 704, 456–460.

[DP80]   J. R. Dormand and P. J. Prince, *A family of embedded runge-kutta formulae*, Journal of Computational and Applied Mathematics **6** (1980), 19–26.

[DS11]   D. Dubbers and M. G. Schmidt, *The neutron and its role in cosmology and particle physics*, Reviews of Modern Physics **83** (2011), no. 4, 1111–1171.

[Dub91] D. Dubbers, *Tests of the standard model with free neutron beta decay*, Nuclear Physics A **527** (1991), no. 0, 239–250.

[Dzh05] S. N. Dzhosyuk, et al., *Determination of the neutron lifetime using magnetically trapped neutrons*, Journal Of Research Of The National Institute Of Standards And Technology **110** (2005), 339–343.

[Eki06] Jack Ekin, *Experimental techniques for low-temperature measurements*, Oxford University Press, 2006.

[Ezh01] V. F. Ezhov, et al., *Permanent-magnet trap for ultracold neutron storage*, Technical Physics Letters **27** (2001), no. 12, 1055–1057.

[Ezh05] V. F. Ezhov, *First ever storage of ultracold neutrons in a magnetic trap made of permanent magnets*, Journal of Research of the National Institute of Standards and Technology **110** (2005), 345–350.

[Ezh09] V. F. Ezhov, et al., *Magnetic storage of UCN for a measurement of the neutron lifetime*, Nuclear Instruments and Methods in Physics Research Section A: Accelerators, Spectrometers, Detectors and Associated Equipment **611** (2009), no. 2–3, 167 – 170.

[Fat75] P. P. Fatouros, et al., *Isotopically pure ^4He*, Cryogenics (1975), 147.

[FC56]   R. P. Feynman and M. Cohen, *Energy spectrum of the excitations in liquid helium*, Physical Review **102** (1956), no. 5, 1189–1204.

[Fer34] E. Fermi, *Versuch einer Theorie der β-Strahlen. I*, Zeitschrift für Physik A Hadrons and Nuclei **88** (1934), no. 3, 161–177.

[Fer36] _____, *Sul moto dei neutroni nelle sostanze idrogenate*, Ricerca scientifica **7** (1936), no. 2, 13–52.

[FGM58] R. P. Feynman and M. Gell-Mann, *Theory of the Fermi interaction*, Physical Review **109** (1958), no. 1, 193–198.

[Fie05] P. Fierlinger, *Losses and depolarization of stored ultracold neutrons on diamond-like carbon*, Ph.D. thesis, Universität Zürich, 2005.

[Fra09] K. Fraval, *Neutron life-time measurement using magnetic trapping of ultracold neutrons*, Internship Report, PHELMA, Grenoble INP, 2009.

[GGS58]   M. Goldhaber, L. Grodzins, and A. W. Sunyar, *Helicity of neutrinos*, Physical Review **109** (1958), no. 3, 1015–1017.

[GL93]   R. Golub and S. K. Lamoreaux, *Production and storage of ultracold neutrons in superfluid ^4He*, Physical Review Letters **70** (1993), no. 4, 517–517.

[Glü93]   F. Glück, *Measurable distributions of unpolarized neutron decay*, Physical Review D **47** (1993), no. 7, 2840–2848.

[Glü05]   F. Glück, et al., *The neutron decay retardation spectrometer aSPECT: Electromagnetic design and systematic effects*, The European Physical Journal A - Hadrons and Nuclei **23** (2005), 135–146, 10.1140/epja/i2004-10057-1.

[Gol79]   R. Golub, *On the storage of neutrons in superfluid ^4He*, Physics Letters A **72** (1979), no. 4-5, 387–390.

[Gol83]   R. Golub, et al., *Operation of a superthermal ultra-cold neutron source and the storage of ultra-cold neutrons in superfluid helium-4*, Zeitschrift für Physik B Condensed Matter **51** (1983), no. 3, 187–193.

[GP77]   R. Golub and J. M. Pendlebury, *The interaction of ultra-cold neutrons (UCN) with liquid helium and a superthermal UCN source*, Physics Letters A **62** (1977), no. 5, 337–339.

[GPS00]   H. Goldstein, C. Poole, and J. Safko, *Classical mechanics - 3rd ed.*, Addison Wesley, 2000.

[GRL91]   R. Golub, D. Richardson, and S. K. Lamoreaux, *Ultra-cold neutrons*, IOP Publishing Ltd., 1991.

[GT36]   G. Gamow and E. Teller, *Selection rules for the β-disintegration*, Physical Review **49** (1936), no. 12, 895–899.

[Hal80]   K. Halbach, *Design of permanent multipole magnets with oriented rare earth cobalt material*, Nuclear Instruments and Methods **169** (1980), no. 1, 1–10.

[HT09]   J. C. Hardy and I. S. Towner, *Superallowed $0^+ \rightarrow 0^+$ nuclear beta decays: A new survey with precision tests of the conserved vector current hypothesis and the standard model*, Physical Review C **79** (2009), no. 5, 055502–29.

[Huf00]   P. R. Huffman, et al., *Magnetic trapping of neutrons*, Nature **403** (2000), no. 6765, 62–64.

[Ign90]   Vladimir Kazimirovich Ignatovich, *The physics of ultracold neutrons*, Clarendon Press, Oxford, 1990.

[ILL08]   ILL, *The yellow book: Guide to neutron research facilities*, Institut Laue-Langevin, 2008.

[Ism10]   C. Ismerie, *Conception and characterization of a He-3 cryostat for the production of ultra-cold neutrons!*, Master's thesis, Grenoble INP Phelma, 2010.

[Ito07]   T. M. Ito, et al., *A multiwire proportional chamber for precision studies of neutron β decay angular correlations*, Nuclear Instruments and Methods in Physics Research Section A: Accelerators, Spectrometers, Detectors and Associated Equipment **571** (2007), no. 3, 676–686.

[Jac98]   J. D. Jackson, *Classical electrodynamics*, Wiley, 1998.

[JTW57]   J. D. Jackson, S. B. Treiman, and Jr. Wyld, H. W., *Possible tests of time reversal invariance in beta decay*, Physical Review **106** (1957), no. 3, 517–521.

[Kat05]   M. Katter, *Angular dependence of the demagnetization stability of sintered Nd-Fe-B magnets*, IEEE Transactions on Magnetics **41** (2005), no. 10, 1–3.

[KD66]   L. J. Kieffer and G. H. Dunn, *Electron impact ionization cross-section data for atoms, atomic ions, and diatomic molecules: I. Experimental data*, Rev. Mod. Phys. **38** (1966), 1–35.

[Kon11]   G. Konrad, et al., *Impact of neutron decay experiments on non-standard model physics*, Proceedings of the 5th International BEYOND 2010 Conference, Cape Town, South Africa (2010), Physics Beyond the Standard Models of Particles, Cosmology and Astrophysics (2011), 660–672.

[Kor02]   E. Korobkina, et al., *Production of UCN by downscattering in superfluid ^4He*, Physics Letters A **301** (2002), no. 5–6, 462–469.

[Kor07]   _____, *An ultracold neutron source at the NC State University PULSTAR reactor*, Nuclear Instruments and Methods in Physics Research Section A: Accelerators, Spectrometers, Detectors and Associated Equipment **579** (2007), no. 1, 530–533.

[Lak]   Lakeshore, *Cernox sensor specifications*, `http://www.lakeshore.com/products/cryogenic-temperature-sensors/cernox/models/pages/overview.aspx`.

[Lak04]   Lake Shore Cryotonics, Inc., *Model 460 3-channel gaussmeter user's manual*, `http://www.lakeshore.com`, May 2004.

[Lam60]   J. H. Lambert, *Photometria sive de mensura et gradibus luminis colorum et umbra*, Eberhard Klett, Augsburg, 1760.

[Lan41]   L. Landau, *Theory of the superfluidity of helium II*, Physical Review **60** (1941), no. 4, 356–358.

[LBCB09] G. Le Bec, J. Chavanne, and C. Benabderrahmane, *Simulation of NdFeB permanent magnets at low temperature*, Proceedings of PAC09, Vancoucer, BC, Canada **T15** (2009), 1–3.

[Leo87]   William R. Leo, *Techniques for nuclear and particle physics experiments*, Springer-Verlag Berlin Heidelberg, 1987.

[Les09]   A. Lesov, *The weak force: From Fermi to Feynman*, ArXiv e-prints (2009), `http://arxiv.org/abs/0911.0058`.

[Leu10]   K. Leung, *Storage of ultra-cold neutrons using a permanent octupole magnet*, Institut Laue-Langevin Experimental Report **3-14-257** (2010), no. 10/2008, 1–4.

[LG93]   S. K. Lamoreaux and R. Golub, *Angular distribution of ultracold neutrons produced by scattering of cold neutrons in superfluid ^4He*, JETP Letters **58** (1993), no. 10, 792.

[LG02]   S. K. Lamoreaux and R. Golub, *Calculation of the ultracold neutron upscattering loss probability in fluid walled storage bottles using experimental measurements of the liquid thermomechanical properties of fomblin*, Phys. Rev. C **66** (2002), 044309.

[Liu10]   J. Liu, et al. (The UCNA Collaboration), *Determination of the axial-vector weak coupling constant with ultracold neutrons*, Phys. Rev. Lett. **105** (2010), 181803.

[LY56]   T. D. Lee and C. N. Yang, *Question of parity conservation in weak interactions*, Physical Review **104** (1956), no. 1, 254–258.

[LZ09]   K. Leung and O. Zimmer, *Proposed neutron lifetime measurement using a hybrid magnetic trap for ultra-cold neutrons*, Nuclear Instruments and Methods in Physics Research Section A: Accelerators, Spectrometers, Detectors and Associated Equipment **611** (2009), no. 2-3, 181–185.

[Mar73]   H. J. Maris, *Hydrodynamics of superfluid helium below 0.6 K. II. velocity and attenuation of ultrasonic waves*, Physical Review A **8** (1973), no. 5, 2629–2639.

[Mär09]   B. Märkisch, et al., *The new neutron decay spectrometer Perkeo III*, Nuclear Instruments and Methods in Physics Research Section A: Accelerators, Spectrometers, Detectors and Associated Equipment **611** (2009), no. 2–3, 216–218.

[Mär10]   B. Märkisch, *Private communication*, 2010.

[Mas11]   Y. Masuda, et al., *A new He-II spallation UCN source*, 8th International Workshop on "Ultracold & Cold Neutrons. Physics & Sources", St. Petersburg - Moscow (not peer-reviewed presentation of proceedings), June 2011.

[Mas12]   ———, *Spallation ultracold neutron source of superfluid helium below 1 K*, Phys. Rev. Lett. **108** (2012), 134801.

[Mat08]   R. Matsumiya, et al., *Measurement of UCN energy spectrum of He-II spallation UCN source*, Osaka University Laboratory of Nuclear Studies, Annual Report (2008), 1–2.

[Mat09]   ———, *Analysis of energy spectrum of UCN from he-ii spallation UCN source*, Osaka University Laboratory of Nuclear Studies, Annual Report (2009), 1–2.

[MD72]   L. P. Mezhov-Deglin, *An apparatus for producing pure ^4He*, Cryogenics (1972), 311.

[Mee06]   D. C. Meeker, *Finite element method magnetics (FEMM), version 4.0.1 (build 03 dec)*, `http://www.femm.info`, 2006.

[Nak96]   H. Nakai, et al., *Superfluid helium flow through porous media*, Cryogenics **36** (1996), no. 9, 667.

[Nak10]   K. Nakamura, et al. (Particle Data Group), *The review of particle physics*, Journal of Physics G: Nuclear and Particle Physics **37** (2010), no. 075021, .

[Nic05]   J. S. Nico, et al., *Measurement of the neutron lifetime by counting trapped protons in a cold neutron beam*, Physical Review C **71** (2005), no. 5, 055502–.

[Nic09]   J. S. Nico, *Neutron beta decay*, Journal of Physics G: Nuclear and Particle Physics **36** (2009), no. 10, 104001.

[OEC12]   OECD Nuclear Energy Agency, *Joint evaluated fission and fusion file project (JEFF-3.1.1)*, www.oecd-nea.org/dbdata/jeff, 2012.

[Oer]   Oerlikon Leybold Vacuum GmbH, *Leybold ceravac CTR100*, http://www.oerlikon.com/leyboldvacuum/products/produktkatalog_03.aspx?cid=60_30_10_20.

[Pat09]   R. W. Pattie, et al., *First measurement of the neutron β asymmetry with ultracold neutrons*, Phys. Rev. Lett. **102** (2009), 012301.

[Pau89]   W. Paul, et al., *Measurement of the neutron lifetime in a magnetic storage ring*, Zeitschrift für Physik C Particles and Fields **45** (1989), no. 1, 25–30.

[Pau09]   S. Paul, *The puzzle of neutron lifetime*, Nuclear Instruments and Methods in Physics Research Section A: Accelerators, Spectrometers, Detectors and Associated Equipment **611** (2009), no. 2-3, 157–166.

[Phe90]   A.V. Phelps, *Cross sections and swarm coefficients for H^+, H_2^+, H_3^+, H, H_2, and H^- in h_2 for energies from 0.1 eV to 10 keV.*, Journal of Physical and Chemical Reference Data **19** (1990), no. 3, 653–675.

[Pic10]   A. Pichlmaier, et al., *Neutron lifetime measurement with the UCN trap-in-trap MAMBO II*, Physics Letters B **693** (2010), no. 3, 221–226.

[Pie]   Florian Piegsa, *Private communication*.

[Pla08]   B. Plaster, et al., *A solenoidal electron spectrometer for a precision measurement of the neutron -asymmetry with ultracold neutrons*, Nuclear Instruments and Methods in Physics Research Section A: Accelerators, Spectrometers, Detectors and Associated Equipment **595** (2008), no. 3, 587 – 598.

[PNHN08]   Yu. N. Pokotilovskii, I. Natkaniec, and K. Holderna-Natkaniec, *The experimental and calculated density of states and UCN loss coefficients of perfluoropolyether oils at low temperatures*, Physica B: Condensed Matter **403** (2008), no. 10–11, 1942 – 1948.

[Pob07]   Frank Pobell, *Matter and methods at low temperatures*, Spring, 2007.

[PR50]   E. M. Purcell and N. F. Ramsey, *On the possibility of electric dipole moments for elementary particles and nuclei*, Physical Review **78** (1950), no. 6, 807–807.

[Pre]   Presspahn Ltd., *High quality synthetic phenolic resin bonded paper (p3) properties*, http://www.presspahn.com/Products/SRBP/P3.htm.

[Pri83]   D. E. Pritchard, *Cooling neutral atoms in a magnetic trap for precision spectroscopy*, Physical Review Letters **51** (1983), no. 15, 1336–1339.

[Ric91]   D. J. Richardson, et al., *Measurement of the energy dependence of the neutron loss per bounce function on reflection from oil and grease surfaces using monochromatic ultracold neutrons*, Nuclear Instruments and Methods in Physics Research Section A: Accelerators, Spectrometers, Detectors and Associated Equipment **308** (1991), no. 3, 568 – 573.

[RMS08]   M. J. Ramsey-Musolf and S. Su, *Low-energy precision tests of supersymmetry*, Physics Reports **456** (2008), no. 1-2, 1–88.

[Rob09]   Owen Roberts, *Development and troubleshooting for a neutron trap made of permanent magnets*, Work placement report, Prifysgol Aberystwyth University., 2009.

[Rosa]   Felix Rosenau, *Private communication*.

[Rosb]   ———, *Private communication and internal group document*.

[Ruo11]   Sami Ruoho, *Modeling demagnetization of sintered NdFeB magnet material in time-discretized finite element analysis*, Ph.D. thesis, Aalto University, School of Electrical Engineering, Janurary 2011.

[Sau04]   A. Saunders, et al., *Demonstration of a solid deuterium source of ultra-cold neutrons*, Physics Letters B **593** (2004), no. 1–4, 55–60.

[SAZ09]   P. Schmidt-Wellenburg, K.H. Andersen, and O. Zimmer, *Ultra cold neutron production by multiphonon processes in superfluid helium under pressure*, Nuclear Instruments and Methods in Physics Research Section A: Accelerators, Spectrometers, Detectors and Associated Equipment **611** (2009), no. 2-3, 259–262.

[SBNC06] N. Severijns, M. Beck, and O. Naviliat-Cuncic, *Tests of the standard electroweak model in nuclear beta decay*, Reviews of Modern Physics **78** (2006), no. 3, 991–50.

[Sch09]   P. Schmidt-Wellenburg, et al., *Ultracold-neutron infrastructure for the gravitational spectrometer GRANIT*, Nuclear Instruments and Methods in Physics Research Section A: Accelerators, Spectrometers, Detectors and Associated Equipment **611** (2009), no. 2-3, 267–271.

[Sch12]   ———, *Experimental study of ultracold neutron production in pressurized superfluid helium*, (Draft version only. To be published.) (2012), .

[SDG55]   H. S. Sommers, J. G. Dash, and L. Goldstein, *Transmission of slow neutrons by liquid helium*, Physical Review **97** (1955), no. 4, 855.

[Ser03]   A. P. Serebrov, et al., *Low-energy heating of ultracold neutrons during their storage in material bottles*, Physics Letters A **309** (2003), no. 3–4, 218–224.

[Ser05] ———, *Measurement of the neutron lifetime using a gravitational trap and a low-temperature fomblin coating*, Physics Letters B **605** (2005), no. 1-2, 72–78.

[Ser08] ———, *Neutron lifetime measurements using gravitationally trapped ultracold neutrons*, Physical Review C **78** (2008), no. 3, 035505.

[Ser09] ———, *Ultracold-neutron infrastructure for the PNPI/ILL neutron EDM experiment*, Nuclear Instruments and Methods in Physics Research Section A: Accelerators, Spectrometers, Detectors and Associated Equipment **611** (2009), no. 2–3, 263–266.

[Ser11] A. P. Serebrov, *Supersource of ultracold neutrons at the WWR-M reactor and the program of fundamental research in physics*, Crystallography Reports **56** (2011), no. 7, 1230–1237.

[Sev04] N. Severijns, *Weak interactions studies by precision experiments in nuclear beta decay*, Lecture Notes in Physics **651** (2004), 339.

[Sim07] M. Simson, et al., *Detection of low-energy protons using a silicon drift detector*, Nuclear Instruments and Methods in Physics Research Section A: Accelerators, Spectrometers, Detectors and Associated Equipment **581** (2007), no. 3, 772–775.

[Sim10] M. Simson, *Measurement of the electron antineutrino angular correlation coefficient a with the neutron decay spectrometer aspect*, Ph.D. thesis, Technischen Universität München, 2010.

[SM58] E. C. G. Sudarshan and R. E. Marshak, *Chirality invariance and the universal fermi interaction*, Physical Review **109** (1958), no. 5, 1860–1862.

[SM89] A. Steyerl and S. S. Malik, *Sources of ultracold neutrons*, Nuclear Instruments and Methods in Physics Research Section A: Accelerators, Spectrometers, Detectors and Associated Equipment **284** (1989), no. 1, 200–207.

[Ste86] A. Steyerl, et al., *A new source of cold and ultracold neutrons*, Physics Letters A **116** (1986), no. 7, 347–352.

[Ste02] ———, *Experimental study of quasi-elastic scattering of ultracold neutrons*, The European Physical Journal B - Condensed Matter and Complex Systems **28** (2002), 299–304, 10.1140/epjb/e2002-00233-7.

[Str00] A.V Strelkov, et al., *Identification of a new escape channel for ucn from traps*, Nuclear Instruments and Methods in Physics Research Section A: Accelerators, Spectrometers, Detectors and Associated Equipment **440** (2000), no. 3, 695 – 703.

[Suo06] P. Suominen, *Modified multipole structure for electron cyclotron resonance ion sources*, Ph.D. thesis, University of Jyväskylä, 2006.

[SW09] Philipp Schmidt-Wellenburg, *Production of ultra-cold neutrons in superfluid helium under pressure*, Ph.D. thesis, Technische Universität München, 2009.

[SWZ06] P. Schmidt-Wellenburg and O. Zimmer, *Helium liquefaction with a commercial 4K Gifford-McMahon cryocooler*, Cryogenics **46** (2006), no. 11, 799–803.

[Tho53] W. Thomson, *On the thermal effects of fluids in motion*, Philosophical Transactions of the Royal Society of London **143** (1853), 357–365.

[TM04] Stephan T. Thornton and Jerry B. Marion, *Classical dynamics of particles and systems 5th ed.*, Brooks/Cole, Thomson, 2004.

[Tri00] U. Trinks, et al., *Concepts of UCN sources for the FRM-II*, Nuclear Instruments and Methods in Physics Research Section A: Accelerators, Spectrometers, Detectors and Associated Equipment **440** (2000), no. 3, 666–673.

[TS00] Tatsuo Tabata and Toshizo Shirai, *Analytic cross sections for collisions of H^+, H_2^+, H_3^+, H, H_2, and H with hydrogen molecules*, Atomic Data and Nuclear Data Tables **76** (2000), no. 1, 1 – 25.

[Umr98] Walter Umrath, *Fundamentals of vacuum technology*, Leybold, 1998.

[Vac] Vacuumschmelze GmbH., *Rare-earth permanent magnets Vacodym and Vacomax catalogue*, http://www.vacuumschmelze.de.

[VL] The Vacuum Lab, *Gas loads from elastomer and metal seals*, http://www.vacuumlab.com/Articles/Gas%20Loads%20Elastomer-Metal%20Seals.pdf.

[Vla61] V. V. Vladimirskii, *Magnetic mirrors, channels and bottles for cold neutrons.*, Sov. Phys. JETP **12** (1961), 740–746.

[VR08] Guglielmo Ventura and Lara Risegari, *The art of cryongenics, low-temperature experimental techniques*, Elsevier, 2008.

[WG11] F. E. Wietfeldt and G. L. Greene, *Colloquium: The neutron lifetime*, Reviews of Modern Physics **83** (2011), no. 4, 1173–1192.

[Wu 57] C. S. Wu ,et al., *Experimental test of parity conservation in beta decay*, Physical Review **105** (1957), no. 4, 1413–1415.

[Yan06] Liang Yang, *Towards precision measurement of the neutron lifetime using magnetically trapped neutrons*, Ph.D. thesis, Harvard University, 2006.

[Yao06] W. M. Yao, et al. (Particle Data Group), *Review of Particle Physics*, Journal of Physics G **33** (2006), 1+.

[YNG05] H. Yoshiki, H. Nakai, and E. Gutsmiedl, *A new superleak to remove ^3He for UCN experiments*, Cryogenics **45** (2005), no. 6, 399–403.

[Yos92] H. Yoshiki, et al., *Observation of ultracold-neutron production by 9Å cold neutrons in superfluid helium*, Physical Review Letters **68** (1992), no. 9, 1323.

[Yos93] H. Yoshiki, *Yoshiki et al . reply*, Phys. Rev. Lett. **70** (1993), 518–518.

[You01]   A. R. Young, *Fundamental physics with pulsed neutron beams*, edited by C. R. Gould, G. L. Greene, F. Plasil and W. M. Snow. (Singapore: World Scientific), 2001.

[Zen32]   Clarence Zener, *Non-adiabatic crossing of energy levels*, Proceedings of the Royal Society of London. Series A **137** (1932), no. 833, 696–702.

[Zim00]   O. Zimmer, *A method of magnetic storage of ultra-cold neutrons for a precise measurement of the neutron lifetime*, Journal of Physics G: Nuclear and Particle Physics **26** (2000), no. 1, 67–77.

[Zim05]   O. Zimmer, *Transmission of ultra-cold neutrons through a weakly absorbing foil*, Nuclear Instruments and Methods in Physics Research Section A: Accelerators, Spectrometers, Detectors and Associated Equipment **554** (2005), no. 1-3, 363–373.

[Zim07]   O. Zimmer, et al., *Superfluid-helium converter for accumulation and extraction of ultracold neutrons*, Physical Review Letters **99** (2007), no. 10, 104801–4.

[Zim10]   _____, *Ultracold neutrons extracted from a superfluid-helium converter coated with fluorinated grease*, Eur. Phys. J. C **67** (2010), 589–599.

[ZPI11]   O. Zimmer, F. M. Piegsa, and S. N. Ivanov, *Superthermal source of ultracold neutrons for fundamental physics experiments*, Physical Review Letters **107** (2011), no. 13, 134801.